MODELING FOR THE SIMULATION AND CONTROL OF NUCLEAR REACTOR ROCKET SYSTEMS

by

JONATHAN KEAY WITTER

B.S., Nuclear Engineering, Rensselaer Polytechnic Institute (1982)
M.E., Nuclear Engineering, Rensselaer Polytechnic Institute (1983)

SUBMITTED TO THE DEPARTMENT OF NUCLEAR ENGINEERING
IN PARTIAL FULFILLMENT OF THE REQUIREMENTS
FOR THE DEGREE OF

DOCTOR OF PHILOSOPHY

at the

MASSACHUSETTS INSTITUTE OF TECHNOLOGY

April, 1993

Signature of Author ______________________
Department of Nuclear Engineering
April 30, 1993

Certified by ______________________
David D. Lanning, Ph.D.
Professor of Nuclear Engineering
Thesis Supervisor

Certified by ______________________
John E. Meyer, Ph.D.
Professor of Nuclear Engineering
Thesis Supervisor

Accepted by ______________________
Allan F. Henry, Ph.D.
Chairman, Departmental Committee on Graduate Studies

MODELING FOR THE SIMULATION AND CONTROL OF NUCLEAR REACTOR ROCKET SYSTEMS

by

Jonathan Keay Witter

Submitted to the Department of Nuclear Engineering on April 30, 1993
in partial fulfillment of the requirements for the degree of
Doctor of Philosophy

Abstract

The recent interest in space exploration to Mars has renewed the development of the nuclear reactor rocket engine concepts. The Nuclear Engine for Rocket Vehicle Application (NERVA) program of the early sixties completed several ground tests of the engine systems and developed several computer simulation models in parallel for design studies. New engine concepts, new computer technology, and higher experimental test costs make it necessary for new simulation models to be developed. These can be used to study the steady state and transient behavior of the reactor fuel type and engine systems. Several computer codes, existing and under development, are reviewed in this report for their applicability. This research focused on the development of thermal hydraulic and power models for the Particle Bed Reactor (PBR) fuel element and of an engine system capable of utilizing NERVA or PBR concept fuel geometry.

A one dimensional model for the PBR fuel element has been developed that utilizes the Ergun relation for pressure drop and the Achenbach correlation for the heat transfer in a packed bed of spheres. The single element models include the inlet plenum region, the porous outer retention wall (cold frit), the packed bed of fuel particles, the inner porous retention wall (hot frit), and the outlet channel. The NASA hydrogen properties routine, NBSpH2, is used to determine the state conditions of the gas from enthalpy and pressure inputs. The models have been benchmarked to earlier work for steady state and transient cases. The advancements completed in this research include adding point kinetics and the MIT/SNL control laws to simulate reactor power and allowing multiple transients of the element flow stream boundary conditions. The model was also utilized to perform flow instability studies, by iteratively determining the minimis of the pressure drop versus flow rate curve at different element power levels. By plotting the temperature rise factor and fuel region inlet Reynolds number found at this minimis, a flow stability map can be generated that delineates possible stable/unstable operation regions. The maps are used to determine element design and operational constraints during startup and shutdown. A two dimensional computer model of the PBR element, SIMBED, developed by U. Mass. Lowell and Brookhaven National Laboratory, was used to study the flow behavior in the element. The code was modified to model cold frit flow resistance distributions, non-uniform power shapes, and single node void fraction perturbations. Graphical presentation of the results of studies on these modifications show the impact of these element design features on the thermal hydraulic performance.

A full engine thermal hydraulic model has also been developed in this research. The engine system modeled is a expander/topping cycle in which the turbopump drive energy is derived from a portion of the propellant flow before it reaches the reactor and after it has been heated from cooling segments of the rocket nozzle and the reflector region. The user is able to define the flow path geometry; heat volume material properties; turbo-pump, turbine bypass control valve, and control drum performance; and reactor type for a predefined system configuration. Steady state versions are used to model the bleed flow and pump flow operation. Results from these cases are used to generate nozzle chamber pressure and temperature operating maps that indicate allowed powers and flows of the rocket engine. The transient simulation model has been benchmarked to computer codes and data curves from the NERVA program and has been extended to the PBR concept. The simulation provides insights to the interrelation of the various components and controllers and the performance capability of a particular engine under user defined power increase and decrease transients.

This research was made possible through the NASA Graduate Student Researcher Program funded by the Nuclear Propulsion Office, NASA Lewis Research Center, Cleveland, OH. Additional support was provided by the MIT Nuclear Engineering Department.

Thesis Supervisor: David D. Lanning
Title: Professor of Nuclear Engineering

Thesis Supervisor: John E. Meyer
Title: Professor of Nuclear Engineering

Acknowledgments

I would first like thank my thesis supervisors Professor David L. Lanning and Professor John E. Meyer for their guidance and interest in my work over the years. It was always easy to stop in and discuss the latest results and the next area to attack. I was fortunate enough to enter MIT during the cycle that Professor Neil Todreas was teaching the thermal hydraulic classes and Professor Allan Henry was teaching the reactor physics classes. I thank them for their "concise but precise" discourses.

Acknowledgments are also extended to my fellow students who helped make nuclear engineering at MIT enjoyable: Dr. Jess Gehin for showing me the ways of Athena; Dr. Mark Byers for the thermal hydraulic discussions over at the Thirsty Ear; Tom "D'oh" Delorey and Santiago "Jimmy" Parra for making the "Room of Pain" not so painful; Tim Lawrence and Dave Suzuki for their Air Force SNTP connections; and finally the gang that always invaded the office in the afternoons so I had to work late at night. The wonders of email and internet require me to thank Dr. Mike Houts at Los Alamos National Laboratory for the arrangement of a computer account. The Sigma Alpha Epsilon undergraduates at Rensselaer also deserve credit for keeping this old man young enough to complete his studies (and no, it did not take me ten years).

I would also like to thank John Clark at the Nuclear Propulsion Office of NASA Lewis Research Center for financial support and for allowing me the freedom to pursue research in space nuclear propulsion. James Walton, also at NASA Lewis, deserves thanks for sending the NASA computer codes and obtaining many of the NERVA program reports reviewed during this research.

To my parents, thanks for putting up with my idiosycnchrosies and supporting my pursuits. I guess now I can finally say I understand those equations dad used to bring home in the Journal of Naval Engineering.

Finally, I would like to dedicate this thesis to the memory of Don Farkouh and Stewart Guild, whose tragic losses in 1989 and 1993 made me more determined to pursue my goal for a doctorate and made me realize that life is to short not to dedicate yourself to learning, to doing all that one can, and to enjoying life to the fullest. This is true, despite my favorite lines from Goethe's Faust -

Habe nun, ach! Philosophie,
Juristerei und Medizin
Und leider auch Theologie
Durchaus studiert mit heißem Bemühn.
Da steh ich nun, ich armer Tor!
Und bin so klug als wie zuvor.......

Biographical Note

Jonathan K. Witter was born on August 23, 1960, in Honolulu, Hawaii. He spent many years traveling around the East Coast as a Coast Guard brat and gaining an appreciation for math and science. He graduated from J. P. McCaskey High School in Lancaster, Pennsylvania in 1978.

The author attend Rensselaer Polytechnic Institute in Troy, New York, where he studied nuclear engineering. He was inducted into Alpha Nu Sigma and Tau Beta Pi as an undergraduate and was awarded the Erwin R. Gaerttner Prize in recognition of outstanding achievement and promise for a successful career. The author was awarded a Bachelor of Science, Cum Laude, in Nuclear Engineering with a Minor in German in May 1982. The following year, he was awarded a Master of Engineering in Nuclear Engineering from the same institute.

The author worked at Knolls Atomic Power Laboratory as a Nuclear Plant Engineer for Training from 1983 to 1985. He then worked for the New York Power Authority as a Reactor Engineer at the James A. FitzPatrick Nuclear Power Plant until 1989. In September of 1989, the author enrolled in graduate school in the Nuclear Engineering Department at Massachusetts Institute of Technology.

During the years of 1990 through 1993, the author became involved with the NASA Nuclear Thermal Propulsion community and was awarded the NASA Space Grant Fellowship and a NASA Graduate Student Researcher Fellowship for the completion of his thesis research. This research involved the modeling of the Particle Bed Reactor fuel element and the engine systems for nuclear thermal propulsion.

Publications:

J. K. Witter, D. D. Lanning, J. E. Meyer, "Flow Stability Analysis of a Particle Bed Reactor Fuel Element," in Proceedings of Tenth Symposium on Space Nuclear Power and Propulsion, CONF-930103, M. S. El-Genk and M. D. Hoover, eds., American Institute of Physics, New York, 1993 1541.

Table of Contents

List of Tables

List of Figures

Chapter One - Introduction

1.1 Introduction

Nuclear Thermal Propulsion for space vehicles may sound futuristic, but is actually a concept which was well developed during the 1960's and early 1970's. The Nuclear Engine for Rocket Vehicle Application (NERVA) program tested a series of rocket engines and was ready to produce a flight engine when the program was canceled in 1972. The advantage of using a nuclear reactor to heat the gaseous propellant is that the lowest molecular weight gas (hydrogen) can be used and higher temperatures (above 2500K) can be reached to give higher specific impulses (Isp). Typical chemical systems are limited by the chemical reaction to 500 seconds Isp while solid core nuclear rockets can obtain in excess of 1000 seconds of Isp.

In the Summer of 1989, President Bush announced the Space Exploration Initiative (SEI) to coincide with the 20th anniversary of the first manned landing on the moon. The plan was to return to the Moon by the end of the century and use it as a stepping stone to reach Mars by 2019. In order to meet most mission requirements for a Mars mission, the Stafford report recommended using nuclear propulsion [S-1]. This prompted an effort by the National Aeronautic and Space Administration (NASA) Lewis Research Center to resurrect the old nuclear propulsion documentation and analytical methods, as well prompt investigations of new core designs. Among the key issues were the evaluation of the thermal hydraulic and neutronic calculation capability for both design and transient studies and the improvement of the control strategy methods of the rocket for a proposed unmanned first mission.

This report presents work completed towards understanding rocket behavior and improving modeling of the engine systems.

1.1.1 Nuclear Thermal Propulsion

1.1.1.1 History - The NERVA Program

The NERVA program was an effort by NASA and the then Atomic Energy Commission (AEC) to develop the feasibility of a nuclear thermal propulsion system. The goals of the program were to assess the real performance and operating characteristics of the engine concepts. Because exact missions were not specified, the range of power levels and operating conditions was large to ensure the performance was understood and could be predicted for new designs[R-1].

A series of nuclear rocket system tests were performed at Jackass Flats, Nevada. These tests were successful in proving that such systems could be built and controlled. A summary of the test program dates and accomplishments is presented in Table 1.1[B-1]. A comprehensive summary of experience gained during the NERVA program and a useful reference listing for various aspects of the program is contained in Reference [K-1]. The test program performance records are summarized in Table 1.2[K-1].

Table 1.1 Summary of NERVA Reactor/Engine Test Program

Date of Testing	*Test Article*	*Maximum Power (MWth)*	*Time at Maximum Power*	*Max. Fuel Exit Temp. (K)*
July 1, 1959	KIWI-A	70	5 min.	
July 8, 1960	KIWI-A	85	6 min.	
October 10, 1960	KIWI-A3	100	5 min.	
December 7, 1961	KIWI-B1A	300	30 sec.	
September 1, 1962	KIWI-B1B	900	Several sec.	
November 30, 1962	KIWI-B4A	500	Several sec.	
May 13, 1964	KIWI-B4D	1000	40 sec.	2222
July 28, 1964	KIWI-B4E	900	8 min.	2389
September 10, 1964	KIWI-B4E	900	2.5 min. restart	
September 24, 1964	NRX-A2	1100	3.4 min.	2300
October 15, 1964	NRX-A2	Restart	(mapping)	
April 23, 1965	NRX-A3	1165	3.5 min.	
May 20, 1965	NRA-A3	1122	13 min.	2450
May 28, 1965	NRX-A3	≤500	1.5 min.(28.5 min.)	
June 25, 1965	PHOEBUS 1A	1090	10.5 min.	2478
March 2,16,23, 1966	NRX-EST	1100	1.5, 14.5, 8 min.	2450
June 23, 1966	NRX-A5	1140	15.5, 14.5 min.	2450
February 23, 1967	PHOEBUS 1B	1500	30 min.	2445
December 13, 1967	NRX-A6	1100	62 min.	2550
June 26, 1968	PHOEBUS 2A	4300	12 min.	2306
December 3-4, 1968	PEWEE	514	40 min.	2750
June 11, 1969	XE-PRIME	1100	11 min.	2450
June 29 - July 27, 1972	NUCLEAR FURNACE	44	109 min. (4 tests)	2450

Table 1.2 Performance Records for the NERVA Engine Test Program

PARAMETER	*VALUE*
Power (Phoebus-2A)	4100 MW
Thrust (Phoebus-2A)	930 kN
Hydrogen Flow Rate (Phoebus-2A)	120 kg/s
Equivalent Specific Impulse (Pewee)	845 s
Minimum Specific Mass (Phoebus-2A)	2.3 kg/MW
Average Coolant Exit Temperature (Pewee)	2550 K
Peak Fuel Temperature (Pewee)	2750 K
Core Average Power Density (Pewee)	2340 MW/m^3
Peak Fuel Power Density (Pewee)	5200 MW/m^3
Accumulated time at Full Power (NF-1)	109 min
Greatest Number of Restarts (XE)	28

1.1.1.2 Current Efforts - SEI, SNTP

During the later 1970's and early 1980's not much work was performed on nuclear propulsion. The SEI announcement provided a catalyst for renewing the work of the NERVA program. The NASA Lewis Research Center's Nuclear Propulsion Office (NPO) is the project office for the civilian side of nuclear propulsion. The mission of this office is to coordinate the joint efforts of NASA, the Department of Energy (DOE) and, the Department of Defense (DOD). They have sponsored research projects at universities and aerospace contractors to evaluate the technology readiness level (TRL) of the propulsion concepts. In the Summer of 1990 a workshop was held to assemble the various concept groups and to institute working groups for safety, test facilities, fuels development, and modeling[C-1]. After reviewing diverse concepts such as the NERVA reactor, particle bed reactor, wire core, cermet core, and gaseous core, the candidates with the highest evaluated readiness levels were the "NERVA derivative" and "particle bed" concepts. These concepts are described in detail in Chapters 3 and 4.

The Air Force Phillips Laboratory is the lead center for the DOD Space Nuclear Thermal Propulsion (SNTP) program. The SNTP concept is based on the particle bed reactor. The particle bed reactor is believed to be able to operate at much higher chamber temperatures and power densities, and thus with improved performance, due to the high heat transfer surface area of the packed bed of coated fuel particles[P-1]. The Air Force program was originally a classified project, but a version of the program was declassified in January of 1992 at the 9th Space Nuclear Power Symposium in Albuquerque, New Mexico. The program goals are to bring the particle bed concept through a series of experiments to evaluate the behavior of reactor physics, the properties of fuel materials, the dynamics of single element gas flow, and the operation of a prototypic engine system. The single element flow tests, named Nuclear Element Tests (NET), are expected to be completed over the course of 1993 and 1994. The full core test of a 7 element core, named PBR Integrated Performance Element Test (PIPET), are planned to be initiated in 1996, based upon the availability of a test facility that meets the environmental regulations of the 1990's.

Both the SEI and SNTP programs are directed at developing the nuclear thermal propulsion technologies. The primary investigations to be carried out involve 1) high temperature, long life fuels, 2) low mass, high performance nozzles, 3) high efficiency, low mass turbo-pumps, and 4) reliable, autonomous control and health management systems[W-1]. In order to evaluate and predict performance of designs, models of the varying detail are required. The next section provides a discussion on some of these models.

1.1.2 Thermal Hydraulic Modeling

1.1.2.1 History - NERVA

Aerojet General and Westinghouse were the lead contractors for the NERVA engine program. In order to minimize costs of the program, a large effort was made in developing analytical tools. Parallel with the testing and designing, computer codes were being developed to benchmark results and to predict the response of new designs. The analytic tools included large detailed digital computer codes, simplified models, and analog simulations. The simple models were used for trend analysis, the analog computers for controller analysis, and the detailed codes were used to confirm and refine test results. The simulations proved to be valuable resources over the course of the program in predicting system oscillations and understanding engine conditions that did not meet the initial expectations[M-1]. The lessons learned from the close cooperation between the test engineers and the design engineers have been carried forward to the current nuclear thermal propulsion program, as will be discussed in the next section. A summary of the design and analysis techniques is contained in Reference [W-5].

1.1.2.2 Current Efforts - Nuclear Propulsion Office, NASA Lewis

During the Summer of 1991, several efforts began for the modeling of nuclear thermal propulsion systems. At NASA Lewis, the Core Analytic Code (CAC), originally written in 1960, was resurrected from hardcopy text to a working computer program[C-2,W-1]. The NPO also began an effort to combine a detailed reactor code from Westinghouse, with a detailed rocket engine code from Science Application International Corporation (SAIC). This effort resulted in the Nuclear Engine System Simulation (NESS) code, that solves for an optimized system design from a given input of a state performance point[P-2]. However, any code to model the engine system must have adequate models for the gas propellant used. James Walton at NASA Lewis has developed a subroutine package for the hydrogen properties bases on National Bureau of Standards (NBS) that is applicable over a wide range of temperatures and pressures[W-2].

A joint NASA-DOE-DOD team was formed to develop and implement a plan of action to bring modeling of the engine systems to ever greater levels of detail for design[W-3]. The phases of this program are outlined in Table 1.3.

Table 1.3 Levels of Model Development for Nuclear Thermal Propulsion

Level I	Relatively simple parametric system modelling primarily to be used for steady state performance.	3/92 - 4/93
Level II	Near term, detailed transient system analysis using point kinetics for reactor dynamics; couple to neutronic multidimensional calculations in later stages of development.	9/92 - 6/93
Level III	Far term transient models that include multi-dimensional neutronics and two phase and multidimensional thermal hydraulics.	10/92 - 1/96
Level IV	Similar to Level III, but the geometries and reactivities are tailored to an actual experimental or flight engine.	6/96 - 7/97
Level V	Envisioned as a real time, transient simulation for the experimental or flight engine for possible operator training and/or performance review.	6/96 - 4/99

Level I of this NASA-DOE-DOD project is nearly completed and the Sandia National Laboratories code System Analysis Flow SIMulator (SAFSIM) has been selected as the foundation for the Level I modeling. Other possible computer codes are listed in the next section.

1.1.2.3 Existing Codes

There are several computer codes being developed to study the nuclear thermal propulsion rocket systems. The rocket companies are trying to adapt their chemical rocket codes to utilize a reactor core instead of a combustion chamber. Pratt & Whitney is adapting the ROCket Engine Transient Simulation (ROCETS) code to include reactor component modules. They are also working with the University of Florida to couple their code with a spatial neutronics and have a steady state model of the Pratt & Whitney XNR2000 advanced design engine concept[A-1].

John Clark at NASA Lewis developed a code that predicts the temperatures and pressures for a core with axial hydrogen flow and circular passages. It has been shown to provide good agreement with experimental and analytical results for the NRX reactor experiments[C-3]. Known as CAC, it requires the input of the power, flow and inlet pressure and temperature as boundaries at various time points, so it is intended for use with other system analysis codes and for simulating thermal hydraulic response to a known transient.

More general codes allow the user to define the system. An adaptation of the RELAP5 code to space systems called ATHENA, is a code developed at the Idaho National Engineering Laboratory (INEL)[I-1]. This code is more suited for closed loop systems such as the SP-100 or TOPAZ electric power reactors, but can model open systems as well. Dean Dobranich at Sandia National Laboratories has developed a program for the simulation of generic flow systems, known as SAFSIM[D-1]. It has been used by Sandia to help model the particle bed reactor and recently was benchmarked to steady state NERVA NRX-1A test conditions[W-4, L-1]. Another code developed for the particle bed reactor is SIMBED. It is a two-dimensional code developed by the University of Massachusetts- Lowell and Brookhaven National Laboratory that models the fuel element[C-4]. These major codes will be discussed in more detail in Section 1.2.

1.1.3 Operational Considerations

1.1.3.1 General Requirements

The rocket engine must be capable of operating over a broad range of power conditions and be able to maneuver quickly to ensure the desired mission thrust and Isp profiles can be met[M-1]. Because no specific mission has been specified, the NASA Lewis Nuclear Propulsion Office has established generic design goals for a nuclear rocket system. The top level requirements for a single rocket engine are presented in Table 1.4[N-1].

Table 1.4 Top Level Nuclear Thermal Propulsion Engine Requirements

PARAMETER	*REQUIREMENT*
Thrust	100kN - 350kN
Thrust/Weight (w/Internal Shield)	≥ 4
Specific Impulse	≥ 850 seconds
Throttling	25% Thrust @ Rated Temperature
Reuse	Multiple (Mission dependent ≥ 10
Single Burn Duration	60 minutes (Maximum)
Engine Life	> 270 minutes at Rated Thrust
Reliability	Piloted Systems

1.1.3.1 Operating Maps

The operating map for a nuclear engine defines the combinations of chamber pressure and temperature at which the engine can be operated. Because the nozzle is choked, the pressure and temperature determine the flow through the system, and therefore the reactor power level. The flow is, to a first order approximation, proportional to the nozzle chamber pressure divided by the square root of the chamber temperature. The power is then approximately proportional to the pressure times the square root of the temperature. A sample operating map from the NERVA program is shown in Fig 1.1[M-2]. The upper temperature limit is set by the maximum allowable fuel temperature. Because the NERVA type fuel has larger differences in temperature from the maximum fuel to the bulk hydrogen, the maximum allowed chamber temperature is lower than for the proposed particle bed reactors. The right side limit of the map is partially defined by the turbo-pump performance and the energy required to drive the turbine. Because the turbine draws its power from a portion of the flow stream, there must be sufficient energy to drive the total amount of flow through the pump. The right side limit is also set by the desire to limit the reactivity feedback effects due to higher pressure, lower temperature hydrogen. The left side limit of the map is determined by structural, pump stall, and flow stability considerations. The lower left portion of the map is limited by the ability of the control system to control the parameters at the low end of its regime. Operation is allowed within these defined boundaries, but other limits are placed on the rates of temperature and pressure changes. These are based on the ability of the fuel system to take the thermal and pressure stress loads. The controls for maneuvering around the operation map are discussed in the next section.

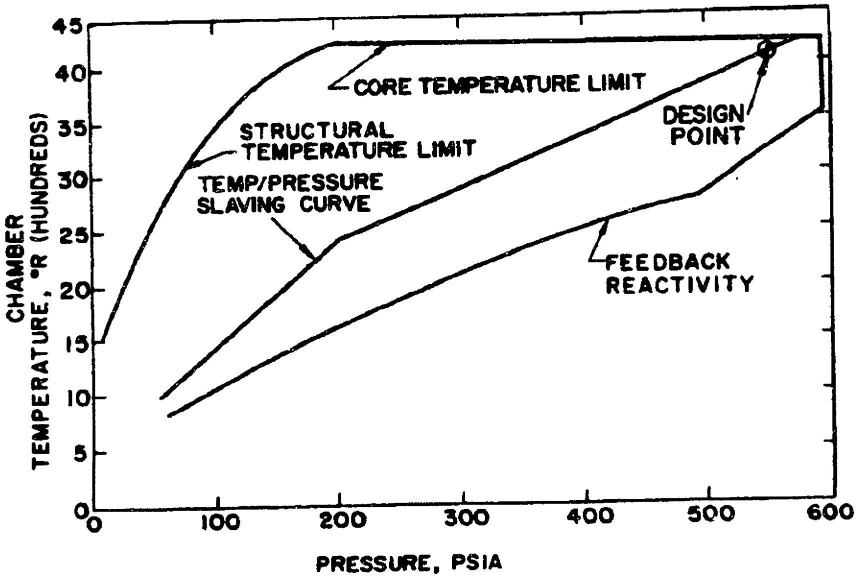

Figure 1.1 NERVA Engine Operating/Performance Map from Reference [M-2]

1.1.3.2 Controls

The control system for the nuclear propulsion engine must keep the engine within the bounds of the operating map, while also keeping the reactor in a safe condition. The

Mars mission planners also place design considerations in order to minimize the engine and propellant weights and to optimize the thrust and Isp behavior over the period of operation. The engines will be operated multiple times and for a maximum of one hour for any one burn. The control system must be operated in a manner to minimize the time spent at lower temperatures, thus fast startups and shutdowns are required. There are three main phases of reactor operation. The first phase involves starting the reactor up from the source level to a power level sufficient to bring chamber temperatures and pressures within a controllable range. The second phase consists of the power operation at rated conditions or maneuvering within the allowable regions of the chamber temperatures and pressures. Some of the maneuvers for the NERVA engines included ramps from 1% to 100% conditions in less than a minute. For the PBR, it is envisioned that startups can occur even more quickly. In the third phase, the engine is throttled back to an intermediate power level to reduce the initial decay heat load and then the reactor is scrammed. This phase of operation must also provide a means for removing the reactor decay heat. Each phase requires a different set of controls that can maximize the performance and maintain the engine within allowable component limitations[S-2].

The controls for the NERVA program varied over the life of the program, but typically the engine was controlled using the chamber pressure and temperature and neutron power as the controlled variables[S-2,M-1,N-2]. The chamber pressure is chosen as a convenient control variable because it is easily measured and provides a measure of the thrust level of the rocket. The thrust is proportional to the chamber pressure times the nozzle throat area. The pressure can be controlled by the turbo-pump speed due to the relation of pump head rise to the pump speed. The pump speed is maintained by altering the power of the turbine via its control valve. The chamber temperature is another convenient control variable because it also is easily measured and it determines the rocket specific impulse. The specific impulse (Isp) is proportional to the square root of the ratio of chamber temperature to the gas molecular weight. The temperature is controlled by altering the reactor power level. The neutron power is also monitored and controlled for the temperature control and to ensure the reactor power itself is maintained within safe operating conditions. A schematic of a NERVA control system is shown in Figure 1.2[S-2].

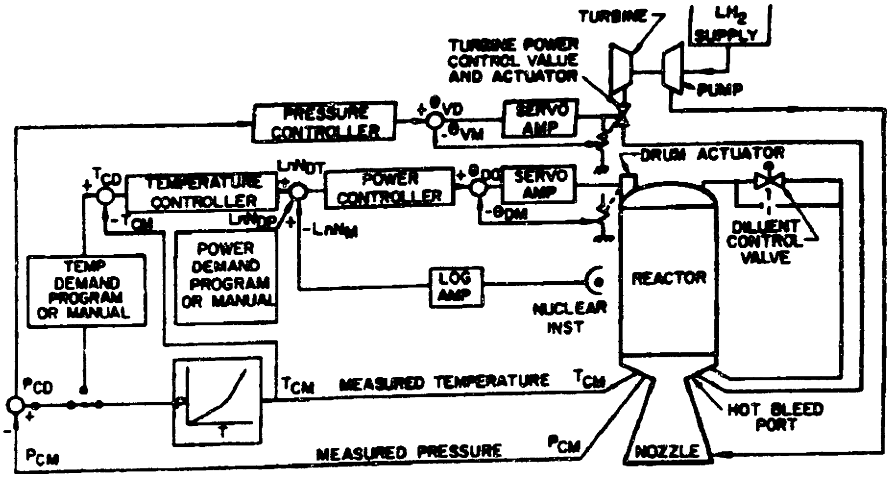

Figure 1.2 NERVA Engine Control System from Reference [S-2]

Reference [W-6] outlines in detail the startup requirements for the NERVA engine. A typical operation cycle for a single rocket thrust burn would include the following steps[W-6,M-2]:

1. The reactor is made critical and the power raised to a level between 0.1% and 1.0% of full power.
2. The engine is conditioned by bleeding flow through the system to chill the pump assembly for a few seconds while maintaining power at less than 1.0%.
3. The turbo-pump is "Bootstrapped" whereby the pressure and temperature are rapidly increased to allow turbo-pump operation from the heat energy of the engine system. This phase usually is on the order of a few seconds.
4. The engine is then placed on a thrust build up ramp with the pressure increasing slowly and the temperature increasing more rapidly. This phase is on the order of 15-30 seconds.
5. Once the rated temperature is reached, the pressure is rapidly increased to its rated condition. This phase is on the order of 5-10 seconds.

6. Rated conditions are held for the required thrust period. Typical thrust duration is from 600 to 3600 seconds.
7. After the thrust period, a throttle back is initiated in which the pressure is ramped back while maintaining the temperature at rated conditions. The ramp proceeds at the maximum allowable pressure ramp rate and then the power is held constant for a period to allow some reduction in the decay heat load.
8. A scram is initiated and the temperature is ramped back in a controlled manner at its maximum cooldown rate by manipulating the pressure. The ramp is stopped once the desired cooldown mode temperature is reached. This usually last for 15-30 seconds
9. A period of engine cooldown at some set temperature is maintained as long as necessary to keep components below their temperature limitations while the fission product heat power decays. The cooldown may occur in a continuous flow or pulse cooled mode. The duration of the cooldown period depends on the duration of the power operations.

The startup and shutdown requires maneuvering through a narrow space of the operating map and the controls must operate in order to maintain the engine safely within those bounds. Several new reactor control strategies, such as the Three Bean Salad and the MIT/SNL Control Laws appear to be well suited for controlling the reactor under rapid transients[B-2, B-3]. The implementation of the MIT/SNL control laws will be considered in Chapter 2.

1.1.3.3 Flow Stability

One consideration for the operation of the reactor includes avoiding operating conditions that may be susceptible to flow instabilities. The flow instability can arise in heated passages that have a decreasing pressure drop with an increasing flow of a gas, that has a viscosity that increases with temperature and that is flowing with a Reynolds number in the laminar range[B-4, B-5]. These conditions could be possible during the cooldown phase of operation due to the low flow rates and the several hundred parallel cooling passages connected at common plenum regions[B-6, H-2]. The basic problem is that for some combinations of coolant flow and power levels, there exist two possible flow rates for a given pressure drop across the channel. If the flow is perturbed and the conditions happen to be in the unstable region, the flow will tend to decrease and thus the temperature will increase driving the viscosity and pressure drop up so the flow again decreases. This could continue until the local passage is damaged from overheating. The stability is affected by the temperature rise along the channel. Because the channels are connected at common plenums, some flow channels could operate at higher flows, while others could operate in the low flow mode. If the system is operated so all regions have an increasing pressure drop with increasing flow - in other words with Reynolds numbers above the laminar range - channel flow stability can be shown to be maintained[B-4].

In a particle bed similar effects can be theorized. The pressure drop versus flow rate exhibits the similar U shape behavior. Orificing the element entrance or varying the resistance of cold frit can help the core wide flow stability. However, further consideration must be given to the flow once it enters the packed bed region, due to the multiple directions in which the flow can travel. If one considers the packed bed as a series of parallel flow channels, perturbations such as local porosity or local heating could alter the flow in that region. If the flow regime is in the laminar region, the same scenario as occurred for the NERVA type passages could happen[M-3, V-1]. This is described further in Chapter 3.

In order to avoid these regions, operating strategies need to be developed that ensure sufficient flow margin is maintained. Having to maintain higher flows for a lower temperature rise across the core requires that more hydrogen be carried on board and lowers the overall Isp for the engine cycle. The higher propellant requirement adds weight and cost to the system and the lower Isp impacts the mission trajectory plans, so tradeoffs must be made. The identification of the possible unstable regions and the methods to avoid them is discussed in Section 3.5

1.2 Research Objectives

1.2.1 General

There were several basic objectives of this research project. An early objective was to search for and review existing thermal hydraulic codes in order to evaluate whether a new model was required. Another objective was to extend work on single particle bed reactor fuel element computer models to include reactor dynamics, in order to allow more realistic evaluation of element designs. Finally a simulation of a nuclear thermal propulsion system was to be used to develop and validate operating and control strategies for the rocket engine. A discussion of the existing codes found to be pertinent to this research is presented in the next section as a means of introducing the thermal hydraulic capabilities and limitations. A brief overview of the other research objectives follows the code review.

1.2.2 Review of Existing Thermal Hydraulic Capabilities

1.2.2.1 General

One goal of this research was to obtain and evaluate currently existing thermal hydraulic codes for space reactor applications. There were several codes that were either proprietary or only had information specifications available. This section briefly describes the codes that were obtained, and that are applicable to the study of the nuclear thermal propulsion reactors and engines.

1.2.2.2 The ROCket Engine Transient Simulation (ROCETS) Code

The ROCETS code is a generic rocket engine simulation program developed by Pratt & Whitney that was originally used to model chemical rocket systems. It is a component based performance architecture that interfaces component modules into user defined configurations, interprets user commands, creates a FORTRAN computer program and executes the program. Pratt & Whitney has recently added component modules for nuclear rockets. These include reactor and reflector thermal hydraulics modules, nozzle and chamber cooling modules, and hydrogen propellant and nozzle performance modules[A-1]. The code has limited distribution and the user's manual is proprietary, so it is difficult to use. Although a version of the code was obtained through the NASA Lewis Research Center that runs on a personal computer, no simulations were attempted due to the large learning curve associated with its use and the code is not kept on file at the MIT Nuclear Engineering Department.

1.2.2.3 The Nuclear Engine System Simulation (NESS) Code

The NESS code was developed to provide the system designers with a tool that will give detailed evaluation and optimization for the reactor performance and design. The code is a combination of the SAIC Expanded Liquid Engine Simulation (ELES) code and the Westinghouse ENABLER reactor system code. Given a performance state point, the code will iterate to find the optimum core size and flow rates using sizing parametrics. Once the core is sized, the code proceeds to find the balance of the system piping and components, again using parametrics. The output includes details of the engine performance parameters, including component weights. A diagram of the NESS analysis logic appears in Figure 1.3[P-1]. Currently it is being used by NASA and SAIC to model the NERVA and its derivative cores, but in the future it is envisioned that it will have reactor modules for the other concepts such as the particle bed reactor. The code continues to evolve and is not ready for general use at this time. It will run on a VAX or a personal computer and is intended for use by engine designers and assessors in the future[S-3].

1.2.2.4 The Core Analysis Code (CAC)

The CAC code was originally developed by NASA in the 1960's[C-2, C-3]. During the Summer of 1991, it was updated to be available to the nuclear propulsion community through the COSMIC Software Center[W-1]. It calculates, as a function of time and radial core position, flow rates in the coolant passages, wall temperatures of the passages, and approximate maximum solid material temperatures. The input deck for the code requires the general core geometry, the core material properties as a function of temperature, the core power profile, and the core inlet conditions as a function of time. Schematics of the fuel and core geometry model used in the CAC code are shown in Figure 1.4[C-2]. The code utilizes the hydrogen properties routine STATE , that solves various curve fits to hydrogen property data. The properties routine states that caution must be used if temperatures are greater than 1800K[H-2]. The program is useful for evaluating the NERVA fuel element type cores and the personal computer version of the

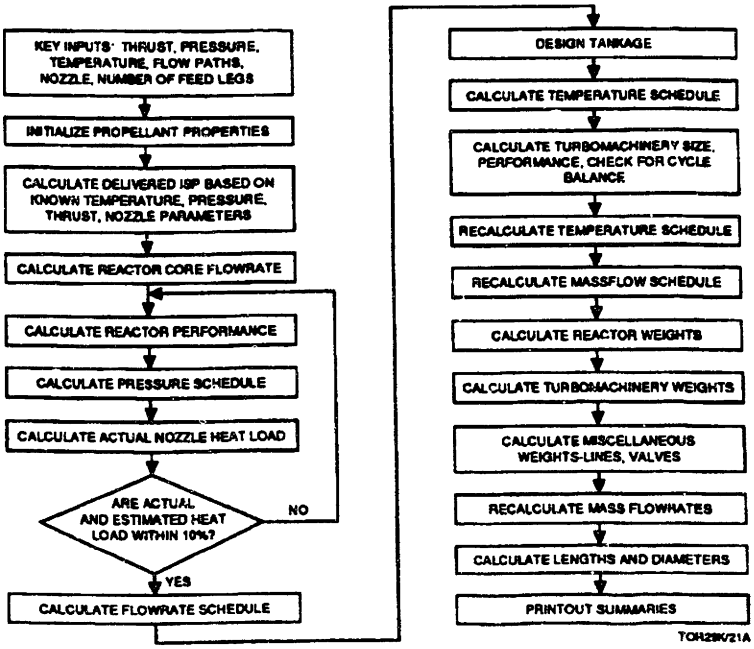

Figure 1.3 NESS Computer Code Analysis Logic Diagram from Reference [P-1]

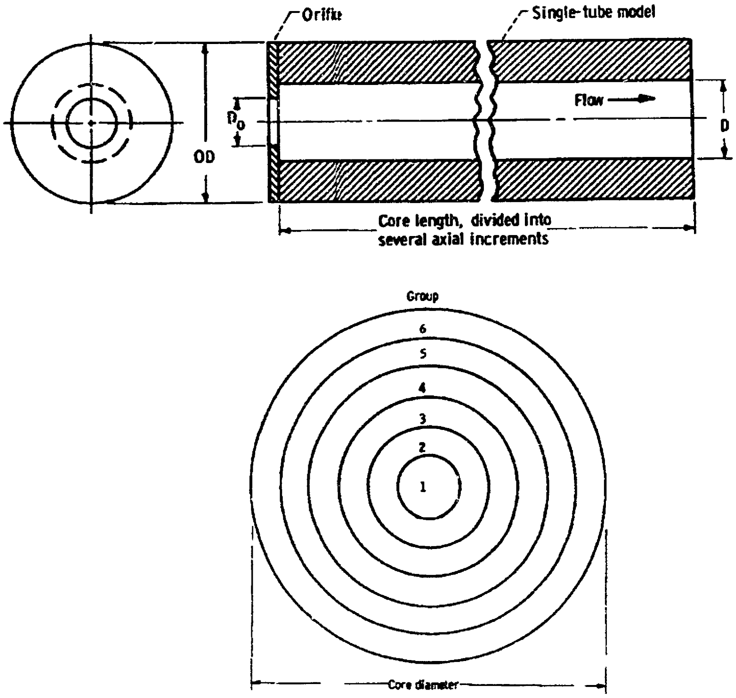

Figure 1.4 Schematic of Fuel Channel and Core Models used by CAC Code from Reference [C-2]

code was used to verify the NERVA reactor model in the engine system model developed as part of this research (see Chapter 4).

1.2.2.5 The System Analysis Flow SIMulation Code (SAFSIM)

The SAFSIM code was developed to simulate any user defined flow network that involves fluid flow, heat transfer, and/or reactor dynamics[D-1]. It contains modules for one-dimensional finite element fluid mechanics, one-dimensional finite element heat transfer structures, and a point kinetics reactor module with reactivity feedback and decay heat. The code is versatile enough to allow the user to define the system, to choose the pressure drop and heat transfer correlation, to setup control modules, and to specify the data to print to file. It has various time stepping and numerical integration scheme in order to maximize the computational speed. It has been used by Sandia to model the particle bed reactor fuel element[D-2]. As part of the NASA-DOE-DOD modeling technology development effort, SAFSIM was identified as the potential baseline computational computer code[W-3]. It has recently been benchmarked to the NERVA test data [L-1]. At MIT, David Suzuki has been using SAFSIM as a module in his Master's thesis work to model the PBR engine system[S-4]. An input manual was issued as the first step of creating a larger users base[D-1]. Manuals on the model governing equations and sample SAFSIM inputs are intended to be published in the near future. This code was not selected for use in this research because it still requires a few additional component modules such as a turbo-pump assembly in order to evaluate a full engine system. At this writing, the code continues to evolve, so it is anticipated that the additional models will be added to make the computer code even more robust.

1.2.2.6 The SIMBED Code

The SIMBED code was developed by Mujid Charmchi at the University of Massachusetts - Lowell for the Brookhaven National Laboratory[C-4]. The code consists of a family of programs that model the particle bed reactor fuel element in either two or three dimensions and for steady state or transients. The user defines the element dimensions and material properties, the inlet boundary conditions of pressure, temperature and mass flow rate, and the bed power density. The code finds the pressure, temperature, and velocity fields within the defined element. It also has the ability to model conical shaped elements. A schematic of the SIMBED element geometry is shown in Figure 1.5.

A two dimensional, steady state version of SIMBED was obtained from Brookhaven and was used to evaluate the performance of various PBR element geometries as discussed in Chapter 3. SIMBED was found to be a relatively fast code for the detail of the solution. The code was modified by this author to allow power shapes and cold frit resistance tailoring. A description of these enhancements is included in Chapter 2. These enhancements allow a more realistic study of the impact of power profiles and the tailoring of the cold frit on the overall element thermo-hydraulics. The code has had limited distribution and is being used primarily by Brookhaven to aid with design considerations for the PBR fuel element.

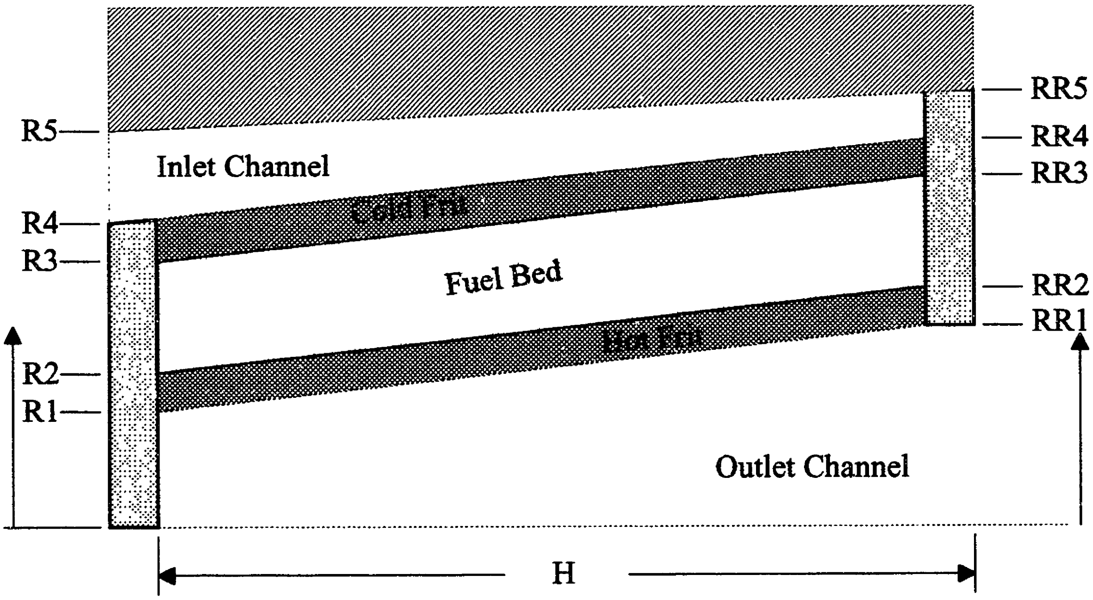

Figure 1.5 Schematic of PBR Element Geometry Used by SIMBED Code

1.2.3 Enhancement/Improvement of MIT Codes for PBR

1.2.3.1 General

A part of this research program was to enhance the computer codes developed for the particle bed fuel element by past students of the MIT Nuclear Engineering

Department. This was completed for the one dimensional flow model, but was abandoned for the two dimensional model, when the SIMBED computer code was obtained. This section summarizes the existing codes and the newly developed codes.

1.2.3.2 Tuddenham's HTWCOOL - switched to SIMBED

Initial work to model the particle bed reactor at MIT was performed by Reid Tuddenham[T-1] In his Engineer's thesis he presented the methods for a two dimensional transient model of a particle bed fuel element. This was developed to model an initial test element for the particle bed reactor, known as Pulsed Irradiation of a Particle Bed Element (PIPE). The code has the capability to model up to ten axial nodes and five radial nodes in the fuel region. The geometry is limited to cylindrical elements and to flow that enters and exits from the 'top' of the element. HTWCOOL utilizes a table lookup routine for the NBS standard hydrogen properties. The computer code was to be a first step in developing a thermal hydraulic model of a PBR element that could be used to predict hydrogen conditions for feedback reactivity models of a controller. It divides the problem into two phases; a solid phase and a gaseous phase. In solid phase, the calculations are concerned with the heat generation within the solid and the heat transfer through the particles to the solid/gas interface. The gas phase portion solves the mass, momentum, and energy equations in an r-z geometry, with heat added across the interface from the solid phase. The fluid conditions are calculated using a predictor corrector method know as Pressure Implicit with Splitting of Operators (PISO)[T-1].

This code was found to have long run times and required a large input for solution initialization. Consideration was given to altering the flow path and to add reactor kinetics, but this was abandoned once the SIMBED code was available. A comparison of Tuddenham's thesis results and those obtained from SIMBED is given in Chapter 3.

1.2.3.3 Casey's 1D Codes - evolved to Witter's PBR codes

In order to attempt a faster running model of the particle bed element that could possibly be used as part of a control model, William Casey developed the one dimensional steady state and transient programs STEADY and UPPOWER as part of his Master's thesis at MIT[C-5]. These codes made use of simple relations for the hydrogen properties and modeled the element as three control volumes. The first control volume included the inlet channel and cold frit. The second control volume contained the fuel region. The third volume included the hot frit and exit channel. The heat transfer was treated in a similar fashion to that used by HTWCOOL. Casey benchmarked his results to the Tuddenham code HTWCOOL. The code limitations were that the boundary conditions were limited to specifying the inlet and outlet pressures, the inlet temperature, and the power level. From these inputs, the mass flow and the outlet temperatures are determined.

These codes were translated by this author from the C language to FORTRAN and then several additions were made. The family of codes generated were named the PBRFMP and TRITRAN series. The changes included: 1) adding more control volumes to the fuel bed region, 2) changing the energy calculations from ones based on the heat capacity to being based on the enthalpy, 3) adding the hydrogen properties routine developed at NASA Lewis, 4) allowing different boundary conditions to be specified, and 5) implementation of the MIT/SNL control method for the power transients. These codes have proved useful for fast scoping evaluations of element sizing and pressure drop characteristics. Results of studies using these codes will presented in Chapter 3.

1.2.4 Full Engine Simulation Development

In order to evaluate the response of the full nuclear rocket engine, a simulation model must include the key components of the system. The existing codes were either limited in their application or too complicated to implement. The general requirements for an engine code were that the user be able to define the system piping geometry for an engine cycle, define the core geometry for either a NERVA or particle bed type reactor, define the characteristics of the turbo-pump assembly and control valve, allow for variable materials properties, and allow the input of transient ramps based on the usual propulsion requirements of nozzle chamber pressure and temperature.

Figure 1.6 depicts typical engine cycles used for nuclear propulsion[C-1]. The expander cycle is one that pumps liquid hydrogen from a supply tank, through nozzle and reflector cooling holes, splits to use the heat for turbine power and turbine control, and then rejoins before flowing through the reactor and out the nozzle. It differs from a bleed cycle, in which a small amount of the nozzle chamber gas is used to drive the turbine.

The expander cycle generally has a better system Isp performance because all the flow that passes through the core exits the main nozzle.

The codes developed in this research are based on a simple expander cycle engine. The governing equations and component models used by the engine codes are described in detail in Chapter 2. The results of this effort are reported in Chapter 4. The models are shown to be able model steady state points for both the NERVA and PBR types of reactor concepts, as well as to handle various startup, throttling, and shutdown transients.

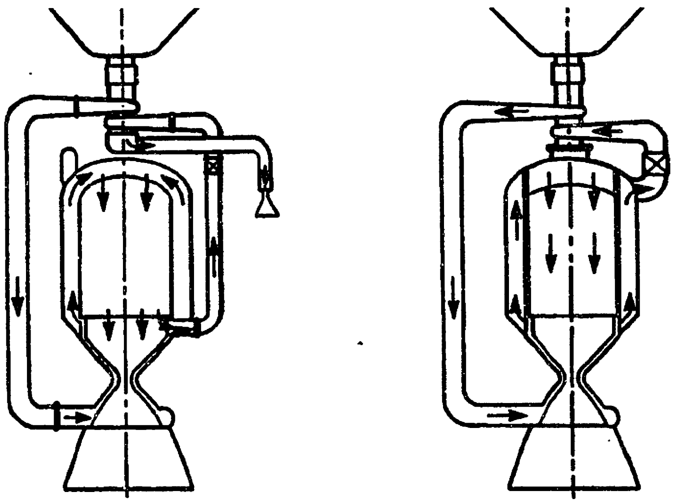

Hot-Bleed Cycle

Expander/Topping Cycle

Figure 1.6 Nuclear Rocket Engine Cycles from Reference [C-1]

1.2.5 Control and Operational Strategies

The development of an engine model was required in order to study engine control and operation. The next objective of this research was to determine how to operate the systems using various control strategies. It was decided to target the strategies at operating the engine by attaining desired chamber pressure and temperature conditions. In so doing, thrust, Isp, and propellant usage can be better predicted and input into the mission plans. A general method for determining the operating maps and transient ramps was undertaken in order to define the turbopump requirements and the requirements for the control mechanism. As a result, a design approach and response tool was developed for the development of nuclear thermal propulsion systems as discussed in Chapter 4.

1.3 Organization of This Report

The report is organized in an attempt to place the phases of the research in coherent sections. Chapter 2 contains a summary of the thermal hydraulic, power, and control model governing equations used in the computer simulations is presented. The chapter serves as the foundation for the computer models and as a reference source from which enhancement of the programs can begin. Chapter 3 outlines the modeling effort aimed at the particle bed reactor fuel element. This provides an understanding of the operation of, and issues associated with, this reactor concept. Chapter 4 presents the results of the full engine modeling effort. Several cases are presented to benchmark the code to the NERVA experience and then to show the extension of the code for the particle bed reactor. The robustness of the engine model is demonstrated through example cases of startup, steady state, throttle back, and shutdown transients. A summary of the work, conclusions, and recommendation for future work is outlined in Chapter 5. Finally, an appendix is included to provide the reader with sample input and output sets for several of the cases presented in the report.

Chapter Two - Thermal Hydraulic Model Development

2.1 Introduction

A major portion of the research focused on thermal hydraulic modeling of the nuclear rocket engine and the reactor fuel elements. Various component models were developed or combined from other computer codes to simulate their thermal hydraulic behavior. In order to simulate the reactor behavior with thermal hydraulic feedback, several reactivity coefficients were used in conjunction with the point kinetics model for reactor power. The following sections describe the approach and present the basic equations used in each of the major components.

2.2 General Pipe and Tee Components

The models for piping are based on a control volume approach. Figure 2.1 shows the geometry and nomenclature used.

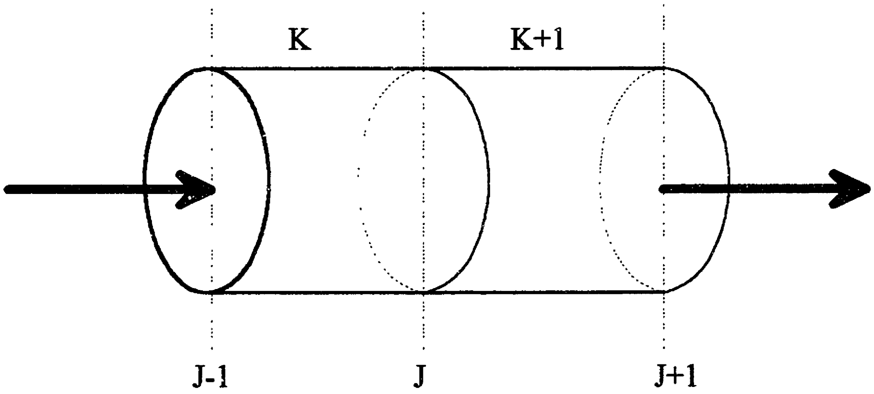

Figure 2.1 Schematic of General Pipe Control Volumes and Junctions

The conservation of mass equation is written for control volume K as

$$\frac{dM_K}{dt} = w_{J-1} - w_J, \qquad [2.1]$$

where: M = the mass of the hydrogen in the volume and
w = mass flow rate through the junction areas.

Throughout this report the subscript J will be for junctions and K will be used for volumes. Because the time steps are small and the flow is moving at rates much less than Mach speeds, the flow through the system is assumed to be constant at any time step. This quasi-steady state, incompressible assumption causes the time derivative to be zero. This simplifies the calculations involved for the transient case. The values for the properties are assumed to vary linearly across the control volume, so the control volume states can be determined as the simple arithmetic mean of the junction values.

The equation for the conservation of energy is written for control volume K as

$$\frac{dU_K}{dt} = w_{J-1}h_{J-1} - w_J h_J + Q_K - I_K \frac{d}{dt}\left(\frac{w_K^2}{\rho_K}\right), \qquad [2.2]$$

where: U = internal energy of the control volume fluid,
Q = heat source term,
h = enthalpy at the junction,
ρ = density of the fluid in the control volume,
$I = \frac{L}{A}$ = inertia of the control volume,
L = length of control volume and,
A = average flow area of control volume.

The last term is an acceleration term that is small compared the other terms and therefore can be neglected. The internal energy may be written in terms of enthalpy and pressure as $U_K = M_K\left(h_K + \frac{P_K}{\rho_K}\right)$. Using this relation, the definition that $M_K = \rho_K V_K$, and the assumption that $\frac{dM_K}{dt} = 0.0$, the energy equation becomes

$$\frac{dU_K}{dt} = M_K\frac{dh_K}{dt} + V_K\frac{dP_K}{dt} = w_J(h_{J-1} - h_J) + Q_K. \qquad [2.3]$$

Another simplifying assumption is that the time rate of change of the control volume enthalpy is approximately the same as that of the exit junction enthalpy. Using this assumption, the final form of the energy equation used by the transient model is represented as

$$\frac{dh_J}{dt} = \frac{1}{M_K}\left[w_J(h_{J-1} - h_J) + Q_K - V_K\frac{dP_K}{dt}\right]. \qquad [2.4]$$

The conservation of momentum can be represented using the momentum integral form used by Casey[C-5]. It is simply the sum of the forces on the control volume, once again assuming the mass flow rate is the same everywhere at any time. In equation form this becomes

$$I_K\frac{dw_K}{dt} = P_{J-1} - P_J - \sum_{n=1}^{N}(F_{eq})_n \qquad [2.5]$$

where: P = pressure at the junction and
F_{eq} = equivalent resistive pressure drop.

The equivalent resistive pressure drops are due to effects such as volume friction, volume flow area changes, sudden flow area contraction or expansion, form losses, and fluid acceleration. These resistive pressure drops can be expressed as equivalent flow resistance's (R) times the flow rate squared. Because the system flow rate is determined by the choked nozzle flow, a quasi-steady state approach was taken to determine the pressure drops for each control volume. Mathematically, the momentum equation then reduces to

$$P_J = P_{J-1} - \sum_{n=1}^{N} R_n w_K^2. \qquad [2.6]$$

The equivalent resistance due to friction in the control volume can be represented by the Fanning friction relation

$$R_f = f_f\left(\frac{L}{D_h}\right)_K \frac{1}{2\rho_K A_K^2} \qquad [2.7]$$

where: $f_f = 0.138\mathrm{Re}^{-0.151}$ = Fanning friction factor[T-1],
$\mathrm{Re} = \frac{D_h w}{\mu A_K}$ = Reynolds number,

$D_h = \frac{4A_K}{P_{wet}}$ = equivalent hydraulic diameter,
μ = fluid viscosity and,
P_{wet} = wetted perimeter of the control volume.

The coefficient on the Reynolds number is a correlated value determined by Tuddenham in Reference [T-1].

The equivalent resistance for spatial accelerations due to area changes across a control volume while holding the density constant can be represented by

$$R_A = \frac{1}{2\rho_J}\left(\frac{1}{A_{K+1}^2} - \frac{1}{A_K^2}\right). \qquad [2.8]$$

The equivalent resistance due to spatial and compressible accelerations, where the area and the density in the control volume is allowed to change, is represented by

$$R_S = \left(\frac{1}{\rho_{J-1}A_{J-1}^2} - \frac{1}{\rho_J A_J^2}\right). \qquad [2.9]$$

The equivalent resistance due to sudden contractions or expansion at a junction can be represented by

$$R_{C/E} = \frac{K_L}{2\rho_J A_{\text{small}}^2}, \qquad [2.10]$$

where: $K_L = \alpha(1-\beta)^2$ = pressure loss coefficient,
$\beta = \frac{A_{\text{small}}}{A_{\text{large}}}$ = ratio of flow area connected at junction,
α = 1.0 for expansions
= 0.5 for contractions.

A similar expression is used for the equivalent resistance due to form losses, where the K_L is a loss term associated with the junction area.

There are some special resistance terms associated with the PBR fuel element. The pressure drop relation for the porous material is presented in Section 2.3.2. Other pressure loss effects are due to the turning of flow from an axial direction to a radial direction in the inlet channel and then from a radial direction to an axial direction in the outlet channel. These can be treated as manifold effects. A second geometry effect is due to the flow area reduction in the radial direction coupled with the density reduction due to being heated by the fuel particles. The equivalent resistance's utilized for the PBR are as follows[C-5]:

For the manifolds:

$$R_M = \Theta \frac{1}{\rho_K}\left(\frac{1}{A_{\text{axial}}^2} + \frac{1}{A_{\text{radial}}^2}\right), \qquad [2.11]$$

where: Θ = 0.95 for the inlet channel
= 1.10 - 2.66 for the outlet channel,
A_{axial} = flow area in the axial direction and,
A_{radial} = flow area in the radial direction.

For the Area/Density Changes:

$$R_{A/D} = \frac{A_{J-1} + A_J}{2A_{J-1}A_J}\left(\frac{1}{\rho_J A_J} - \frac{1}{\rho_{J-1}A_{J-1}}\right). \qquad [2.12]$$

The total pressure drop across the control volume is simply the sum of each of the equivalent resistance's times the square of the flow rate.

Tee junctions were used to connect the turbine bypass control valve lines to the main piping. Figure 2.2 depicts the geometries for the two Tee junctions used in the engine code. Several assumptions were made in order to make a solution possible. The first is that the Tee junction properties are the same as the control volume to which it is attached. The second is that pressure drop is calculated from the straight line path. A turning loss coefficient, that can be specified by the user, is applied to the tee junction.

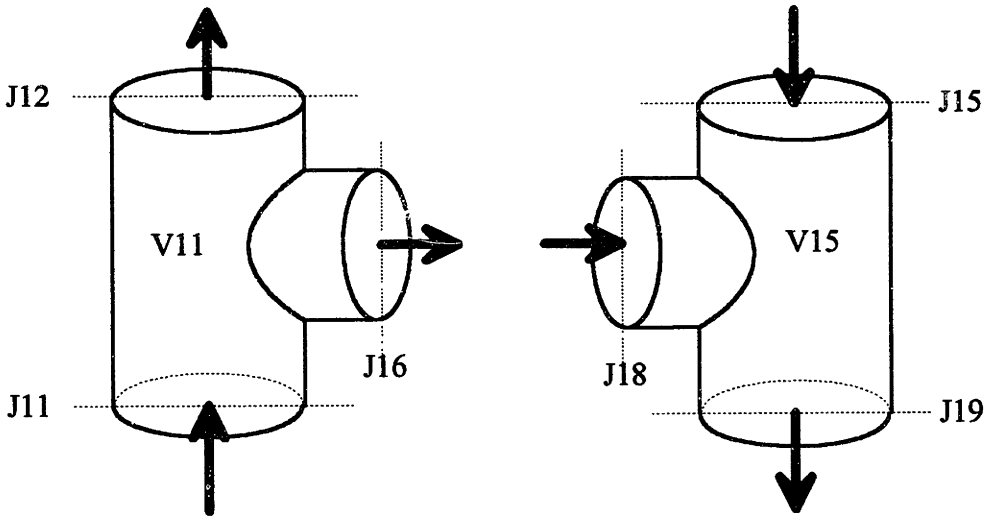

Figure 2.2 Flow Splitting and Joining Tee Junctions

The mass equations for the splitting and joining of flow are

$$\begin{aligned} w_{J11} &= w_{J12} + w_{J16} \\ w_{J19} &= w_{J15} + w_{J18} \ . \end{aligned} \qquad [2.13]$$

The momentum or pressure drop equations are defined using the total equivalent flow resistance for the Tee control volume as

$$\begin{aligned} P_{J12} &= P_{J16} - R_{V11} \\ P_{J19} &= P_{J15} - R_{V15} \\ P_{J16} &= P_{V11} \\ P_{J18} &= P_{V15} . \end{aligned} \qquad [2.14]$$

The energy equations for the junctions are

$$\begin{aligned} \frac{dh_{J12}}{dt} &= \frac{1}{M_{V11}}\left[w_{J11}h_{J11} - w_{J12}h_{J12} - w_{J16}h_{J16} + Q_{V11} + \frac{dP_{V11}}{dt} \right] \\ \frac{dh_{J19}}{dt} &= \frac{1}{M_{V15}}\left[w_{J15}h_{J15} + w_{J18}h_{J18} - w_{J19}h_{J19} + Q_{V15} + \frac{dP_{V15}}{dt} \right] \\ h_{J16} &= h_{V12} \\ h_{J18} &= h_{V15} , \end{aligned} \qquad [2.15]$$

and for the control volumes

$$h_{V12} = \frac{(h_{J11} + h_{J12})}{2}$$
$$h_{V15} = \frac{(w_{J15}h_{J15} + w_{J18}h_{J18} + w_{J19}h_{J19})}{2\,w_{J19}}. \qquad [2.16]$$

2.3 Fuel Elements

2.3.1 NERVA Element

2.3.1.1 Single Tube Model

Various models for the hexagonal fuel element have been used. The model used for this work simulates the reactor core as repetitive unit hexagonal cells translated into equivalent cylinders.[C-2, S-6, W-6, W-7] Figure 2.3 shows the general geometry for the calculations.

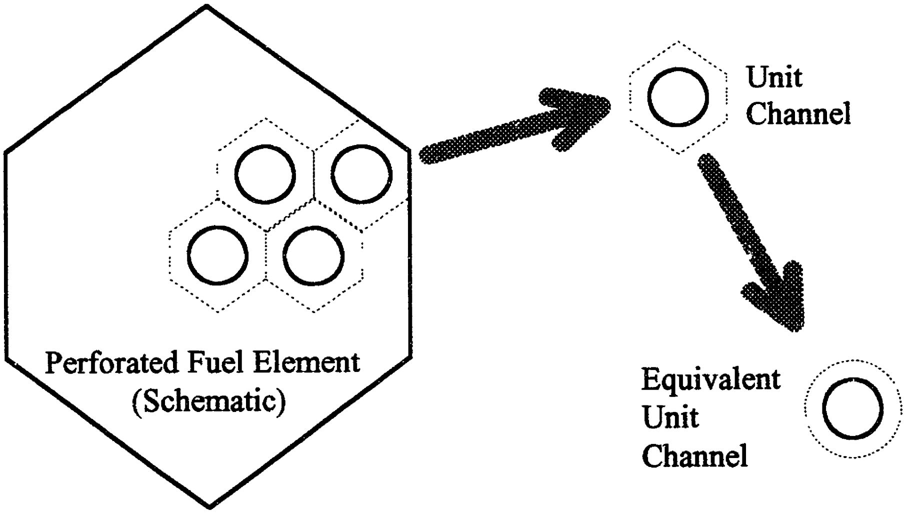

Figure 2.3 Equivalent Heat Transfer Geometry for the NERVA Fuel Element

Components that have this type of geometry are the NERVA derived fuel element and core, the particle bed reactor moderator block, and assumed for the reflector region. The large regions are subdivided in to smaller unit cell regions which are assumed to represent the entire region. The enthalpy change and pressure drops are calculated in the same manner as the pipe components with heat addition. An additional pressure loss resistance term is utilized to allow for the orificing at the inlet to the fuel element. This term is added to the first node of the fuel element. The orifice resistance term, as developed for the CAC computer program is written as[C-2]

$$\mathrm{R}_{\mathrm{O}_n} = \frac{K_n}{2\rho_{\mathrm{J}} A_{\mathrm{K}}^2 \mathrm{ORF}_n}, \tag{2.17}$$

where: $\mathrm{ORF}_n = \left(\frac{\mathrm{D}_{orfice}}{\mathrm{D}_{channel}} \right)^2$ = orificing factor for *n*th core ring,

$\mathrm{D}_{orifice}$ = effective equivalent flow diameter at the orifice,

$\mathrm{D}_{channel}$ = flow diameter of the channel.

The heat addition is an effective interface volumetric heat source determined from the solid material internal heat generation and thermal capacitance. The heat transfer equations from the references were arranged to yield effective heat transfer coefficients based on the solid material average temperature and the bulk coolant temperature. This was done in order to facilitate the use of variable material conductivities and heat capacities. A separate subroutine, written by this author, to solve the heat transfer is described in the next section.

2.3.1.2 HEXHEAT - Cylindrical for Hexagonal Geometry

The subroutine HEXHEAT calculates the hexagonal geometry element's effective temperature for steady state and transient conditions. This subroutine was adapted from the model in CAC, but also includes the effect of the thermal capacitance of the material. Some of the methodology is the same as References [W-7] and [W-8], however no axial conduction is considered. The material conductivities and heat capacities given in Reference [W-8] were used for the solid material temperature calculations. Figure 2.4 depicts the geometry breakdown for the hexagonal geometry and effective cylindrical geometry and defines the variables used in the equations.

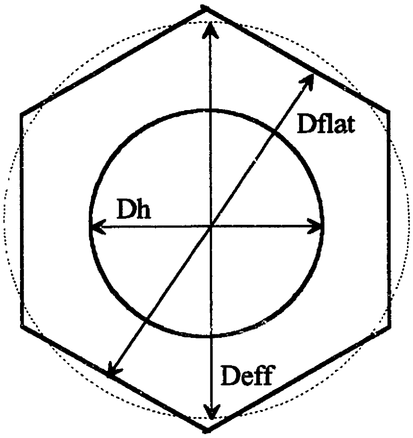

Figure 2.4 Hexagonal Geometry for HEXHEAT Subroutine

The effective solid diameter is determined such that the volume of solid material is conserved. Therefore for a unit axial cell, the effective equivalent unit cell diameter, D_{eff}, is found from

$$A_{hex} = \frac{\sqrt{3}}{2} D_{flat}^2 = \frac{\pi}{4} D_{eff}^2$$

$$D_{eff} = \left[\frac{2\sqrt{3}}{\pi} \right]^{0.5} D_{flat}. \qquad [2.18]$$

The steady state equations for the heat transfer and material temperatures are found from the energy balance on the control volume.

$$\dddot{q}_s V_s - U_T A_h (T_s - T_b) = Q_s - U_s A_h (T_s - T_w) - h_t A_h (T_w - T_b) = 0.0 \qquad [2.19]$$

$$\Psi \equiv \frac{1}{2}\left[\left(\frac{D_h}{D_{eff}} \right)^2 - 3 \right] - \frac{\ln\left(\frac{D_h}{D_{eff}} \right)^2}{1 - \left(\frac{D_h}{D_{eff}} \right)^2} \qquad [2.20]$$

$$\frac{1}{U_s} = \frac{D_h \Psi}{4k(T_s)\left[1 - \left(\frac{D_h}{D_{eff}} \right)^2 \right]} \qquad [2.21]$$

$$\frac{1}{U_T} = \frac{1}{U_s} + \frac{1}{h_t} \qquad [2.22]$$

where: Ψ = geometric constant factor,
U_s = heat transfer coefficient for solid material,
U_T = overall heat transfer coefficient based on mean temperature of solid,
$A_h = \pi D_h \Delta z$ = heat interface area,
$V_s = \pi(D_{eff}^2 - D_h^2)\,\Delta z$ = solid material volume,
Δz = axial node length,
$h_t = \dfrac{k_b\,Nu}{D_h}$ = fluid heat transfer coefficient,
$Nu = 0.023 Re^{0.8} Pr^{\,0.4}\left(\frac{T_w}{T_b}\right)^{-0.3}$ = Nusselt number (Wolf-McCarthy)[W-7],
$k(T_s)$ = solid material thermal conductivity as a function of temperature
k_b = bulk gas thermal conductivity,
$Pr = \dfrac{\mu c_p}{k_b}$ = Prandtl number of the fluid,
$\ddot{q}_s$ = power density in solid material,
T_b = temperature of the bulk fluid,
T_w = temperature of the fluid at the wall and,
T_s = solid material average temperature.

So then, $T_s = T_b + \dfrac{Q_s}{U_T A_h}$

and for the gas phase, the interface volume heat input is $Q_{int} = U_T A_h (T_s - T_b)$.

The transient equations for the material temperatures is written as

$$\rho_s V_s c_p \frac{dT_s}{dt} = Q_s - U_T A_h (T_s - T_b). \qquad [2.23]$$

In semi-implicit finite difference form, it appears as

$$T_s^{t+1} = \frac{\rho_s V_s c_p T_s^t + \Delta t\left[Q_s + U_T A_h T_b\right]^t}{\left[\rho_s V_s c_p + \Delta t U_T A_h\right]^t}. \qquad [2.24]$$

The interface heat source for the gas volume is then found by using the new solid temperature and the volume bulk gas temperature from the previous time step. The wall temperature and the solid material maximum temperature are the found from this interface heat source. The wall temperature is simply

$$T_s = T_b + \frac{Q_{int}}{h_t A_h}. \qquad [2.25]$$

The maximum temperature is found by using an effective heat transfer coefficient for the solid material and combining it with the gas heat transfer coefficient, as was done in equation 2.22. The equations used are[W-6]:

$$\frac{1}{U_m} = \frac{-D_h}{4k(T_s)\left[1-\left(\frac{D_h}{D_{eff}}\right)^2\right]}\left\{\ln\left(\frac{D_h}{D_{eff}}\right)^2 + \left[1-\left(\frac{D_h}{D_{eff}}\right)^2\right]\right\} \qquad [2.26]$$

$$\frac{1}{U_{max}} = \frac{1}{U_m} + \frac{1}{h_t} \qquad [2.27]$$

$$T_{max} = T_b + \frac{Q_{int}}{U_{max} A_h} \qquad [2.28]$$

Once the interface heat source is known, the gas phase calculations are carried out as outlined in Section 2.2.

2.3.2 PBR Element

2.3.2.1 Ergun Pressure Drop Correlation

The Ergun correlation [E-1] was chosen for the pressure drop relation for the particle bed fuel element. The expression for the flow pressure loss in a packed bed is a combination of viscous and kinetic energy loss terms. It was derived with consideration given to 1) the rate of fluid flow, 2) the viscosity and density of the fluid, 3) the closeness and orientation of the packing, and 4) the size, shape, and surface of the particles[E-1]. The form of the correlation used for the particle bed fuel element pressure drop calculation is

$$\frac{dP}{dr} = A\mu u_s + B\sqrt{A}\,\rho u_s^2, \qquad [2.29]$$

where: u_s = superficial or free stream fluid velocity,
$A = 150\,\frac{(1-\varepsilon)^2}{D_p^2\,\varepsilon^3}$ = viscous term coefficient,
$B = 1.75\,\frac{1}{\sqrt{150\,\varepsilon^3}}$ = inertial term coefficient,
D_p = particle diameter and,
$\varepsilon = \frac{\text{Gas Volume}}{\text{Total Volume}}$ = packed bed porosity (void fraction).

or equivalently for the development using mass flow rate

$$\frac{dP}{dr} = \left[\frac{A\mu}{\rho A_f w} + \frac{B\sqrt{A}}{\rho A_f^2}\right] w^2, \qquad [2.30]$$

where: $A_f = \pi(r_i + r_o)L$ = average superficial free stream flow area,
$r_{i,o}$ = inner and outer radius of ring node volume and,
L = axial length of the node.

The term "superficial" used here means the values of the parameters if there was no solid material in the node volume flow path. An effective resistive loss can be defined in the same manner as outlined in Section 2.2 and written as

$$R_E = \left[\frac{A\mu}{\rho A_f w} + \frac{B\sqrt{A}}{\rho A_f^2}\right] \Delta r. \qquad [2.31]$$

The Ergun correlation is used not only for the packed fuel bed, but also for the cold and hot frits. For these component models, effective values are used for the viscous and inertial coefficients in the same manner as developed for the frits in the SIMBED code[C-4].

2.3.2.2 Achenbach Heat Transfer Correlation

There are multiple equations for the heat transfer in packed beds that could be used, but the correlation developed by Achenbach [A-2], has become the most widely used relation for the particle bed reactor. The Nusselt number is given by

$$\mathrm{Nu}=\left[\left(1.18\mathrm{Re}^{0.58}\right)^4+\left(0.23\mathrm{Re}^{0.75}\right)^4\right]^{0.25}, \qquad [2.32]$$

where: $\mathrm{Re}=\dfrac{\rho \mathrm{D}_p u_s}{\mu}=\dfrac{\mathrm{D}_p w}{\mu \mathrm{A}_f}$ = superficial Reynolds number based on particle diameter.

This equation for the Nusselt number was derived for a geometry with porosity of 0.387 and a gas with a Prandtl number of 0.71. The equation needed to be generalized to allow for different geometries and Prandtl numbers. By backing out the particle diameter, bed porosity, and Prandtl number, the Nusselt number becomes

$$\mathrm{Nu}=\frac{1-\varepsilon}{\varepsilon}\left[0.622926\left(\frac{\mathrm{Re}}{1-\varepsilon}\right)^{2.32}+6.44603\times10^{-4}\left(\frac{\mathrm{Re}}{1-\varepsilon}\right)^{3}\right]^{0.25}\mathrm{Pr}^{0.33}. \qquad [2.33]$$

The Nusselt number is used to determine the heat transfer coefficient from the solid surface to the bulk gas by

$$\mathrm{h}_t=\mathrm{Nu}\frac{\mathrm{k}}{\mathrm{D}_p}. \qquad [2.34]$$

2.3.2.3 Solid to Gas Phase Heat Transfer

The heat transfer from the solid phase to the gas requires some special treatment for the fuel particles. First the general steady state and transient equations will be presented with an overall heat transfer coefficient and then the coefficient will be derived for an effective temperature of the multilayered fuel particle. This follows the work presented by Casey in Reference [C-5]. For the steady state case

$$\mathrm{Q}_s-\mathrm{U}_\mathrm{T}(T_s-T_b)=0.0, \qquad [2.35]$$

where: $\mathrm{U_T} = \dfrac{\mathrm{U}_s \mathrm{h}_t}{\mathrm{h}_t\,\mathrm{F} + \mathrm{U}_s}$ = effective overall heat transfer coefficient,

$\mathrm{Q}_s = \dfrac{\dddot{q}_s}{A_v}$ = effective volume heat deposition per particle surface area,

$A_v = \dfrac{S_p}{V_{cv}}$ = particle surface area per unit volume of the node,

$S_p = 2\pi \mathrm{D}_p^2$ = particle surface area,

$V_{cv} = \dfrac{V_p}{(1-\varepsilon)} = \dfrac{\pi \mathrm{D}_p^3}{6(1-\varepsilon)}$ = superficial volume of the node,

U_s = solid particle effective heat transfer coefficient and,

F = normalization factor based on mass and specific heat.

The effective particle temperature to remove the heat generation is defined by

$$T_s = T_b + \frac{\mathrm{Q}_s}{\mathrm{U_T}} \qquad [2.36]$$

and the steady state interface heat source to the gas phase is

$$\mathrm{Q}int = \mathrm{Q}_s A_v V_{cv} = \mathrm{U_T}(T_s - T_b) A_v V_{cv}. \qquad [2.37]$$

Because the particles consist of coating layers around a fuel kernel, the temperature found from the equation 2.36 is an effective mean temperature. The normalization factor and the solid heat transfer coefficient are determined from the particle material properties at each layer. Figure 2.5 depicts the geometry and radial nomenclature for the coefficient development.

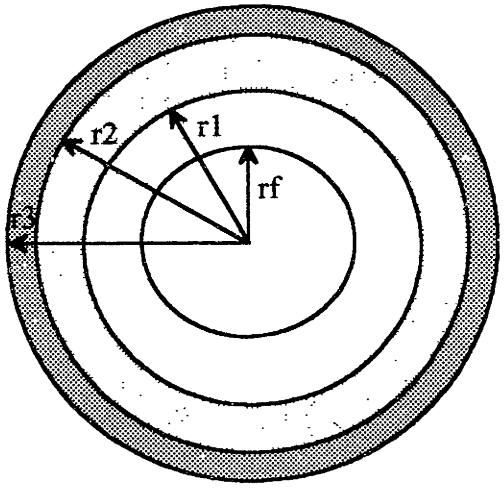

Figure 2.5 Fuel Particle Geometry for Heat Transfer

The particle mass per unit surface area for each layer can be determined as

$$ma_f = \frac{\rho_f r_f^3}{3r_3^2} \quad ma_1 = \frac{\rho_1\left(r_1^3 - r_f^3\right)}{3r_3^2} \quad ma_2 = \frac{\rho_2\left(r_2^3 - r_1^3\right)}{3r_3^2} \quad ma_3 = \frac{\rho_3\left(r_3^3 - r_2^3\right)}{3r_3^2} \qquad [2.38]$$

and the total effective mass per unit surface area, ma_{T} is simply the summation of the individual specific masses.

The average specific heat can be determined as the specific mass weighted average, or mathematically

$$C_p = \frac{\sum ma_n\, c_{pn}}{ma_{\mathrm{T}}}. \qquad [2.39]$$

The overall effective solid heat transfer coefficient is equal to

$$\mathrm{U}_s = \left(\sum \frac{1}{\mathrm{U}_n}\right)^{-1}, \qquad [2.40]$$

where the individual heat transfer coefficients are equal to

$$U_f = \frac{2k_f}{3r_3} \qquad U_1 = \frac{r_f r_1 k_1}{(r_1 - r_f) r_3^2} \qquad U_2 = \frac{r_1 r_2 k_2}{(r_2 - r_1) r_3^2} \qquad U_3 = \frac{r_2 k_3}{(r_3 - r_2) r_3} \tag{2.41}$$

The normalization factor F is then determined by the following equations

$$MCpF = ma_f c_{pf}\left(f_1 + 1\right) + ma_1 c_{p1}\left(f_1 + f_2\right) + ma_2 c_{p2}\left(f_2 + f_3\right) + ma_3 c_{p3} f_3 \tag{2.42}$$

and

$$F = \frac{MCpF}{2ma_T C_p}, \tag{2.43}$$

where the layer normalization factors (f) are

$$f_1 = \frac{U_s}{U_1} + f_2 \qquad f_2 = \frac{U_s}{U_2} + f_3 \qquad f_3 = \frac{U_s}{U_3} \tag{2.44}$$

These effective coefficients are also used for the transient calculations in the following manner:

$$MCpF \frac{dT_s}{dt} = Q_s - U_T(T_s - T_b), \tag{2.45}$$

from which the discretized equation for the effective solid material temperature is

$$T_s^{t+1} = \frac{T_s^t + \Delta t\left(\frac{Q_s + U_T T_b}{MCpF}\right)}{1 + \Delta t \frac{U_T}{MCpF}}. \tag{2.46}$$

The interface heat source to the gas phase is the same as for the steady state case, except the new solid temperature is used with the previous time step bulk gas temperature in equation 2.37. The particle surface temperature can then be found from this interface heat source by

$$T_w = T_b + \frac{Q_{int}}{h_t A_v V_{cv}}. \qquad [2.47]$$

These equations have been implemented in the computer programs with constant fuel region properties. The coding, however, is set up so that when the properties as a function are available, it will be a simple process to add the interpolation routines into the program. This completes the heat transfer considerations for the particle bed fuel element.

2.4 Nozzle

2.4.1 Regeneratively Cooled Nozzle Flow

Flow rates for ideal gases through isentropic nozzles can be easily determined from the chamber conditions and the area of the throat by [B-5]

$$w_{isentropic} = A_t P_c \sqrt{\frac{\gamma \, MW}{R_g T_c}\left(\frac{2}{\gamma+1}\right)^{\frac{\gamma+1}{\gamma-1}}}, \qquad [2.48]$$

where: A_t = nozzle throat area,
P_c = nozzle chamber pressure,
T_c = nozzle chamber temperature,
R_g = gas constant,
MW = molecular weight of the gas and,
γ = ratio of the gas specific heats $\left(\frac{C_p}{C_v}\right)$.

The determination of nozzle flow for non-isentropic nozzles can be a challenge, due to the complications of adding or removing heat from the flow stream. The simple equation for isentropic flow would approximate the flow to a first order, but would not account for any heat transfer. Therefore a method to determine the flow and the hydrogen properties needed to be developed. Using a simple conical shape for the nozzle and the assumptions that the Mach number is 1.00 at the throat and the hydrogen heat properties are 'frozen' to the chamber conditions, a numerical scheme that follows the methodology for nozzle flow with heat transfer in References [S-5] and [B-7] was developed. Assumptions made with this methodology are that the flow is one-dimensional and steady, changes in the stream properties are continuous, and that the gas is semi-perfect. By also assuming frictionless flow, constant molecular weight and specific heat, the differential equation for the nozzle Mach number simplifies to

$$\frac{dM^2}{M^2} = -\frac{2(1+\frac{\gamma-1}{2}M^2)}{1-M^2}\frac{dA}{A} + \frac{(1+\gamma M^2)(1+\frac{\gamma-1}{2}M^2)}{1-M^2}\frac{dT^o}{T^o}\,, \qquad [2.49]$$

where: M = Mach Number,

A = nozzle area,

$T^o = T_b + \frac{u^2}{2c_p}$ = stagnation temperature of the gas and,

u = velocity of gas in the control volume.

Figure 2.6 depicts the geometry layout for the nozzle modeled in the engine system computer code.

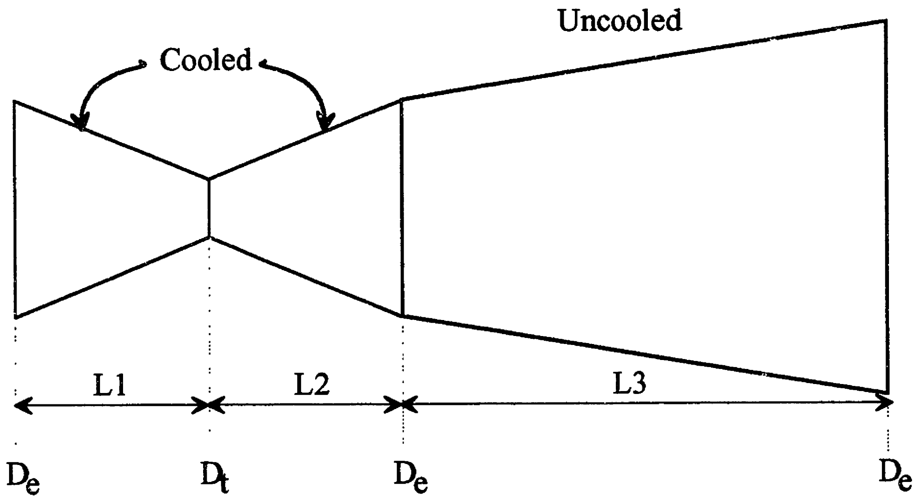

Figure 2.6 Engine System Nozzle Model Schematic

The flow area is a linear function of the nozzle length due to the assumption of a conical nozzle. Thus

$$A(x)=\frac{\pi}{4}\left(D_t+(D_e-D_t)\frac{x}{L}\right)^2, \qquad [2.50]$$

where: D_e = diameter of nozzle at large end,
D_t = diameter of the nozzle throat,
L = length of the nozzle segment and,
x = distance from nozzle junction.

The stagnation temperature is related to the volume heat source term for a quasi-steady state condition by

$$Q_N=wc_p\,(T_2^o-T_1^o). \qquad [2.51]$$

If one assumes that the heat transferred per unit length of nozzle travel is constant, the stagnation temperature will have a linear relation with the nozzle position as follows

$$T^o(x)=T_1^o+(T_2^o-T_1^o)\frac{x}{L}. \qquad [2.52]$$

These equations for the area and temperature are inserted into the Mach number differential equation and then equation 2.49 is numerically integrated from the throat, back to the chamber to find the chamber Mach number. A mesh of 200 intervals was found to be sufficient for convergence to a junction Mach number. Once the Mach number at the chamber is known, the mass flow rate can be found. The other parameters of interest can be found from the hydrogen properties at the nozzle entrance chamber junction. The equations for the junction pressure, temperature, density, velocity, and viscosity are given by[S-5]:

$$\frac{P_2}{P_1}=\frac{w_2}{w_1}\frac{A_1}{A_2}\frac{M_1}{M_2}\sqrt{\frac{1+\frac{\gamma-1}{2}M_1^2}{1+\frac{\gamma-1}{2}M_2^2}}\sqrt{\frac{T_2^o}{T_1^o}},$$

$$\frac{T_2}{T_1}=\frac{T_2^o}{T_1^o}\frac{1+\frac{\gamma-1}{2}M_1^2}{1+\frac{\gamma-1}{2}M_2^2},$$

$$\frac{\rho_2}{\rho_1} = \frac{P_2 T_1}{P_1 T_2},$$
$$\frac{V_2}{V_1} = \frac{M_2}{M_1}\sqrt{\frac{T_2}{T_1}},$$
$$\frac{\mu_2}{\mu_1} = \left(\frac{T_2}{T_1}\right)^{0.667}. \qquad [2.53]$$

This process is then repeated for the next two segments of the nozzle. A calculation was performed to benchmark the method to the results of a sample calculation in Reference [B-7]. The results are summarized in Figures 2.7 and 2.8 and in Table 2.1. This calculation was done assuming ideal gas conditions for an oxygen-kerosene mixture. The differences in the curve shapes are due to the assumption of simple conical nozzle shape versus the ideal nozzle shape of Reference [B-7].

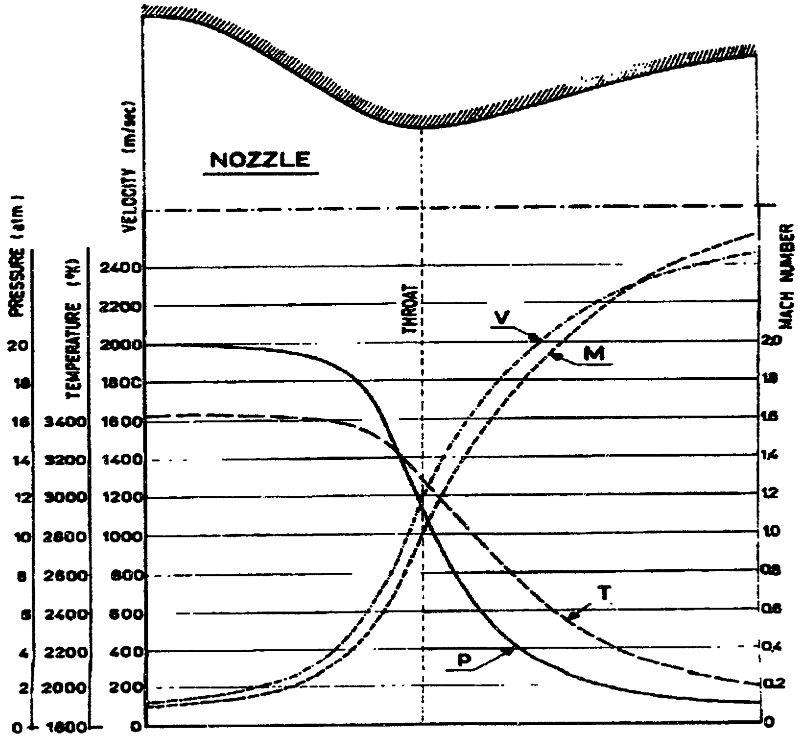

Figure 2.7 Reference Gas Flow Conditions Along Nozzle Length from Reference [B-7]

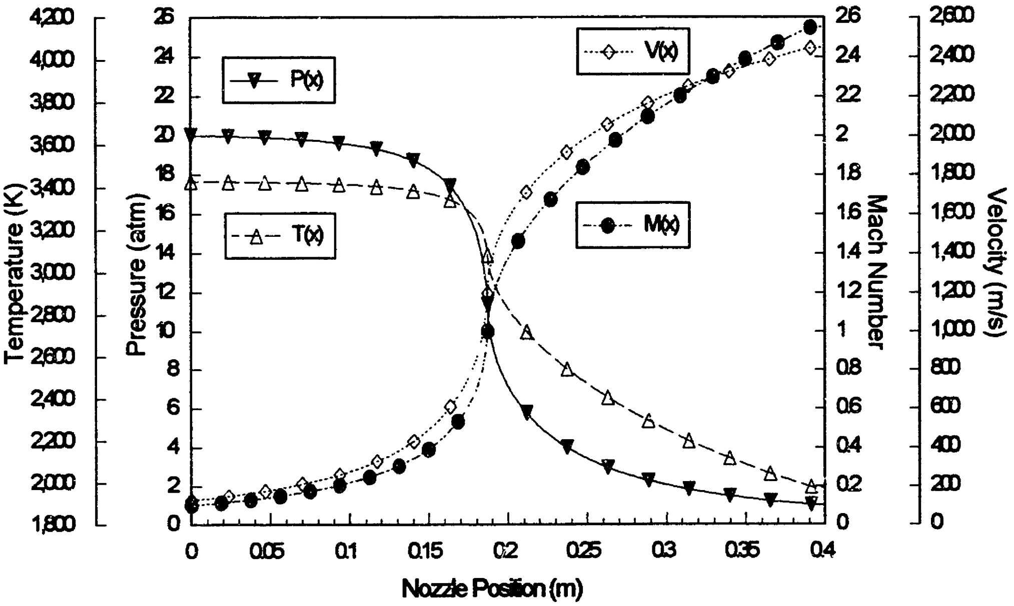

Figure 2.8 Benchmark Results for Gas Flow Conditions Along Nozzle Length

Table 2.1 Nozzle Flow Gas Condition Benchmark Results

Nozzle Location	*Calculation Model*	*Pressure*	*Temperature*	*Velocity*	*Mach Number*
Chamber	Ref. [B-7]	2020.00 kPa	3430.00 K	112.40 m/s	0.1055
D_c=37.134 mm	FLOWNOZZ	2020.00 kPa	3430.00 K	126.49 m/s	0.1003
Throat	Ref. [B-7]	1131.00 kPa	3082.00 K	1196.65 m/s	1.0000
D_t=15.160 mm	FLOWNOZZ	1152.38 kPa	3085.25 K	1196.65 m/s	1.0000
Exit	Ref. [B-7]	102.84 kPa	1976.36 K	2444.84 m/s	2.5525
D_e=28.367 mm	FLOWNOZZ	103.24 kPa	1977.76 K	2445.58 m/s	2.5525

Figure 2.9 depicts the trends for the various gas properties as a function of nozzle length using the hydrogen properties routine and the nozzle dimensions chosen for the PBR concept. The trends of the Mach number, velocity, temperature, and pressure follow those presented for real nozzles in References [B-7, S-5, S-7]. The mass flow determined when there is no heat addition or removal from the cooled sections compares to the isentropic mass flow calculations over a broad range of chamber conditions and nozzle throat diameters, with a maximum error of 2.26%. Table 2.2 summarizes some of these calculations. For transient flow calculations, the flow is treated quasi-statically,

using updated volume heats from the heat transfer calculations. The heat transfer calculations are treated in the next section.

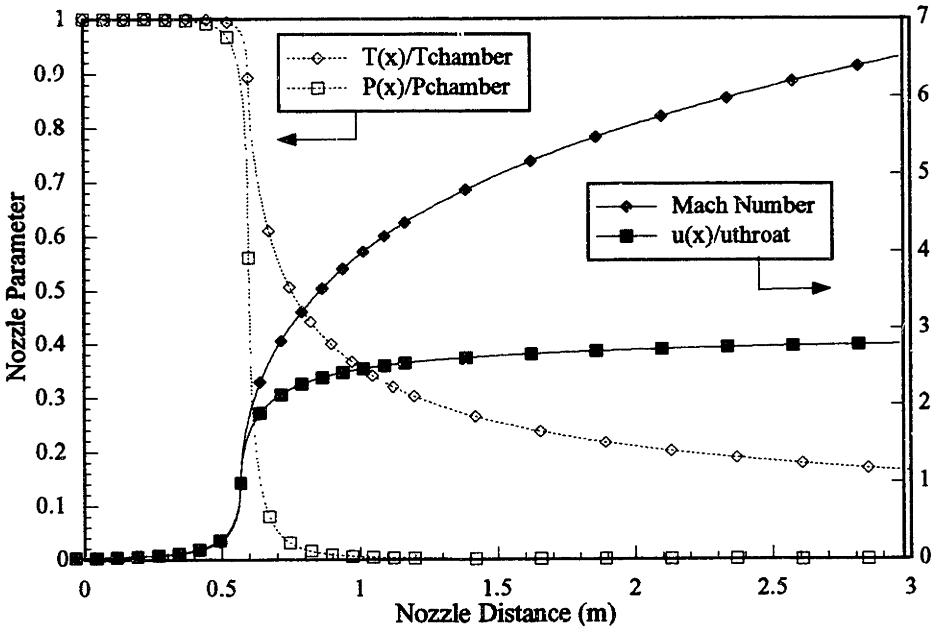

Figure 2.9 Hydrogen Gas Flow Conditions Along Typical Nozzle Length

Table 2.2 Comparison of Isentropic Flows to Numerical Calculations

Chamber Pressure	*Chamber Temperature*	*Throat Diameter (m)*	*Vr ume Heat (MW)*	*Isentropic Flow (kg/s)*	*Calc'd Flow (kg/s)*	*Percent Error (%)*
7.00 MPa	3000 K	0.1350		18.7026	18.9350	1.2424
7.00 MPa	3000 K	0.1350	-10 MW	18.7026	19.0218	1.7066
7.00 MPa	3000 K	0.1350	+10 MW	18.7026	18.8407	0.7704
5.25 MPa	3000 K	0.1350		14.0098	14.1698	1.1416
3.50 MPa	3000 K	0.1350		9.3244	9.4129	0.9492
1.75 MPa	3000 K	0.1350		4.6370	4.6717	0.7465
3.80 MPa	2275 K	0.2200		31.4828	32.0924	1.9362
2.85 MPa	2275 K	0.2200		23.5657	24.0756	2.1637
1.90 MPa	2275 K	0.2200		15.7096	16.0442	2.1299
0.95 MPa	2275 K	0.2200		7.8403	8.0174	2.2593

Nozzle performance is measured by the thrust and specific impulse. The equations used for the thrust (*Th*) and *Isp* are

$$Th = w(u_e - u_c) + P_e A_e \qquad [2.54]$$

$$Isp_1 = \frac{v_e}{g} \qquad [2.55]$$

$$Isp_2 = \frac{Th}{wg}, \qquad [2.56]$$

where the subscript e refers to the nozzle exit conditions and c refers to the chamber conditions.

2.4.2 Regeneratively Cooled Nozzle Heat Transfer

For the heat transfer in the nozzle, the nozzle is treated as a large single diameter pipe, cooled by a jacket of many smaller cooling tubes. The basic geometry is depicted in Figure 2.10.

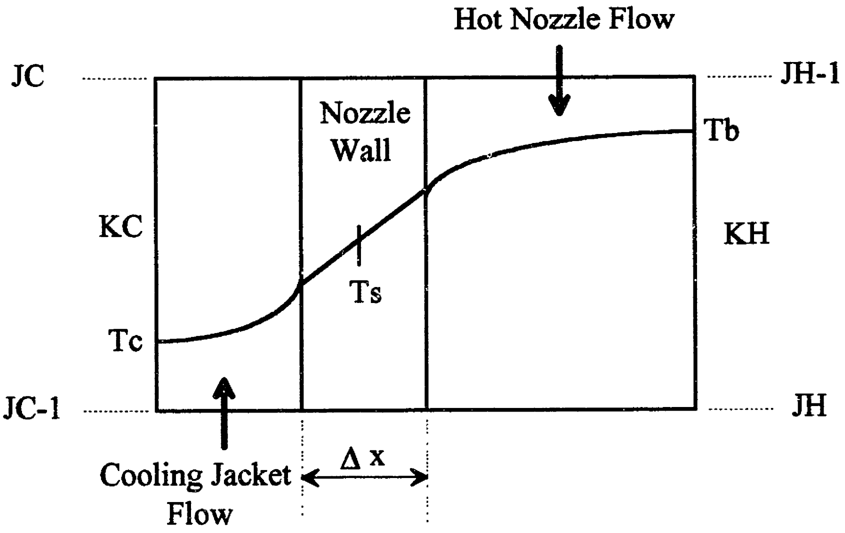

Figure 2.10 Nozzle Heat Transfer Control Volumes

The steady state conservation of energy equation for the solid is

$$Qnozz - Qint_h - Qint_c = 0.0 \qquad [2.57]$$

or equivalently,

$$\dddot{q}_s V_s \; - \; U_h A_h (T_s - T_{haw}) \; - \; U_c A_c (T_s - T_c) = 0.0, \qquad [2.58]$$

where: $A_h = \pi D_h L_h$ = hot gas side surface area,

$A_c = \pi (D_h + 2\Delta x) L_c \beta_c$ = cold side surface area,

D_h = hot side control volume mean diameter,

β_c = fraction of total area that is flow area,

$\dddot{q}_s V_s = PKN \times Q_{total}$ = internal solid heat generation as fraction of total reactor power,

PKN = fraction of total power deposited in the nozzle

$T_{haw} = T_{hb} + RF\left(T_h^o - T_{bh}\right)$ = hot gas adiabatic wall temperature

$T_h^o = T_{bh} + \frac{u^2}{2c_{ph}}$ = hot gas stagnation temperature

$RF = \frac{T_{haw} - T_{bh}}{T_h^o - T_{bh}} \approx Pr^{0.33}$ = recovery factor [B-7]

$U_i = \left(\frac{1}{h_i} + \frac{\Delta x}{2k_s(T_s)}\right)^{-1}$ = effective heat transfer coefficient for both sides

$h_c = 0.023 Re^{0.8} Pr^{0.4} \frac{k_c}{D_c}$ = cold side gas heat transfer coefficient

$h_h = 0.0364 Re^{0.75} Pr^{0.75} \frac{k_h}{D_h}$ = hot side gas heat transfer coefficient [S-5].

Solving for the effective average temperature of the nozzle yields

$$T_s = \frac{(U_h A_h T_{haw} + U_c A_c T_c + Qnozz)}{(U_h A_h + U_c A_c)}. \qquad [2.59]$$

The interface volume heat input to the gas phase is then simply

$$Qint_i = U_i A_i (T_s - T_i). \qquad [2.60]$$

Similar methodology leads to the transient equation

$$\rho_s V_s c_p \frac{\partial T_s}{\partial t} = \dddot{q}_s V_s - U_h A_h (T_s - T_{haw}) - U_c A_c (T_s - T_c). \qquad [2.61]$$

Solving for the solid temperature using an implicit finite difference approximation yields

$$T_s^{t+1} = \frac{\rho_s V_s c_p T_s^t + \Delta t\left[\dddot{q}_s V_s + (U_h A_h T_{haw} + U_c A_c T_c)\right]^t}{\left[\rho_s V_s c_p + \Delta t (U_h A_h + U_c A_c)^t\right]}. \qquad [2.62]$$

The interface heat sources to the gas phases are found using equation 2.60, but using the new solid temperature and the bulk fluid temperatures from the previous time step.

2.5 Turbo-Pump Assembly

2.5.1 Homologous Pump Performance Curves

The turbo-pump assembly (TPA) consists of a single shaft unit that connects the turbine blading to the pump blading. The model for the pump performance is based on linear interpolation of a set of homologous curves for the volumetric flow rate (Q), pump head (H), the efficiency (η), and the rotation speed (N). The steady state program enters the curves knowing the pressure rise and the flow rate and iterates to find the pump speed and the pump efficiency. The transient program enters knowing the pump speed and the mass flow rate and solves for the pressure rise and the efficiency. A set of curves from Grumman [S-8] is currently utilized, but the computer program allows the user to define the set of curves. The head and efficiency curves are curves are shown in Figure 2.11.

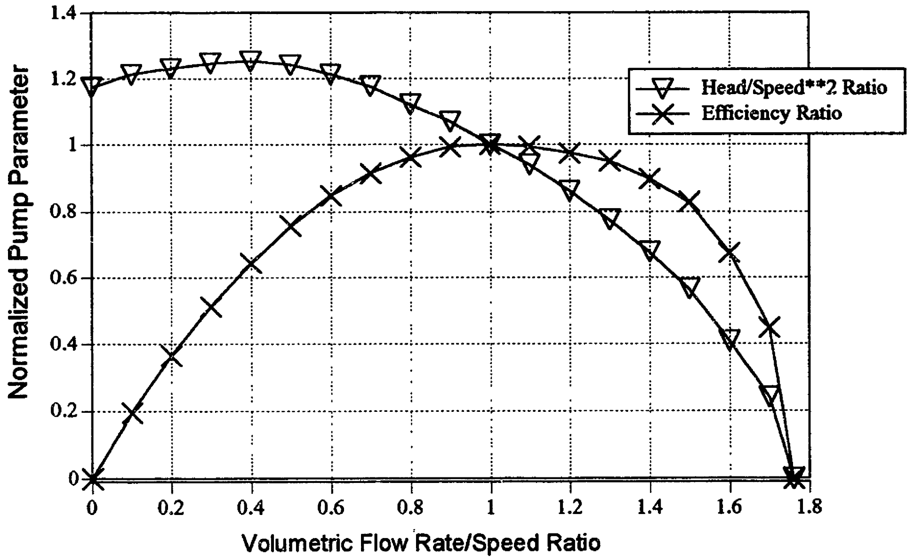

Figure 2.11 Homologous Curves for Turbo-pump Performance

The pump pressure rise (ΔP_p) is related to the pump head by

$$\Delta P_p = \rho_p g H, \qquad [2.63]$$

where: ρ_p = average density of fluid in the pump volume
g = gravitational constant

The volumetric flow rate is related to the mass flow rate by $Q = \frac{w}{\rho_p}$.

The pump power (W_p) is determined from the pressure rise and the mass flow rate by

$$W_p = \frac{\Delta P_p w}{\rho_p}. \qquad [2.64]$$

The enthalpy rise across the pump (Δh_p) can be determined from the pump power and the efficiency by

$$\Delta h_p = \frac{W_p}{w \eta_p}. \qquad [2.65]$$

The pump changes speed by a mismatch in the applied turbine torque (τ_t) and the resistive pump torque (τ_p) and is influenced by the turbo-pump's inertia (I_p). In order to change the speed from a steady state match, the turbine power is changed. The equations for determining the pump speed are written as follows

$$I_p \frac{d\omega}{dt} = \tau_t \eta_t - \frac{\tau_p}{\eta_p}, \qquad [2.66]$$

where: $\omega = \frac{N}{2\pi}$ = the pump speed in radians per second,
$I_p = \frac{1}{2} M_{tpa} r_{tpa}^2$ = the inertia of the turbo-pump assembly,
M_{tpa} = the mass of the turbo-pump assembly and,
r_{tpa} = the effective radius of the turbo-pump assembly.

Another expression for the power of the turbine or pump is simply the torque multiplied by the speed in radians per second. Substituting this relation and converting the speed into revolutions per second, the expression for the pump speed becomes

$$\frac{I_p N}{4\pi^2} \frac{dN}{dt} = \frac{I_p}{4\pi^2} \frac{d}{dt}\left(\frac{N^2}{2}\right) = W_t \eta_t - \frac{W_p}{\eta_p}. \qquad [2.67]$$

This can be discretized in order to find the pump speed at a particular time step as

$$N^{t+1} = \sqrt{\left(N^2\right)^t + \Delta t \frac{8\pi^2}{I_p}\left(W_t \eta_t - \frac{W_p}{\eta_p}\right)^t}. \qquad [2.68]$$

2.5.2 Turbine Performance Equations

The turbine model is a simple choked nozzle model, due to lack of a better model. Assumptions of constant turbine efficiency and pressure ratio were used in References [L-2], [S-9],and, [S-10], and this method was adopted for this work. This allows relatively simple equations to be used for the determination of the turbine power and flow. The equation for the power, enthalpy and flow rate are as follows:

$$W_T = w_{turb}(h_e - h_i) \approx w_{turb} c_p T_i \left[1 - \left(\frac{P_e}{P_i}^{\frac{(\gamma-1)}{\gamma}} \right) \right], \qquad [2.69]$$

where: subscripts i,e = denote turbine inlet and exit conditions and
w_{turb} = mass flow rate through the turbine.

The assumption of a constant pressure ratio for the turbine is based on choked flow in the turbine blading. This allows the turbine flow or the turbine power to be directly determined without an iteration once the turbine inlet conditions of temperature and specific heat are know. For the steady state calculations the upstream flow conditions are calculated. In the transient case, the downstream conditions are determined. In both cases the gas enthalpies are calculated by the methods outlined in Section 2.2. A turbine bypass control valve is used in order to control the flow to the turbine. In the next section, the model for the control valve and for the method of balancing pressures at is presented.

2.5.3 Turbine Bypass Control Valve

The turbine bypass control valve (TBCV) is used to control the flow to the turbine, so as to match the desired pump flow rate and power requirements. For the topping cycle engine modeled in this report, the TBCV is placed in the bypass line around the turbine. In order for flows and pressures to be balanced at the Tee junctions, the valve must have flow resistance or pressure loss coefficients as a function of valve position. In Reference [W-6] a curve of effective loss coefficient versus position is presented for the NERVA engine design. This method was adopted for the valve model. The coefficients on the exponential need to be generated for the particular engines to ensure that the system can operate over a wide range of conditions.

The steady state engine system code is used to find the valve pressure loss required to match turbine flows needed to drive the total flow at various operating points. A schematic of the turbine and bypass piping with the junction is shown in Figure 2.12. The pressure loss (ΔP_{TBCV}) is converted into an effective resistance term ($R_{TBCV}(x)$) times the square of the bypass mass flow rate (w_{byp}), from which loss coefficients as a function of valve stem travel are determined. These coefficients are used by the transient code to determine the positioning of the TBCV in the turbine control model and the pressure drop in the thermal hydraulic calculations.

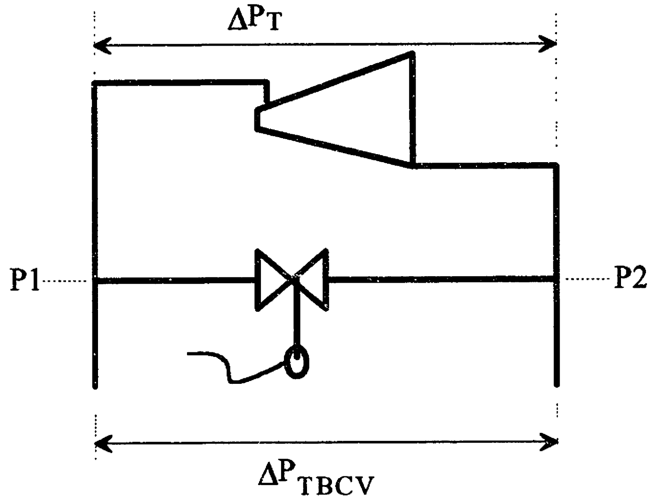

Figure 2.12 Schematic of Turbine and Bypass Control Flow Network

The equations used to find the TBCV pressure loss parameters as a function of valve stem travel are as follows:

$$P_1 - P_2 = \Delta P_T = \Delta P_{TBCV}, \tag{2.70}$$

$$\Delta P_{TBCV} = \left[R_{piping} + R_{TBCV}(x)\right] w_{byp}^2, \tag{2.71}$$

$$\Delta P_T = P_1 - \left(R_{piping} w_{turb}^2 + \frac{P_{turb}}{PR}\right), \tag{2.72}$$

$$R_{TBCV}(x) = \frac{\Delta P_T - R_{piping} w_{byp}^2}{w_{byp}^2} = \frac{K_{TBCV}(x)}{\rho_{TBCV}}, \tag{2.73}$$

$$K_{TBCV}(x) = \frac{K_l}{2A_v^2(x)} = \exp(\alpha - \beta x), \tag{2.74}$$

where: R_{piping} = effective resistances for piping segments,
PR = turbine pressure ratio (assumed constant) and,
P_{turb} = turbine inlet pressure.

Equation 2.73 is used to find the K values required for the steady state solution. Equation 2.74 is used to find the α and β terms of the exponential from the steady state solution of the required valve pressure loss. The exponential coefficients are input by the user to allow the determination of the valve pressure drop for a given valve stem position. In the transient part of the engine code, the equivalent pressure loss equation becomes

$$\Delta P_{TBCV} = \frac{K_{TBCV}(x)}{\rho_{TBCV}} w_{byp}^2 . \qquad [2.75]$$

The flow balancing method employed for the turbine is the same as utilized for the multi-radial zone core as discussed in the Section 2.6.

In order to simulate the lag time of the valve stem motion in response to a control signal demanded position, a simple exponential growth equation is utilized as

$$\frac{1}{\lambda_{TCBV}} \frac{dx_{actual}}{dt} = x_{demand} - x_{actual} . \qquad [2.76]$$

Discretizing leads to determining the position at the next time step by

$$x_{actual}^{t+1} = x_{demand}^{t} - \left(x_{demand}^{t+1} - x_{actual}^{t} \right) \exp\left(-\lambda_{TBCV} \Delta t\right) \qquad [2.77]$$

or by

$$x_{actual}^{t+1} = \frac{x_{actual}^{t} + \lambda_{TBCV} \Delta t \, x_{demand}^{t+1}}{1 + \lambda_{TBCV} \Delta t} . \qquad [2.78]$$

2.6 Multi-Region Reactor Core

2.6.1 Pressure Drop and Flow Balancing - CAC Code

For a multiple region core connected at plenums, the method employed in the CAC code [C-2] was utilized. The basic scheme is to iterate the region flows until the pressure drops across the passages have converged to a certain level of agreement. Once the flows are determined, the heat transfer can be determined. The equations used are

$$w = \sum_{n=1}^{N} w_n$$

$$w_n = R_n \, (\Delta P_n)^{X_n}, \qquad [2.79]$$

where: w = total mass flow rate,
w_n = mass flow rate in the nth ring,
R_n = equivalent flow resistance term for the nth ring,
ΔP_n = pressure drop across the nth ring control volume,
X_n = proportionality coefficient relating pressure to mass flow rate and,
N = total number of concentric rings for the reactor core region.

The flow resistances for each ring are calculated in the same manner as described in Sections 2.2 and 2.3. The first guess for the steady state ring mass flow rates splits the flows so that the mass flow per unit area is constant. For the transient case the previous time step flow rates are used. Once each ring's pressure drop is calculated, the requirement that all the channel pressure drops be the same within a certain error band is imposed. An iteration process is used to adjust the ring mass flow rates until this requirement is met. The pressure drops are compared to a flow weighted average pressure drop for the core. Stepping between iteration α and β, the proportionality coefficient and the pressure drop are determined as follows

$$X_{\beta,n} = \frac{\ln\left(\dfrac{w_\beta}{w_\alpha}\right)_n}{\ln\left(\dfrac{\Delta P_\beta}{\Delta P_\alpha}\right)_n} \qquad [2.80]$$

and

$$\Delta P_{\beta,avg} = \left[\frac{w}{\sum_{n=1}^{N} \left(\frac{w_\alpha}{\Delta P_\alpha^X} \right)_n} \right]^2 . \qquad [2.81]$$

Then, because the ring pressure drops are required to be equal, the ring mass flows at the next iteration step can be found from

$$w_{\beta,n} = w_{\alpha,n} \left(\frac{\Delta P_{\beta,avg}}{\Delta P_{\alpha,n}} \right)^{X_n} . \qquad [2.82]$$

For the first two iterations, X_n is assumed to be 0.5 so the process can be started. The iterations continue until the individual pressure drops are converged to agreement with the average value to a value of 0.1%. The same method is also applied to the flow determination around the turbine and bypass paths.

Once the ring mass flows are determined, the enthalpy rises and solid material temperatures are calculated using the HEXHEAT general pipe methods outlined in Sections 2.2 and 2.3 for each axial and radial control volume node.

2.6.2 Radial Power Distribution Factors

The power generation profile for the nuclear reactor is generally not uniform in the axial or radial directions. Some power shaping can occur through design measure, but thermal hydraulic modeling should allow for non-uniform power distribution. The methods for handling the axial power shape will be discussed in section 2.8. For the radial power profile, a radial peaking factor method will be employed. The peaking factors for each ring (PKR_n) are determined such that the volume (or really the area) weighted average of the factors is unity. The radial zones are depicted in Figure 1.4. Numerically, this implies:

$$\frac{\sum_{n=1}^{N} PKR_n \, A_n}{A_{core}} = 1.0, \qquad [2.83]$$

where: $A_n = \pi\left(r_n^2 - r_{n-1}^2\right)$ = area of core ring region *n*,
$A_{core} = \sum_{n=1}^{N} A_n = \pi\, r_N^2$ = total core area and,
r_n = radius to outer portion of *n*th ring.

The peaking factors can be determined from a predetermined power shape in the following manner:

$$PKR_n \equiv \frac{Q_n}{A_n}\frac{A_{core}}{Q_{core}} = \frac{\dddot{q}_n}{\dddot{q}_{core}}, \qquad [2.84]$$

where: Q_n = total power input to *n*th ring,
Q_{core} = total core power and,
$\dddot{q}_{n,core}$ = average power density for the ring and core respectively.

The power density used in the solid material for the heat is determined from the average volume power density and the core voidage as follows

$$\dddot{q}_{solid,n} = \frac{Q_n}{A_n(1-\varepsilon)\Delta z}, \qquad [2.85]$$

where: $\varepsilon = \dfrac{\text{Core Flow Area}}{\text{Total Core Area}}$ = core voidage.

The solid power densities are used for the calculation of the heat transfer from the solid phase to the gas phase in each of the core rings.

2.7 Feedback and Control Reactivity

2.7.1 Point Kinetics - MIT/SNL Laws

The MIT/SNL Minimum Time Control Laws have been implemented in model and actual operational reactors[B-8, B-9]. Their utility in maintaining control of the reactor under many possible power trajectories, make it a strong candidate for the control of space propulsion reactors. The fast startup and shutdown strategies required for missions, require a robust and automatic control. The control laws have been implemented in the single PBR element transient codes and the engine transient code.

The implementation for the single element models, allow a desired power ramp rate to be defined for the controller and the control drums are manipulated to obtain that trajectory nearly exactly. The basic point kinetics equations are [H-3]

$$\frac{d}{dt}T(t) = \frac{\rho(t) - \boldsymbol{\beta}}{\Lambda}T(t) + \sum_{i=1}^{I} \lambda_i C_i(t)$$

$$C_i(t) = \frac{\beta_i}{\Lambda}T(t) - \lambda_i C_i(t), \quad i = 1,2....I \qquad 2.81$$

where: T = amplitude or magnitude of the power,
ρ = net reactivity,
C_i = concentration of the ith delayed neutron precursor group,
β_i = fractional yield of the ith delayed neutron group,
$\boldsymbol{\beta}$ = total delayed neutron fraction ($\boldsymbol{\beta} = \sum \beta_i$),
λ_i = decay constant of the ith precursor group,
Λ = prompt neutron generation lifetime and,
I = number of delayed neutron precursor groups.

Six delayed neutron precursor groups are used for this study and the values used are given in Table 2.3[P-3].

Table 2.3 Default Six Group Delayed Neutron Fractions and Decay Constants

β_i	λ_i (sec^{-1})
0.00029	0.01323
0.00168	0.03900
0.00149	0.13900
0.00322	0.35900
0.00101	1.41000
0.00021	4.03000
$\boldsymbol{\beta} = 0.00790$	$\Lambda = 33.5$ μsec

Inverse kinetics is used to determine the power level due to changes in reactivity. The reactivity changes are caused by feedback effects and from the control devices. The MIT/SNL control laws make use of the time rate of change of the reactivity and the desired power periods for different portions of a power ramp. The desired control drum reactivity for a particular ramp can be determined as follows

1. A desired period (ω_D) for reactor power is determined for a particular ramp time interval. The specification of this period for the transient engine model is based of the nozzle chamber temperature and will be discussed in Chapter 4.
2. The desired period is compared to the measured actual period ($\frac{1}{\tau}$) to determine the desired rate of change of the period ($\dot{\omega}_D$) to bring the reactor to the desired period,
   $$\dot{\omega}_D = \frac{\left(\omega_D - \frac{1}{\tau}\right)}{k\Delta t}. \tag*{[2.87]}$$
3. The total reactivity (ρ) at a particular time is the sum of the control drum reactivity (ρ_c) and the feedback reactivity (ρ_f). The details of these reactivities will be presented in the next section, but for now the total feedback reactivity will be considered as the sum of the various feedbacks
   $$\rho_f = \sum_{g=1}^{G} \rho_{f,g} \tag*{[2.88]}$$
   and the control reactivity is determined from the position of the control drum.
4. The rate of change of the feedback reactivity ($\dot{\rho}_f$) is determined from the modeling of the feedback reactivities at various timesteps. Thus
   $$\dot{\rho}_f^t = \frac{\left(\rho_f^t - \rho_f^{t-1}\right)}{\Delta t}. \tag*{[2.89]}$$
5. The desired rate of change of the control reactivity can be found using the Alternate MIT/SNL Period-Generated Minimum Control Law [B-8] as
   $$\dot{\rho}_c = (\beta - \rho)\,\omega_D - \lambda_{eff}\rho - \sum_{i=1}^{I} \beta_i\left(\lambda_i - \lambda_{eff}\right) - \dot{\rho}_f + \Lambda\left[\dot{\omega}_D + \omega_D\left(\omega_D + \lambda_{eff}\right)\right] \tag*{[2.90]}$$
   where: $\lambda_{eff} = \frac{\sum \lambda_i^2 C_i}{\sum \lambda_i C_i}$.
6. If the control drums were perfect, this reactivity would be instantaneously added to the system. The total reactivity would be used to determine the new reactor power level by
   $$\rho_f^{t+1} = \rho_f^t + \dot{\rho}_f^t \Delta t,$$

$$\begin{aligned}\rho_c^{t+1} &= \rho_c^t + \dot{\rho}_c^t \Delta t,\\ \rho^{t+1} &= \rho_f^{t+1} + \rho_c^{t+1},\\ T^{t+1} &= \frac{T^t + \Delta t \sum \lambda_i C_i^t}{1 + \Delta t \frac{\left(\beta - \rho^{t+1}\right)}{\Lambda}} \text{ and,}\\ C_i^{t+1} &= \frac{C_i^t + \Delta t \frac{\beta_i}{\Lambda} T^{t+1}}{1 + \Delta t \lambda_i}.\end{aligned} \qquad [2.91]$$

For actual control drum movement there are constraints on the speed of drum rotation and possibly other reactor safety constraints that would make the reactivity from the control different than from the calculated desired reactivity. These adjustments would be incorporated into the determination of the control reactivity and then the total reactivity. The power and neutron precursor calculations would remain the same for the actual input total reactivity. The next section describes the feedback and control reactivities associated with the NERVA and PBR reactors.

2.7.2 Feedback Reactivity

2.7.2.1 Moderator Temperature Coefficient

A simple moderator coefficient of reactivity was used for the particle bed reactor. The coefficient of reactivity has been found to be slightly positive due to the increase of thermal utilization factor with an increase of moderator temperature. Simple equations for the coefficients were used, but more realistic equations could easily be added by adding the coding to the COREHEAT subroutine. The basic equation is

$$\rho_m = \alpha_m \left(T_m - T_{ref} \right), \qquad [2.92]$$

where: ρ_m = feedback reactivity due the moderator temperature,
α_m = moderator temperature reactivity coefficient,
T_m = average moderator solid temperature and,
T_{ref} = reference temperature (300K).

This coefficient is used only for the PBR reactor as its core has a heterogeneous arrangement, while the NERVA core is nearly homogeneous.

2.7.2.2 *Fuel Temperature Coefficient*

A simple equation for the Fuel Doppler/Temperature coefficient for reactivity was chosen. The Doppler effect is small due to the highly enriched fuel, but never the less important for initial transient response. It is especially important for the PBR due to the positive moderator coefficient. The basic equation is

$$\rho_D = \alpha_D\left(T_f - T_{ref}\right), \qquad [2.93]$$

where: ρ_D = feedback reactivity due to the fuel temperature,
α_D = fuel temperature reactivity coefficient and,
T_f = average fuel solid temperature.

2.7.2.3 *Reactor Region Hydrogen Content Coefficient*

There are several regions of the core that the hydrogen affects the reactivity of the core. In the reflector region, hydrogen enters either as a liquid or a cool gas, while in the core the hydrogen enters as a cool gas and exits as a hot gas. Studies for the NERVA program split the worth of the hydrogen between these two regions[H-4,W-6]. The hydrogen number density in a particular region determines its importance to the moderating process. The density is roughly proportional to the fluid pressure and inversely proportional to the fluid temperature. For the particle bed reactor, Reference [P-3] used coefficients based on the temperature and pressure of the hydrogen. Reference [H-4] and [W-6] used a hydrogen coefficient based on the mass content in the volume. The mass and pressure coefficients will be positive due to the increase of hydrogen content with each of these parameters. The temperature coefficient is in general negative, due to the loss of moderating material with increasing temperature. The basic equation used for the NERVA and PBR engines are

$$\rho_H = \alpha_H M_H$$

$$\rho_P = \alpha_P \left(P_H - P_{ref}\right)$$

$$\rho_T = \alpha_T \left(T_H - T_{ref}\right), \qquad [2.94]$$

where: ρ_H = feedback reactivity due to the mass of hydrogen in the region,
α_H = hydrogen mass reactivity coefficient,
M_H = mass of hydrogen in the region,
ρ_P = feedback reactivity due to the pressure of hydrogen in the region,
α_P = hydrogen pressure reactivity coefficient,
P_H = average pressure of hydrogen in the region,
P_{ref} = reference hydrogen pressure (101000 Pa),
ρ_T = feedback reactivity due to the temperature of the hydrogen in the region,
α_T = hydrogen temperature reactivity coefficient,
T_H = average temperature of hydrogen in the region and,
T_{ref} = reference hydrogen temperature (300K).

2.7.2.4 Reflector Region Hydrogen Content Coefficient

The reflector is cooled from gamma and neutron heating by hydrogen gas flowing through cooling passages. Because the hydrogen is a strong moderator, the amounts of hydrogen in this region can have a large affect on the reactivity. The hydrogen can be in the gaseous phase or near liquid phase as is passes through the reflector. Coefficients based on the hydrogen mass content and the reflector solid material temperature were used in the NERVA program[H-4,W-6] and was implemented in this research. The reactivity worth equation used is

$$\rho_R = \alpha_{RH} M_{RH} + \alpha_{TR}\left(T_{Rs} - T_{ref}\right), \qquad [2.95]$$

where: ρ_R = feedback reactivity due to the reflector conditions,
α_{RH} = reflector hydrogen mass reactivity coefficient,
M_{RH} = mass of hydrogen in the reflector region,
α_{TR} = reflector temperature reactivity coefficient and,
T_{Rs} = average reflector solid temperature

2.7.3 Control Reactivity

2.7.3.1 Control Drum Worth

The control mechanisms for the space nuclear propulsion concepts consist of cylindrical drums located symmetrically in the reflector region outside of the core. A typical drum will be made of some moderating material, such as beryllium (Be). The poison material, such as boron carbide (B_4C) is located over a 120 degree arc of its outer surface. With the drum rotated fully inward, the arc of poison material is centered at the zero degree position. As the drums are rotated outward to the 180 degree position, the poison material is replaced by moderating material, thus adding reactivity. A schematic of the layout for one control drum is shown in Figure 2.13.

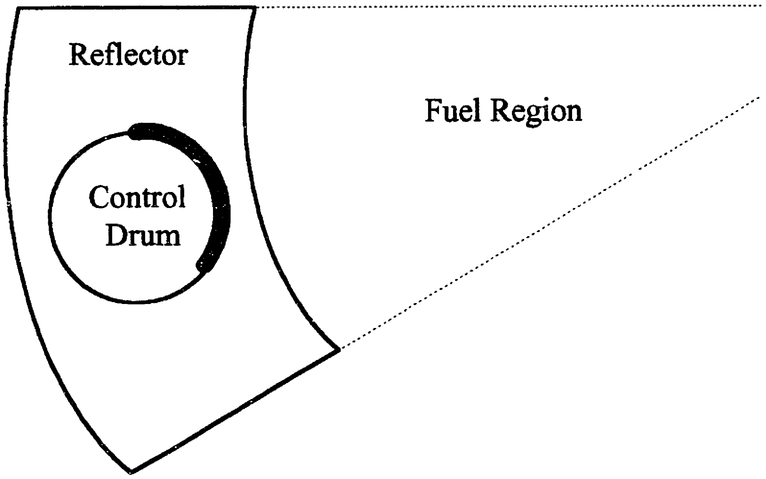

Figure 2.13 Typical Control Drum and Reflector Layout

The differential control drum worth is assumed to be sinusoidal. The user specifies the total rod worth and the computer programs determine the reactivity as a function of drum rotation by the equation[W-6]

$$\rho_c = \boldsymbol{\beta}\, ICW \cos(\theta_c), \qquad [2.96]$$

where: ρ_c = control drum reactivity,
ICW = integral control worth for the full span of drum rotation in units of $\boldsymbol{\beta}$,
θ_c = angle of control drum rotation.

The $\dot{\rho}_c$ determined by equation 2.90 is the desired rate of reactivity change in order for the reactor to have the desired power trajectory. This desired reactivity rate is used as the control signal for the control drum positioning. Because the control drums have limits on how fast and far they can be rotated and have a positioning lag time, these considerations must be modeled. The following equations show the process by which the simulated "actual" drum position and rate of change of reactivity are determined. The demanded reactivity is found from the demanded rate of change of reactivity by

$$\rho_{c,d}^{t+1} = \rho_c^t + \Delta t\, \dot{\rho}_{c,d}^{t+1}. \qquad [2.97]$$

The demanded drum rotation angle is found by inverting equation 2.96, where

$$\hat{\theta}_{c,d}^{t+1} = \arccos\left(\frac{\rho_{c,d}^{t+1}}{\beta\, ICW}\right). \qquad [2.98]$$

The drum inertia time lag effect is accounted for in a similar fashion to the TBCV stem positioning in equation 2.78. The actual drum position, with no speed limit on the drum rotation, is found by

$$\theta_c^{t+1} = \frac{\theta_c^t + \lambda_{CRD}\Delta t\, \hat{\theta}_{c,d}^{t+1}}{1 + \lambda_{CRD}\Delta t}. \qquad [2.99]$$

The required drum rotation speed is then found by finite difference with respect to time,

$$\hat{\dot{\theta}}_{c,d}^{t+1} = \frac{\theta_c^{t+1} - \theta_c^t}{\Delta t}. \qquad [2.100]$$

The value determined by equations 2.100 is capped so that the maximum speed in either direction is the user defined maximum rotation speed,

$$\dot{\theta}_c^{t+1} = \pm\min\left(\dot{\theta}_{c,\max};\ \left|\hat{\dot{\theta}}_c^{t+1}\right|\right). \qquad [2.101]$$

Then the actual control drum position is found from the actual drum speed,

$$\theta_c^{t+1} = \theta_c^t + \Delta t\, \dot{\theta}_c^{t+1}. \qquad [2.102]$$

The rate of change of reactivity is than found from the time derivative of equation 2.96,

$$\dot{\rho}_c^{t+1} = \boldsymbol{\beta} ICW \sin(\theta_c^{t+1})\dot{\theta}_c^{t+1} . \qquad [2.103]$$

Equation 2.96 is then used to find the reactivity due to the control drums and the equation 2.91 is used to find the current time step power level and delayed neutron precursor concentrations. The power level represents the total energy released. A certain fraction of this power will be delayed by fission product decay heat precursors. The modeling of the decay and the impact on the total power is included in the next section.

2.8 Decay Heat Power

Decay heat has been modeled using six groups of decay heat precursors. The SAFSIM code has definitions for up to eleven groups[D-1], but five of the groups have decay constants that are long enough and effective yields that are low enough that they can be neglected. This is justifiable because the maximum single burn time for a rocket engine is only one hour. The decay power is included in the total heat power added to the regions much the same way that the delayed neutron population is included in the total neutron population. The total decay power is the sum of the effective decay powers from the individual decay heat precursors. The power that is released almost immediately from fission will be considered as prompt power and it is weighted by a factor to account for the fraction of total power that is not decay heat power. In equation form, the individual decay heat power and the total effective power (Q_{tot}) are

$$Q_{DH,i}^{t+1} = \sum \left[\Gamma_i (1 - e^{-\lambda_i \Delta t}) Q_P^{t+1} + Q_{DH,i}^{t} e^{-\lambda_i \Delta t} \right]$$

$$Q_{tot} = (1 - \boldsymbol{\Gamma})\, Q_P + \sum Q_{DH,i} , \qquad [2.104]$$

where: $\boldsymbol{\Gamma} = \sum_{i=1}^{6} \Gamma_i$ = total effective decay heat precursor fraction,

Γ_i = fractional yield of the *i*th decay heat precursor group,

$Q_{DH,i}$ = effective decay power from *i*th decay precursor group,

Q_P = prompt fission power calculated from the point kinetics and,

λ_i = decay heat precursor decay constant for the *i*th group.

The default values used for the decay heat precursor fractions and decay constants are given in Table 2.4[D-1].

Table 2.4 Default Decay Heat Precursor Fractions and Decay Constants

Γ_i	λ_i (sec^{-1})
0.00299	1.77200
0.00825	0.57240
0.01550	0.06743
0.01935	0.00621
0.01165	4.739e-4
0.00645	4.810e-5
$\beta = 0.00790$	$\Lambda = 33.5\ \mu sec$

2.9 Power Shape and Flow Resistance Distributions

2.9.1 Axial Power Distribution - Skewed Sine with Extrapolated Length

A means for providing variable power shapes based on the cosine shape was developed. Shapes can be generated that allows variable locations of the peak power and variable amounts of peaking of the power shape. Peaking factors based on the number of axial positions are generated that are defined so that the average power density of the core is maintained. Figure 2.14 depicts the general shape and parameters used to define the power shape.

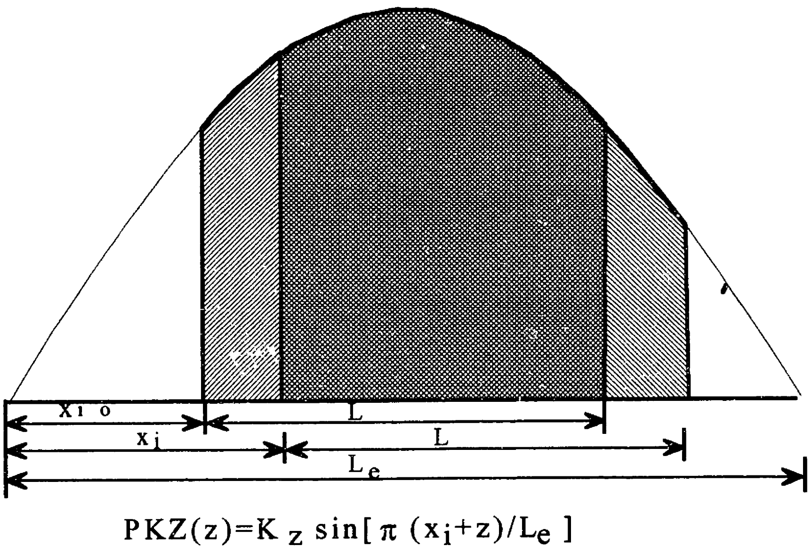

Figure 2.14 Skewed Sine with Extrapolated Length Axial Power Shaping

The average power density along the axial direction can be determined from

$$\langle \dddot{q} \rangle \pi r_o^2 L = \int_0^{ro} \int_0^L \dddot{q}\,(r,z)\, 2\pi r\, dr\, dz, \qquad [2.105]$$

where: $\langle \dddot{q} \rangle$ = average core power density,
$\dddot{q}\,(r,z)$ = power density of core as a function of position,
L = axial length of active core and,
r_o = outer radius of the active core.

Using separation of variables, the power density can be define as

$$\dddot{q}\,(r,z) \equiv PKR(r) \cdot PKZ(z) \cdot \langle \dddot{q} \rangle \qquad [2.106]$$

The core radial power distribution function (PKR(r)) has already been discussed in Section 2.6.2 and is implemented through peaking factors. The axial power shape function is assumed to be a sine function with extrapolated lengths. In other words

$$PKZ(z) \equiv K_Z \sin\left(\frac{\pi(x_i + z)}{L_e}\right)$$

$$K_z = \frac{\pi L}{L_e}\left[\cos\left(\frac{\pi x_i}{L_e}\right) - \cos\left(\frac{\pi (x_i + L)}{L_e}\right)\right]^{-1} \qquad [2.107]$$

where: $L_e = C_e \cdot L$ = extrapolated length,
C_e = extrapolation length multiplication factor,
$x_i = S_e \cdot x_{io}$ = position on the extrapolated length that fuel begins,
x_{io} = position on the extrapolated length that fuel begins when the peak is at the center of the active fuel length,
S_e = skewing factor to determine the beginning of active fuel,
z = axial position, measured from the start of active fuel and,
K_z = factor found by integrating the power shape and normalizing to 1.0

By defining C_e and S_e the power shape is determined by only knowing the active fuel length. The power shape is discretized for the number of axial nodes and is normalized to ensure that the average of the axial peaking factors is equal to unity. These variables are coded into the simulation model variable COSCHOP by ss0cc.cc, where ss is equal to ten $10 \cdot S_e$ and cc.cc is equal to C_e.

2.9.2 PBR Element Radial Power Distribution - Exponential

The particle bed reactor fuel has a large amount of self shielding of neutrons and the hot frit can act as a neutron poison. In order to simulate this effect, an exponential decay shape was chosen for the radial profile in the bed. Equation 2.106 defines the core power density as a combination of a radial shape function and an axial shape function. For the particle bed reactor, this shaping can be applied to the element itself. Figure 2.15 depicts the general shape and parameters used to define the radial power shape.

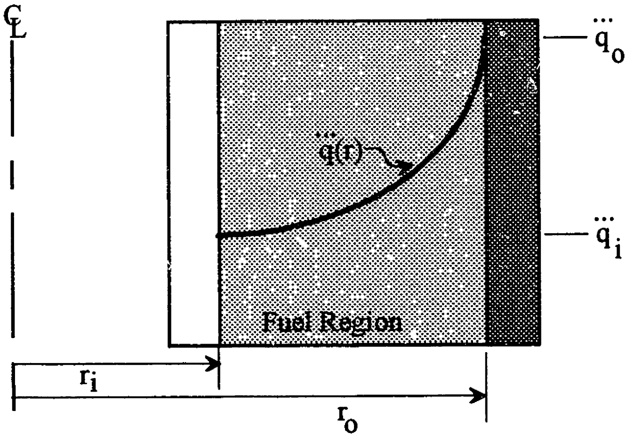

Figure 2.15 Exponential Power Shaping for the PBR Fuel Element

The radial power shaping function is defined as

$$PKR(r) \equiv K_r e^{\tau(r-r_i)}$$

$$K_r = \frac{\tau^2\left(r_o^2 - r_i^2\right)}{2[\tau(r_o R - r_i) - (R-1)]}, \qquad [2.108]$$

where: $\tau = \dfrac{\ln(R)}{(r_o - r_i)}$ = exponential power shape factor,
r_i = inner radius of the fuel bed,
r = radial position in the fuel bed as measured from the inner radius,
$R = \dfrac{\dddot{q}_o}{\dddot{q}_i}$ = ratio of outer edge power to the inner edge and,
K_r = factor found by integrating the power shape and normalizing.

As was performed for the axial power shape, the radial shape is discretized for the number of radial nodes. The node peaking factors are normalized so that the average is equal to unity. Typical values for R range from 2.5 to 4.0. This variable is named TAUFAC in the simulation model input files. The power shaping for the one dimensional element model only requires the radial peaking factors developed here. For the two dimensional SIMBED model, both the axial and the radial peaking factors can be applied to the fuel bed nodes. The peaking factors were used to allow the implementation of power shapes determined from reactor physics calculations. These calculations could be performed using the thermal hydraulic and control drum feedback values. The output from these calculations could then be used to determine the peaking factors that are used in the engine simulation code.

2.9.3 PBR Cold Frit Flow Resistance Distribution

2.9.3.1 Introduction

Modifications were made to the SIMBED code to allow evaluation of a PBR fuel element with an cold frit with variable flow resistance along its length. Varying the resistance has been proposed as a means of distributing the flow to ensure proper fuel cooling. Simple linear and parabolic shapes were selected as representative distributions.

These distributions were normalized so that the average resistance is equal to the original uniform resistance. This section describes the methodology used for generating these distributions.

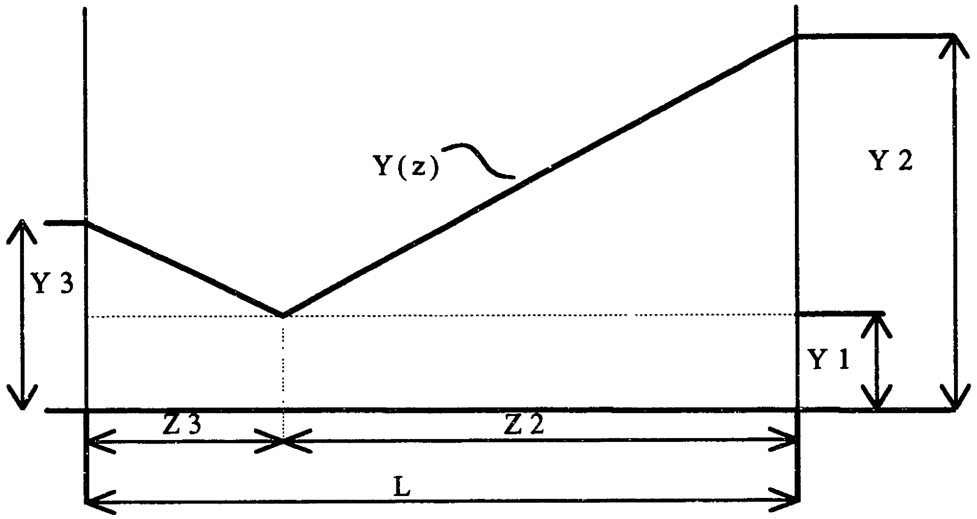

Figure 2.16 Linear Cold Frit Flow Resistance Parameter CFDIST Nomenclature

2.9.3.2 Linear Distribution

The generalized shape used is depicted in Figure 2.16. By specifying the ratio of maximum to minimum flow resistance, the relative axial position of the minimum resistance, and that the slopes of the lines are equal in magnitude, the distribution is defined. Integrating along the length of the cold frit allows one to find the normalization coefficients and the distribution equation. This is developed in the following equations.

The area beneath the curve is normalized to one by equation 2.109.

$$L = Y1 \cdot L + 0.5\,(Y2 - Y1) \cdot Z2 + 0.5\,(Y3 - Y1) \cdot Z3$$

$$1 = Y1 + 0.5\,Y1\,\frac{Z2}{L}\left(\frac{Y2}{Y1} - 1\right) + 0.5\,Y1\,\frac{Z3}{L}\left(\frac{Y3}{Y1} - 1\right). \qquad [2.109]$$

Because the magnitude of the slopes of the lines are assumed to be equal:

$$\left(\frac{Y3}{Y1} - 1\right) = \left(\frac{Y2}{Y1} - 1\right) \cdot \frac{Z3}{Z2} \text{ (from slopes assumption)} \qquad [2.110]$$

Substituting Equation 2.110 into 2.109 yields

$$1 = Y1\left[1.0 + 0.5\,SSJ(CFJ-1) + 0.5\,\frac{(1-SSJ)^2}{SSJ}(CFJ-1)\right] \qquad [2.111]$$

where: SSJ = Z2/L
CFJ = Y2/Y1.

Finally, the coefficient of interest, Y1, is determined by the inverse of 2.111 as:

$$Y1 = SSJ \cdot \{SSJ + 0.5(CFJ-1)[SSJ^2 + (1-SSJ)^2]\}^{-1} \qquad [2.112]$$

The cold frit resistance distribution is then found by:

$$Y(z) = Y1 + \left[1.0 + (CFJ-1)\frac{|z/L - (1-SSJ)|}{SSJ}\right] \qquad [2.113]$$

This was derived for the case where Z2/L is greater than 0.5, but by a simple transformation, the same equations hold for the case when Z2/L is less than 0.5. The input variable for the simulation models is CFDIST as is coded as ss0cc.cc, where ss is equal to 100 SSJ and cc.cc equals CFJ.

2.9.3.3 Parabola Distribution

The distribution shape used for the parabola, of general form $y=az^2$, is shown in Figure 2.17. The same definitions for SSJ and CFJ will be used in the development of the distribution coefficient and equation. The CFDIST is also defined the same, except that a minus sign is put in front to specify the parabola distribution.

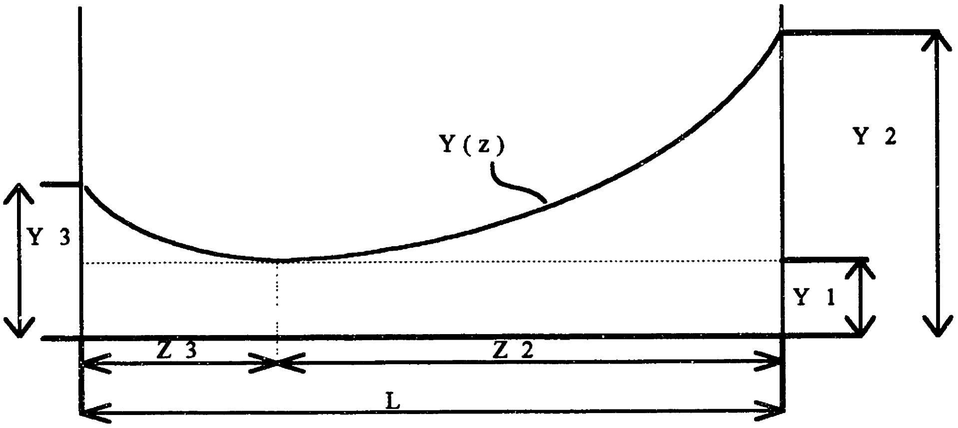

Figure 2.17 Parabolic Cold Frit Flow Resistance Parameter CFDIST Nomenclature

Integrating and normalizing the distribution function yields the following:

$$L = Y1 \cdot L + \int_0^{Z3} (Y3 - Y1)\left(\frac{z - Z3}{Z3}\right)^2 dz + \int_{Z3}^{L} (Y2 - Y1)\left(\frac{z - Z3}{Z2}\right)^2 dz$$

$$L = Y1 \cdot L + \frac{(Y3 - Y1)}{3} Z3 + \frac{(Y2 - Y1)}{3} Z2$$

$$3 = Y1\left[3 + \left(\frac{Y3}{Y1} - 1\right)(1 - SSJ) + \left(\frac{Y2}{Y1} - 1\right)SSJ\right]. \qquad [2.114]$$

Since the distribution is a parabola, the following relation holds

$$\left(\frac{Y3}{Y1} - 1\right) = \left(\frac{Y2}{Y1} - 1\right)\left(\frac{Z3}{Z2}\right)^2 = (CFJ - 1)\left(\frac{1 - SSJ}{SSJ}\right)^2. \qquad [2.115]$$

Substituting these relations into Equation 2.114 yields,

$$3 = Y1\left[3 + (CFJ - 1)\frac{(1 - SSJ)^3}{SSJ^2} + (CFJ - 1)SSJ\right]. \qquad [2.115]$$

The Y1 normalization factor is found by the inverse of Equation 2.115 as

$$Y1 = 3\,SSJ^2\{3\,SSJ^2 + (CFJ-1)[(1-SSJ)^3 + SSJ^3]\}^{-1} \qquad [2.116]$$

The parabolic cold frit resistance distribution is then

$$Y(z) = Y1\left\{1 + \frac{(CFJ-1)}{SSJ^2}\left[\frac{z}{L} - (1-SSJ)\right]^2\right\}. \qquad [2.117]$$

2.10 Hydrogen Properties Routines

2.10.1 General

Thermal Hydraulic analysis is often limited by the thermal property values used by the computer codes. The hydrogen propellant used in the nuclear rocket systems is stored and pumped as a liquid, is heated to a low temperature gas before entering the core, and then is rapidly heated to dissociation temperatures. This makes it impossible to simply assume perfect gas relations. The properties of hydrogen over this broad range are not easily placed in simple equation form. Figure 2.18 shows the behavior of the heat capacity of hydrogen as a function of pressure and temperature[M-4]. It was decided to derive the calculations with enthalpy rather than temperature and heat capacity due to the two phase conditions in part of the flow stream and the steepness in portions of the heat capacity curves. Once the enthalpy and pressure are known, the other properties including temperature can be determined.

Routines have been developed to either fit to correlation curves or perform tabular lookup of National Bureau of Standards properties. Several codes were investigated by the author and are summarized in the next sections.

2.10.2 NASA Lewis - STATE Properties Subroutine to 5000K

The routine STATE was used by the CAC code [C-2, H-2]. It consists of curve fits over three ranges of pressure and temperature. The code is able to model hydrogen properties up to 5000 K. The code, however, does not account for dissociation at the higher temperatures. This introduces some errors. Reference [H-2] indicates that the model is accurate to a 2% standard deviation to 1800 K at 0.1 MPa and to 2200 K at

10MPa. Above these temperatures, the errors grow as more dissociation occurs in the real gas properties. Because most chamber temperatures are anticipated to be higher that 1800 K, this code was not selected for use.

2.10.3 Brookhaven - Tabular NBS Properties to 3000 K

The hydrogen properties routines used in the SIMBED code are in the form of separate subroutines. The temperature is if found from the enthalpy and pressure, and then all other properties are found and a function of temperature and pressure. Values for the heat capacity, viscosity, thermal conductivity, density, and volumetric heat capacity can be determined. The data sets for these routines are limited to 3000 K. Above this temperature, the routines will simply use the property values associated with 3000 K. Because some reactor concepts have chamber temperatures above 3000 K, this set of subroutines was not selected for use in the modeling developed in this research.

2.10.4 NASA Lewis - NBS-pH2 Properties Subroutine to 10,000K

As part of the NASA Lewis Research Center modeling effort, James Walton has developed a computer program that provides hydrogen properties over the temperature range of 13 K-10000 K and the pressure range of 1 kPa-16 MPa[W-2]. The properties provided are: heat capacity, ratio of specific heats, speed of sound, Prandtl number, thermal conductivity, density, viscosity, gas constant, and two phase quality. It consists of tables generated from the NBS nomographs and calculated extrapolations for data above 3000K. It accounts for the dissociation of hydrogen at the higher temperatures. It should be noted that there is limited test data at the higher temperatures and much of the extrapolation method is based on chemical theory. The NBS-pH2 routine was selected for use due to the wide temperature and pressure range for the hydrogen properties and because accommodations are made for the dissociation of hydrogen.

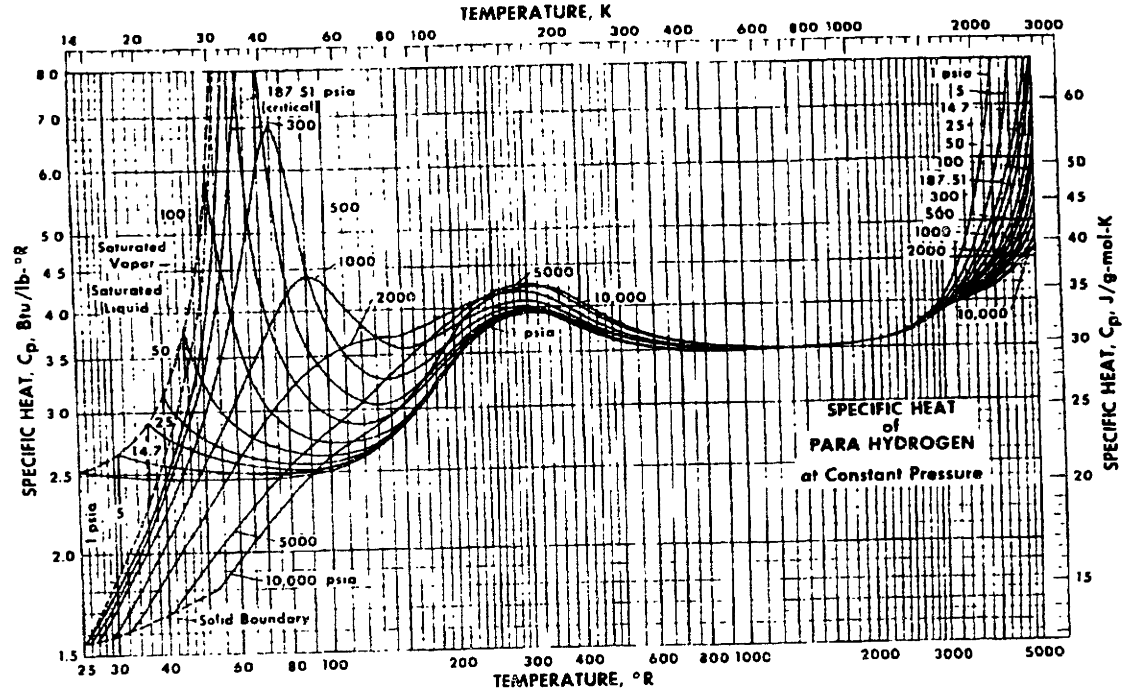

Figure 2.18 Specific Heat of Parahydrogen at Constant Pressures from Reference [M-4]

2.11 Chapter Summary

This chapter has presented the basic models and governing equations used by the various computer codes developed as part of this research. This includes equations for the fluid pressure drops, for the heat transfer from the solids to the fluid for various geometries, and for the power shaping peaking factors. Reactivity models and the point kinetics models for transient power and control of the reactor is also presented. A brief discussion on the available hydrogen properties routines is provided. In the next chapter, results of efforts to model the particle bed reactor fuel element will be presented.

Chapter Three - Particle Bed Reactor Modeling

3.1 Introduction

In this Chapter, the modeling of the particle bed reactor fuel element is presented. A basic overview of the fundamentals of porous media flow is given in order to better understand some of the implications of the multidimensional flow patterns in the packed bed. The discussion proceeds to one dimensional radial modeling of prototypic fuel elements under steady state and transient conditions. The improvements and enhancements to existing computer models is presented as a means to benchmark the element model that is to be used in the full core model. A discussion on the effort to model the PBR element in a radial and axial directions is then presented in Section 3.4. In that section, the capability to model the basic flow characteristics is used as a way to show confidence in the models. Finally, an analysis on the flow stability in the bed is presented in Section 3.5. The results of this analysis have been used to identify operating conditions of the element that could lead to unstable flow conditions and fuel damage.

For the PBR fuel element studies two element geometries were selected. The PIPE experiment element dimensions are used to benchmark the new computer codes relative to the ones presented in References [T-1] and [C-5]. For the baseline PBR fuel element, a geometry is selected so that the power and flow requirements of the core can be meet while maintaining the exit Mach number less than 0.25. A full listing of the input files is given in Appendix A. The key dimensions of these elements are given in Table 3.1

Table 3.1 Fuel Element Dimensions used for PIPE and Baseline PBR

Parameter	*PIPE*	*Baseline PBR*	*Units*
Hot Frit Inner Radius	14.250	20.200	mm
Hot Frit Outer Radius	15.000	22.700	mm
Cold Frit Inner Radius	27.500	32.700	mm
Cold Frit Outer Radius	29.434	35.700	mm
Inlet Plenum Inner Radius	44.580	38.700	mm
Fuel Bed Length	0.256	0.600	m
Fuel Particle Outer Diameter	0.500	0.500	mm

Parameter	*PIPE*	*Baseline PBR*	*Units*
Fuel Region Porosity	0.400	0.370	
Cold Frit Porosity	0.685	0.500	
Cold Frit Particle Diameter	2.700	2.700	um
Cold Frit Viscous Coefficient	7.410 E+12	1.307 E+13	m^{-2}
Cold Frit Inertial Coefficient	6.860 E+5	4.252 E+7	m^{-1}
Hot Frit Porosity	0.230	0.500	
Hot Frit Hydraulic Diameter	0.100	0.100	mm
Hot Frit Viscous Coefficient	3.000 E+10	6.882 E+9	m^{-2}
Hot Frit Inertial Coefficient	7.000 E+4	2.0276 E+4	m^{-1}

3.2 Porous Media Flow

In order to adequately model the particle bed reactor fuel element, an understanding of the flow in the porous media is required. The Ergun relation, or correlations in the form of viscous and inertial terms, have become the standard form for the pressure drop[E-1,C-4,S-11,V-1]. As presented in Section 2.3.21 it is a function of the solid material porosity and shape, and the fluid viscosity, density, and velocity:

$$\frac{dP}{dr} = 150\frac{(1-\varepsilon)^2}{D_p^2\varepsilon^3}\mu u_s + 1.75\frac{(1-\varepsilon)}{D_p\varepsilon^3}\rho u_s^2. \qquad [2.29]$$

The solid material geometry can be designed so as to minimize adverse effects on the flow pattern. The impacts of the porosity and particle size are discussed in the next two sections. Section 3.2.3 is a consolidated presentation on the effects of varying the system pressure and flow rate, hence the impact of the density and the viscosity of the gas on the pressure drop.

3.2.1 Material Size Effects

The packed bed material size and shape affect the pressure drop across the bed. Because the PBR fuel particle is generally spherical, only size effects need to be considered for nominal operating conditions. By holding all terms but the particle diameter constant, the impact of the particle size can be shown. As the particle size is increased the pressure drop across the bed for a fixed flow rate is reduced. This is due to the Reynolds number and the interstitial flow area becoming larger. The trend for the flow resistance with respect to the particle size is represented in Figure 3.1 for the baseline PBR fuel element in terms of the effective flow resistance.

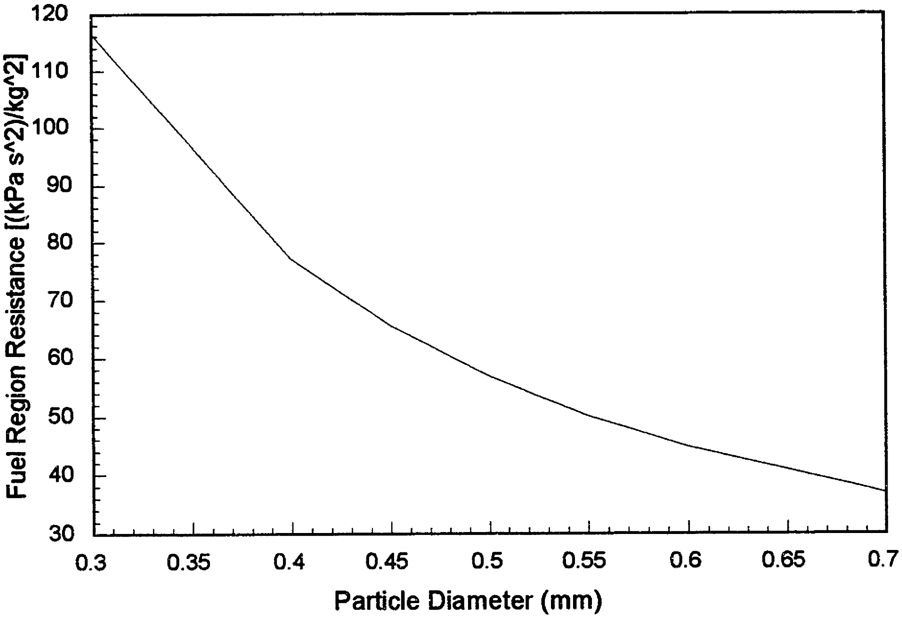

Figure 3.1 Impact of the PBR Particle Diameter Size on the Pressure Drop

3.2.2 Material Porosity Effects

The porosity of the packed bed is another important term in the pressure drop correlation used for the study of the PBR fuel element. Holding all but the porosity constant, the impact of the bed porosity can be shown. As porosity is increased, the pressure drop is reduced due to the reduced flow resistance of the larger flow area. Figure 3.2 depicts the flow resistance as a function of porosity for the baseline PBR fuel element.

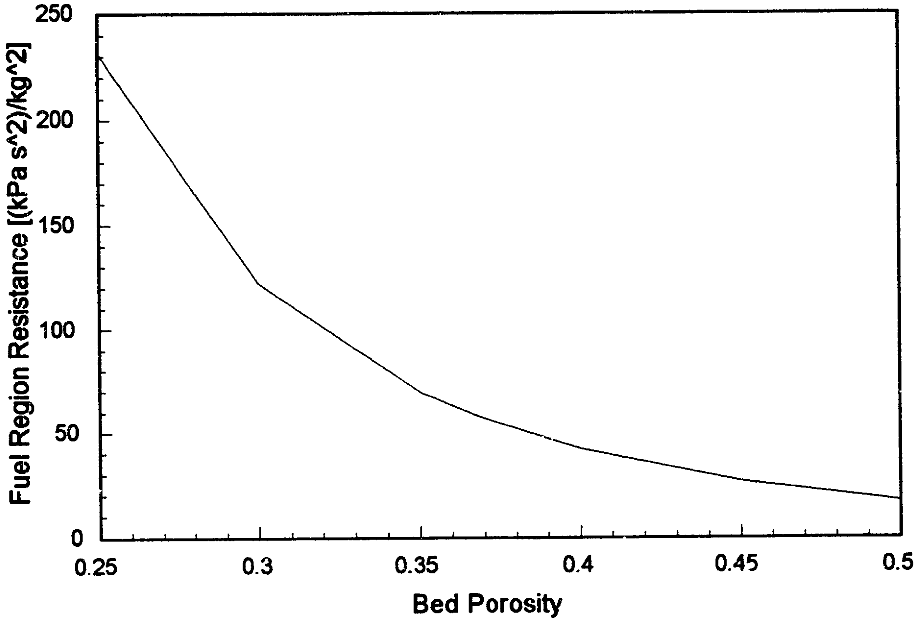

Figure 3.2 Impact of the PBR Fuel Bed Porosity on the Pressure Drop

The average porosity can be used to determine nominal pressure drop response, but multidimensional studies should also include effects due to non-uniformities in the bed packing. Non-uniformities in the porosity may be due to wall effects or due to the randomness of packing in regions not influenced by a wall. The porosity varies as a function of the distance from a wall surface and particle diameter. The distribution has been shown to be an oscillatory exponential decay [B-10, R-2] but can be adequately modeled as a simple exponential decay [C-4, V-2, V-3]. The SIMBED code uses a relation to determine this porosity distribution as[C- 4]:

$$\varepsilon(x) = \varepsilon_\infty \left\{ 1 + \frac{1-\varepsilon_\infty}{\varepsilon_\infty} \exp\left[-b\left(\frac{x}{D_p} \right) \right] \right\}; \qquad [3.1]$$

where: ε_∞ = bed average porosity,
b = fitting parameter, taken equal to 2.0,
x = distance from the wall and,
D_p = particle diameter.

This variation converges to the bed average after a distance of several particle diameters into the bed, but is important because "channeling" of the flow can cause the velocities at the edges to be high. This will cause some amount of flow to bypass the main bed area. This effect is depicted in Figures 3.3 and 3.4 from the results of a SIMBED case run on the baseline PBR fuel element operating at full power. The figures show the radial and axial velocities in the fuel bed region. The channeling flow is clearly shown at the top and bottom of the element. While these velocities are high, the area affected is on the order of three particle diameters. These higher velocity streams cause the temperatures in these regions to be lower than the bed average, as will be shown in Section 3.4. The bed average velocity reaches about 11 m/s for this case, with a slightly higher value at the lower end of the element due to the larger pressure gradient from top to bottom and the resulting larger pressure drop along the bottom radial sections.

Figure 3.4 shows that there is a small tendency for some flow to be directed axially along the bed toward the exit end of the element. As will be shown in Section 3.4, this is due to the pressure gradient in the outlet channel region. Because the PBR fuel element has a hot frit that does not allow axial flow and the axial flow is defined as zero at the wall boundary, the axial flow must mix with the high velocity stream lines at the element top and bottom. This causes the positive peak at the upper end of the element and the negative dip at the lower end of the element.

Local porosity variations within the average bed will also have an effect on the flow distribution. Reference [S-11] describes the two dimensional effect on flow as it passes through a medium with a variable porosity. They indicate that lateral variations in the resistance to flow can cause flow maldistributions and cross flow effects. They also show that the effects are local if there exists sufficient flow length around the area of different porosity. The basic phenomenon observed is that the flow tends to redistribute from lower porosity areas to higher porosity areas. This is expected, due to the reduced flow resistance of the larger porosity, as was discussed earlier in this section. A further discussion of this effect is given in Section 3.4.2.3 as a means of demonstrating the capabilities of the SIMBED code.

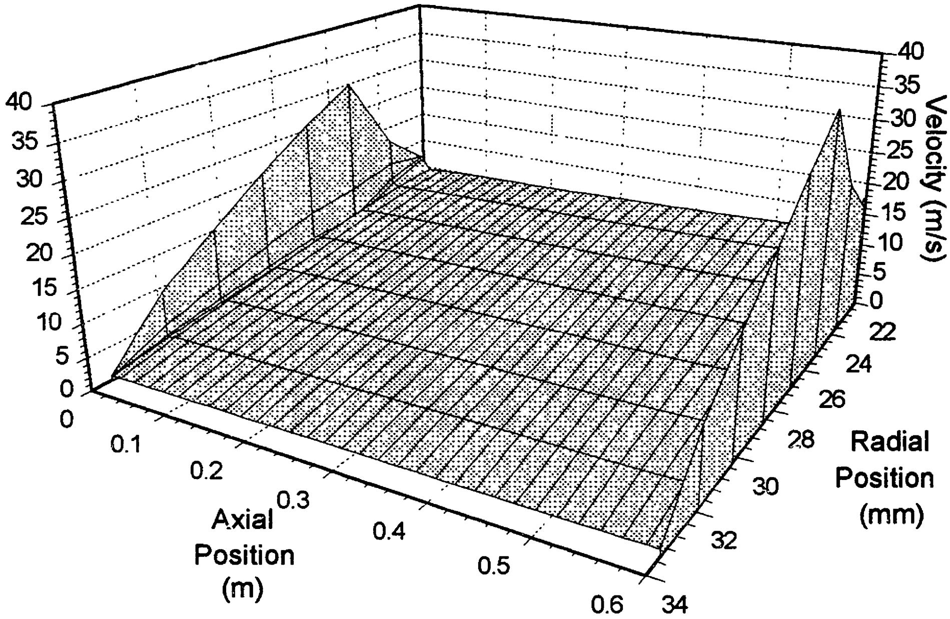

Figure 3.3 Radial Velocity Distribution in PBR Fuel Element (from SIMBED)

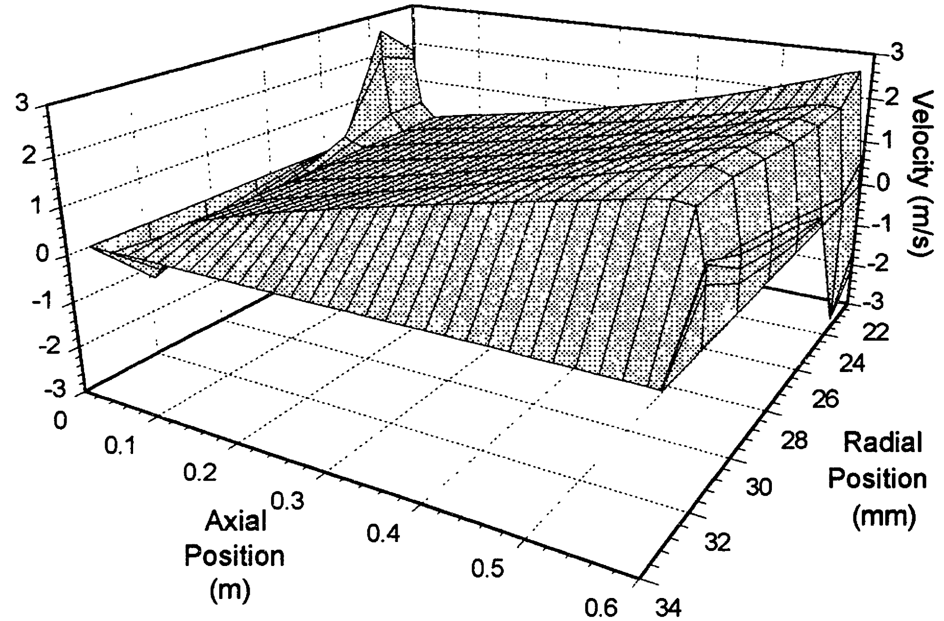

Figure 3.4 Axial Velocity Distribution in PBR Fuel Element (from SIMBED)

3.2.3 Heat Transfer Effects

For the heat transfer, a good reference for various correlations in use is Reference [B-11]. The Nusselt number developed by Achenbach has been used for the heat transfer in the fuel bed region by several authors and was chosen for use in the modeling for the PBR in this study[A-1, C-4, D-3]. The use of a properties code that accounts for the dissociation of hydrogen at higher temperatures allows the affects of the widely varying heat capacity of the hydrogen to be shown. By varying the system outlet pressure while maintaining the same power, the effect on the pressure drop due to the gas density can be shown; as is depicted in Figure 3.5. The flow rate at the higher pressure is actually slightly higher, due to the lower heat capacity of the gas. In order to maintain the same temperature rise across the bed, the flow rate at lower pressure was 0.531 kg/s, while at the higher system pressure the flow rate required was 0.543 kg/s.

The influence of the viscosity on the pressure drop is seen in Equation 2.29. Any rise in the gas temperature will raise the average viscosity and therefore the pressure gradient. This is more of an effect at lower flows, because the second inertial term will begin to dominate at the higher flow rates.

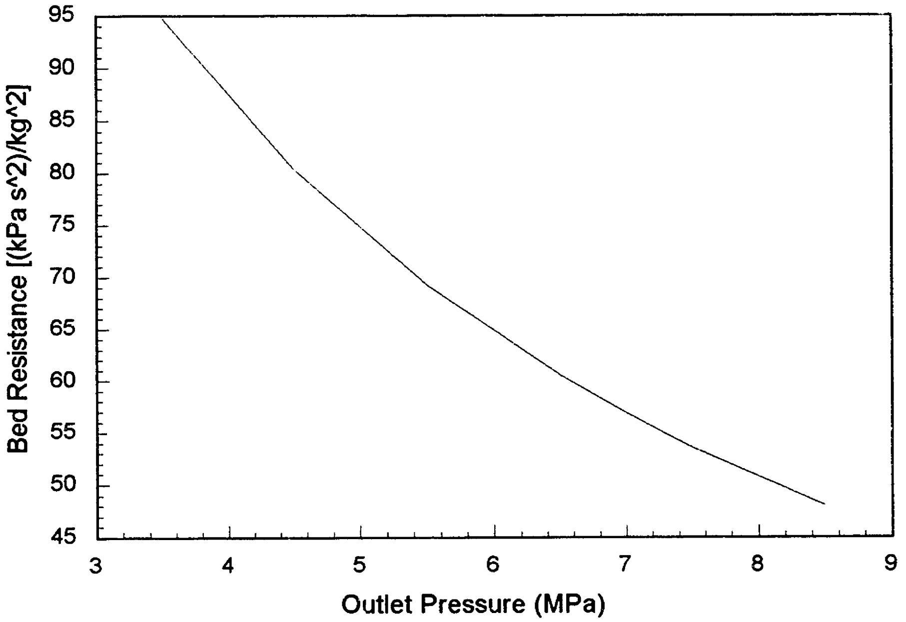

Figure 3.5 Impact of the System Pressure on the Fuel Region Pressure Drop

3.3 One Dimensional PBR Element Model

3.3.1 Steady State

3.3.1.1 Casey's STEADY Computer Code

The steady state code STEADY written by William Casey as part of his Master's Thesis work[C-5], was a program written in the C programming language. It modeled the element in three control volumes and solved for the element conditions given the inlet temperature, inlet and outlet pressures, and the power density. The primary outputs from this program were the outlet temperature and the element mass flow rate. The code was used as a development tool for the transient version of the program. Results from the cases agreed with two dimensional HTWCOOL model developed by Tuddenham in Reference [T-1]. This model is limited in the number of control volumes used and in that the hydrogen properties are based on ideal gas assumptions and curve fits for the thermal conductivity and heat capacity as a function of only the gas temperature. The computer code was reprogrammed in the FORTRAN language by this author and then modified to allow different boundary conditions to be specified. These codes will be discussed in the next section.

3.3.1.2 Witter's Family of Computer Codes

Measures for the performance of a rocket engine usually include the nozzle chamber pressure and temperature. The power density of the fueled region is a performance measure for the reactor core. To accommodate studies based on these performance measures, the program structure of STEADY was altered to specify the inlet and outlet temperatures, the outlet pressure and the fuel region power density. The program Particle Bed Reactor - Find Mass flow rate & Pressure (PBRFMP) iterates to solve for the inlet pressure and flow rate. The Casey STEADY code was also limited in the number of nodes in the fuel region. The capability to study the fuel element temperature profiles was added by allowing the user to specify up to ten zones for the fuel region. This code was named PBRFMPD for PBRFMP Detail. Sample results for the temperature and pressure through the baseline element are shown in Figure 3.6.

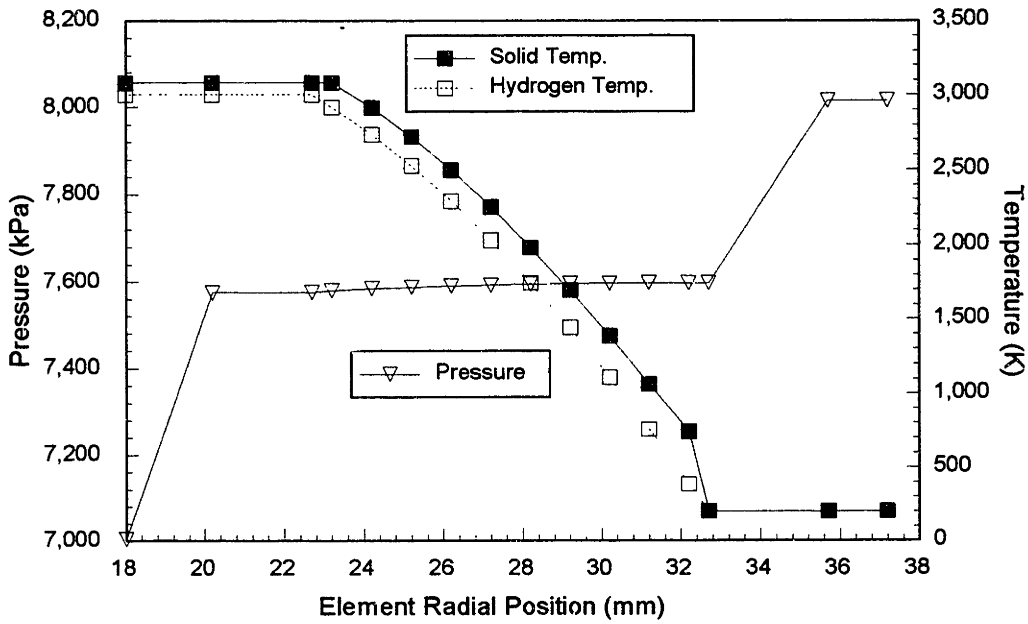

Figure 3.6 Temperatures and Pressures in Baseline PBR Element from PBRFMPD

3.3.1.3 Comparison of results from STEADY and PBRFMP

A comparison was made of the results presented by Casey in Reference [C-5]. The PIPE element dimensions, an inlet temperature of 300 K, an inlet pressure of 2000 kPa, and an outlet pressure of 1915 kPa were used for the calculations. The results for various power levels are presented in Table 3.2. The table shows good agreement with the temperatures and improving agreement for the flow rates as the power levels increase. Some of the differences are due to the additional control volumes modeled and due to using the NASA NBSpH2 hydrogen properties routine.

Table 3.2 Comparison of Casey's STEADY and Witter's PBRFMPD Model Results

Power Level (GW/m^3)	*STEADY Temperature (K)*	*PBRFMP Temperature (K)*	*STEADY Flow Rate (g/s)*	*PBRFMPD Flow Rate (g/s)*
0.000	300.000	300.000	53.200	51.000
1.000	1000.000	1000.000	44.325	43.054
2.000	1868.420	1868.000	36.775	36.722

3.3.2 Transient

3.3.2.1 Casey's UPPOWER Computer Code

Another code written by William Casey was the transient version of the STEADY model, named UPPOWER. This code allows the user to specify ramps for the inlet temperature, the inlet and outlet pressures, and the power level. The program uses these boundary conditions for the solution of the mass flow rate and outlet temperature. The UPPOWER model was shown to agree well with the transient results from Tuddenham's HTWCOOL program[C-5]. In his recommendations and future work section, Casey alluded to an apparent lag in the response of the system and the desire to add some form of power input that would mimic a reactor better than linear power ramp inputs. In the same approach that was use for the STEADY code, the UPPOWER code was rewritten in FORTRAN and the extra control volumes and other enhancements added. Point kinetics and the MIT/SNL control laws were implemented with feedback reactivity in order to model the reactor power transient response. Additionally, the capability for three successive boundary condition ramps was added. The resulting TRIple TRANsient (TRITRAN) code will be discussed in the next section.

3.3.2.2 Witter's TRITRAN Computer Code

The TRITRAN code was written to model the PBR element using point kinetics to model the reactor power level. The inlet temperature, inlet and outlet pressures, the reactor power density at the ramp endpoints, and the duration of the ramps are input by the user. The MIT/SNL control laws are utilized to place the reactor on the user defined power ramps. Sample feedback reactivity coefficients are used for the fuel temperature and the hydrogen pressure and temperature in the fuel region. The required reactivity and the feedback reactivity are used to determine the required control reactivity. This reactivity is then converted into a required control drum response by using the relation of equation 2.97 in Section 2.7.3.

The thermal lag noticed by Casey turned out to be a programming error with respect to the mass of hydrogen in the fuel region control volume. In the code as it appears in his thesis, the mass of the fuel is averaged with the mass of the hydrogen to determine the inertial mass of the control volume. The correct mass to use is only the hydrogen mass in the free volume space of the fuel bed. When this change was made, the response of the system improved, but at the expense of having to reduce the time step down to the level comparable to Reference [T-1]. Once the point kinetics power was added, the time steps used had to be reduced from 100 ms to less than 1 ms in order for the solution to be numerically stable. A change in the heat transfer correlation was also implemented in the TRITRAN code. Instead of using the Nusselt number correlation used in UPPOWER, the Achenbach correlation was implemented.

A second version of the TRITRAN code was written using the same solution method, but takes the inlet temperature, the inlet pressure, the power density, and the mass flow rate as the variable boundary conditions. This allows a more realistic approach to the problem of modeling a rocket system, because the more probable system knowns are these parameters.

The code was benchmarked to the simple transient that appears in Reference [C-5] and was then used to help understand the response on the reactor system to a down power and to a rapid startup. Results of the benchmark cases and one of the rapid triple ramp transients are presented in the next section.

3.3.2.3 Comparison of results

The benchmark uppower case run was for a power ramp from 0.2 to 2.0 GW/m^3 in one second. Because the point kinetics can not start from 0.0 GW/m^3 and the reactor is limited in the period that can be tolerated, a beginning power level of 0.2 GW/m^3 was selected for the starting point. The transient ramp boundary conditions used are given in Table 3.3. The fuel element geometry and material properties are the same as those given in Reference [C-5] and Table 3.1 for the PIPE fuel element.

Table 3.3 TRITRAN Benchmark Case Boundary Condition Endpoints

Boundary Condition	*Start Point*	*End Point*	*Units*
Time	0.200	1.200	sec
Power Density	0.200	2.000	GW/m^3
Inlet Temperature	300.000	300.000	K
Inlet Pressure	2000.000	2000.000	kPa
Outlet Pressure	1915.000	1915.000	kPa

Figures 3.7 through 3.10 depict the results of the case for various output parameters. Figure 3.7 shows the temperature response for the hydrogen at the inlet, outlet, and the fuel zone average and the response of average effective temperature of the solid fuel material. The gas temperature rises as the interface heat is added to the gas phase. The outlet temperature response is faster than that of UPPOWER by approximately 2 seconds. This response better matches the reference standard of HTWCOOL used by Casey as both TRITRAN and HTWCOOL reach the steady state value of 1868 K at about 4 seconds after the end of the of the power ramp. This can be attributed to the correction to the calculation of the hydrogen mass in the fuel control volume.

The neutron power, interface power and required control drum response are shown in Figure 3.8. The control drums rapidly rotate outward until the desired reactor period is satisfied. As the fuel and hydrogen heat up, the drums must rotate outward in order to maintain the neutron power on the desired trajectory and to level it at the desired 2.0 GW/m3. The drum rotation follows the trajectories of the interface power and the temperatures. The interface power is the power that is transferred from the solid material to the gas phase. This power lags the neutron power due to the energy required to heat the fuel particles to the new steady state temperature. As was the case for the temperature trends, the interface power response is faster than that of Reference [C-5], but is closer to the HTWCOOL reference standard. As the temperatures reach near steady state, the control drums begin to rotate inward slowly in order to maintain a zero period while the delayed neutron precursors build in to their new steady state concentrations.

The curves in Figure 3.9 show the response of the mass flow rate and the system pressures. As the element heats up, the flow resistance terms increase as the density of the gas is reduced and the viscosity is increased. This effect was described in Section 3.2. The flow rate is reduced because the inlet and outlet pressures are fixed. The gas conditions at the cold frit do not vary much, therefore, as the flow rate decreases, the pressure drop across the cold frit also decreases. The lower pressure drop causes the fuel region inlet and average pressure to increase. The flow rate converges to a new steady state value of 0.037 kg/s, which is consistent with the flow found for the steady state PBRFMPD case presented in Table 3.2.

Finally, Figure 3.10 shows the response of the various reactivities. There were no constraints put on the reactivity so the initial ramp response adds nearly one dollar of reactivity. The total feedback reactivity is dominated by the temperature feedback and reaches the new steady state value at the same time as the system temperatures. The total reactivity required has the peak shape due to the MIT/SNL control laws operating on the rate of change of reactivity and then continues to drop in order to steadily maintain the 2.0 GW/m3 power level. The build up of the delayed neutron precursors can be inferred from this convergence to a required reactivity of zero. The control drums must initially rotate out more quickly once the end state power is reached due to negative reactivity added by the rapidly increasing system temperatures. Then as the steady state temperature is reached, the drums rotate inward to counteract the build up of the delayed neutron precursors. The control reactivity is then simply the difference between the required reactivity and the feedback reactivity.

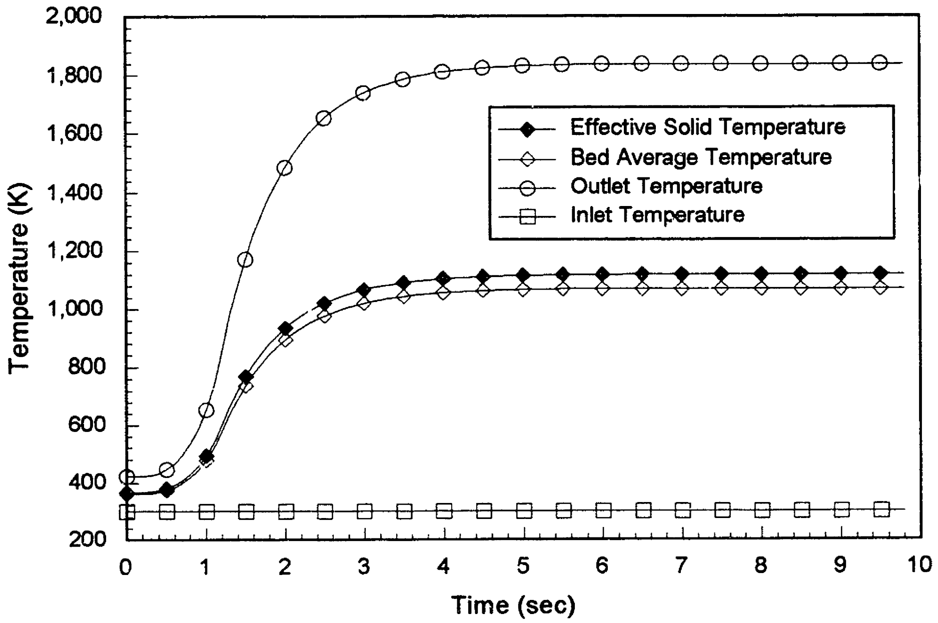

Figure 3.7 Temperature Response to a 0.2 to 2.0 GW/m^3 Power Ramp in 1.0 Second

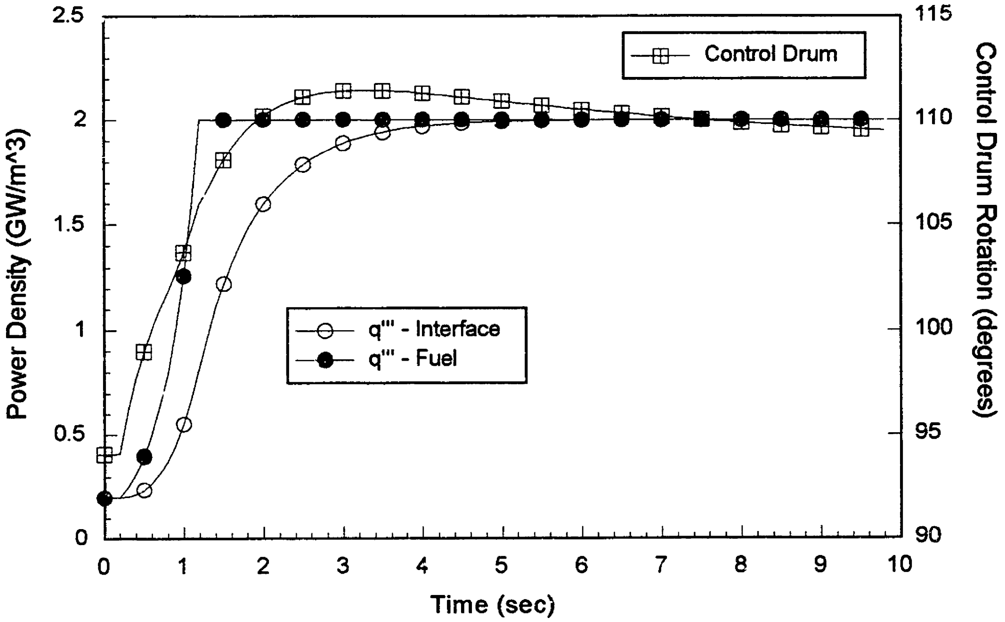

Figure 3.8 Power and Control Drum Response to a 0.2 to 2.0 GW/m^3 Ramp in 1.0 Second

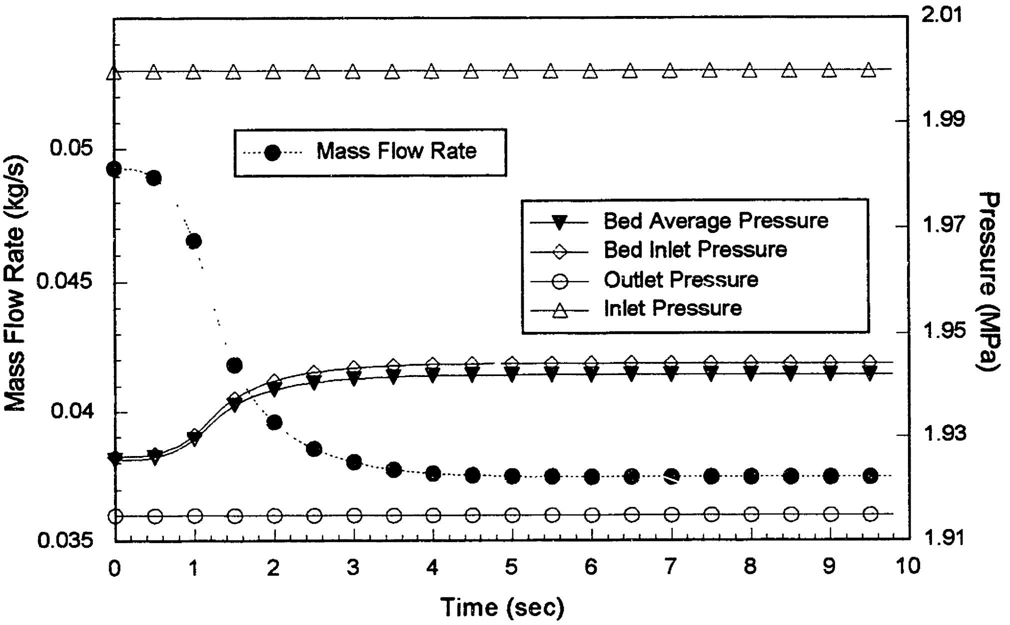

Figure 3.9 Flow Rate and Pressure Response to a 0.2 to 2.0 GW/m^3 Ramp in 1.0 Second

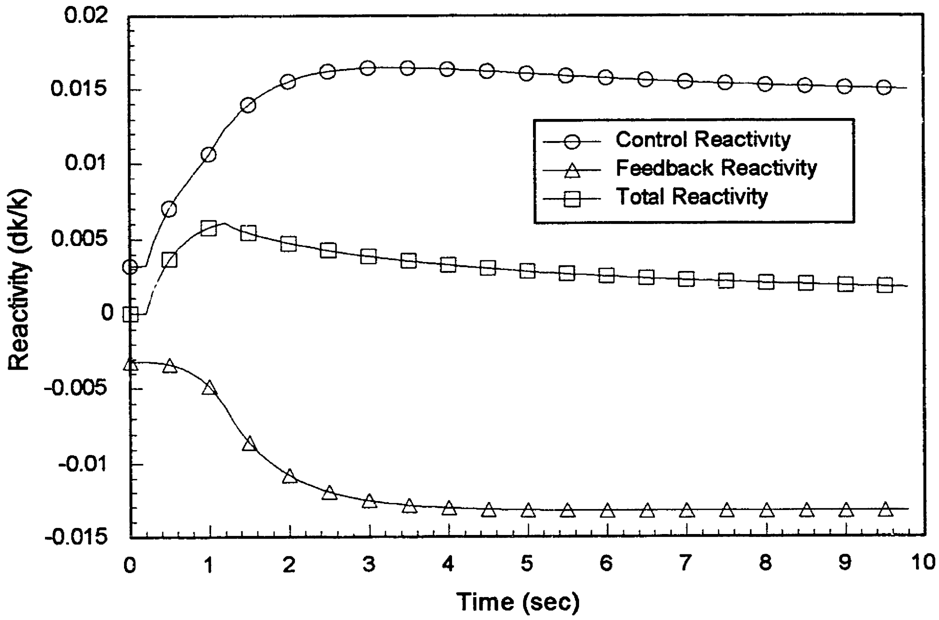

Figure 3.10 Reactivity Response to a 0.2 to 2.0 GW/m^3 Ramp in 1.0 Second

After the successful UPPOWER benchmark case was completed, the TRITRAN program was used to simulate a simple downpower transient. The endpoints used for this transient are given in Table 3.4. The parameter responses to this transient are given in Figures 3.11 through 3.14. The initial and final conditions converge to the values given in Table 3.2 for the steady conditions at 2.0 and 1.0 GW/m^3, respectively.

Table 3.4 Endpoint Values used for 2.0 to 1.0 GW/m^3 Ramp in 1.0 Second

Boundary Condition	*Start Point*	*End Point*	*Units*
Time	0.200	1.200	sec
Power Density	2.000	1.000	GW/m^3
Inlet Temperature	300.000	300.000	K
Inlet Pressure	2000.000	2000.000	kPa
Outlet Pressure	1915.000	1915.000	kPa

Figure 3.11 shows the response of the system temperatures. The temperature reductions lag the neutron power ramp due to the thermal capacitance of the fuel material. There are no cases of this sort in Reference [C-5] or Reference [T-1] with

which to make a comparison, but the temperatures do start and end at the steady state values given by each reference.

The power and control drum response are shown in Figure 3.12. The control drums are required to rotate inward continuously to keep the power on the desired downward trajectory and to counter act the positive feedback from the cooling of the fuel and gas. The neutron power follows the desired 1.0 GW/m^3 ramp in one second, while the interface power lags. This excess interface power is the power mismatch required to cool the fuel particles to the new steady state temperatures. The power eventually converges to the steady state value of 1.0 GW/m^3.

Figure 3.13 shows the response of the system pressures and the element mass flow rate. Because the system is cooling down, the density of the hydrogen is increasing and the viscosity is decreasing. These combine to reduce the flow resistance terms in the Ergun pressure drop relation. The flow rate increases to its steady state value for the fixed inlet and outlet pressure at the new power level. The bed inlet pressure and average pressure decrease due to the increase flow through the cold frit causing a larger pressure drop across this node.

The response of the reactivities is shown in Figure 3.14. The total reactivity required drives negative during the initial ramp down to maintain the reactor on the required negative period. Once the new power level is reached, the positive slope indicates the decay of the delayed neutron precursor concentrations. The total reactivity remains negative until the mismatch is removed between the actual delayed neutron precursors and their steady state values. The feedback reactivity follows the temperature cooling and is a positive addition. The control reactivity is the difference between the required total reactivity and the feedback reactivity, so the control reactivity will converge to a new value less than the original steady state value in order to maintain the total reactivity at zero.

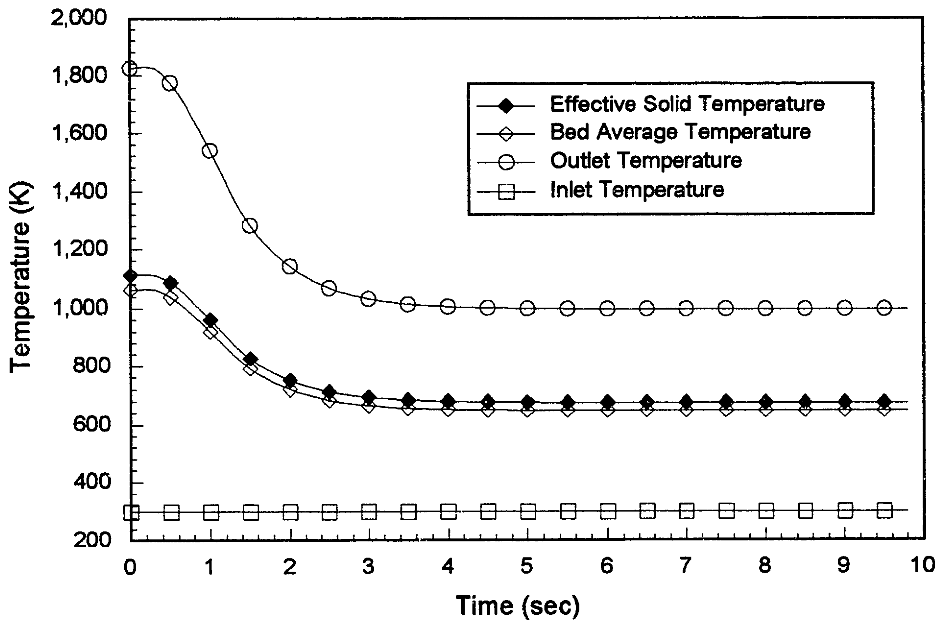

Figure 3.11 Temperature Response to a 2.0 to 1.0 GW/m^3 Ramp in 1 Second

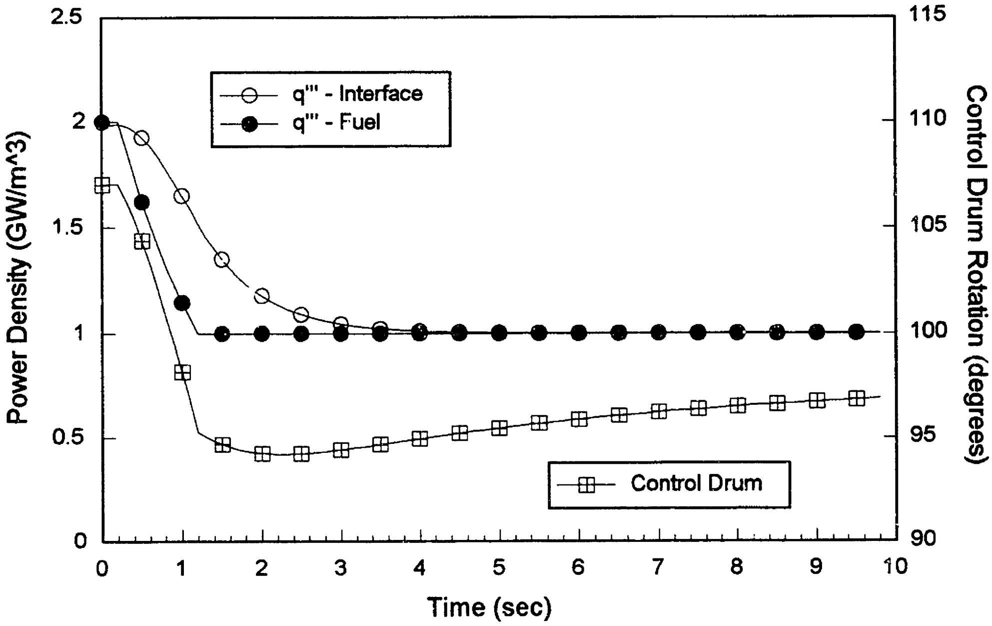

Figure 3.12 Power and Control Drum Response to a 2.0 to 1.0 GW/m^3 Ramp in 1.0 Second

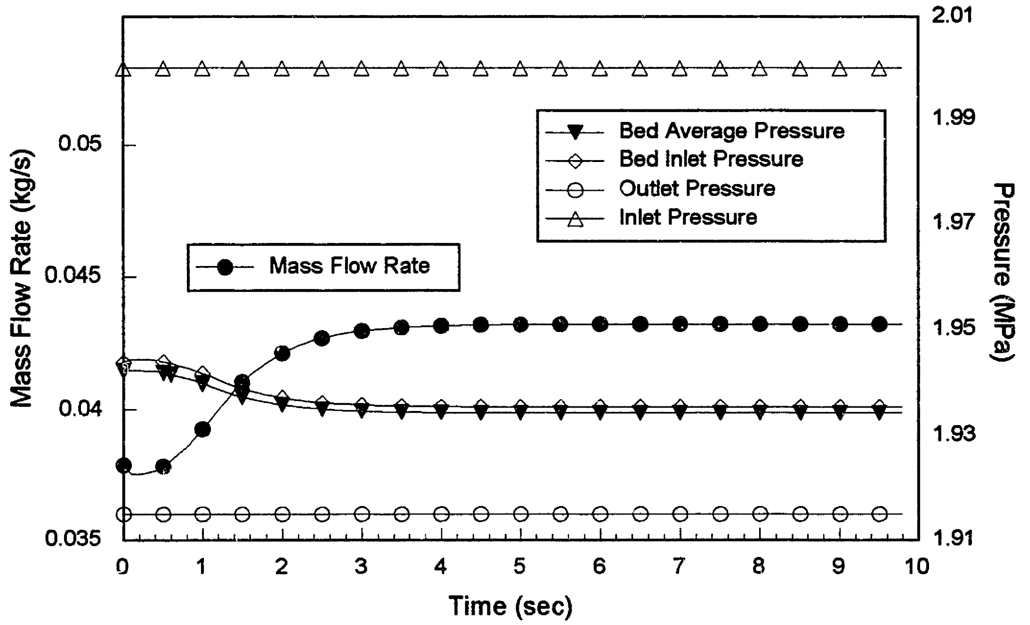

Figure 3.13 Flow Rate and Pressure Response to a 2.0 to 1.0 GW/m^3 Ramp in 1.0 Second

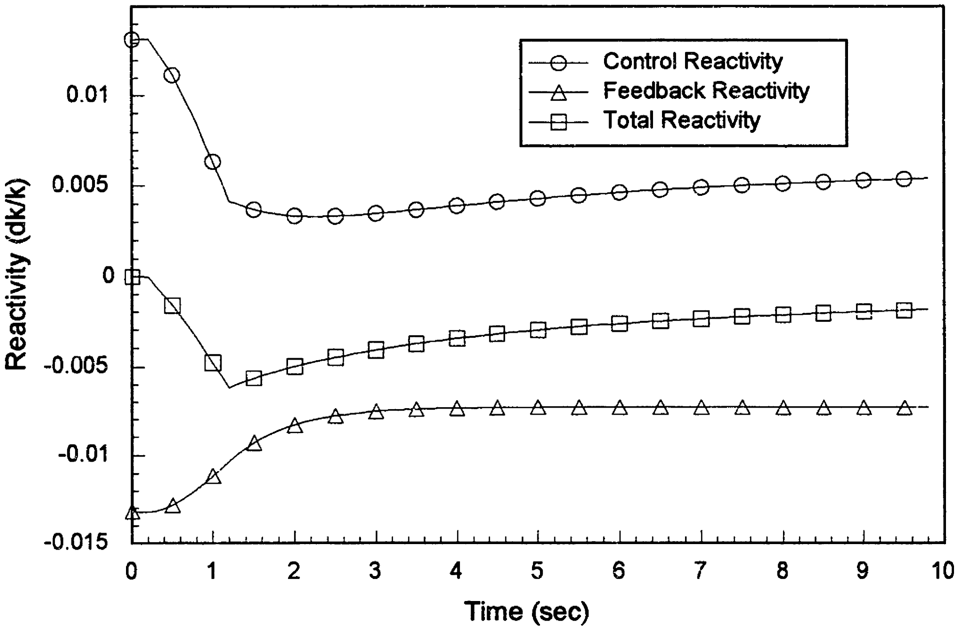

Figure 3.14 Reactivity Response to a 2.0-1.0 GW/m^3 Ramp in 1.0 Second

As a final demonstration of the capabilities of the TRITRAN computer code, a startup scenario was simulated using endpoint conditions from a NERVA engine startup[W-6]. The time chosen for the temperature ramp is much shorter than the NERVA startup in order to demonstrate the rapid response of the particle bed reactor concept. The first ramp is meant to model the initial turbopump bootstrap. The second ramp simulates the rapid increase in the outlet temperature to the rated value in order to minimize the propellant flow at lower temperatures. The final ramp models the final pressure ramp to bring the element to full thrust. Desired outlet pressures and temperatures were input into the PBRFMP steady state code to generate the endpoint inlet pressures. These pressures were then used as inputs to the TRITRAN code. The endpoint values for this transient are given in Table 3.5. The results of this transient are presented in Figures 3.15 through 3.18.

Table 3.5 Endpoints Values for the Triple Transient Ramp Startup Scenario

Boundary Condition	*Start Point*	*Point 1*	*Point 2*	*End Point*	*Units*
Time	1.000	6.000	16.000	19.000	sec.
Power Density	0.010	1.000	7.500	10.000	GW/m^3
Inlet Temperature	300.000	300.000	300.000	300.000	K
Inlet Pressure	350.000	1000.000	2400.000	3475.000	kPa
Outlet Pressure	100.000	500.000	2050.000	3100.000	kPa

Figure 3.15 shows the response of the system temperatures. The inlet temperature was held constant throughout the transient. The outlet temperature near the end of the first ramp begins to rapidly increase as the power is increasing by a factor of 100 in 5 seconds. The second power ramp is slower so the temperature shifts into a new rate of increase. This rate increases as the power increases and the pressure drop across the element is decreased. At the end of the second ramp, the outlet temperature is supposed to have reached its final value. There is a slight over shoot of 20 K above the final desired level of 2750 K which represents an error of less than 1%. The outlet temperature is maintained within this 1% error band during the final 3 second pressure

ramp and then remains steady at the desired level during the post transient steady state hold.

The power and control drum response is shown in Figure 3.16. The control drums must initially ramp out quickly to put the reactor on the desired period. As the temperature begins to rise, the drums must continue to ramp out to balance the negative feedback reactivity. This same response also occurs for the second ramp. At the end of the second ramp the drums must rotate inward to both counter the positive reactivity addition of the pressure increase and the build in of the delayed neutron precursors. The neutron and interface power track together with less than a second lag. The power rises at a near constant rate for the final ramp, because the inlet and outlet temperatures are being held constant and the flow is increasing linearly. The power reaches the final power at the required 19 seconds and maintains this level for the remainder of the transient.

The response of the flow rate to the pressure and power increase ramps is shown in Figure 3.17. The flow rate initially increases due to the inlet pressure increasing faster than the outlet pressure. This increasing pressure drop across the element causes the temperature to increase slightly slower than the interface power rise. During the second ramp, the inlet pressure remains on the same slope, while the outlet pressure is increased at a faster pace. This acts to reduce the flow rate possible through the element and help accelerate the temperature rise. Once the second ramp is completed, only the pressures are increased, so the mass flow rate increases linearly as the system pressure increases. At the end of the third ramp the pressures are held constant and the temperatures are already at their steady state values, so the mass flow rate remains constant as well.

The final figure for this transient shows the response of the reactivities. The initial feedback reactivity remains nearly constant for most of the first ramp due to the competing effects of the positive addition due to the pressure increase and the negative addition due to the temperature increase. Once the temperature begins to increase rapidly, this drives the feedback reactivity more negative. The total reactivity reaches the value required to put the reactor on the required period. This is maintained nearly constant to the beginning of the first ramp by outward rotation of the control drums when the temperature begins to rise rapidly. The second ramp has the reactor on a slower period, so the total required reactivity is less. The outward drum rotation is slowed to allow the total to decrease to the new value and then accelerates again as the temperature again increases. The pressure increase plays a smaller role during this ramp due to the smaller worth of the pressure coefficient for this simulation. During the third ramp, only the pressure is increasing. This accounts for the slight positive direction in the trend for the feedback reactivity. The control reactivity must decrease more rapidly than this increase in order to slow the reactor period to the desired rate for the third ramp, and then to maintain the power at steady level for the remainder of the transient. The feedback reactivity remains constant for the final stages of the transient. The control reactivity must continue to be lowered in order to account for the build up of the delayed neutron precursors. Eventually the total reactivity required will reach zero and the control reactivity will be equal in magnitude, but opposite in sign, to the feedback reactivity.

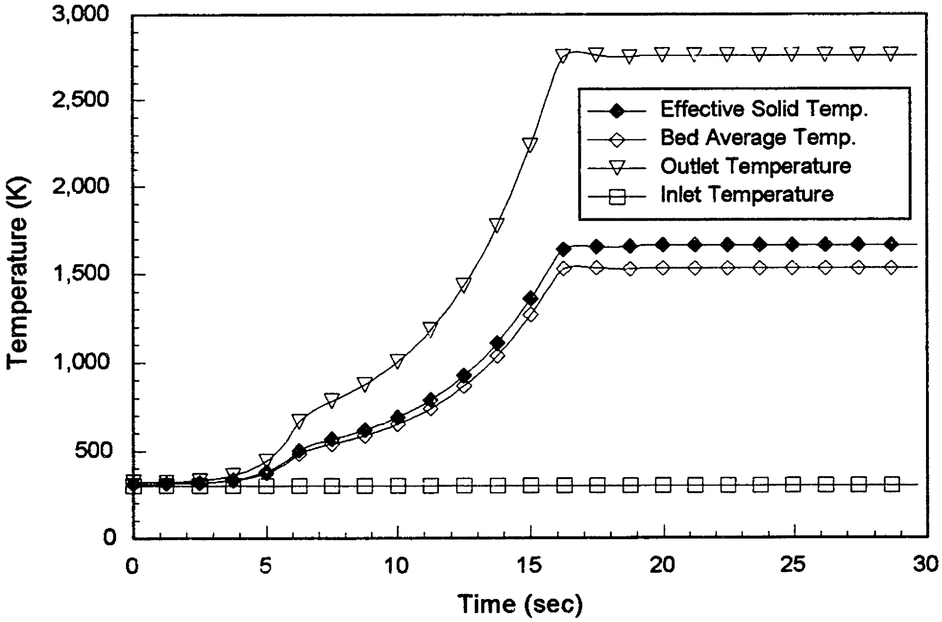

Figure 3.15 Temperature Response for Triple Ramp Startup Scenario

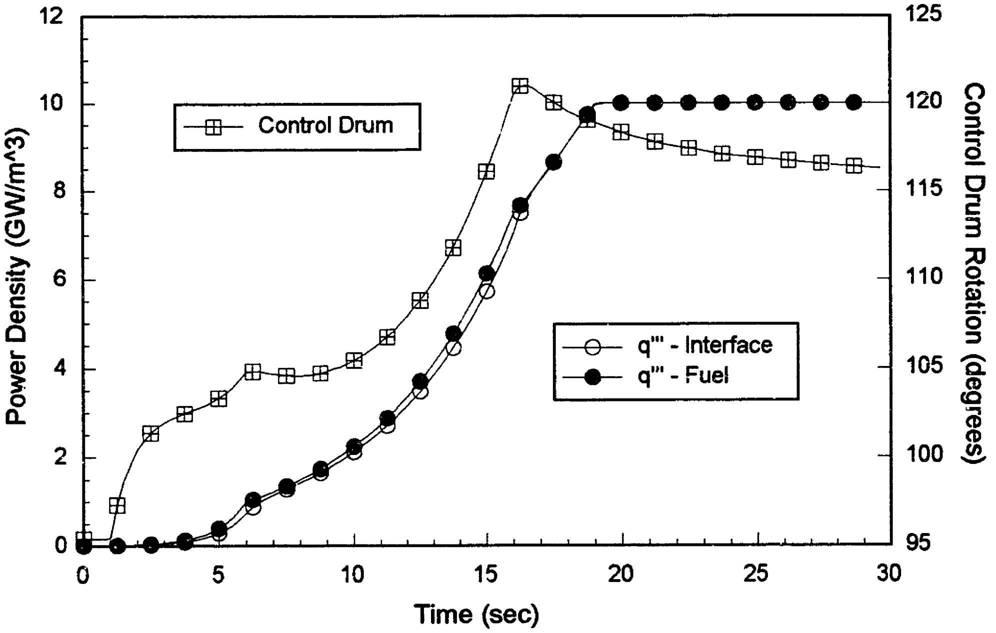

Figure 3.16 Power and Control Drum Response to Triple Ramp Startup Scenario

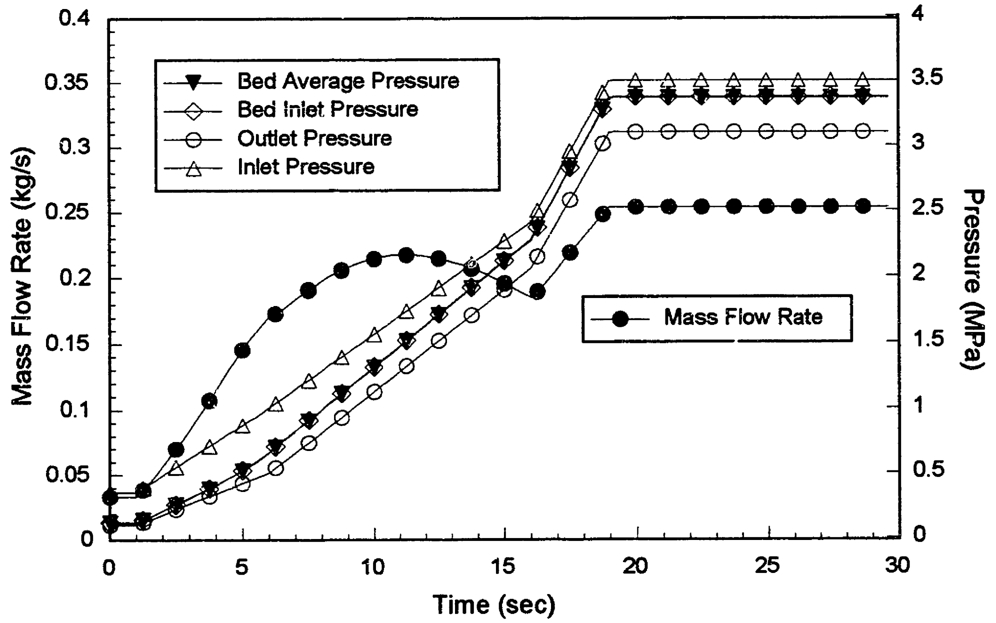

Figure 3.17 Flow Rate and Pressure Response to Triple Ramp Startup Scenario

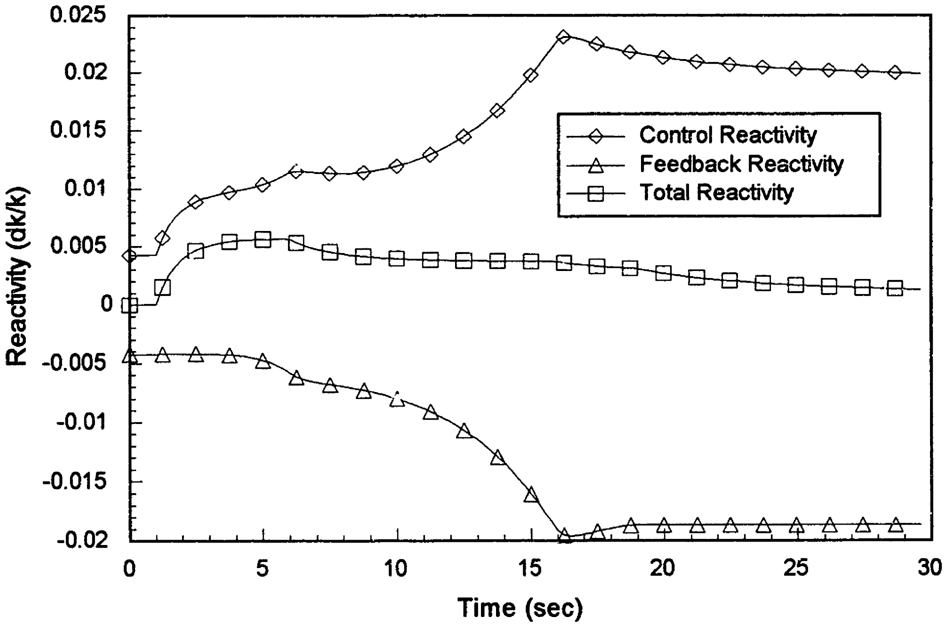

Figure 3.18 Reactivity Response for Triple Ramp Startup Scenario

This concludes the discussion of the single element models developed as part of this research. The steady state and transient models have been shown to yield similar results to that of the more simple one dimensional codes developed in Reference [C-5]. The steady state codes developed in this research effort allow for more detail and accuracy to be included. The transient versions of the code allow a more complicated series of boundary condition ramps to be modeled, as well as simulate the transient behavior of the reactor under the MIT/SNL control law logic.

3.4 Two Dimensional PBR Element Models

3.4.1 Tuddenham's HTWCOOL

3.4.1.1 Issues and reason to switch to SIMBED

The HTWCOOL computer program written by Read Tuddenham as part of his Engineers thesis was found to have long run times and by the time work was ready to proceed on modifying this code, the SIMBED code had been obtained. While only the steady state version of SIMBED was obtained for use, there exists a transient version of the code. Modifications similar to those made to the one dimensional transient model could be made to both HTWCOOL and SIMBED. All that would be required would be a point kinetics model initially to determine the amplitude of an assumed power shape in the fuel bed. A full reactor physics model could interact with the thermal hydraulic model to determine any shape changes due to control volume reactivity changes. The HTWCOOL and SIMBED routines have been written so that the solid phase heat generation is a matrix of mesh node values. The SIMBED code allows a more detailed model of the element and therefore was used for the two dimensional studies in this research. The next section describes some of the analysis performed to compare the results of the codes and to determine how well the one dimensional computer codes can model the element.

3.4.2 BNL/UMass-Lowell's SIMBED

3.4.2.1 Standard Cylindrical Element

The SIMBED code was used to model the PIPE element used in References [C-5] and [T-1]. The SIMBED code uses effective viscous and inertial terms for the cold and hot frit flow resistances. These terms are the A and B coefficients of the Ergun Relation given in Equation 2.29. The coefficients derived from the porosity and particle sizes for the frits are given in Table 3.1. The element was modeled using 40 axial nodes and 30 radial nodes. SIMBED uses ten of the axial nodes for fine meshing of the wall channeling effects. The cold and hot frit nodes each use two radial nodes and the fuel region uses 6 nodes. The outlet plenum uses 14 radial nodes - six of which are used for fine meshing of the turning of the flow from a radial flow to an axial flow. This leaves the required minimum of 6 radial nodes for the inlet region.

One would expect the SIMBED results to be more accurate than the fewer node HTWCOOL and the one dimensional model, due to the larger number of nodes used. A comparison between the results from SIMBED and those presented in Reference [T-1] for the 2.0 GW/m^3 power density shows good agreement. The temperatures along the hot frit and the radial velocities along the cold and hot frits are shown in Figures 3.19 and 3.20. Some of the differences can be accounted for by the different flow path for the flow. For the HTWCOOL case, the gas flows in a U shape (in and out the top of the element), while for the SIMBED case, the flow is an S shape (in the top and out the bottom of the element). The HTWCOOL temperature and velocity profiles were reversed axially to allow a more consistent comparison of results.

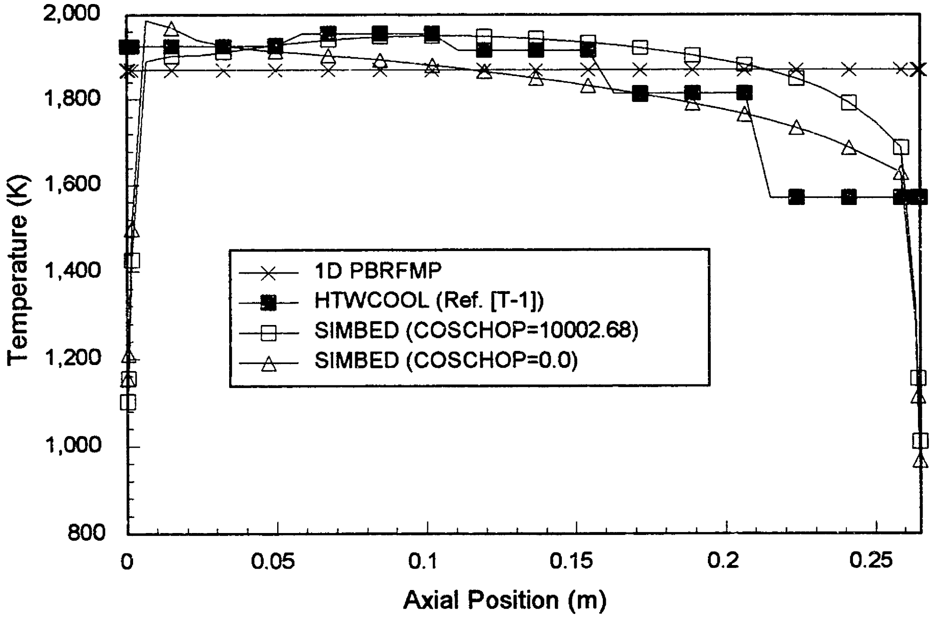

Figure 3.19 Axial Temperature Profiles along PIPE Element Hot Frit

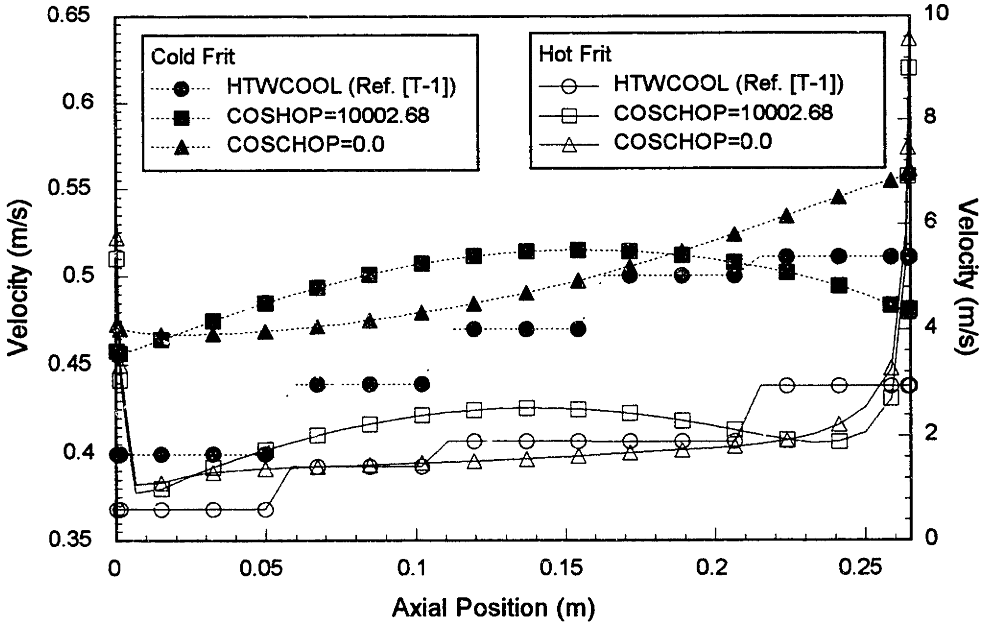

Figure 3.20 Radial Velocity Profiles along the PIPE Element Cold Frit

The power shape and cold frit thicknesses that were used in Reference [T-1] were translated into the required COSCHOP and CFDIST variables used by SIMBED. The values used were COSCHOP equal to 10002.68 and CFDIST equal to -60001.27. A SIMBED case with uniform power profile and cold frit resistance was also run. The results of this run appear in Figure 3.19 and 3.20 as the "COSCHOP=0.0" curves. The results show that the power shape and frit resistance tailoring can have an impact. These impacts are investigated more in the following sections. Figure 3.21 shows the average temperature profiles in the radial direction for the same cases. This indicates that the one dimensional model is a good representation for the temperature profile.

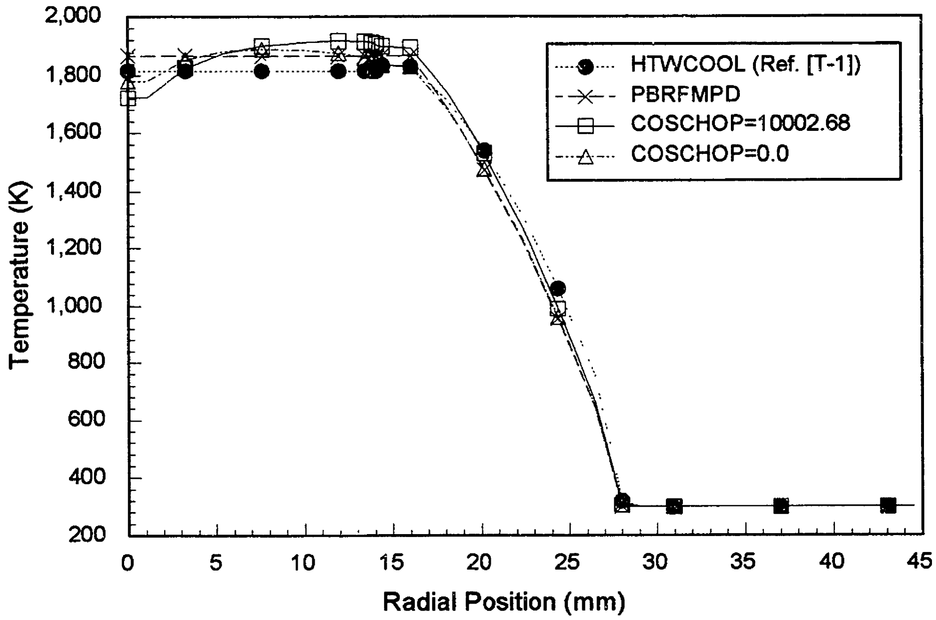

Figure 3.21 Radial Temperature Profile for PIPE Element

3.4.2.2 Power Shaping Effects

The version of SIMBED obtained from Brookhaven National Laboratory allowed only uniform heat deposition and uniform cold frit flow resistance distributions. Any reactor tends to have some sort of a power shape. A typical shape assumed for the axial distribution is of the form of a sine function. For the particle bed reactor fuel element, their is a strong self shielding effect in the radial direction due to the heterogeneous layout of the moderator and fuel. A typical shape used to model this effect is a decaying exponential. The capability to enter shapes into SIMBED was added by this author in order to study the impact of power shapes on the flow distributions. The power peaking factors are determined in the coding by deciphering the input key variable for the axial and radial power shape. These keys are the variables COSCHOP and TAUFAC, respectively. These factors are described in Section 2.9. The cold frit is used to provide a large pressure drop in order to distribute the flow along the axial direction and direct it radially inward.

The baseline PBR element was used to investigate the impact of the power shaping. The distributions for the hydrogen temperature, pressure, radial velocity and axial velocity are depicted in Figures 3.22 through 3.25. These are based on a uniform heat deposition shape and uniform cold frit resistance. There is a slight gradient to the temperature profile represented in Figure 3.22 due to a higher mass flow rate in the lower portions of the element. This higher flow rate is due to the higher pressure drop across the radial direction. This pressure gradient can be seen in Figure 3.23. This gradient is due to mainly due to the pressure drop cause by the axial flow as it increase speed along the axial length. The flow to power mismatch could be possibly be corrected by varying the cold frit resistance, engineering the power shape in the element via fuel enrichment, or by altering the element geometry so that there is a larger outlet channel diameter at the bottom than at the top end. In Figure 3.23, a slight pressure increase is noticeable in the inlet channel as the gas flows down the axial length. This is due to the deceleration of the flow as it turns radially inward. The radial velocity profile shown in Figure 3.24 clearly shows the edge channeling effects and the acceleration of the gas as it is heated by the fuel and the area becomes smaller. The axial velocity profile shown in Figure 3.25 shows the rapid acceleration of the fluid in the outlet channel. The flow accelerates as mass from the lower portions of the element join the flow stream from the upper portions. The opposite effect can be seen in the inlet channel. In this region, the flow decelerates as mass is stripped off as it turns into radial flow through the cold frit. The small axial flow bias is indiscernible on the scale of the figure, but was shown earlier in Section 3.2. This bed axial is influenced by the pressure gradient of the bed, that itself is affected by the pressure drop in the outlet channel.

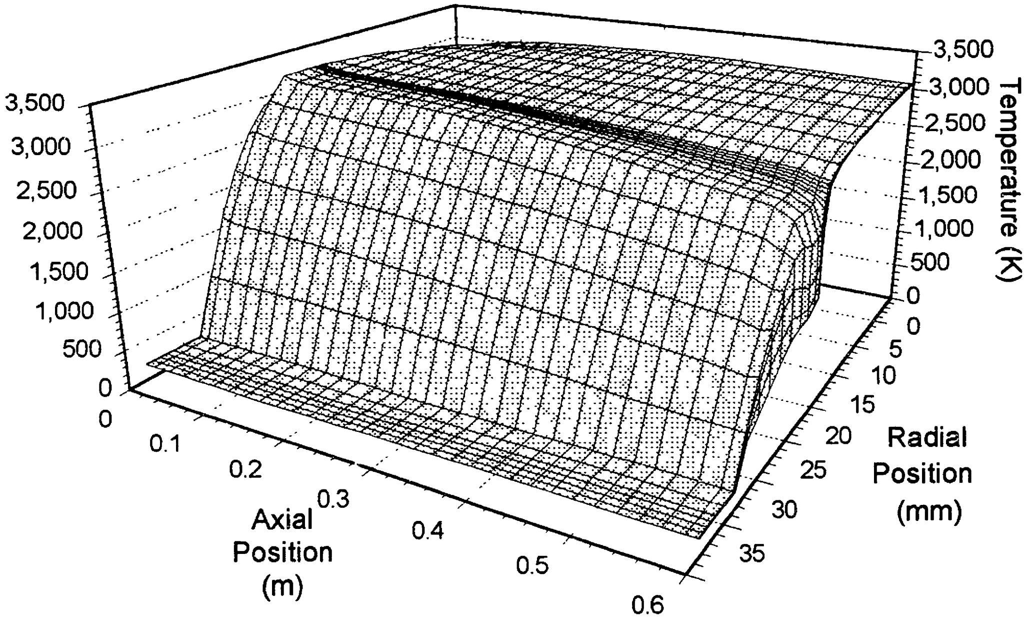

Figure 3.22 Temperature Distribution for Baseline PBR Fuel Element

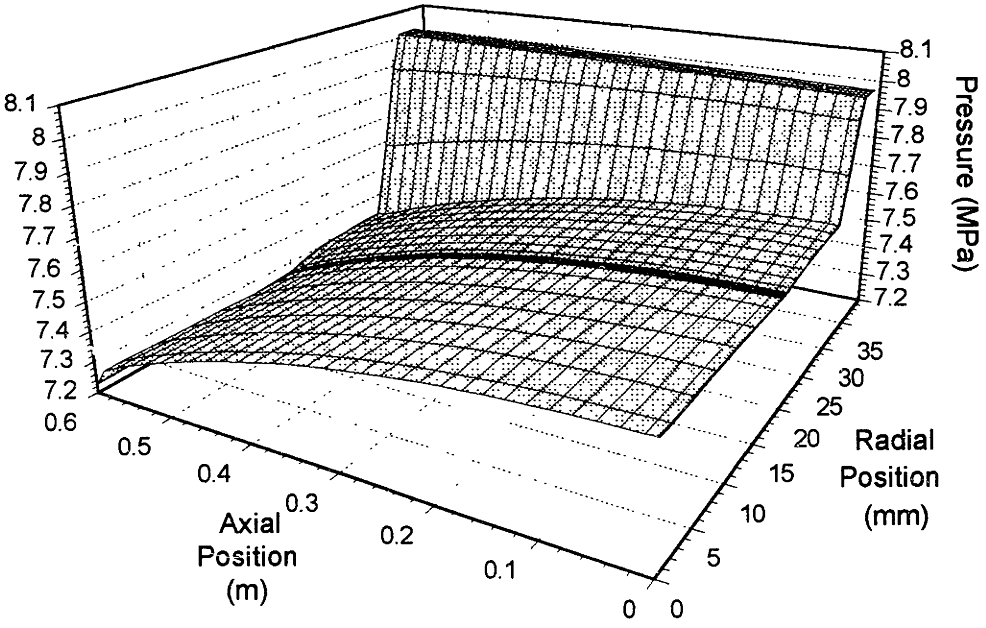

Figure 3.23 Pressure Distribution for Baseline PBR Fuel Element

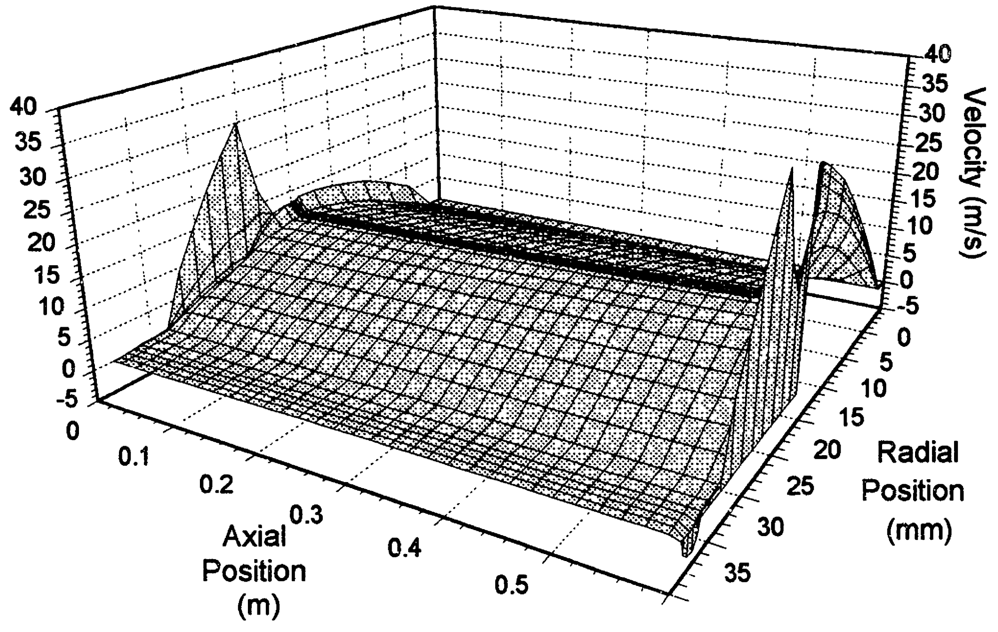

Figure 3.24 Radial Velocity Distribution for Baseline PBR Fuel Element

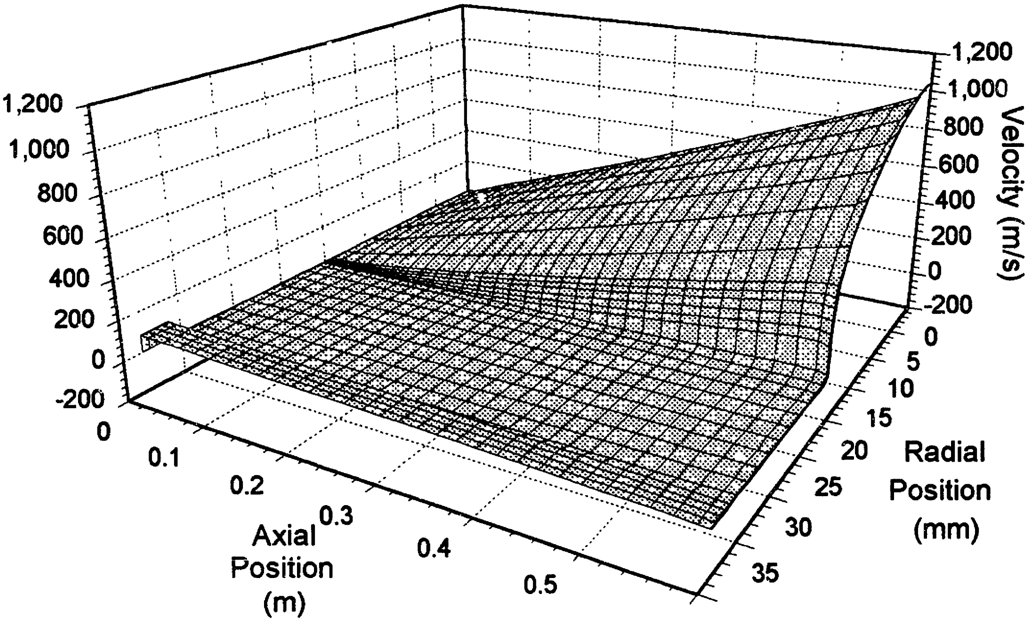

Figure 3.25 Axial Velocity Distribution for Baseline PBR Fuel Element

To study the effect of an axial power shape on the flow distribution, an extrapolated length sine curve, centered at the axial midpoint, was modeled. The extrapolated length used was 1.5 times the fuel bed length. The results of this case are shown in Figures 3.26 and 3.26 as the "COSCHOP=10001.5" curves. The hot frit temperature distribution depicted in Figure 3.26 follows the trend of the power shape. The cold frit mass flux distributions are shown in Figure 3.27. The mass fluxes are similar mainly due to the large pressure drop across the cold frit determining the distribution of flow. The cold frit in SIMBED does receive heat addition by conduction from the fuel region, which causes a shift in some of the flow. The hotter regions in the mid-regions have a higher pressure drop gradient, so less flow will tend to flow in these regions.

Also included in Figures 3.26 and 3.27 are the temperature and mass flux distributions for a study of the impact of the exponential decay power shape in the radial direction. SIMBED was run using a TAUFAC of 2.5, indicating that the outer radius power is 2.5 times the value at the inner radius. The trends are similar to the uniform power case due to the flat axial shape. The impact of the radial power shape is on how quickly the gas temperatures will increase as it travels radially inward. The exponential power shape will cause the temperatures to rise faster than the baseline flat power distribution.

3.4.2.3 Cold Frit Resistance Shaping Effects

It is desired to have a nearly uniform temperature distribution along the hot frit in order to maximize the performance of the element and to avoid any possible viscosity induced flow redistribution. If a uniform power shape is used, the cold frit should be able to have a primarily uniform resistance distribution to ensure the temperatures are uniform For non-uniform power shapes, the cold frit must also have a distribution. This capability was added to the SIMBED program in a similar fashion to the power shaping. A user defined variable CFDIST is used as the key for the program to decipher. The shape defined may either be a linear or parabolic shape. The derivation of the CFDIST factor and resisitance distribution normalization is given in Chapter 2.

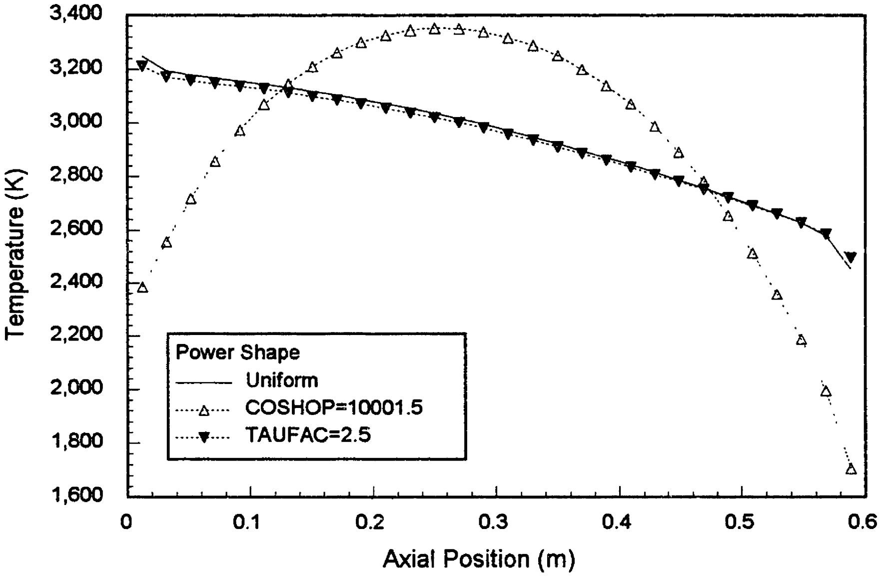

Figure 2.26 Hot Frit Temperature Distributions due to Power Shape Effects

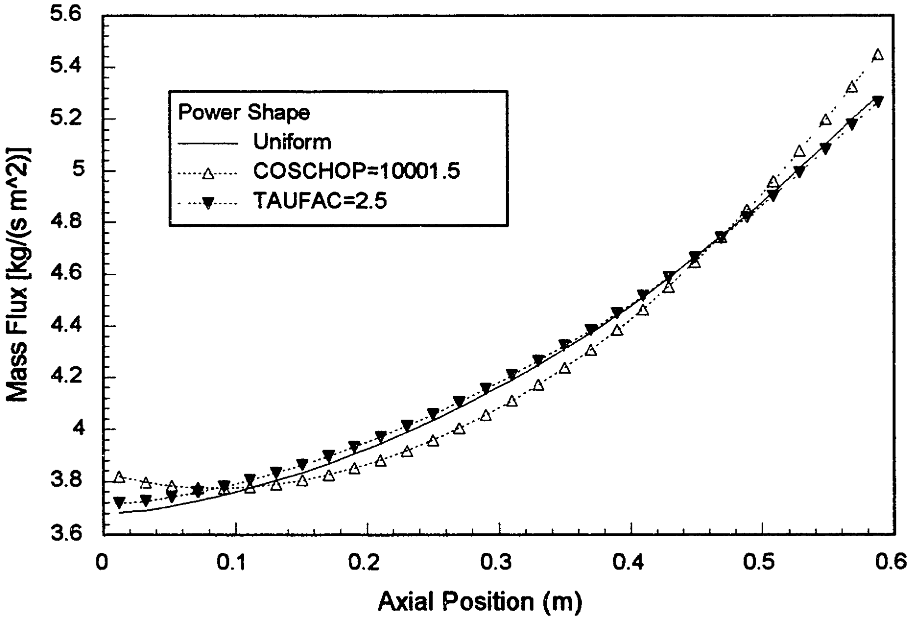

Figure 3.27 Cold Frit Mass Flux Distribution due to Power Shape Effects

The impact of the cold frit resistance distribution can be seen in Figures 3.28 and 3.29. These figures show the results of a SIMBED case run to flatten the temperature distribution that existed in the cosine power shape case presented in the last section. Two different linear distributions of the flow resistance were used. The first case was run with CFDIST equal to 50012.0. This case shows the minimum resistance at the middle of the element length. This is apparent by the peaks in the mass flux at this point and the temperature dip. The temperature was flattened somewhat, but the sine power shape has a strong effect on the temperature distribution. Because the peak temperature from the uniform cold frit being was located above the middle of the bed, the resultant temperature profile still has a bias due to the initial flow distribution. In an attempt to match the maximum flow where the maximum temperature exists, a second linear resistance distribution case was run a CFDIST equal to 60008.0. This places the minimum resistance up 60% of the length from the bottom and makes the bottom resistance equal to 8 times the minimum. This helped to flatten the temperature profile, but the effects of the power shape are still apparent. The mass flux distribution shows how the initial radial flow distribution has been shifted to the upper half of the element. The linear cold frit resistance distributions cause a peak in the mass flux distribution. The use of a parabolic shape to the resistance can help to smooth these peaks and help to flatten the temperature peaks. The final SIMBED case presented here is depicted as the "CFDIST=-75008.0" curves in Figures 3.28 and 3.29. The parabolic shape for this case has its minimum point up 75% of the length from the bottom and peak to minimum ratio of 8.0. The temperature is flattened and the dip associated with the linear distribution is removed. The mass flux distribution has also been flattened. The upper end of the element now is cooler than it was for the uniform cold frit resistance case due to the higher flow rates.

These few studies show that varying the cold frit resistance can effectively alter the temperature profile in the bed. If the cold frit can be ideally engineered, the flow can be directed in the radial direction so as the match the flow to the power and allow operation at higher average outlet temperatures for a given operating point. The problem is that the element must be able to operate over a broad range of operating conditions and possible power shapes, so caution must be given to the concept of flow engineering.

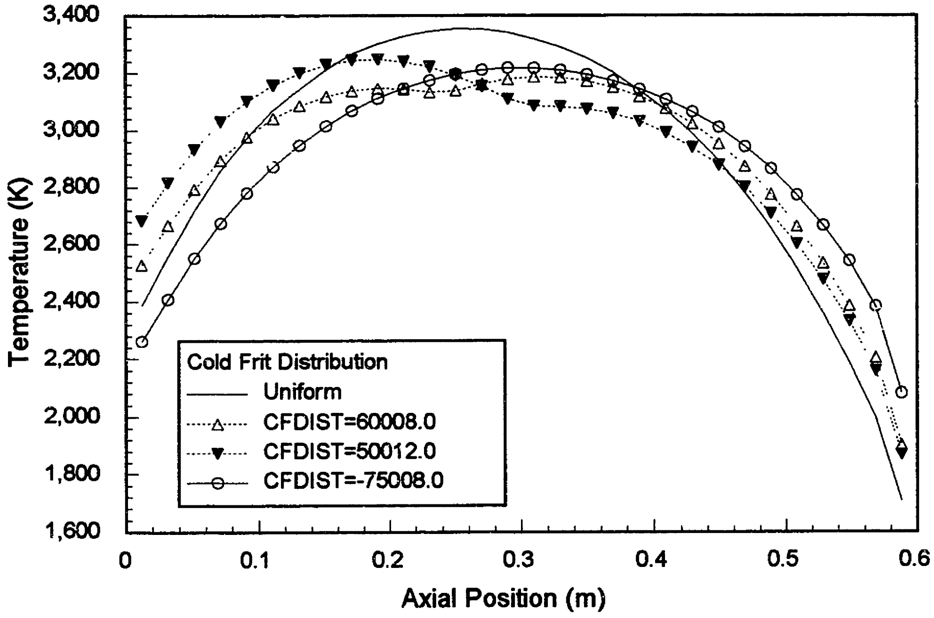

Figure 3.28 Hot Frit Temperature Distribution due to Cold Frit Resistance Shaping

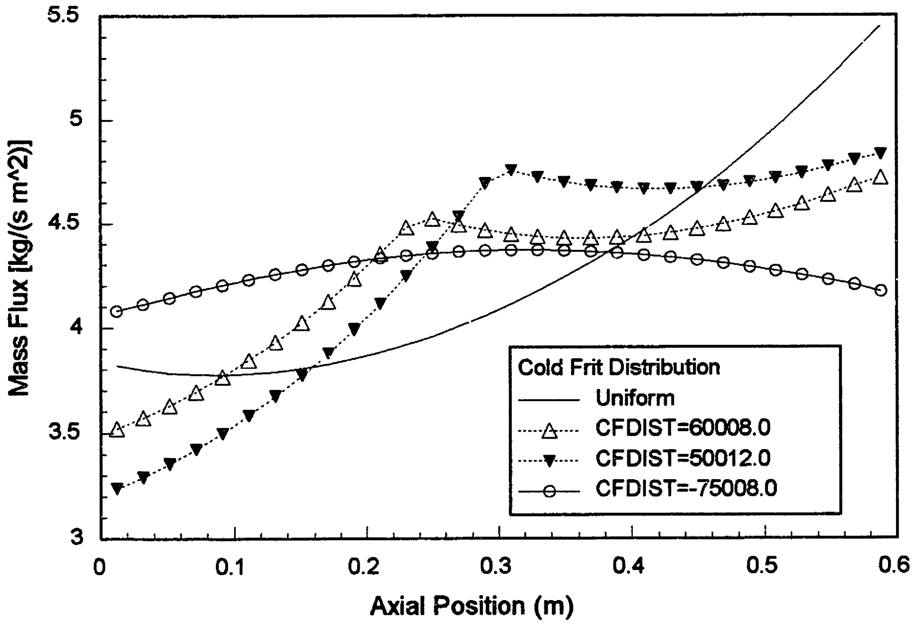

Figure 3.29 Cold Frit Mass Flux Distribution due to Cold Frit Resistance Shaping

3.4.2.3 Local Porosity Variation Effects

Of interest also for the flow in a particle bed is the possibility for a flow maldistribution due to local differences in the porosity from the bed average. The SIMBED code was used to investigate the effect of ± 10% local porosity changes in one node of the fuel region. The SIMBED code was modified by this author to allow one node to have a porosity different than the average value. The middle node of the 40 by 30 node baseline PBR element was selected for the porosity perturbation. The reference case is a SIMBED run on the baseline PBR element with uniform heat deposition and uniform cold frit resistance. Results of these cases indicate that the effect is highly localized, which coincides with the theory discussed in Section 3.1. The impact of the porosity perturbation is best shown by plotting the percent change from the baseline PBR element flat power profile case. These are shown in Figures 3.30 through 3.35. The curves for the radial velocity distributions (Figures 3.30 and 3.31) clearly the show the trend for the flow to redistribute itself towards the higher porosity regions and away from the lower porosity regions. The radial velocity distribution is seen to be affected even out to the cold frit regions. This is due to the increase cooling in the radial streamline before and after the porosity change. The lower temperatures mean that the local density is higher and the viscosity is lower, therefore the pressure drop gradient via the Ergun relation is lower. Likewise, for the lower porosity, the higher temperatures cause the pressure gradient term to be larger. The heat generation in the bed tends to compound the flow distribution effects from porosity alone. However, also shown is that the effects are smaller than the perturbations that caused them. The peak difference in the fuel region occurs at the perturbation node and then reduces in the nodes following it as the velocity is continuing to increase in value as the gas is heated. The large peaks in the outlet channel region are due to the radial velocity decreasing in value as the radial flow turns to axial flow in order to exit the element.

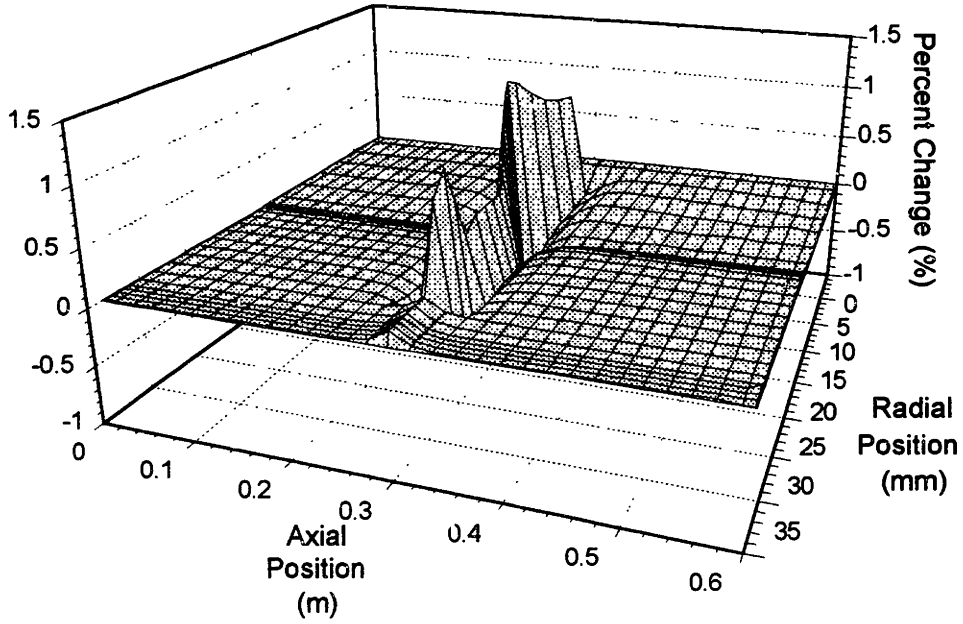

Figure 3.30 Radial Velocity Percent Changes due to +10% Node Porosity Change

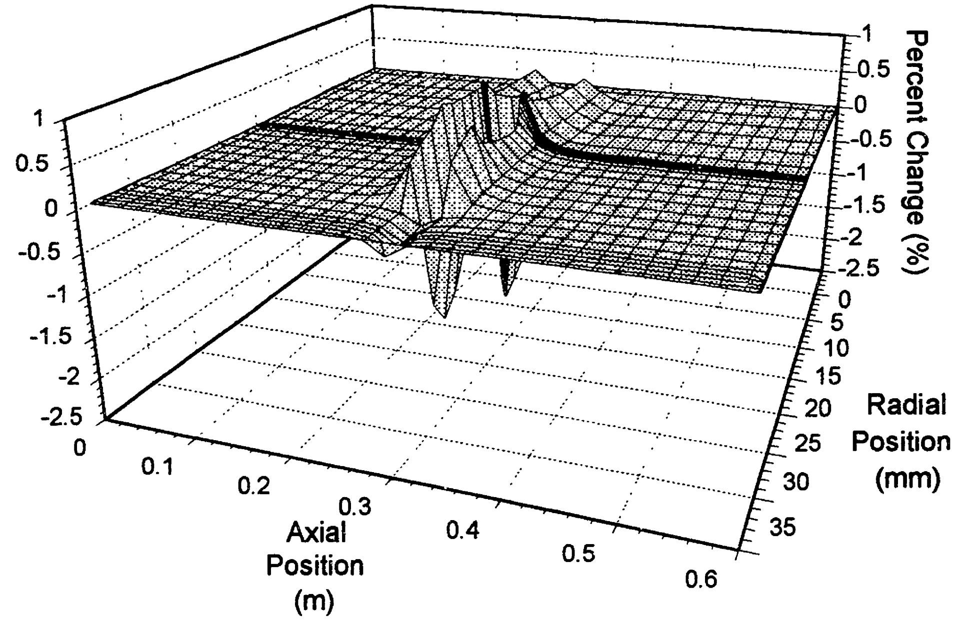

Figure 3.31 Radial Velocity Percent Changes due to -10% Node Porosity Change

The axial percent change distributions shown in Figures 3.32 and 3.33, show how the flow redistribute to and from the effected nodes. For the case of higher porosity, the flow on each side of the node diverts towards the affected node and just after the node the change is reduced. There is still some effect due to the lower flow resistance of the cooler gas in the nodes radially after the affected node. The opposite occurs for the case with lower porosity. The effects on the upper side of the affected node are larger due to the smaller baseline velocity and the natural bias of the flow in directed towards the bottom of the element.

The temperature perturbation shown in Figures 3.34 and 3.35, indicate a change of less than 2.5% for the 10% change in porosity. This is equivalent to 40 to 80 K at rated operating condition. The peak occurs in the affected node, partly due to the flow redistribution, but also due to the change in the heat input into the control volume. The higher porosity node will have less solid material, so the heat deposition due to the hot fuel will be less based on the bed average heat deposition. The radial flow streamline and the axial redistribution effects show up as the peaks and valleys of the opposite sign of the perturbed node. This must be the case, as the adjacent nodes are either losing or gaining mass flow to help balance the mass flow gained or lost in the perturbed node.

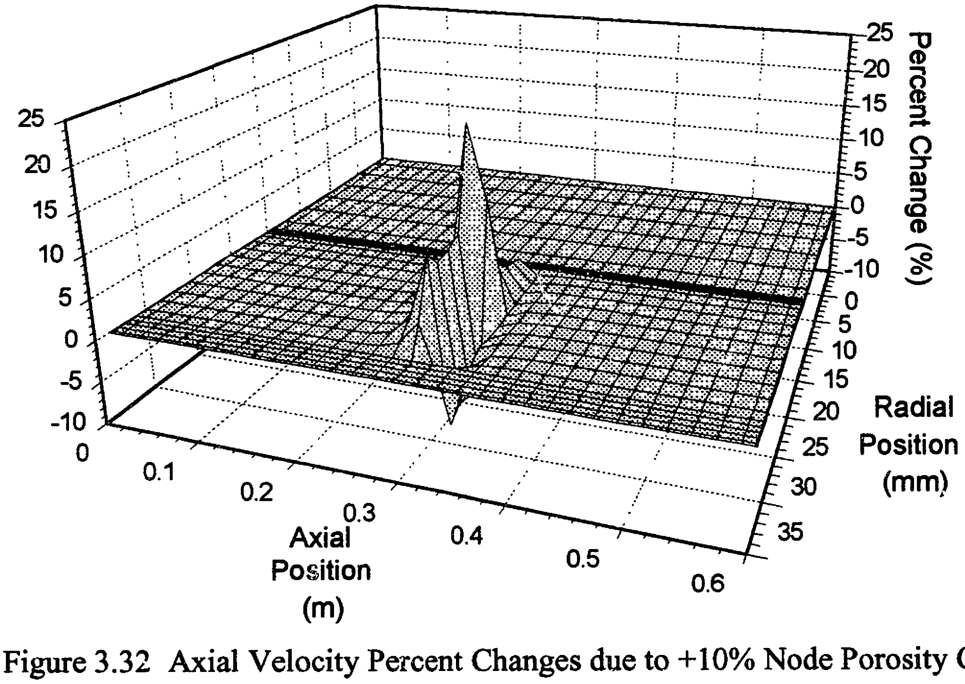

Figure 3.32 Axial Velocity Percent Changes due to +10% Node Porosity Change

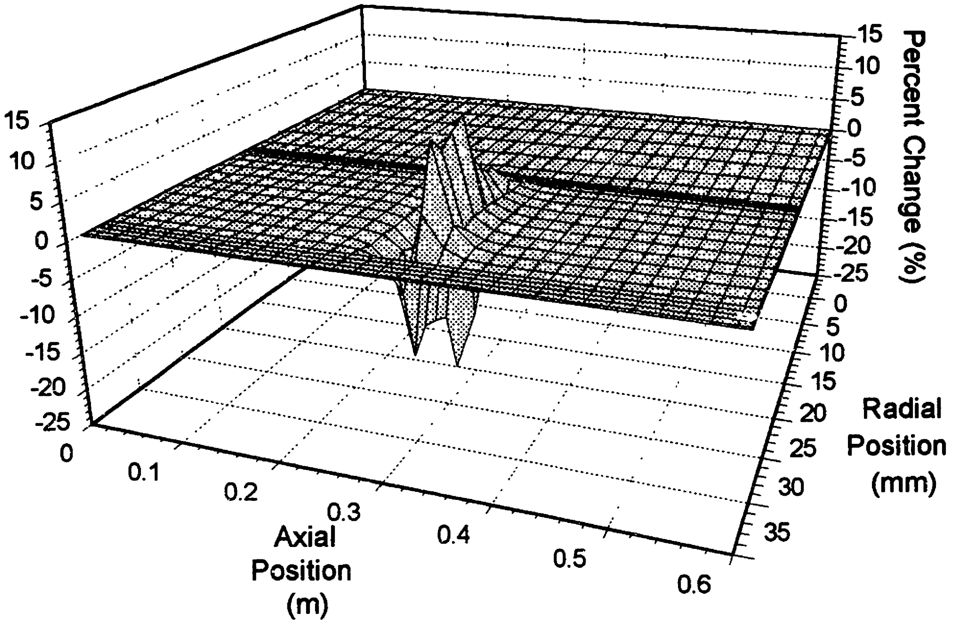

Figure 3.33 Axial Velocity Percent Changes due to -10% Node Porosity Change

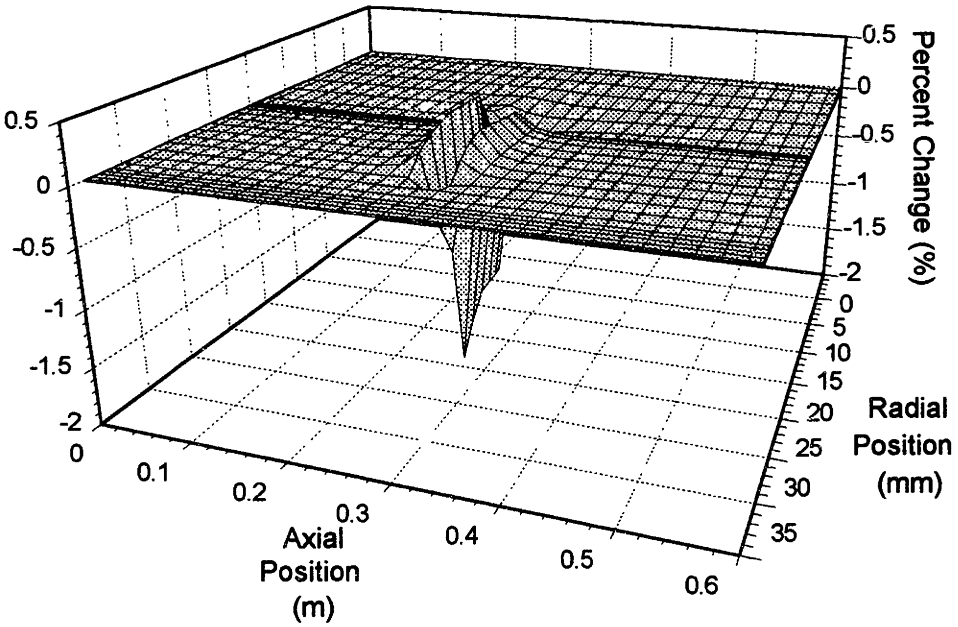

Figure 3.34 Hydrogen Temperature Percent Changes due to +10% Node Porosity Change

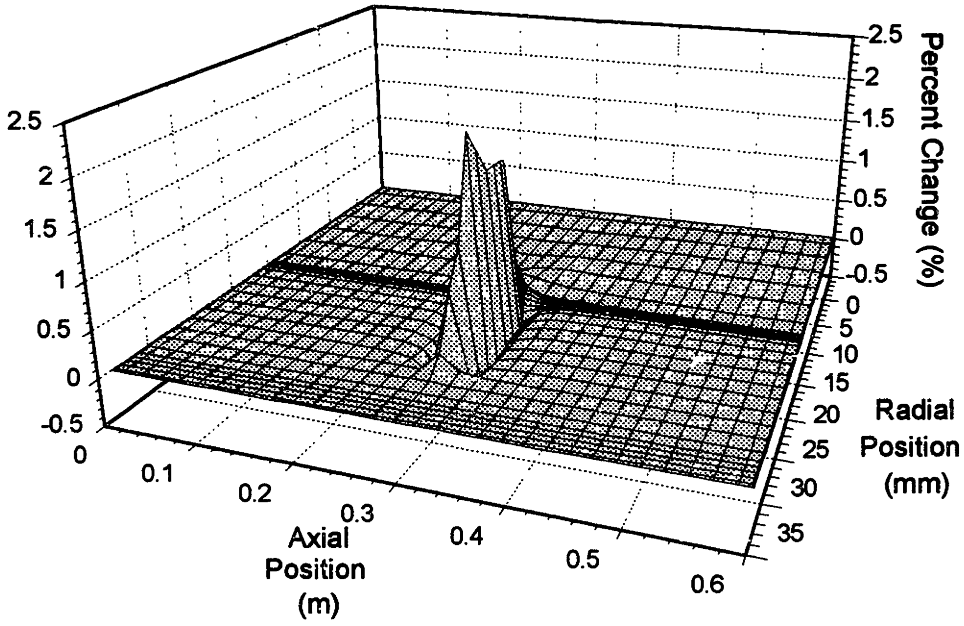

Figure 3.35 Hydrogen Temperature Percent Changes due to -10% Node Porosity Change

3.5 Flow Stability Analysis

3.5.1 Introduction

Flow in reactors that have many parallel paths may be susceptible to laminar flow instabilities that arise due to the heating of the gas at low Reynolds numbers. This phenomenon can occur due to the relation of the pressure drop to the mass flow rate. At low flow rates, the impact of the viscosity and the density relations with temperature can be such that the pressure drop decreases with an increasing flow rate. If a perturbation in a channel causes the temperature to rise, the viscosity will increase and the density will decrease. Because the pressure drop is fixed by the plenums, the mass flow rate in this channel will then decrease, causing a further increase in temperature. As this channel heats up, one or more of the other channels will pick up the extra flow. A measure of the heat addition to the channel is the temperature rise factor ϕ. It is defined as the ratio of the temperature rise along the channel length to the temperature at the inlet. The new equilibrium will be at a higher pressure drop, with one or more channels operating at the lower flows and higher temperature ratio and others operating at higher flows and lower temperature ratios, all with the same pressure drop. This has been shown to be an unstable condition, as the channels will tend to oscillate with which channels are the hot ones and which ones are the cool ones[B-6, B-12, T-2, V-4]

If treated in a one dimensional sense, the pressure drop in the porous media PBR fuel element can undergo similar effects. The curves in Figure 3.36 show the temperature ratio and the pressure drop across the baseline PBR element as a function of the flow rate in terms of the Reynolds number, for average fuel region power densities of 0.05, 0.50, and 5.00 GW/m^3. The Reynolds number here is superficial Reynolds number based on the particle diameter, as is used in the Ergun relation. If the element is operating with a flow rate so that the pressure is decreasing with increasing flow, this is the unstable condition. It is desirable to operate with flow rates so that the pressure drop is increasing with the flow rate. For the 5.00 GW/m^3 case, this appears to be always true, although the slope of the curve is very small. The critical point for stability lies at the minimis of the pressure drop versus flow rate. These points are indicated by lines connecting the critical parameters in Figure 3.35.

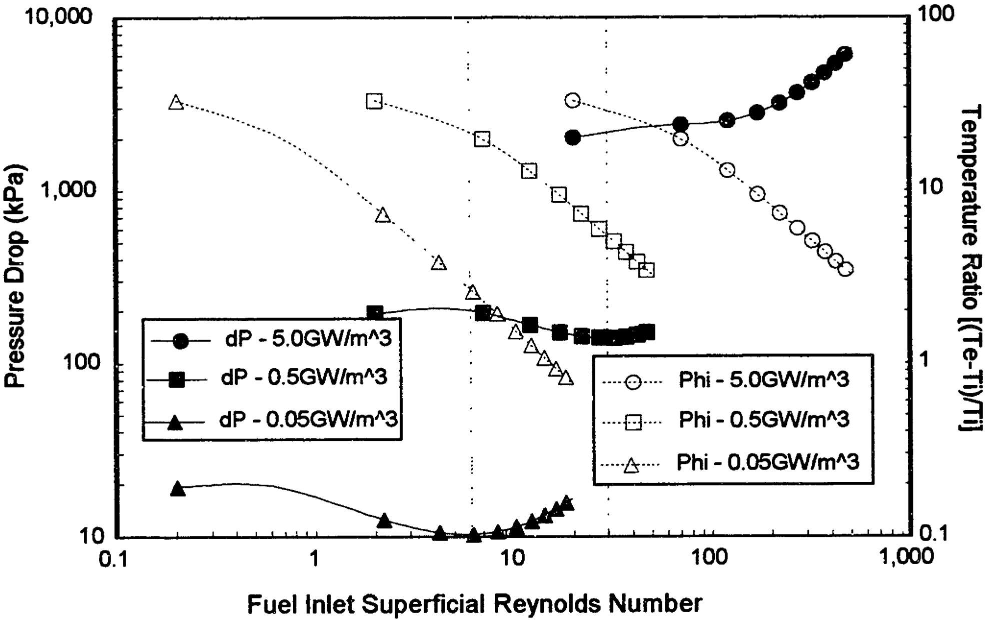

Figure 3.36 Pressure Drop and Temperature Ratio versus Reynolds Number

Because the flow in a PBR fuel element can be three dimensional, another flow stability effect can be proposed. In Reference [V-1], the problem of local perturbations in the bed power, porosity and, particle size was considered. In this case of no uniform flow channels, if a local perturbation is such that the temperature rises locally, the viscosity will also rise. This causes a local shift in the flow pattern away from the hot area in order to maintain the same average pressure gradient. As the flow is redirected, this could cause the temperature to continue to increase until the fuel is damaged. This was proposed to occur in the regions of laminar flow as well[B-4,M-3,V-1]. A means to study the flow stability issues in the PBR fuel element was initially developed at Brookhaven National Laboratory by George Maise [M-3] and then some additional measures were undertaken, as part of this research, to better quantify the regions of stability. The quantification of the stability regions is presented in the next sections.

3.5.2 One Dimensional Analysis

3.5.2.1 Bussard & DeLauer/Maise Correlation Approach

An approach for the prediction of regions of laminar flow instability for the PBR fuel element was suggested by Maise at the Brookhaven National Laboratory[M-3]. The approach is to assume parallel channels for the fuel region and then perform the analytical solution as outlined by Bussard and DeLauer in Reference [B-4]. The stability analysis of Bussard and DeLauer contains several assumptions. They are as follows:

1. Uniform heat deposition in the porous region and a Cartesian geometry.
2. Constant gas heat capacity, so that the temperature rise is linear for a given mass flow rate.
3. The pressure drop gradient is proportional to $Re^{-\beta}\rho V^2$, where Re is the Reynolds number, ρ is the density, and V is the gas velocity.
4. The pressure drop across the region is small compared to the system pressure and the hydrogen exhibits ideal gas properties, so that the density is proportional to the inverse of the gas temperature.
5. The viscosity was assumed to be proportional to the square root of the temperature.

Because the viscosity of hydrogen follows the temperature more closely to the two-thirds power instead of one-half, the equations for the stability criterion were rederived by Maise. Performing the same algebra as outlined in Reference [B-4], the new stability criterion becomes

$$(1+\phi)^{-\left(1+\frac{2\beta}{3}\right)} < 1-\left(\frac{5\beta-3}{9-3\beta}\right)\phi, \qquad [3.1]$$

where: β = coefficient on Reynolds number describing the flow regime,
$\phi = \frac{T_e - T_i}{T_i}$ = temperature rise factor and,
$T_{e,i}$ = temperature at the bed exit and inlet, respectively.

In order for the flow conditions to be considered stable, the inequality must be satisfied. The Ergun pressure drop correlation can be put in terms of an effective friction factor, geometric dimensions, and velocity terms as follows[M-3]:

$$\Delta p = \mathrm{f}_k \frac{(1-\varepsilon)}{\varepsilon^3} \frac{L}{\mathrm{D}_p} \rho \mathrm{V}^2 = \mathrm{f}_e \frac{L}{\mathrm{D}_p} \frac{\rho \mathrm{V}^2}{2}, \qquad [3.2]$$

where: $\mathrm{f}_k = 1.75 + 150\frac{(1-\varepsilon)}{\mathrm{D}_p}$ as defined by Ergun [E-1].

The β coefficient is defined as the negative slope of the log f_e versus log Re curve. Therefore,

$$\beta = -\frac{d[\ln(\mathrm{f}_e)]}{d[\ln(\mathrm{Re})]} = \left[1 + \frac{1.75}{150(1-\varepsilon)}\mathrm{Re}\right]^{-1} \qquad [3.3]$$

Equations 3.1 and 3.3 are used to determine a stability region. For the locus of Reynolds numbers and temperature ratios that lie above the line where the equality of Equation 3.1 is met, the flow will be unstable. If β is less than 0.6, the inequality of equation 3.1 will always be met, and thus indicates flow stability. It β is greater than 0.6 and ϕ is large, the inequality predicts an unstable condition. The point at which this inequality is met is know as the critical stability point and illustrates why at each low flow there can be a limiting temperature ratio that will cause a flow instability. Because the β term is a function of the Reynolds number, a curve of the critical temperature ratio versus the critical Reynolds number can be generated. The curve generated by this method will be labeled the Bussard & DeLauer/Maise curve in the stability map figures in the next sections.

3.5.2.2 Approach for "Real' Geometries and H_2 Properties

The Bussard & DeLauer/Maise approach to the stability question includes several assumptions so that an analytic solution could be determined. Another way to approach the problem is through numerical simulation. This approach allows the actual element geometry, actual gas properties, and actual thermal hydraulic behavior to be modeled. Using the basic PBR element computer models, the minimum pressure drop point of the curve in Figure 3.36 can be determine through an iteration scheme. By stepping the mass flow rate, or Reynolds number, the pressure drop can be compared to the last step's pressure drop. Once the current step pressure drop is greater than the previous step, the critical conditions have be determined. The inlet and outlet temperatures are used to find the temperature rise factor. The Reynolds number is then used in equations 3.2 and 3.1 to determine the Bussard & DeLauer/Maise value for the stability. In this way, a comparison can be made between the analytical and the numerical approaches. Once these are found, the power is stepped to the next value and the iteration process for the minimum pressure drop is repeated.

The fuel region pressure drop and inlet Reynolds number were chosen for the measures of stability. An argument could be made to use the full element pressure drop, but this would really be a measure of core wide stability, rather than a measure of the stability of the flow once it is in the porous fuel region. The use of the cold frit as a stabilizing orifice is possible for the core wide flow and is proposed to help ensure the flow is directed in the radial direction so as to match the power profile. If the full element pressure drop is used for the stability, the system is shown to be very stable. This is depicted in Figure 3.37. The cold frit resistances were varied from zero to the baseline value. As the resistance is increased, the stability line moves higher, indicating a decrease of the unstable region. In fact, for the full cold frit resistance, the element was stable for all flow rates and temperature ratios attainable by the system. The values plotted in Figure 3.37 are for cold frit resistances equal to 0.0, 0.01, and 0.1 times the reference resistance.

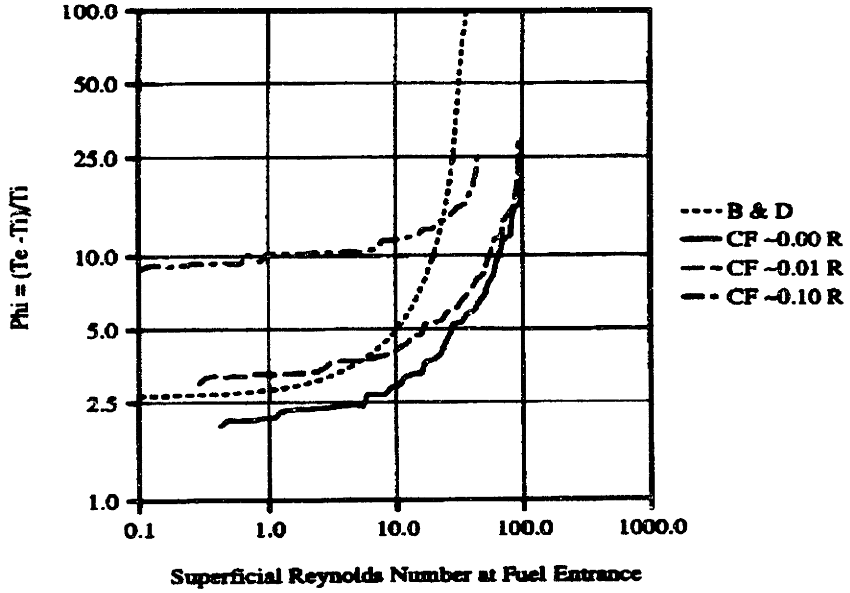

Figure 3.37 Stability Map from Full PBR Element Pressure Drop and Various Cold Frit Resistances

The conservative approach, and the approach required to study laminar effects in the bed itself, is to consider the fuel region pressure drop as the stability criterion. The entire element should still be modeled in order to account for effects due to the pressure drop across the cold frit and the actual gas conditions in the fuel region. Initial applications of this approach were applied to the Flow Instability Test (FIT) element geometry for a screen mesh stability test to be performed at Brookhaven National Laboratory[M-3]. The results of this were reported in Reference [W-9]. Because the numerical analysis showed that the stability line was shifted over to higher Reynolds numbers, and therefore indicating a larger region of instability, the SIMBED code was also run to determine the pressure drop inflection points for the average radial pressure gradient. The results of the one dimensional and the two dimensional approaches are shown in Figure 3.38. The solid line is the stability line determined from the one dimensional analysis. The shorter lines indicate the SIMBED average pressure drops that bound the minimum pressure drop at the particular bed average power density. The curves show that the two numerical methods yield similar results and that the one dimensional method could be used to identify the regions that should be avoided during operation and that may need more detailed studies to show actual flow behavior at those conditions.

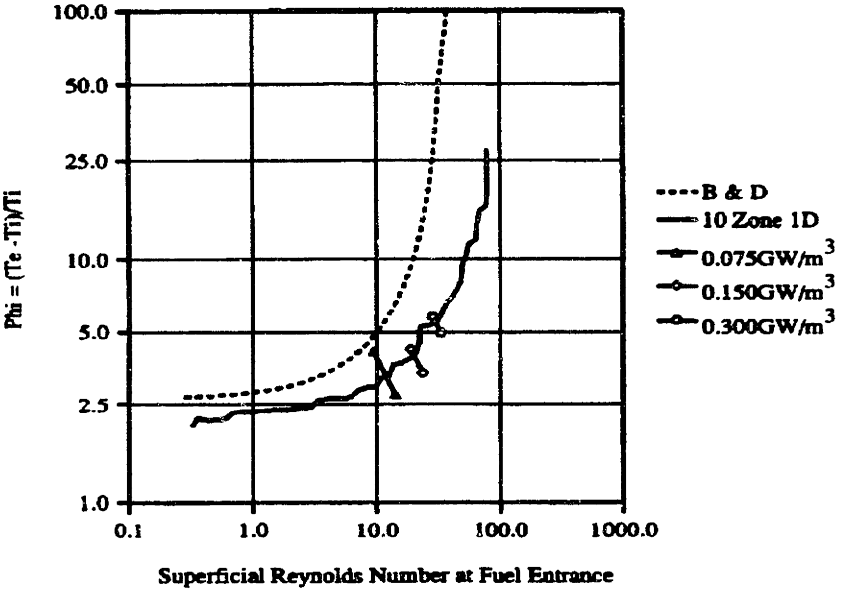

Figure 3.38 One-Dimensional and Two-Dimensional Model Stability Map for FIT Test

The stability maps were also generated for the baseline PBR fuel element and the results are similar. Sensitivities to bed porosity, particle diameter, system pressure and inlet temperature were considered. The bed porosity appears to have the biggest effect, while the particle diameter effect was hardly noticeable. The stability lines generated using bed porosities of 0.25, 0.40, and 0.55 appear in Figure 3.39. The curves shift to shrink the region of stability as the porosity is reduced. The smoothness of these curves is due to a sixth order polynomial fit of the lines generated by the one-dimensional element model. Of note in these curves, is the trend of the stability lines to bend backwards once a certain temperature ratio is reached. The curves in Figures 3.39 and 3.40 were generated using the NASA NBSpH2 properties routine[W-2]. Because dissociation is modeled by the properties routines, the curve bends backwards as the dissociation pressure and temperatures are reached. At a certain point the hydrogen is completed dissociated and the curve then begins to shift back to the right. This effect was not noticed in earlier work, due to use of an earlier version of the hydrogen properties routine and different method of stepping the mass flow rate for the iterations.

The effects of varying the system pressure and inlet temperature can be seen in Figure 3.40. These parameters affect when the dissociation will begin to occur and therefore the position of the stability lines. The system pressure affected the point at which the curve began to bend over and when it would start back to the Bussard & DeLauer/Maise curve. At the lower pressures, the temperature ratio that this occurs at is lower, so the curves tend to indicate that lower pressures could be more stable. The region inlet temperature also has an impact on the stability lines. For the higher inlet temperature, the system tends to be more stable because a lower temperature ratio is required to bring the hydrogen to its dissociation conditions.

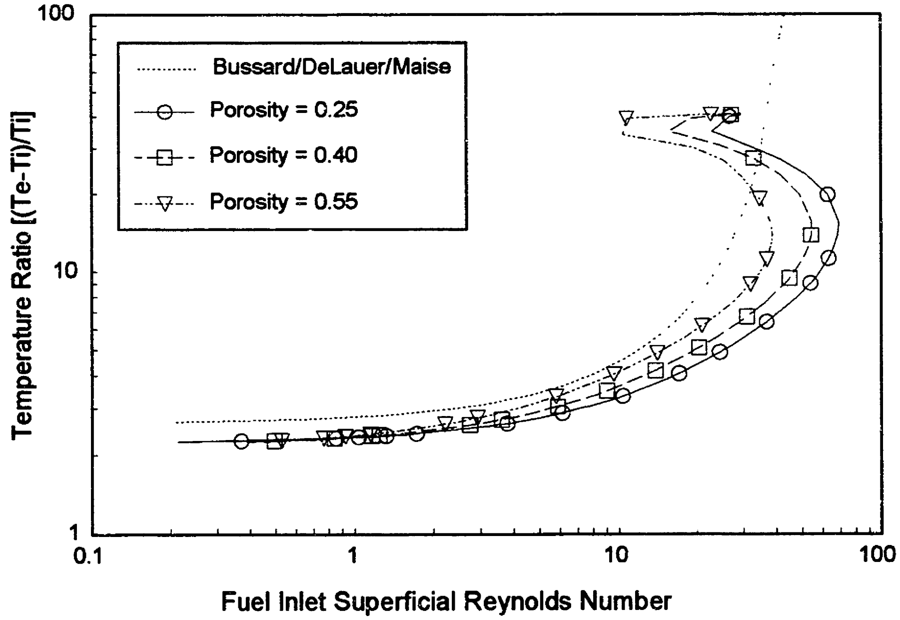

Figure 3.39 Stability Map for Baseline PBR Element with Various Bed Porosities

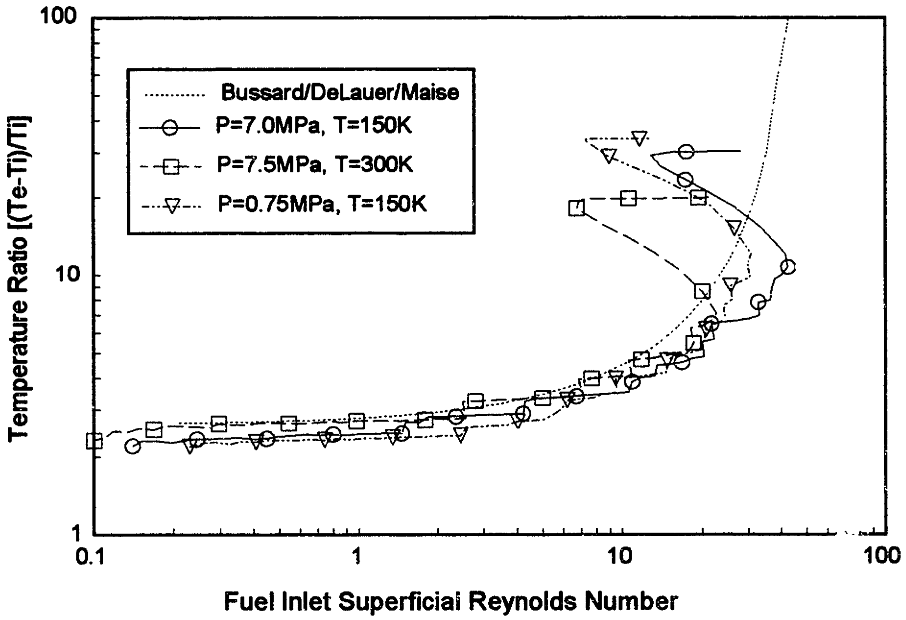

Figure 3.40 Stability Map for Baseline PBR Element with Various Inlet Gas Conditions

3.5.3 Two Dimensional Analysis

3.5.3.1 Impact of Non-Uniform Power Shape

As part of the analysis for the work reported in Reference [W-9], several SIMBED cases were run to study the effect of the power shape on the flow stability of the element. The distributions of the fluid parameters for an element with a cosine power shape were presented in section 3.4. Extending the arguments given in section 3.5.1 for flow instability leads to the possibility for flow maldistributions to be initiated by the power shape. The two-dimensional analysis mentioned in the last section and shown in Figure 3.38 assumes that the mass flow is primarily directed in the radial direction as it travels through the fuel region. The cold frit can help to ensure that this is the case at the bed entrance, but local fuel porosity and heating distributions can affect the flow once it is in the bed. The FIT element geometry was simulated in SIMBED with a sine power shape with an extrapolated length twice the element length. The radial shape was an exponential with a TAUFAC variable equal to 2.5. The total power and flow were such that the element was near the one dimensional flow stability line. Studying the convergence behavior for the code can indicate possible modes for instability. The plots in Figure 3.41 show the hydrogen temperatures at the exit of the fuel region at various numbers of iterations. Figure 3.42 shows the mass flow rate distribution at the bed entrance for the same simulation run. A uniform power shape curve is also presented as a means of comparison. Convergence is measured by the percent difference between the energy of the solid material and the change in energy of the fluid from the point it enters the model to when it leaves the model geometry. The uniform case converged to an energy balance of 5.24% at 1200 iterations, while the non-uniform case reached a minimum of 7.98% at 375 iterations and continued to diverge. At 1600 iterations the difference was 9.85%. In the figures, the CI stands for Cosine Iterations, the FI stands for Flat Iterations, and the number stands for the number of iterations completed for the curve data set. These curves seem to indicate that the hotter regions of the fuel element is operating in a unstable operating regime. In order to determine whether the non-convergence was due to numerical instabilities rather than physical instability, cases were run with 60 and 100 axial nodes. These cases yielded the same trends. The trends displayed are consistent with the scenario presented in Reference [V-1], in that the hotter regions continue to get hotter as flow is diverted from these regions due to the increase in viscosity and flow resistance.

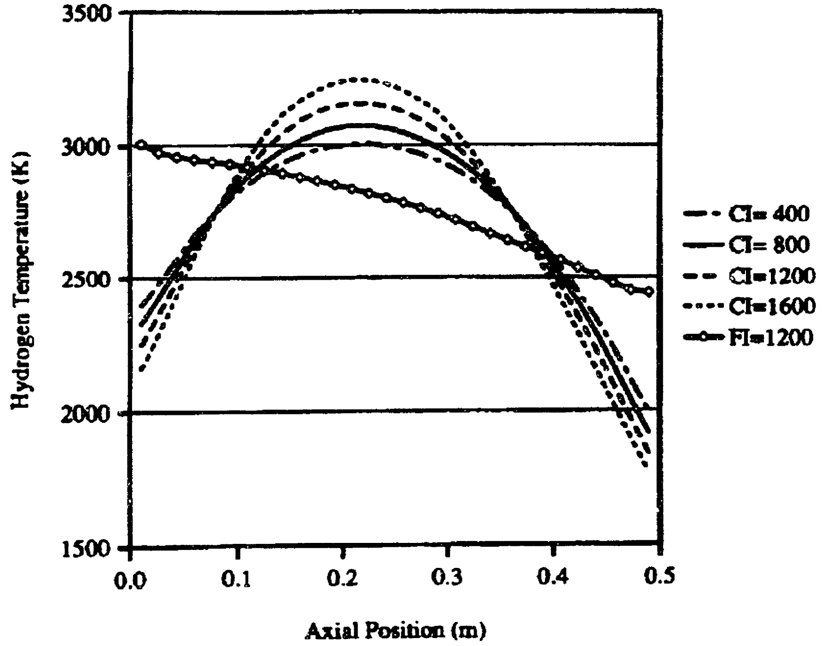

Figure 3.41 Hydrogen Temperature Distribution at Fuel Bed Exit at Various Iterations

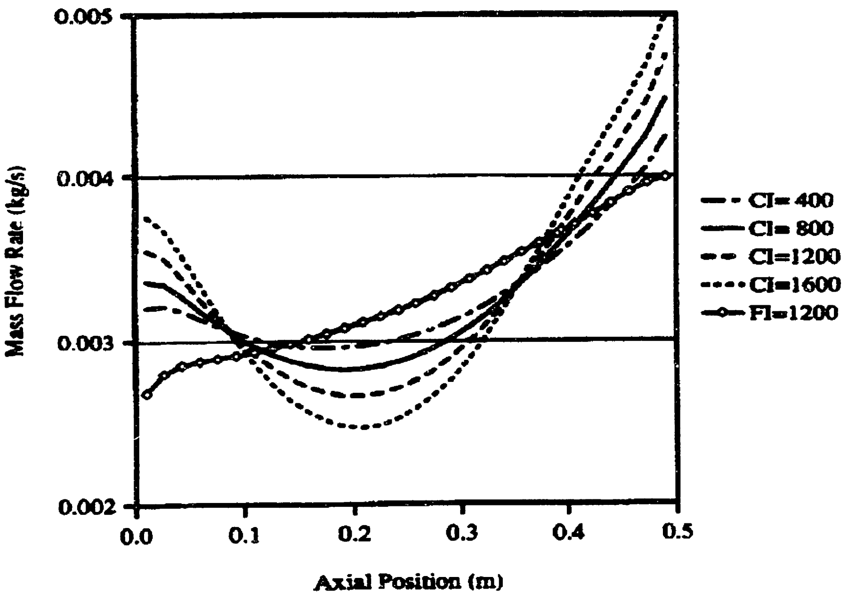

Figure 3.42 Mass Flow Distribution at Fuel Region Entrance at Various Iterations

The SIMBED code used for this analysis is a steady state code, so any thermal conductivity and heat capacity effects are not included. These parameters would determine the rate of change of any instability and could even dampen the flow maldistribution. As recommended in Chapter 5, this analysis should be repeated with the transient version of SIMBED for a null transient to see if the same behavior is noticed.

3.6 Chapter Summary

This Chapter has presented the results from the basic PBR fuel element models used in this research. The one dimensional models have been shown to adequately predict element behavior and as experimental data becomes available, can be easily adapted to any new correlations. The cylindrical geometry of the PBR fuel element makes two dimensional modeling an effective tool to understand the flow patterns and the temperature profiles. The enhancements made to the computer codes allows the modeling of more realistic power shapes and cold frit resistances. The result of both one and two dimensional models have been shown to yield similar results for steady state conditions. This lead to the conclusion that the one dimensional models are adequate for determining the operating regions of interest for more detailed studies for flow stability concerns. In the next chapter, the rocket system modeling effort is presented.

Chapter Four - Nuclear Thermal Propulsion Engine Modeling

4.1 Introduction

In this chapter, the full rocket engine system model is presented. The model components are defined and then results of the computer codes are given. Two steady state codes were developed in order to model the two phases of possible operation. The first is a chilldown mode, where no turbine flow is allowed and the flow is driven by the tank pressure head. This is used for pre-bootstrap and post operation decay heat cooling studies. The second code models the system with the turbopump assembly operating. This is used to benchmark the NERVA engine to existing subsystem codes and to generate the system operating maps. The results from these steady states codes are given in Section 4.2.

The transient computer code developed was developed to study the startup, variable thrust, and shutdown phases of rocket operation. System behavior and turbopump and control requirements can be studied with this model. The results of several transient cases run for both the NERVA and the PBR concepts are given in Section 4.3.

4.1.1 Engine Cycles

4.1.1.1 Bleed Cycle

One engine cycle that had been used in the early phases of the NERVA program is the bleed cycle. This engine cycle is so named, because a portion of the main nozzle chamber flow is "bled" off to drive the turbine. This cycle was depicted in Figure 1.6. Due to the high temperature of the gas, the amount of flow required is usually less than 3% of the total system flow. Due to material temperature limits for piping and the turbine blades, some additional cooler flow needed to be mixed with this hot flow. After passing through the turbine, the flow is exhausted through nozzles. An advantage of this system, is that the one can more easily assure that the turbine will have enough drive flow energy to be able to bootstrap and run the turbopump assembly. Because this gas is exhausted at lower temperatures and the main nozzle flow has been reduced, the total engine performance Isp is reduced. For this reason, later designs for the NERVA engine went to the Expander/Topping cycle.

4.1.1.2 Expander/Topping Cycle

The NERVA designs evolved to the topping cycle over the course of engine development. This was done in order to maximize the specific impulse and reduce the propellant penalty. In this cycle, the turbine driving flow is a fraction of the full system flow taken from before the reactor core. The energy required to drive the system is obtained from the cooling of the nozzle, reflector, and other structures. The flow can be split before the component cooling, to ensure higher turbine inlet temperature, or the flow can be split after the component cooling. The NERVA designs had several flow paths that would be recombined in various sections of the flow paths.

To reduce piping requirements and flow balancing issues, it was decided to model the engine as a simple topping cycle. The engine was broken into the minimum number of control volumes required to model the system, but still provide an adequate level of detail. The system model is shown in Figure 4.1 and Table 4.1 defines each of the components used. By allowing the reactor to modeled as a separate control volume, it is conceivable that any reactor concept can be modeled. For this study, the NERVA and PBR core geometries have been modeled. The current computer programs do not model the tank pressurization nodes, nor the tank outflow effects. The boundary condition for the tank assumes constant properties at the first junction, J1. The input routine, however, does allow for the user to define these components. This may allow an easier implementation of these components in the future, as is recommended in Chapter 5.

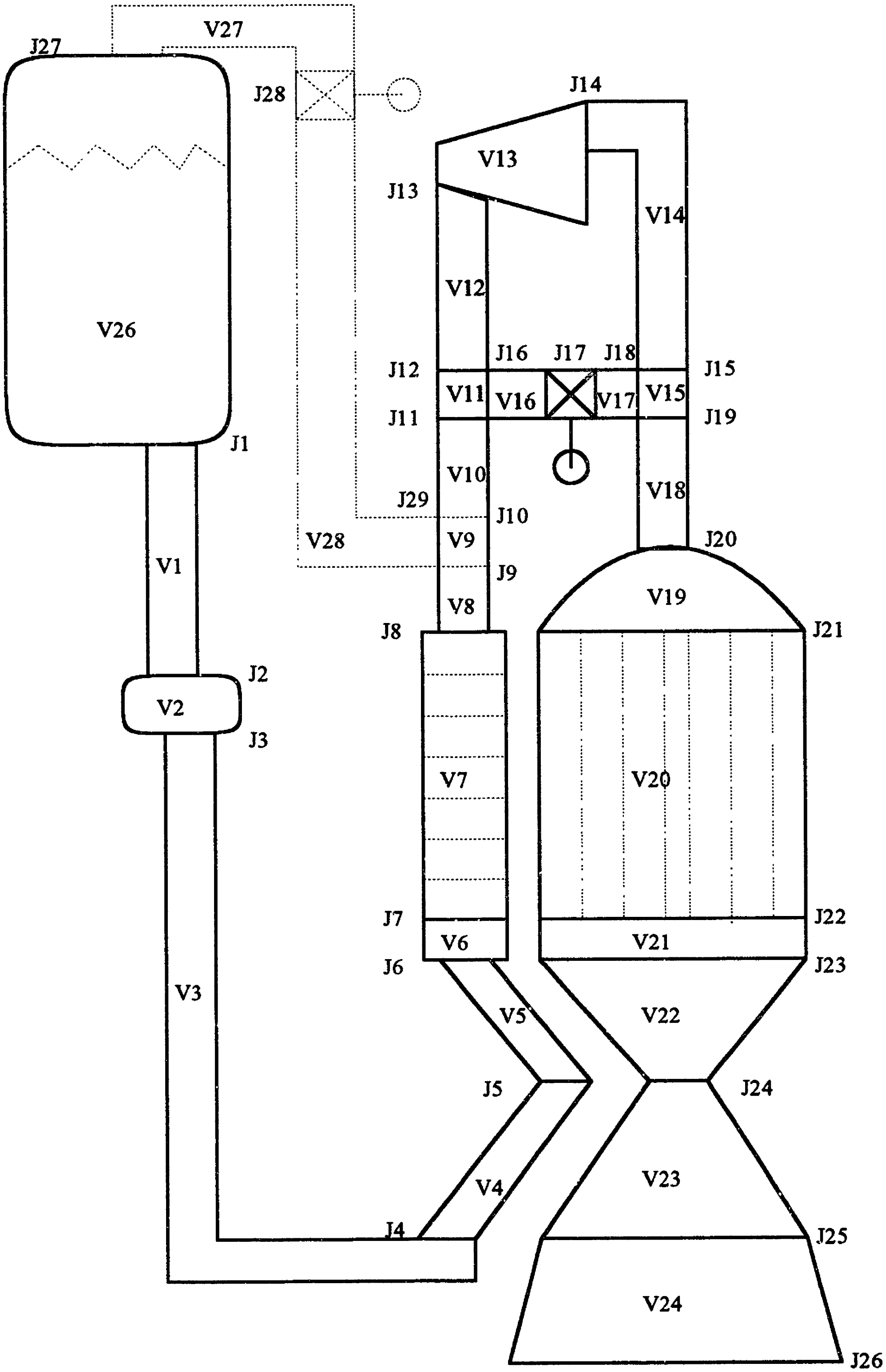

Figure 4.1 Engine System Model Control Volumes

Table 4.1 Definitions of Engine System Control Volumes

Component ID	*Component Definition*
V1	Piping - Tank to Pump
V2	Pump
V3	Piping - Pump to Nozzle Cooling
V4	Nozzle Cooling Jacket - Section I
V5	Nozzle Cooling Jacket - Section II
V6	Mixing Plenum
V7	Reflector
V8	Mixing Plenum and Piping to Tank Pressurization Tee
V9	Piping Tee for Tank Pressurization (future model)
V10	Piping to Turbine Bypass Flow Splitter Tee
V11	Piping Tee for Turbine Bypass Flow Splitting
V12	Piping to Turbine
V13	Turbine
V14	Piping to Turbine Bypass Flow Mixer Tee
V15	Piping Tee for Turbine Bypass Flow Mixing
V16	Piping from Splitter Tee to Turbine Bypass Control Valve
V17	Piping from Turbine Bypass Control Valve to Mixer Tee
V18	Piping to Reactor Inlet Plenum
V19	Reactor Inlet Plenum
V20	Reactor Core
V21	Reactor Outlet Plenum
V22	Nozzle Section I - Cooled
V23	Nozzle Section II - Cooled
V24	Nozzle Section II - Uncooled
V25	Space Environment (future model)
V26	Tank (future)
V27	Piping from Tank Pressure Control Valve to Tank (future)
V28	Piping from Tee to Tank Pressure Control Valve (future)
J17	Turbine Bypass Control Valve
J28	Tank Pressure Control Valve (future)

4.2 Steady State Analysis

4.2.1 Chill Down - Low Power, No Turbine Flow

4.2.1.1 Description of Method

The chill down phase of operation uses no turbopump assembly to drive the flow. Instead, the only driving head is the tank pressure. The nozzle is assumed to have choked flow, so that the system flow rate is determined from the nozzle chamber conditions and the nozzle cooling. The bypass valve is used to create the required pressure drop to match the tank driving head capability to the nozzle chamber conditions. The system flow is limited by the available tank driving head, so the chamber pressure must always be less than the tank pressure. A computer program ENGine BLEED (ENGBLEED) was developed by this author to model this phase of operation. The outputs from this include the system flow rate and the reactor power requirements in order for the chamber conditions to be met. The flowchart for this computer model is shown in Figure 4.2. The general flow for the program is described in the next paragraph.

After reading the user input problem description file, the code determines the first guess for the system mass flow rate using the NOZZFLOW subroutine described in Section 2.4. Using this, the volume flow resistances are calculated. These are used to find the pressure drops and component pressures. The pressures are matched at the turbine control bypass valve by calculating the pressures from the nozzle back to the junction J18 and from the tank forward to the junction J16 and determining the required bypass control valve loss coefficient from the pressure drop across the junction J17. The program determines the required reactor power from an energy balance across the volume V20, updates the heat inputs to the volumes using the subroutines NOZZHEAT, REFLHEAT, and COREHEAT. These heat inputs are used to determine the junction and volume enthalpies. Once the new enthalpies are found, they are used with the previously determined pressures to find the hydrogen state properties with the subroutine NBSpH2. The valve loss coefficient is used for the iteration convergence criteria. If not converged to within the required error limit, the program steps to find the new flow and begins the iteration process again. If it is converged, the program writes the output file and terminates.

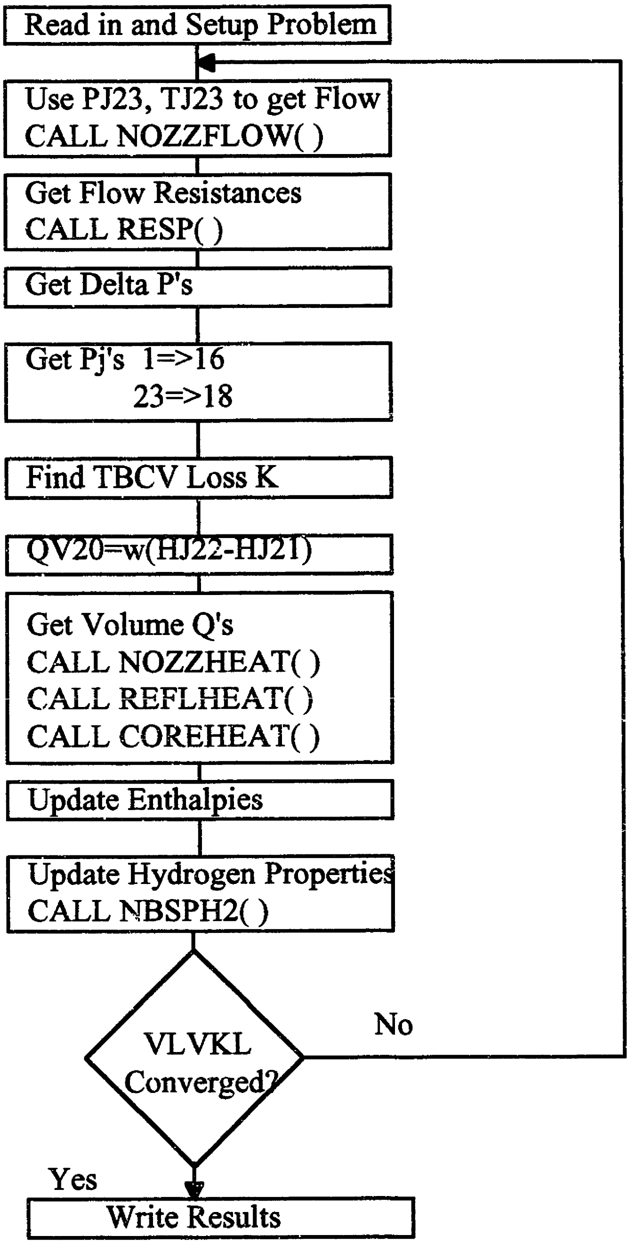

Figure 4.2 Flowchart for Chill Down Computer Code, ENGBLEED

This code was used to map out regions of power and flow that could be tolerated using only the tank head to drive the flow. Another concern is for the hydrogen to be in a gas phase when is reaches the core region. The critical temperature for hydrogen is 33.3 K and critical pressure is 1283 kPa. This code can also be used to find the point when the system has enough energy to allow turbine flow to be initiated or to determine the decay heat power level that can maintain the system cool with only bleed flow.

4.2.1.2 NERVA Core

The NERVA core geometry for this analysis was determined from the dimensions given in Reference [W-6]. The tank pressure and temperature conditions used were 250 kPa and 20 K respectively[L-2]. The full input file for this core is given in Appendix A. Because the input subroutine is the same for all the engine computer codes, the input files for the chilldown, steady state, and transient can be the same. The operating points attainable in the chilldown mode for this system configuration are given in Table 4.2. The input nozzle chamber temperature and pressure boundary conditions are labeled TJ23 and PJ23. The primary outputs are the effective engine power (QTOTE), the system mass flow rate (W), and the TBCV resistance term (VLVKL). Of note is the capability for this mode to be able to remove 45 MW or about 3 % of full power. The TBCV valve information is given in terms of its resistance, because the steady state version of the code is used to determine the range of resistance required for the valve stem travel position used by the transient computer code. The bleed flow results will be coupled with the pumped flow, steady state results to generate the operating map described in Section 4.2.3.

Table 4.2 Chill Down Phase Operating Conditions for NERVA Engine

PJ23 (kPa)	*TJ23 (K)*	*QTOTE (MW)*	*W (kg/s)*	*VLVKL* $(*10^{-6})$
25.0000	500.0000	5.3040	0.7330	0.5203
	750.0000	6.5160	0.6040	0.3612
	1000.0000	7.4280	0.5170	0.3246
50.0000	250.0000	7.5090	2.0500	1.4740
	500.0000	10.7250	1.4700	0.1299
	750.0000	13.0300	1.2000	0.0894

PJ23 (kPa)	*TJ23 (K)*	*QTOTE (MW)*	*W (kg/s)*	*VLVKL* $(*10^{-6})$
	1000.0000	15.0300	1.0400	0.0772
75.0000	250.0000	11.2780	3.0800	0.5643
	500.0000	16.0960	2.2140	0.0535
	750.0000	19.5900	1.8070	0.0355
	1000.0000	22.6000	1.5640	0.0318
100.0000	250.0000	15.0500	4.1060	0.2590
	500.0000	21.4730	2.9500	0.0255
	750.0000	26.1560	2.4100	0.0162
	1000.0000	30.1800	2.0850	0.0134
150.0000	250.0000	22.6000	6.1600	0.0564
	500.0000	32.2400	4.4230	0.0049
	750.0000	39.3000	3.6160	0.0022
	1000.0000	45.3500	3.1280	0.0014

4.2.1.3 PBR Core

The PBR reactor module was determined by designing the core performance to obtain a 225 kN thrust engine with nozzle chamber conditions of 7 MPa and 3000 K. A 37 element core, was chosen in this case to ensure the element outlet channel conditions always have a Mach number less than 0.2. The element was sized to yield an average bed power density of 25 GW/m^3. The operating parameters were chosen to yield a prototypic 37 element core configuration that could meet the requirements of Reference [N-1], show the capabilities of the simulation models, and were not meant to imply a final design rocket engine.

The results of the chill down cases for the PBR are given in Table 4.3. In addition to the parameters listed in Table 4.2, the fuel inlet Reynolds number and the temperature rise factor (ϕ) are included. When these points are placed on the stability map in Figure 3.38, they show there may be some operational constraints when using a 37 element core. This will be discussed more in section 4.2.3. No heat is added to the system before the reactor, except a fraction of the total power in the reflector and nozzle. This results in higher temperature rise factors, because the inlet temperature is extremely low. If there is latent heat in the system or a preheater, the rise factor would be reduced.

Table 4.3 Chill Down Phase Operating Conditions for PBR Engine

PJ23 (kPa)	*TJ23 (K)*	*QTOTE (MW)*	*W (kg/s)*	*Reynolds Number*	ϕ *($\Delta K/K$)*	*VLVKL* ($*10^{-6}$)
25.0000	250.0000	1.8600	0.2710	11.2400	15.4000	51.6000
	500.0000	1.3400	0.1920	4.3500	8.2000	3.7700
	750.0000	1.6400	0.1580	2.7600	6.8300	2.8800
	1000.0000	1.8600	0.1360	1.9500	6.6500	2.7200
50.0000	250.0000	1.9200	0.5370	22.9500	14.2200	14.1960
	500.0000	2.7200	0.3870	8.9300	9.2900	0.9870
	750.0000	3.3000	0.3150	5.5900	7.5300	0.7100
	1000.0000	3.8000	0.2730	4.0000	7.2500	0.6180
75.0000	250.0000	2.8900	0.8050	34.8100	13.1800	5.9700
	500.0000	4.1000	0.5790	13.5100	9.9000	0.4230
	750.0000	4.9700	0.4730	8.4900	7.9700	0.2810
	1000.0000	5.7300	0.4090	6.0800	7.6100	0.2260
100.0000	250.0000	3.8600	1.0740	46.7300	12.2800	2.9700
	500.0000	5.4800	0.7720	18.1400	0.3700	0.2110
	750.0000	6.6600	0.6310	11.3800	8.2800	0.1263
	1000.0000	7.6700	0.5460	8.1900	7.8600	0.0890
125.0000	250.0000	4.8300	1.3400	58.6700	11.4900	1.5700
	500.0000	6.8700	0.9600	22.7600	10.7000	0.1090
	750.0000	8.3400	0.7880	14.3200	8.5200	0.0538
	1000.0000	9.6100	0.6820	10.3000	8.0500	0.0263
140.0000	250.0000	5.4200	1.5030	65.8100	11.0600	1.0720
	500.0000	7.7000	1.0800	25.5400	10.8600	0.0702
	750.0000	9.3500	0.8830	16.1100	8.6500	0.0275
	1000.0000	10.7800	0.7640	11.5900	8.1500	0.0041

4.2.2 Power Operation

4.2.2.1 Description of Method

The normal operating phase implies that the turbopump is in operation. For this phase the steady state condition is determined in a similar fashion to the chill down phase, except the convergence variable is the pump outlet pressure, PJ3. The computer program ENGine Steady State (ENGSS) was written by this author to find the steady state operating conditions of the rocket engine system. A flow chart for the computer program is given in Figure 4.3. The program begins by reading the input file and setting up the problem geometry. The chamber pressure and temperature are used to calculate the first guess for the system mass flow rate. An initial guess for the turbine mass flow rate is set to 25% of the total flow rate. This value will change with the iterations because the turbine power and flow are determined by the pump power requirements. From the system flow rate and the initial hydrogen conditions, the volume flow resistances are determined. These are used to find the system pressures, by backing the pressures from the given chamber pressure through the turbine flow path. A pressure balance across the turbine control bypass line is used to determine the TBCV pressure loss coefficient. The pressures are then backed out to the pump exit. The pump pressure rise is determined and used to set the required pump speed, head, and power. The enthalpy difference across the core determines the core region heat input and the system total power. This power is multiplied by distribution factors and is used to determine the enthalpy rises across the nozzle and reflector control volumes. The turbine flow is found from the turbine power requirement to drive the pump and the turbine inlet temperature. The bypass flow used to calculate the TBCV loss coefficient in the next iteration loop is simply the difference between the total flow and the turbine flow. Once all the control volume enthalpies have been calculated, the hydrogen properties are updated using the pressure and enthalpy as inputs to the NBSpH2 properties routine. If the pump outlet pressure is converged to within the criterion limit, the program writes the output file and terminates. If the system has not converged, the program returns to calculate a new system flow and the process is repeated until convergence has been met.

The steady state code allows quick studies of a particular reactor engine system. Both the NERVA core and PBR core can be modeled to varying levels of detail. The simplest case is to run with the core modeled with one ring of uniform radial power profile and one node of axial power shape. The detailed model will be used in the next sections to show the capability of the steady state code to predict reactor and engine conditions.

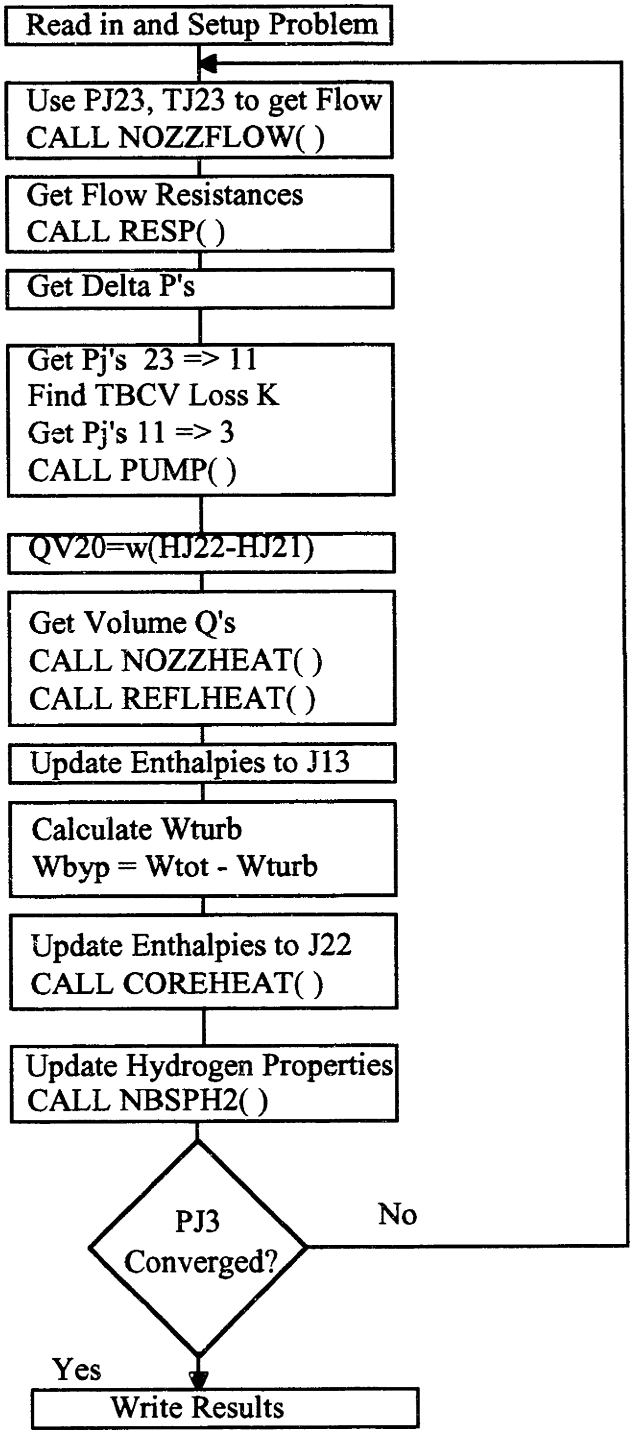

Figure 4.3 Flowchart for Steady State Engine Code, ENGSS

4.2.2.2 NERVA Core

The NERVA engine data set from Reference [C-3] was used to benchmark the ENGSS code. A detailed six radial zone, ten axial zone case was used to show the versatility of the user input deck. The results from the steady state engine code were compared to results from a CAC case run for the same reactor geometry and operating conditions. A table of the key reactor radial inputs is given in Table 4.4. Results for the core ring and fuel channel conditions appear in Figures 4.4 through 4.7. The full input and output files for the CAC and the ENGSS appear in Appendix A. The radial temperature distribution is shown in Figure 4.4. The maximum temperature difference is 80 K which represents a difference of less than 4%. Some differences are expected due to slightly different methods for the pressure drop and heat transfer calculations. The radial mass flux distribution is shown in Figure 4.5. Again there is good agreement shown, with a maximum difference of 0.05g/s/channel with a difference of approximately 4%. If one considers the rings flow rates, the maximum error is 0.2kg/s/ring with a difference of less than 2%. The axial distributions for the maximum fuel temperature (labeled TMax) and the bulk hydrogen temperature (labeled TH2), along with the axial power peaking factors (labeled PKZ), are shown in Figure 4.6 for the sixth ring of the reactor. The curves show that the shapes are similar, with the gas temperatures being nearly identical. The axial pressure distribution for the same reactor ring is given in Figure 4.7. The difference in the first node pressure is due to the different method for calculating the entrance effects. The rest of the nodes indicate the same trend shape. The results of these calculations show that the reactor portion of the code can predict conditions similar to those found using the CAC code.

Table 4.4 Radial Parameters for CAC/ENGSS Benchmark

Ring Number	*Radial Position (m)*	*Orifice Factor (ORF)*	*Entrance Loss (CAYL)*	*Radial Peaking (PKR)*
I	0.0686	0.2339	1.4400	1.1030
II	0.1410	0.1769	1.5200	1.0770
III	0.2065	0.1433	1.5750	1.0430
IV	0.2555	0.1204	1.6100	0.9950
V	0.3653	0.0995	1.6450	0.9330
VI	0.4267	0.1278	1.6000	1.0430

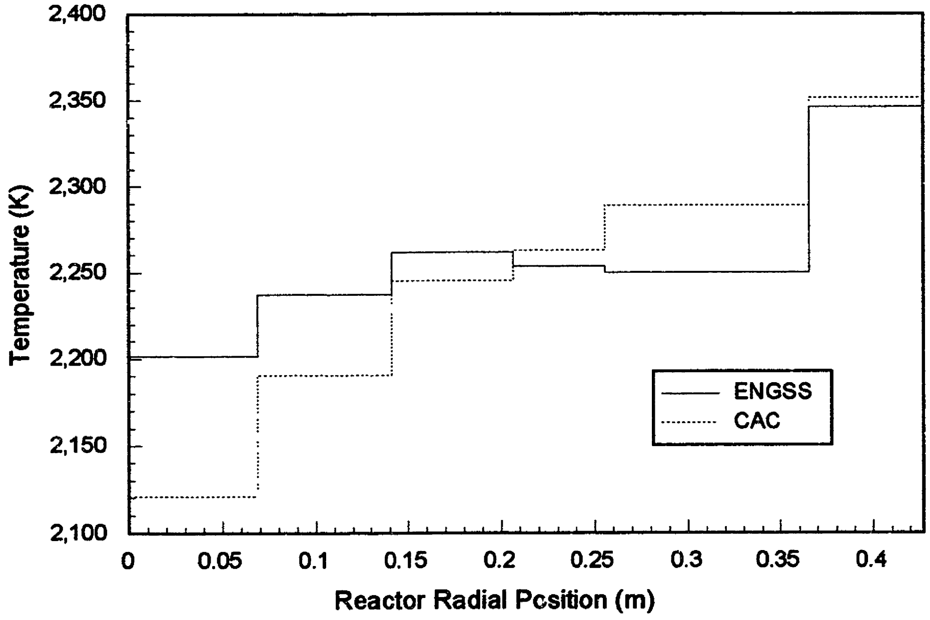

Figure 4.4 NERVA Core Radial Distribution of Exit Temperatures

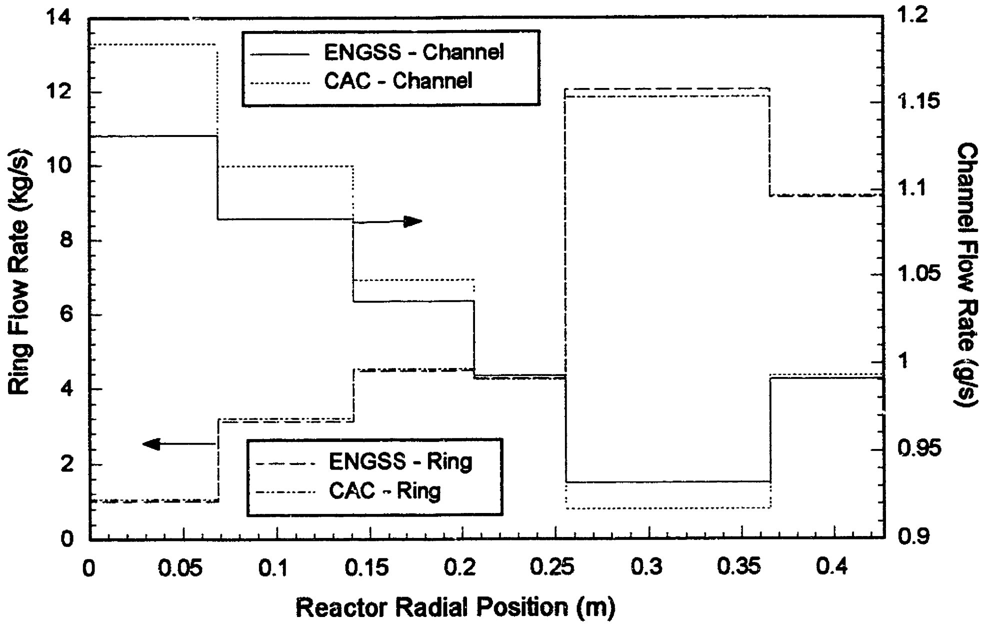

Figure 4.5 NERVA Core Radial Channel and Ring Mass Flow Rate Distributions

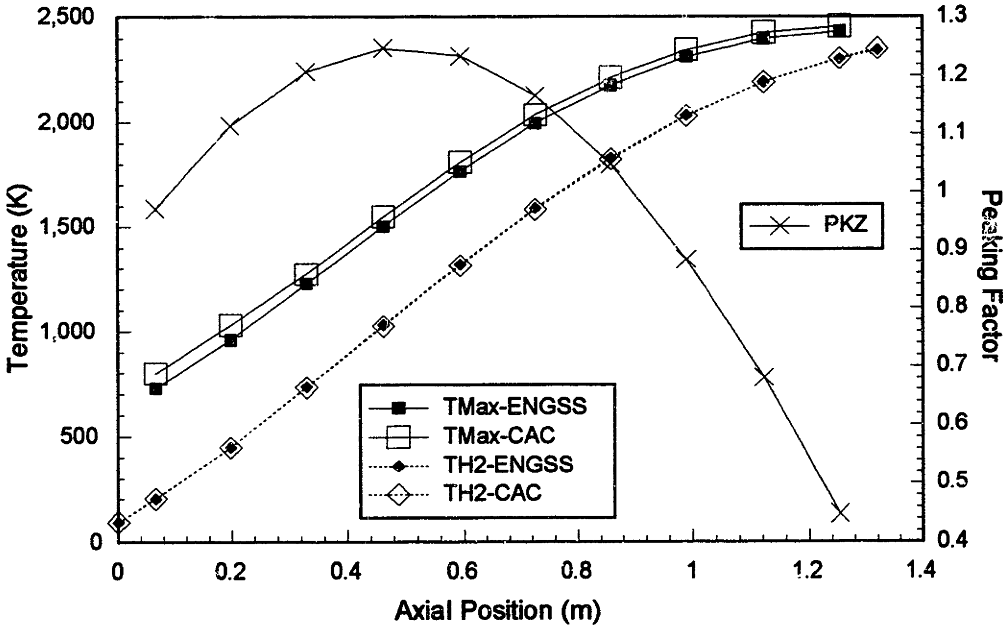

Figure 4.6 NERVA Fuel Element Axial Temperature and Power Distributions in Ring 6

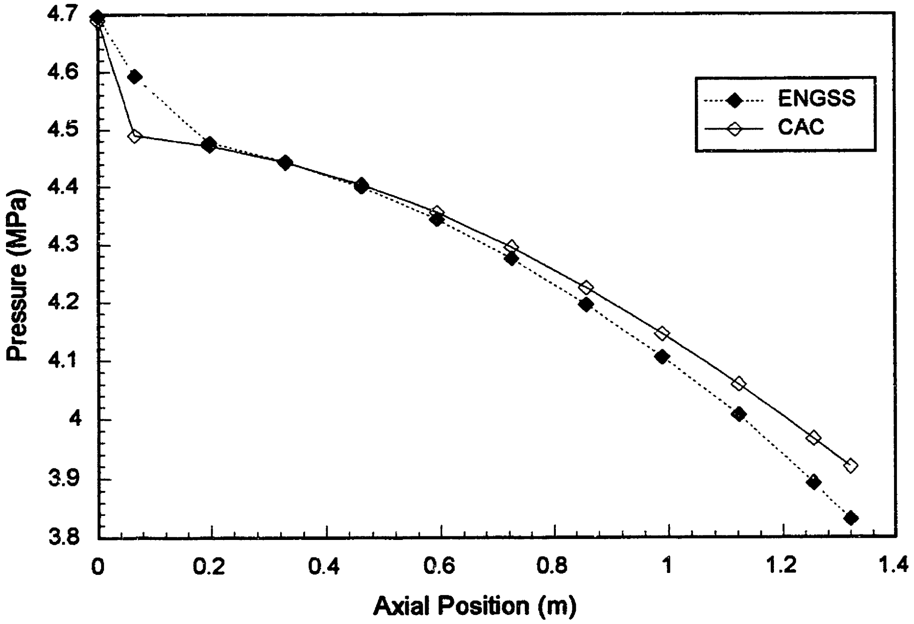

Figure 4.7 NERVA Fuel Element Axial Pressure Distribution in Ring 6

4.2.2.3 PBR Core

A detailed PBR core model was used to show the versatility of the ENGSS code for modeling this reactor type. The model used for the fuel element is the same model that was described and benchmarked in Chapter 3. Figure 4.8 shows the temperatures and pressures across the element operating at rated conditions. The temperature difference between the effective fuel temperature and the bulk hydrogen temperature is around 450 K in the first node of the bed and lowers to about 90 K in the last node. This reduction is caused by the changing heat transfer coefficient and accelerating flow. The lower temperature difference at the exit node can allow operation at much higher gas temperatures. For a similar core power NERVA engine, the temperature differences are about the same, but the power density is about one-tenth that of the PBR. This demonstrates why the PBR can be a much smaller core than the NERVA engine. Also shown in the figure is the large pressure drop across the cold frit region of the element.

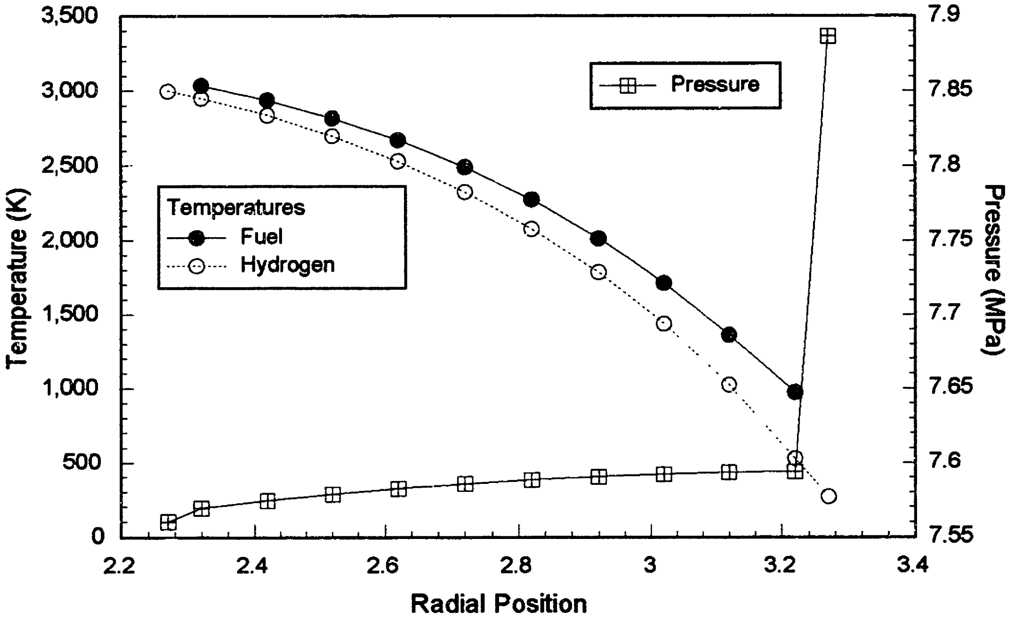

Figure 4.8 Temperature and Pressure Profile in Baseline PBR Fuel Element

The effectiveness of orificing to help flatten out the temperature distribution across the rings of the core can be shown by running cases with a radial power shape. The power shape and orifice parameters used for these runs are given in Table 4.5. The radial temperature distributions for an unorificed core and an orificed core is shown in Figure 4.9. The figure indicates that without orificing some of the elements may be operating with temperatures that may exceed material limits. The orificing helps to reduce the temperature peaking factors. The orificing could be done at the entrance to the element flow channel or with the cold frit resistance. As was discussed in Chapter 3, the cold frit resistance can be varied along the axial and azimuthal direction about some mean value. If the mean resistance value is varied among the radial elements, orificing would now occur at the cold frit. The ideal orificing values would be such that the outlet temperatures from each ring are the same value. The element mass flows for the orificing case are shown in Figure 4.10. As can be seen in the figure, the lower orifice loss terms increase the flow for the higher powered regions in order to bring the outlet temperatures close to those in the flat power case. The detailed input and output files from the orificed case are given in Appendix A.

Table 4.5 Radial Peaking Factors and Orificing Factors for ENGSS PBR Case

Ring Number	I	II	III	IV
Peaking Factor (PKR)	1.1500	1.0750	1.0250	0.9500
Orifice Loss Term (CAYL)	0.6500	1.0000	1.0750	1.4000

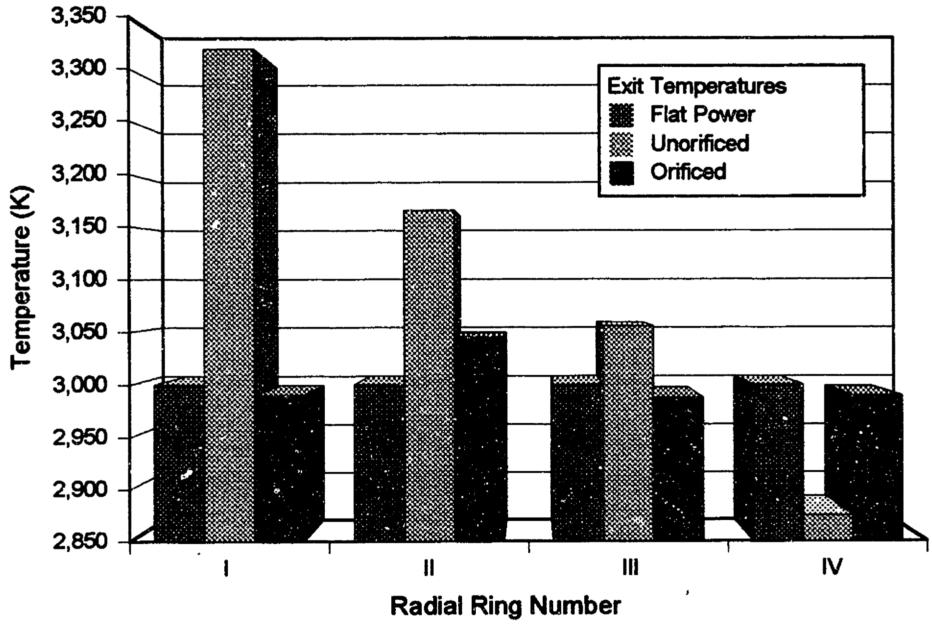

Figure 4.9 PBR Radial Distribution of Element Exit Temperatures

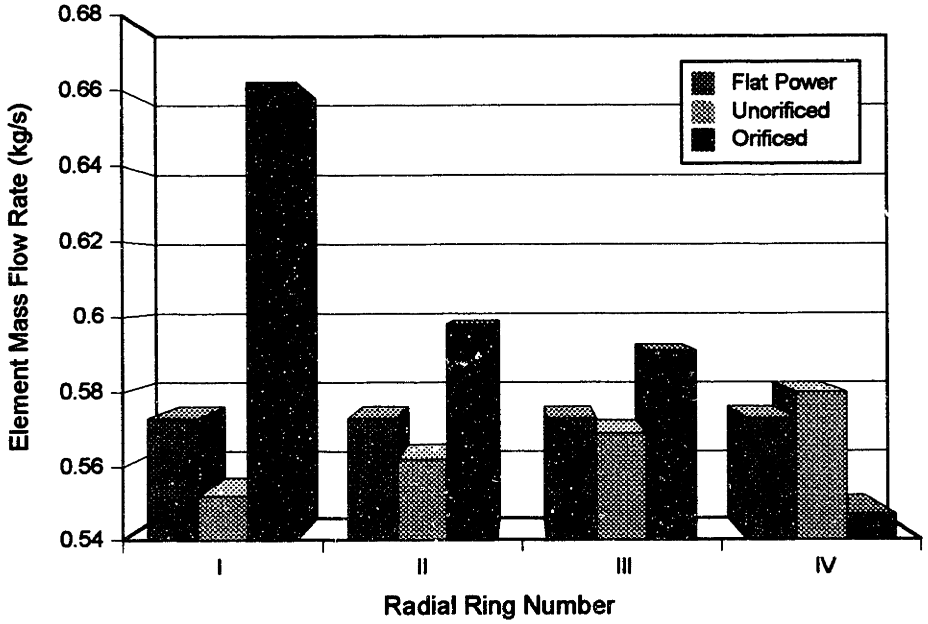

Figure 4.10 PBR Radial Distribution of Element Mass Flow Rates

4.2.3 System Operating Map Generation

4.2.3.1 Description of Operating Maps

The reactor engine system is able to operate over a wide range of conditions, however, there are some limitations. These include turbopump capabilities, fuel material limits, core reactivity constraints, and system pressure limits. Operating maps provide an easy means to determine allowable engine conditions. Typically these are plotted in terms of the nozzle chamber temperature versus pressure. Lines of constant mass flow rate and constant power can be included on these to further clarify the operating conditions. A sample of a detailed operating map from the NERVA program is shown in Figure 4.11[M-2]. In this figure, the bold lines show the typical paths that would be followed for startups and shutdowns. The pump and controller limits are also depicted. For the NERVA program, the controllers were scheduled to bring the rocket system to full power along the desired pressure and temperature trajectory. In order for transient cases to be run, some form of operating map must be generated for the defined rocket. These can be used to determine the trajectories that may be possible within the capabilities of the system. The next section describes how maps can be generated and provides the operating maps for the NERVA and PBR engines used in the transient runs.

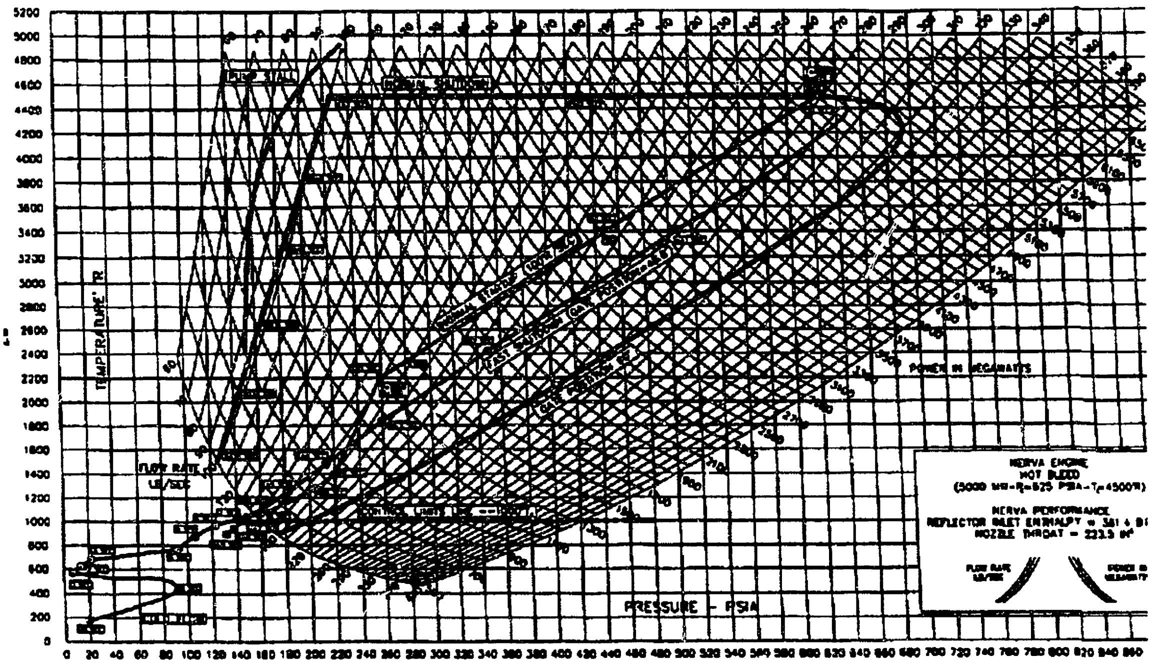

Figure 4.11 Prototypic NERVA Engine Operating Map from Reference [M-2]

4.2.3.2 Generation from Steady State Operating Points

Generating operating maps is a straight forward process once an engine system design has been specified. Usually the generation of operation maps will require some iteration on the engine design in order for the engine to meet the full range of operating requirements. The ENGSS code can be used to determine the operating conditions for both the NERVA and PBR reactor systems from a given nozzle chamber pressure and temperature and system geometry definition. The maps allow the designer to determine some of the limits of operation within turbo-pump and control drum worth constraints. The procedure for generating an operating map is as follows:

1. Determine the initial rocket system piping, turbopump, reactor, and control worth sizes. The nozzle should be sized to give the desired thrust and Isp at the design rated nozzle chamber pressure and temperature.
2. Generate a table of required nozzle chamber pressure and temperature conditions as inputs. The outputs that will be considered for the map include the total reactor power, the TBCV loss coefficient, the turbine inlet temperature, the pump speed, the mass flow rates for the system, turbine, and bypass, and the pump head.
3. Run the ENGSS computer code to generate the matrix of outputs for the given inputs of chamber pressure and temperature. This must be repeated for as many data points as desired.
4. Limits of operation are found when certain design constraints are exceeded. Among these are when there is not enough bypass or turbine flow for a particular condition, when the TBCV loss coefficient goes negative, when the pump speed reaches some predetermined limit, when the turbine inlet temperature is below some predetermined limit, and when the fuel element flow stability criterion is not met.
5. The standard operating map is then generating by plotting the limits of operation found in step 4. If these do not meet the operational requirements, the design must be changed and the process repeated.
6. A detailed operating map, like Figure 4.11, can be generated by plotting the power and flow contour lines as a function of pressure and temperature on the final version of the operating limits map.
7. The TBCV valve loss coefficient can be converted into the function of valve stem travel by the inverse of Equation 2.74. The TBCVA and TBCVB coefficients should be chosen to have the majority of control over a range of 80% of the travel.

Operating maps generated for example NERVA and PBR rocket designs are given in Figures 4.12 through 4.14. The WANL NERVA engine is intended to model the engine design given in Reference [W-6] and the CAC NERVA engine is modeled after the reactor core in Reference [C-2]. The PBR engine is sized to provide 225 kN of thrust and an Isp close to 1000 seconds. The NERVA operating maps are not limited by any flow instability, while the PBR map shows that certain low pressures and high temperatures are not allowed due to the stability criteria discussed in Chapter 3. In fact, during the course of designing the PBR engine, the 37 element core used for discussion of the code capabilities in earlier sections had to be changed to a 19 element core in order to enlarge the stable operating range. The power density was increased from 25 to 40GW/m^3 to maintain the same core power and the element radii were raised to keep the exit Mach number less than 0.2.

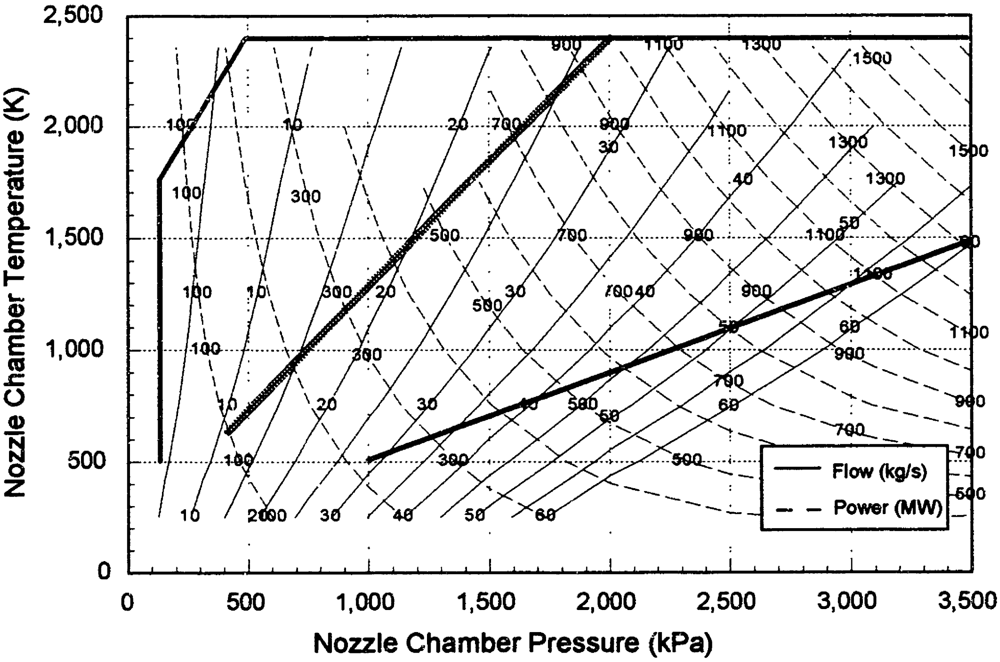

Figure 4.12 WANL NERVA Engine Operating Map

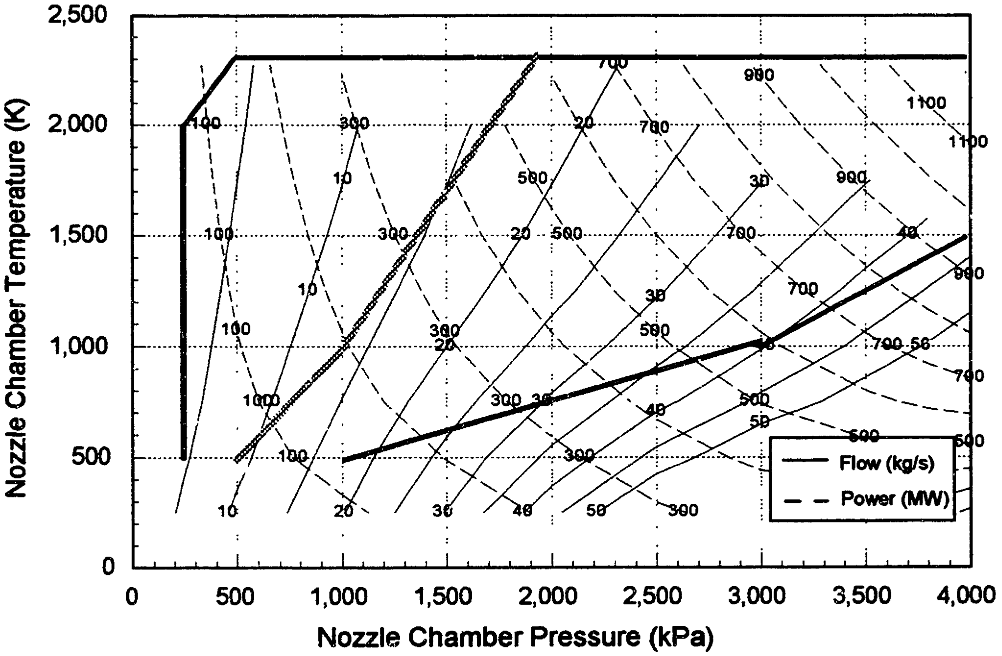

Figure 4.13 CAC NERVA Engine Operating Map

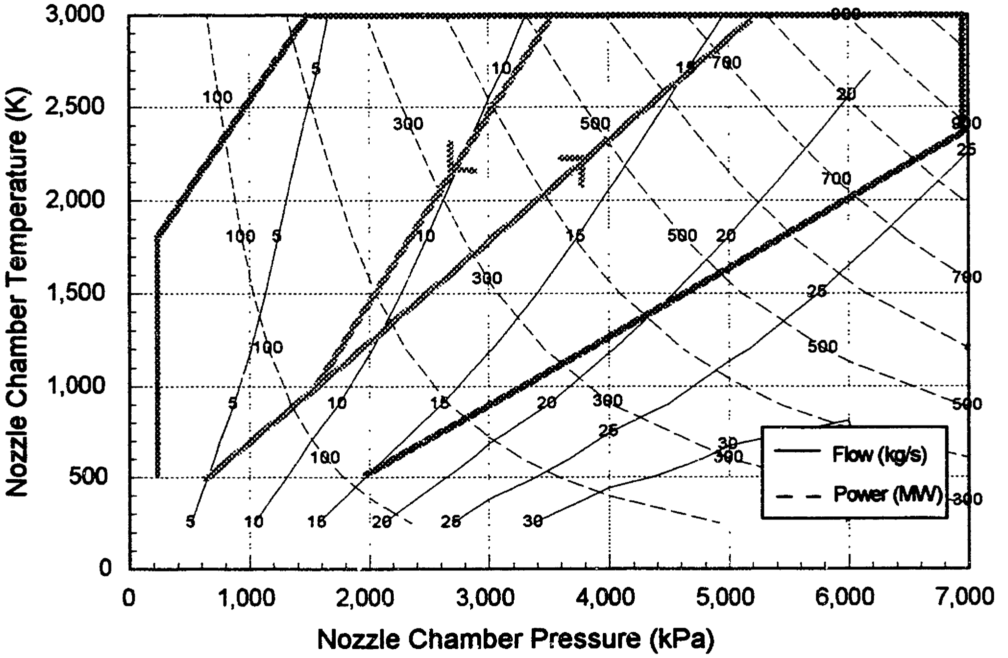

Figure 4.14 19 Element PBR Engine Operating Map

Once the map has been completed, transient cases may be run to evaluate the system response and develop startup and shutdown strategies. Power ramp lines are shown on each of the operating maps to show possible thrust ascension and reduction trajectories. These lines will be used to determine the parameter ramp endpoints for the transient calculations in the next section. The speeds at which these paths are traversed are determined by the system and material structural limits.

4.3 Transient Analysis

4.3.1 Description of Method

The transient analysis of the nuclear rocket systems is the final goal for this research. The computer code ENGine TRANSient (ENGTRANS) was developed by this author using the models from Chapter 2 to evaluate the operational behavior of the NERVA and PBR engine systems. Due to the different heat transfer characteristics, the engines are expected to need different operating strategies and control requirements. Transient simulations can help the designer understand the different plant behaviors and specify the requirements for various components. The approach for the transient simulation is an extension of the detailed the steady state engine computer code and the solution method of the one dimensional PBR element computer models.

The transient case is initialized at a steady state condition using the same method as described in section 4.2.2. The transient calculation loop begins with a determination of the desired nozzle chamber conditions. These are used as demand signals for the control model portion of the code. The user is able to define endpoints and durations for three transient ramps for the nozzle chamber pressure and temperature. Unlike the TRITRAN ramps, the pressure and temperature ramp durations can be different lengths. Additionally, periods of steady state holds are allowed at the beginning and the end of the ramps. A sample diagram for the pressure, temperature, and duration input variables for a uppower ramp is given in Figure 4.15. In the figure, the TCx and PCx terms are the demanded temperature and pressure and the DURyCx are the ramp duration times. The demanded temperature and pressure are used to determine the control drum and TBCV positioning requirements. The next section describes in more detail the philosophy behind these controls. Once the positions are determined, the program proceeds to calculate the neutron and decay heat power of the system from the point kinetics equations. The pump speed is determined from the turbine power to pump power mismatch from the previous time step using equation 2.68. This is then used to determine the pump pressure, power, and enthalpy rise. The control volume enthalpies up to the turbine bypass tee are then updated using the subroutines NOZZHEAT and REFLHEAT. The control volume flow resistances and pressures are also updated to this position. At this point, because the TBCV position is set by the pressure controller output, an iteration must take place to balance the flows and pressure drops from the splitter tee (V11) to the mixer tee (V15). This is performed in a similar manner to the core radial region flow balancing. Once the turbine and bypass flows and the turbine power have been determined, the control volume flow resistances and pressures are updated and the program proceeds to the core region. The subroutine COREHEAT is used to determine the core thermal hydraulic conditions and the reactor exit junction (J22) conditions. The enthalpies are then stepped to the chamber junction. These calculated conditions are used to determine the system mass flow rate by the NOZZFLOW subroutine. These conditions also used to generate the error signal for the pressure and temperature/power controllers. The total feedback reactivity for the next time step is calculated from the individual reactivity feedback effects that were determined in the COREHEAT and REFLHEAT subroutines. Because small time steps are required, the output to files is written only at user specified intervals. The detailed output file is usually written at longer intervals than the trend data files, because it will quickly grow in size and put a strain on any computer's memory quotas. After the output section, the transient run times are updated and the program returns to the beginning of the transient calculation loop. Once the total run time has reached the maximum time, the program terminates. Figure 4.16 gives a representative flowchart for the transient computer model.

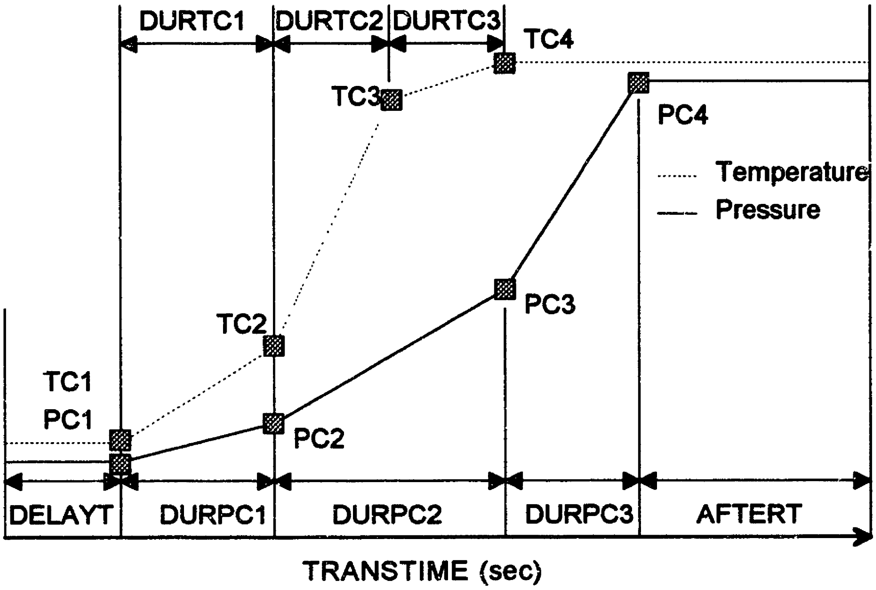

Figure 4.15 Sample Pressure and Temperature Trace for ENGTRANS Simulation

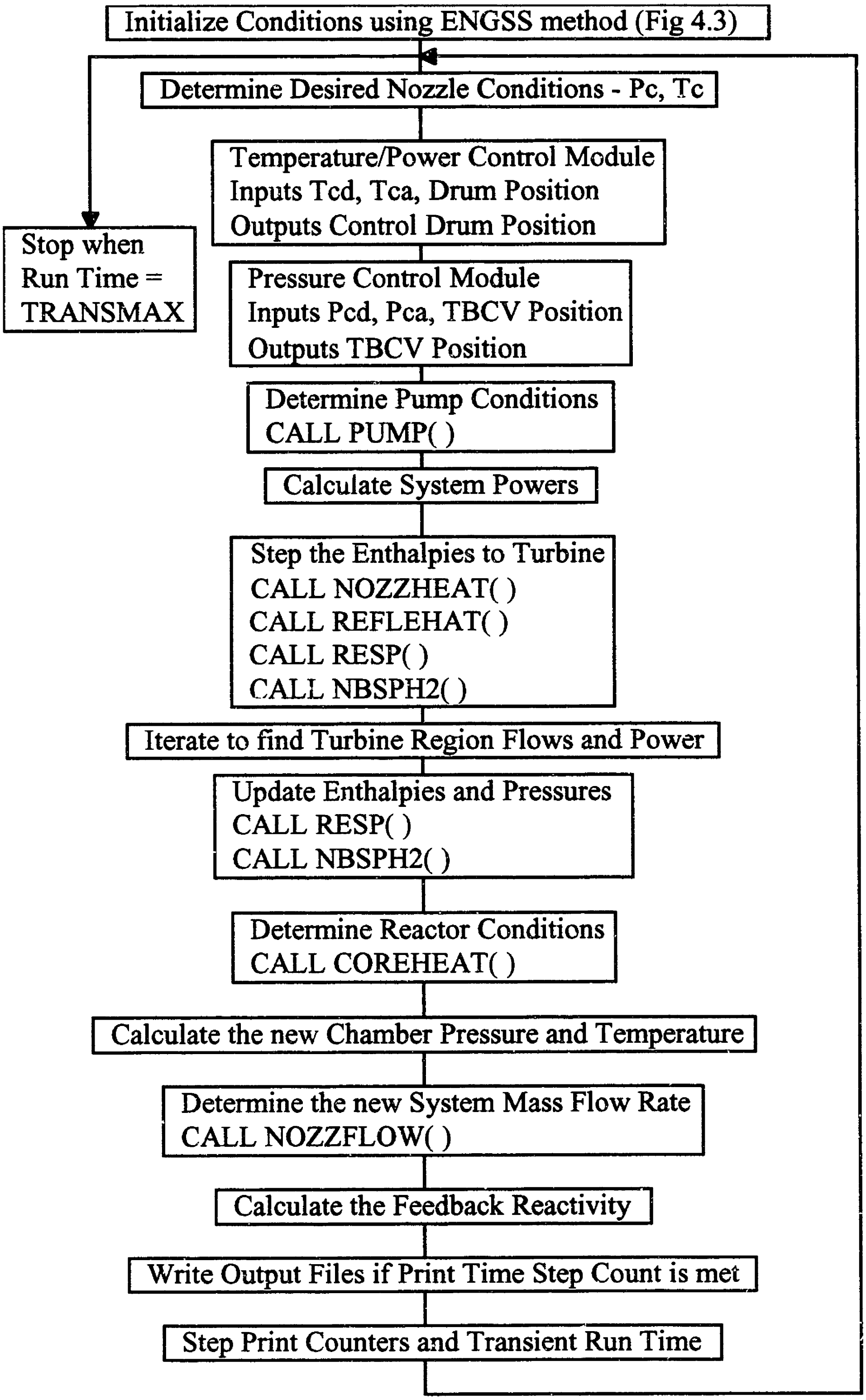

Figure 4.16 Flowchart for the Transient Engine Simulation Model, ENGTRANS

4.3.2 Control Strategy and Model Development

4.3.2.1 Strategy

The performance of a nuclear rocket is measured by the thrust and specific impulse. Past NERVA engine control consisted of a pressure controller and a temperature controller. The controllers were simple open and feedback controllers applied over a specific range of operation. The variables controlled were the chamber pressure and the chamber temperature. The pressure was controlled by varying the turbopump speed and the temperature was controlled by varying the power level. The beginning of the startup transient and the end of the shutdown transient involved some preset manipulation of the controllers. This was done to ensure stable operation of the reactor during these phases. New control strategies, such as the MIT/SNL method, should allow control over the range of the operating map and be able to yield the desired temperature and pressure performance from the rocket engine. The temperature controller implemented in ENGTRANS utilizes the MIT/SNL control logic to place the reactor on the required periods to obtain the desired ramp rate. Instead of the usual fixed ramp rate for the power, the power must be adjusted for the chamber temperature behavior due to the heat capacity of the fuel and system. This controller and some design considerations that affect its performance are described in section 4.3.2.2. The pressure controller implemented in ENGTRANS is similar to that used in the NERVA program. It is discussed in section 4.3.2.3.

4.3.2.2 Chamber Temperature/Reactor Power Control Model

The nozzle chamber temperature control is based on the premise that for a constant flow rate and core inlet temperature, the change in outlet temperature is proportional to the change in reactor power. The desired temperature is determined from the user input transient temperature trace. The desired temperature is used along with power calculations to determine the desired power trajectory. Ultimately, the control module output is a desired control drum position, which the power calculations require. The determination of the control drum position is as follows:

1. The desired nozzle chamber pressure and temperature are used to determine the desired nozzle flow rate and desired heat power of the reactor.

2. The ratio of the desired power to the actual power is used as one portion of the desired reactor period. The ratio of the desired temperature to the actual temperature is used as the other portion of the control signal. The latter is used to ensure faster response to the temperature demand and to ensure that the steady state conditions reach the desired levels. For this study, a signal combination of 5% power and 95% temperature was selected as the final mix.
3. The inverse reactor period is also determined as a combination of the "measured" neutron power period and the "measured" chamber temperature period. The temperature signal is used to ensure the rate of rise of the temperature is not excessively fast. Currently the simulation uses a mix 50% neutron and 50% temperature signals.
4. The desired reactor period is used in the MIT/SNL control logic to determine the desired rate of change of inverse period. This value is constrained, so that the shortest period demanded is 0.1 seconds. A constraint on the maximum power allowed is also checked and the demanded period is adjusted so this power will not be exceeded.
5. Equations 2.90 and 2.91 are used to determine the desired rate of change of reactivity and the desired control reactivity.
6. The desired control reactivity and rate is converted into a desired drum position and rotation speed from the drum worth relation. If the desired speed is more than the user defined maximum, the rate is capped at this maximum and the desired position is limited to that reached in the next time step from the maximum rate.
7. The desired control drum position is used as the output of the controller and the drum rotation response delay is applied to this output to determine the actual drum position to be used for the next calculation step. The user defined delay variable CRDLAM is the λ_{CRD} term in equation 2.99.

The impact of the control drum response speed and the drum rotation speed is an important consideration for the design of the rocket engine system. A simple throttle back to 75% thrust case was used to show the effect of different delay constants on the system response. The drum speed for these runs is capped at 10 degrees/second, as was used in the NERVA program[W-6]. The transients were run with the user defined variable CRDLAM equal to 2.0, 20.0, and 200.0. The controller for this case used 99% temperature signal and 1% neutron power signal for the desired period calculations. Figures 4.17 through 4.20 clearly show that a fast responding control drum actuators are desired. (Table 4.6 provides definitions for the legend variables in these and all the transient plots.) The CRDLAM equal to 2.0 case is unstable and unsatisfactory. This is due to the feedback mechanisms of the core trying to hold the temperature constant during the downpower. The transient begins with the demanded pressure to ramp from 3.8 MPa to 2.85 MPa in three seconds. The TBCV valve opens to reduce the turbine drive flow and thus the pump power. The opening of the control valve causes the bypass flow to increase and the total flow to decrease. The reactor power must also be lowered in order to maintain the temperature at 2275 K with the lower system flow rate. The pressure reduction helps to lower the power some, due to the positive hydrogen mass reactivity coefficient, but the control drums must also be rotated inward. The faster responding drums are able to maintain the temperature with minimum oscillation. The slowest drums do not lower the power quickly enough, so the chamber temperature rises about 25 K above its setpoint. Once the desired pressure is reached at t=4 seconds the power transient must also be terminated. The drums must be rotated outward to terminate the transient at the desired power level and to counter the decay of the delayed neutron precursors. The faster rods are able to compensate for this effect as well as the nozzle temperature perturbations relatively quickly. The CRDLAM equal to 20.0 case has some oscillations, but these die out within ten seconds of reaching the throttle point. The CRDLAM equal to 2.0, however continues to drive the rods inward to reduce the nozzle temperature back to its setpoint. Once the setpoint temperature is met, the rods begin to rotate outward. Again, because of the slow drum response, the power to flow mismatch now tends to overcool the fuel, thus the power must be raised higher to bring the temperature back up. Because the reflector power is dependent on the reactor power, the turbine inlet temperature also changes. This affects the turbine flow requirements, so the TBCV must be manipulated to maintain the constant nozzle chamber pressure. This process continues until, at the end of the case, the drums are rotating at their maximum speed and the power is reaching its maximum power constraint level. The order of the phasing of the parameters is: 1) the control drums rotate, 2) power responds nearly in phase with the rod motion, 3) the reflector power changes to affect the turbine inlet temperature, 4) the TBCV moves in phase with the turbine inlet temperature as does the bypass flow rate, 5) the turbine flow is 180 degrees out of phase with the bypass flow, 6) the nozzle chamber temperature lags the power rise due to the thermal inertia, and 7) since the pressure is nearly constant, the total flow rate is approximately 180 degrees out of phase with the chamber temperature. Because the system pressure response has fewer system lags and the TBCV actuator is fast enough and independent of the temperature, the nozzle chamber pressure is not affected by the power and temperature perturbations.

Table 4.6 Transient Plot Legend Variable Definitions

Variable	*Definition*
CRD	Control Rod Drum Position
PJ23	Junction 23 Pressure (i.e. chamber pressure)
TJ4,-7,-13,-23	Junction 4, 7, 13, 23 Gas Temperature
P-,T-,Wdmd	Demanded Pressure, Temperature, Mass Flow Rate
TBCVx	Turbine Bypass Control Valve Travel
Qtote, Qprmpt	Total Effective and Prompt Neutron Thermal Power
Thrust	Nozzle Exit Thrust
Isp1, Isp2	Specific Impulse as calculated by Eqs. 2.55 and 2.56
Wtot,Wbyp,Wturb	Total, Turbine Bypass, and Turbine Mass Flow Rates

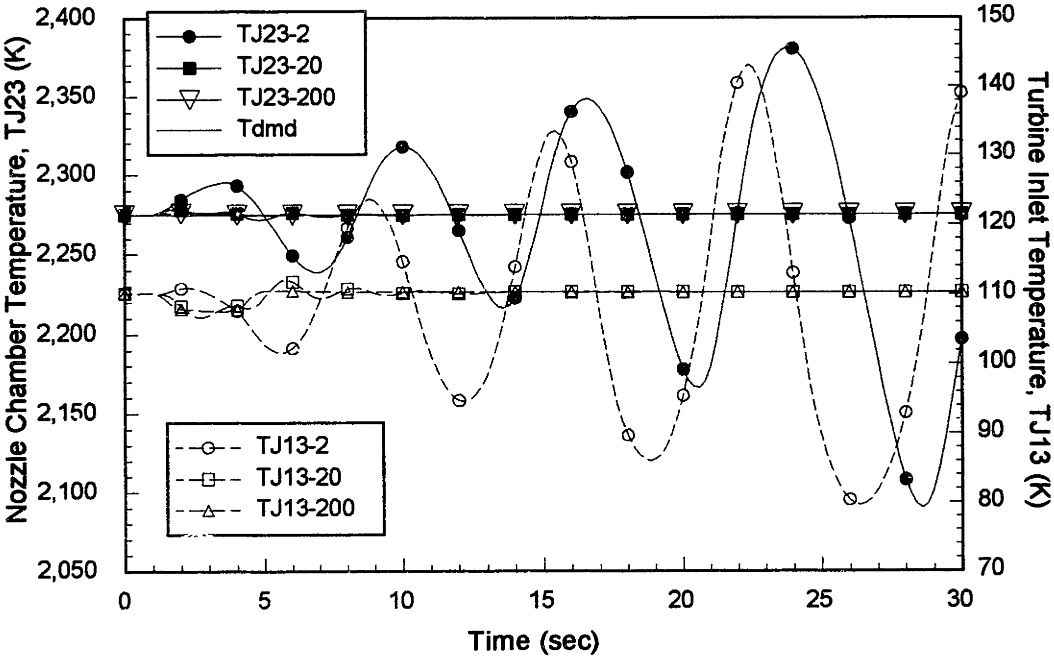

Figure 4.17 Temperature Response During Throttle to 75% with Different CRDLAM's

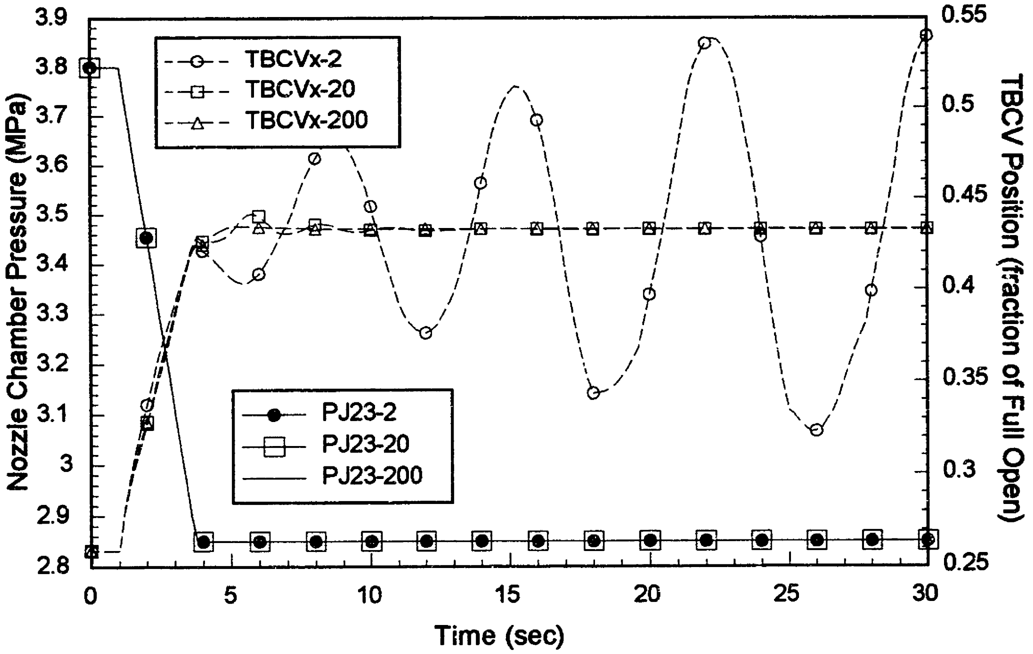

Figure 4.18 Pressure and TBCV Position Response During Throttle to 75% with Different CRDLAM's

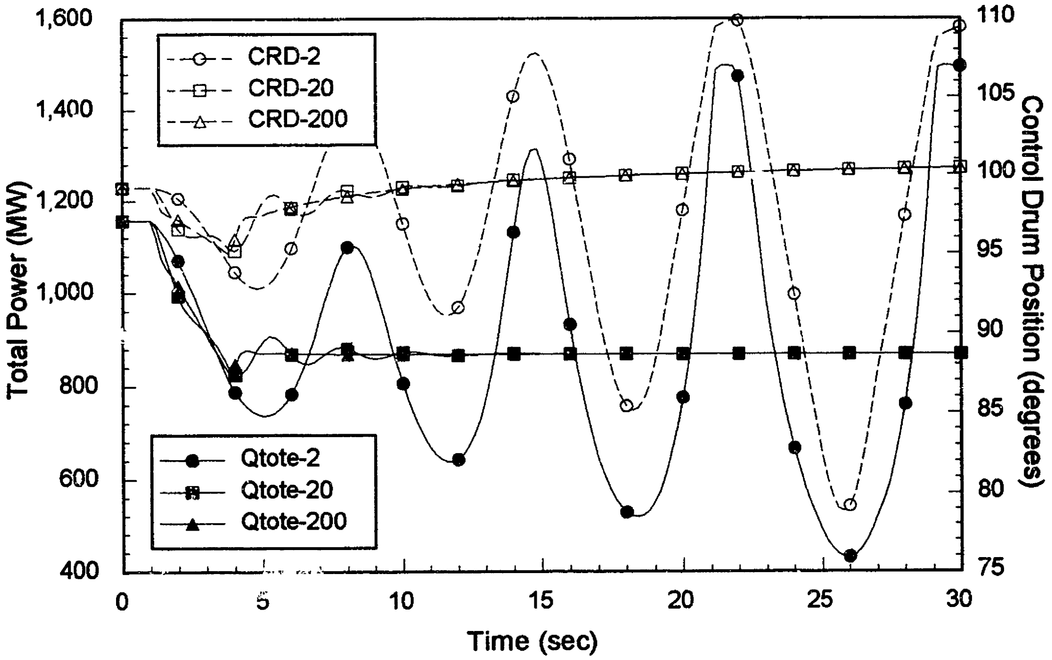

Figure 4.19 Power and CRD Response During Throttle to 75% with Different CRDLAM's

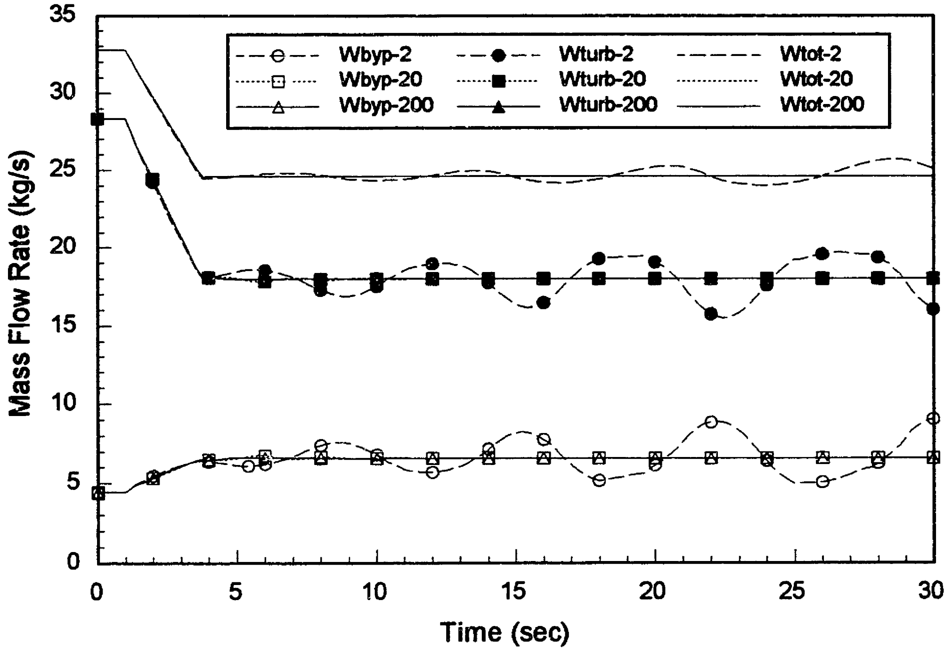

Figure 4.20 Mass Flow Rates Response During Throttle to 75% with Different CRDLAM's

The ENGTRANS code can be used to show the impact of control drum rotation speed on the control and behavior of the rocket system. Because the MIT/SNL control laws depend on the rate of change of reactivity, the drum speed is an important parameter. The drum speed used in the NERVA program was 10 degrees/second and this was found to be sufficient for downpower maneuvers, but insufficient for uppowers. If the drums are limited in their speed, the demanded and actual periods begin to be too far out of phase and then the thermal lag feedback will cause the system to go on radical power swings. Recent work has been completed on a proof of concept design for an actuator that is able to move the drums at 180 degrees/second, which is better for the implementation of the MIT/SNL control laws[T-3]. The effect of using these two rod speeds is shown in Figures 4.21 through 4.24 for a simulated uppower ramp on a NERVA engine. Two case were run with rod speeds of 10 degrees/second and they are labeled "-99/01" and "-50/50" suffixes. These stand for the demanded period calculated with temperature signal portions of 99% and 50% respectively. The 180 degrees/second drum speed case run with 99% temperature signal is labeled as "-180" in each of the figures. The cases run with the maximum rod speed of 10 degrees/second make it through the transient, but the power behavior is clearly undesirable. The faster rod speed shows a much smoother trace and the temperature follows the demanded trace more closely.

The temperature transient involves a step change in the demanded nozzle chamber temperature from 750 to 800 K and then ramps from 800 to 1000 K in 5 seconds and 1000 to 2275 K in 14 seconds. The pressure transient involves a ramp from 700 to 1700 kPa in 19 seconds and then a rapid ramp from 1700 to 3800 kPa in 6 seconds. The temperatures in Figure 4.21 show that the control needs to have a higher temperature portion of the signal to have the temperature reach the desired endpoint within a reasonable amount of time. (Cases were run with signals of 50/50 for faster rod speeds to determine if this would improve the temperature response, but they did not.) For the slower rod speed, the temperatures oscillates around the desired trajectory, because the rod motion can not keep up with the demanded speed and position required for the power trajectory. The turbine inlet temperature trend follows the trend of the power transient due to the power input to the nozzle and reflector. The temperature trend for the 50/50 control is smooth mainly due to the slower power response. The pressure response shown in Figure 4.22, like for the CRDLAM variation cases, follows the demanded trajectory very well. The oscillations in the pressure for the 99/01 case occur as the temperature is crossing over its demanded trajectory. The large spike at the lower pressure is a combination of the power controller limiting the reactor period and the temperature crossing the trajectory line. The major parameter affected by the rod speed is the reactor power. As shown in Figure 4.23, the drums in the 99/01 case must rotate at maximum speed in both directions in order to try to bring the nozzle chamber temperature along the desired path. Because the rods can not move fast enough, power overshoots and undershoots are required. During the second and third uppower ramps the power reaches the maximum constraint and the controller is able to stop the power rise and maintain it at this level until the power is required to be reduced. Once the final pressure ramp is over, the system is able to settle down to the new steady state value within 5 seconds. For the fast drum speed, the power is able to the manipulated quickly enough to bring the temperature along the trajectory path and finish the ramp with less than 50 K overshoot for less than 5 seconds. The initial short period is required to handle the step change in the demanded temperature. Another startup scheme could eliminate the step change and simply ramp the temperature from one point to the next. This would eliminate the need to have a sharp initial power rise. The total and bypass flow rates are shown in Figure 4.24. The spike in flow is a result of the spike in pressure explained before. At lower pressure and temperature, the mass flow rate through the nozzle is more sensitive to small changes in these parameters, as is shown by the perturbations at the beginning of the transient. The controllers are able to handle these perturbations and eventually return the system to a more stable transient. Some of these effects may also be due to the hydrogen properties, both physically and numerically.

In the last few paragraphs, the control drum response time and rotation speed have been shown to be important considerations for the design and control of the rocket engine systems. The versatility of the transient code has also been shown by allowing the study of these impacts on the control of the power and temperature. The CRDLAM value selected for use in later transients is 20.0 with drum speeds of 10 degrees/second for the NERVA throttle and shutdown studies and 180 degrees/second for the NERVA startup and all the PBR cases. In the next section, a study of the impact of the TBCV positioning response time on the pressure control is presented.

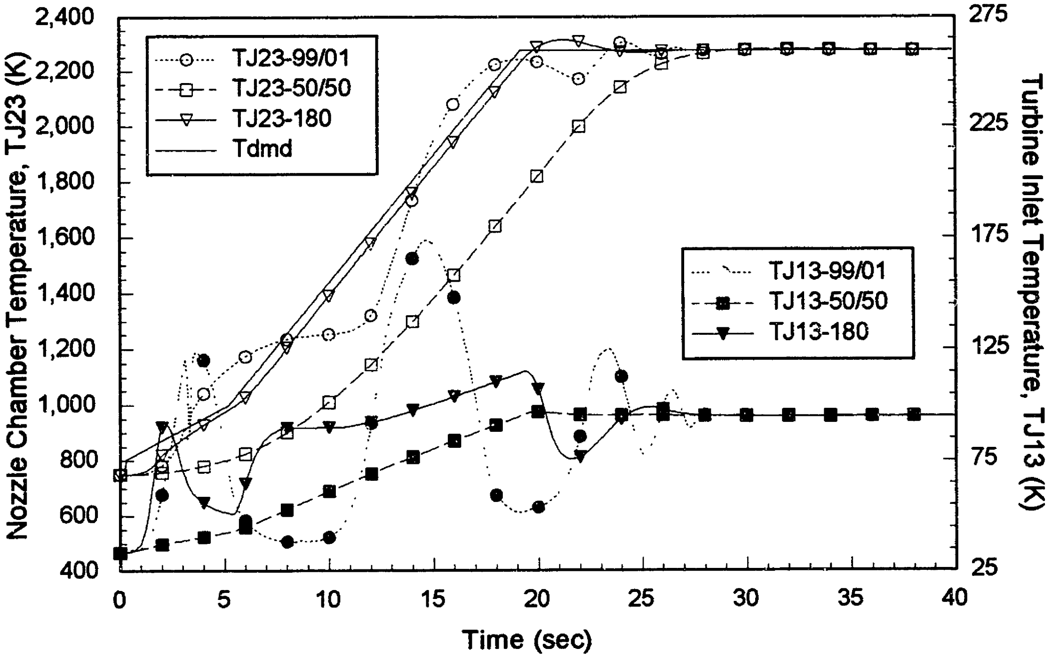

Figure 4.21 Temperature Response to Uppower with Different Control Drum Speeds

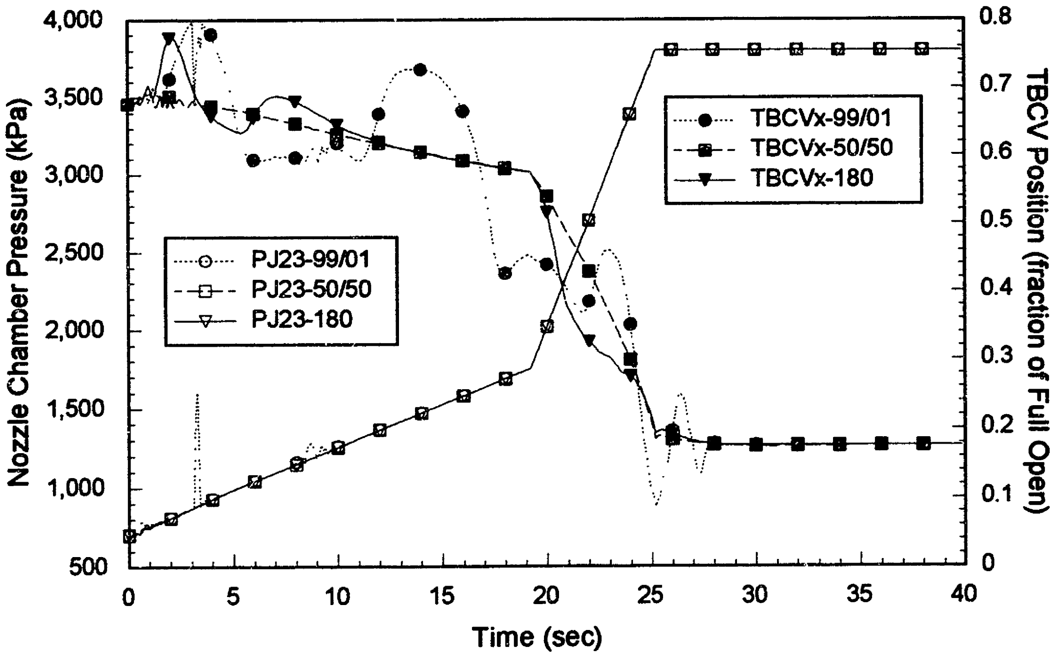

Figure 4.22 Pressure and TBCV Position Response to Uppower with Different Control Drum Speeds

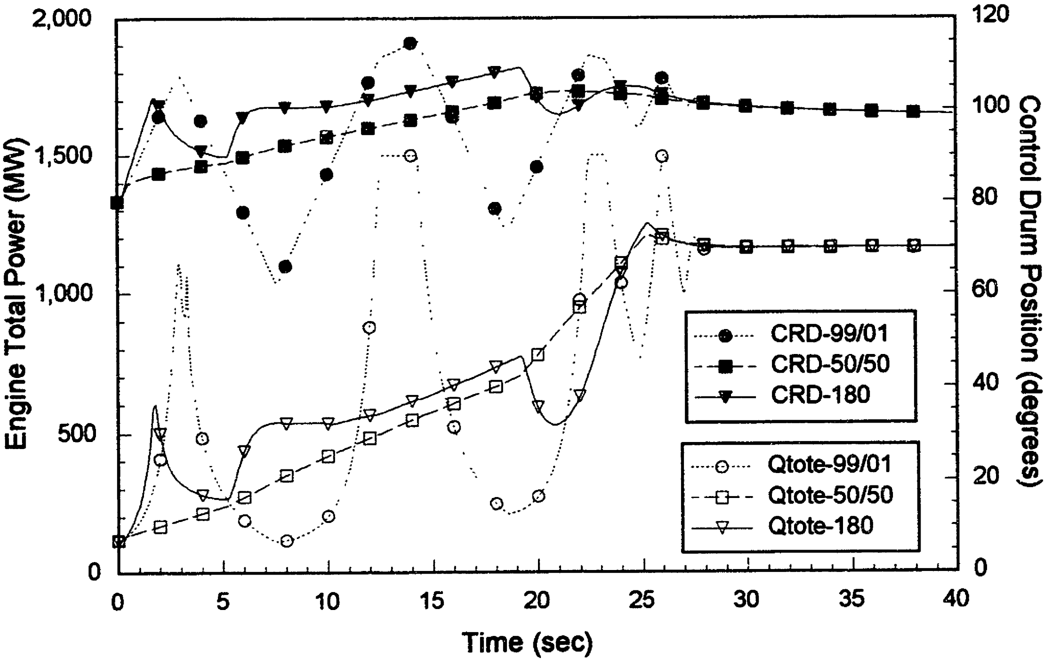

Figure 4.23 Power and CRD Response to Uppower with Different Control Drum Speeds

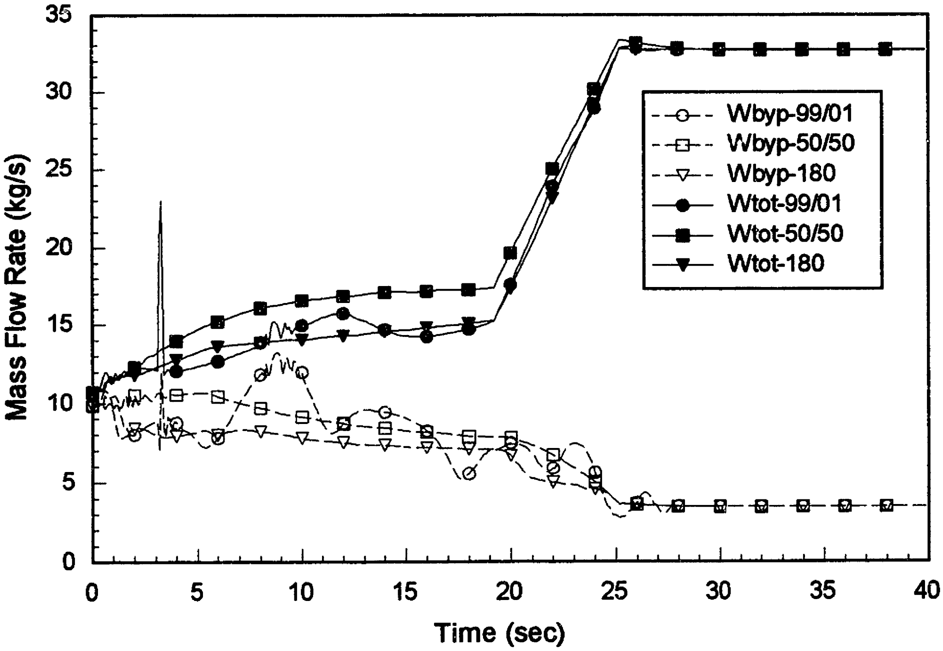

Figure 4.24 Mass Flow Rate Response to Uppower with Different Control Drum Speeds

4.3.2.3 Chamber Pressure Control Model

The nozzle chamber pressure control is implemented as a simple feedback controller. The "desired" pressure is determined from the input transient trace. The "actual" pressure is taken as the Junction 23 pressure calculated by the simulation. For a constant fluid density, the mass flow rate is nearly proportional to the pump rotation speed and for a constant nozzle chamber temperature, the mass flow rate is nearly proportional to the nozzle chamber pressure. Using these assumptions, the chamber pressure is then proportional to the pump speed. The process to determine the desired and actual TBCV position is as follows:

1. The ratio of the desired pressure to the actual pressure is used to determine the desired pump speed from the actual pump speed.
2. The pump speed is used to calculate the pumping power and the requisite turbine power.
3. The turbine power is used to determine the desired turbine mass flow rate assuming the same hydrogen state properties exist.
4. The desired bypass flow is found from the difference of the total mass flow and the desired turbine flow.

5. The desired bypass flow is used in conjunction with the hydrogen properties in the bypass line and the user defined TBCV valve resistance to determine a desired valve position.
6. The desired valve position is used as the output of the controller and the valve travel response delay is applied to this output to determine the actual valve position to be used for the next calculation step. The user defined delay variable VLVLAM is the λ_{TBCV} term in Equation 2.78.

The effects of the valve response time capabilities can be shown be varying the valve response delay constant, VLVLAM. The 3 second throttle to 75% transient was run with VLVLAM equal to 0.1, 1.0, and 10.0 to graphically show the effects. The cases were run with the maximum control drum speed at 10 degrees/second and CRDLAM equal to 20.0. The Figures 4.25 through 4.28 show that the impact of the TBCV response is not as important is the control drum response characteristic. The slowest TBCV response causes the pressure to reached the desired throttle position approximately 2 seconds late. The fastest responding TBCV causes the control drums to have to rotate more frequently and to oscillate about the smooth trace of the middle response speed. This is due to the effects of the positive hydrogen mass reactivity coefficient. The figures indicate that system design must consider the interrelations of the controllers and behavior of the entire system in order to assure stable operation.

The nozzle chamber and turbine inlet temperature traces are shown in Figure 4.25. The chamber temperature initially increases due to the flow reduction and thermal inertia of the reactor. The turbine inlet temperature decreases as the power decreases. Once the pressure is at the throttle point, the temperatures proceed to their new steady state values. The chamber temperature for the middle response speed case promptly turns at the 4 second point from a 10 K overshoot and returns to the 2275 K setpoint value with only a 2 K undershoot. The turbine inlet temperature returns to nearly the same temperature due to the lower flow rate through the reflector. Figure 4.26 shows the pressure and TBCV position behavior during the transient. The pressure in the two faster response cases follows the demanded pressure ramp exactly, while the slower response case clearly does not. For the fastest response case, the TBCV must compensate for the turbine inlet temperature swings in order to hold the chamber pressure constant. The other cases respond more smoothly due to the smoother power response. The power and control drum response are shown in Figure 4.27. The power is dropping more quickly because the initial chamber temperature rise is slightly faster than the middle case. The temperature rise is faster due to the quicker reduction of the pressure and flow. This causes the controller to demand the power to drop more quickly and drives the control drums inward faster. As the temperature turns, the drums react to try and hold the temperature. The result is that the temperature over- and undershoots are kept to less than ± 4 K, but because the drum speed is too slow to properly follow the temperature changes, it oscillates more. The drums must continue an outward rotation to counter act the decay of the delayed neutron precursors. The final position is slightly greater than the original position due to the lower pressure. For these cases, the mass reactivity coefficient is 0.001 dk/k/kg. If a higher coefficient was used, the change in position would be greater. The total and turbine mass flow rates are depicted in Figure 4.28. Because the chamber temperature is held nearly constant, the mass flow rate follows the pressure trends. At the end of the throttle, the turbine flow rates oscillate slightly for the fast response case in order to compensate for the turbine inlet temperature swings.

In all cases, the controller is able to hold the parameters at the desired levels with no oscillations occurring after approximately 10 seconds from reaching the throttle point. The controller for the pressure is shown to bring the pressure along the desired trajectories under various response times. The study on the response time also shows that consideration must be given to the effects that the pressure control response time has on the temperature control and system transient behavior. The VLVLAM selected for use in cases later in this report is 5.0. This was found to yield adequate response without requiring faster control drum response times.

This concludes the study of the controller response times and their impact on the system behavior. In the next sections the analysis of the NERVA engine is performed to benchmark the engine codes. The ENGTRANS engine code is also used to analyze prototypic uppower and downpower transients on the PBR rocket concept. The results will be shown graphically, as was done in this section, to better show the behavior of the important parameters.

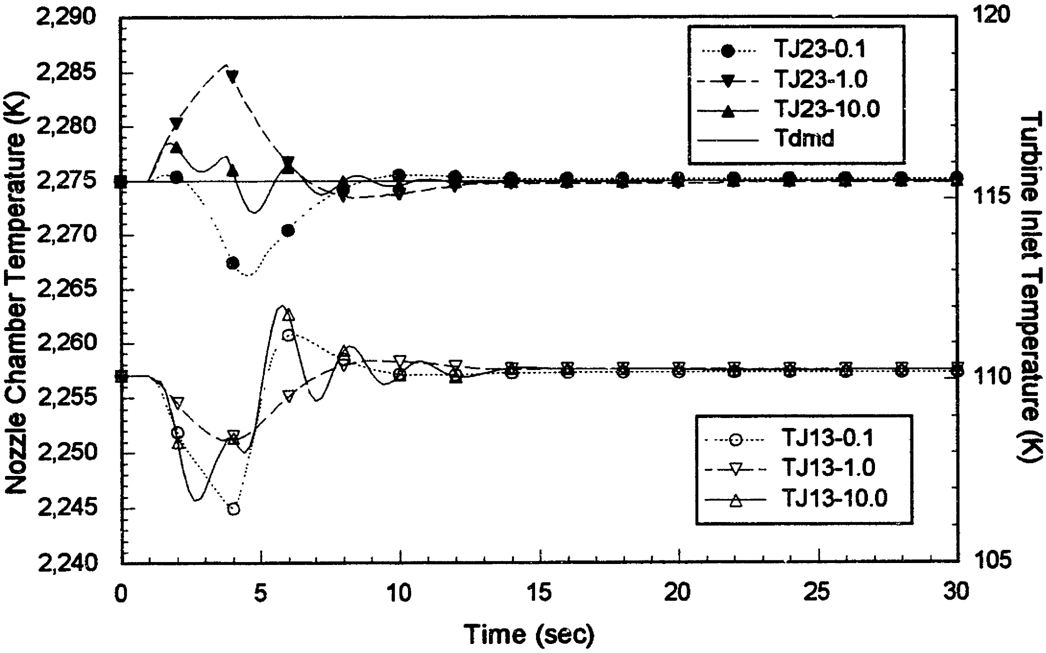

Figure 4.25 Temperature Response During Throttle to 75% with Different VLVLAM's

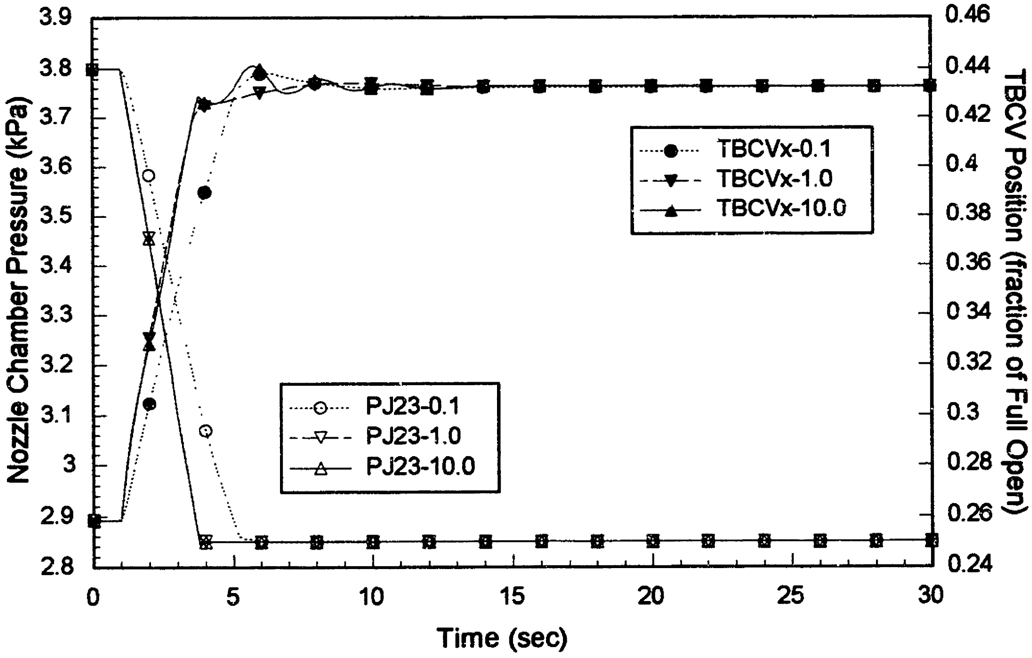

Figure 4.26 Pressure and TBCV Position Response During Throttle to 75% with Different VLVLAM's

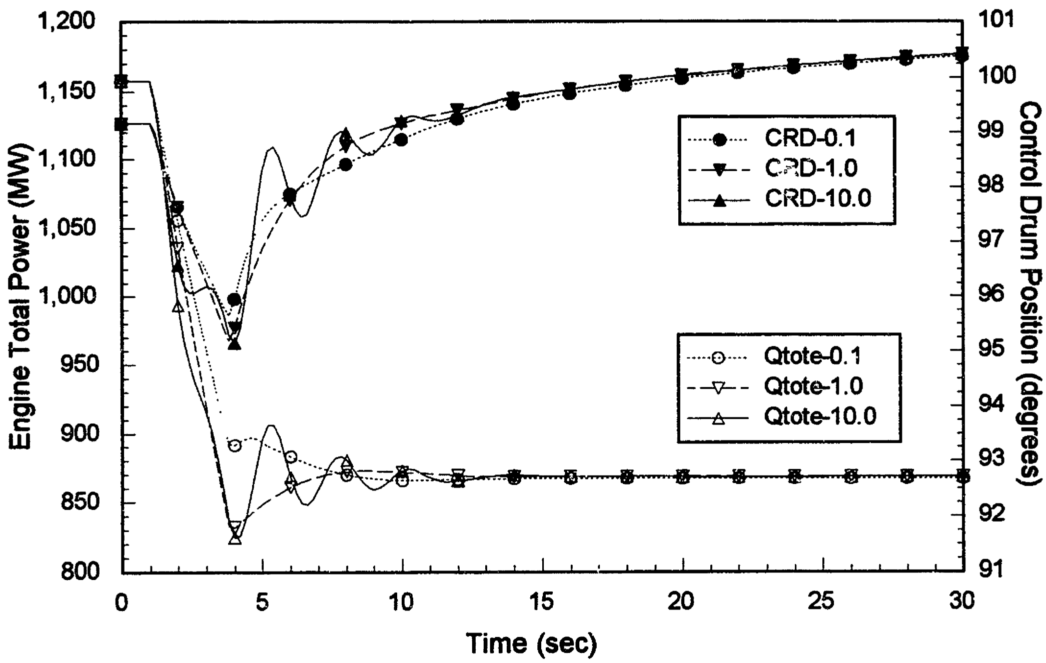

Figure 4.27 Power and CRD Position Response During Throttle to 75% with Different VLVLAM's

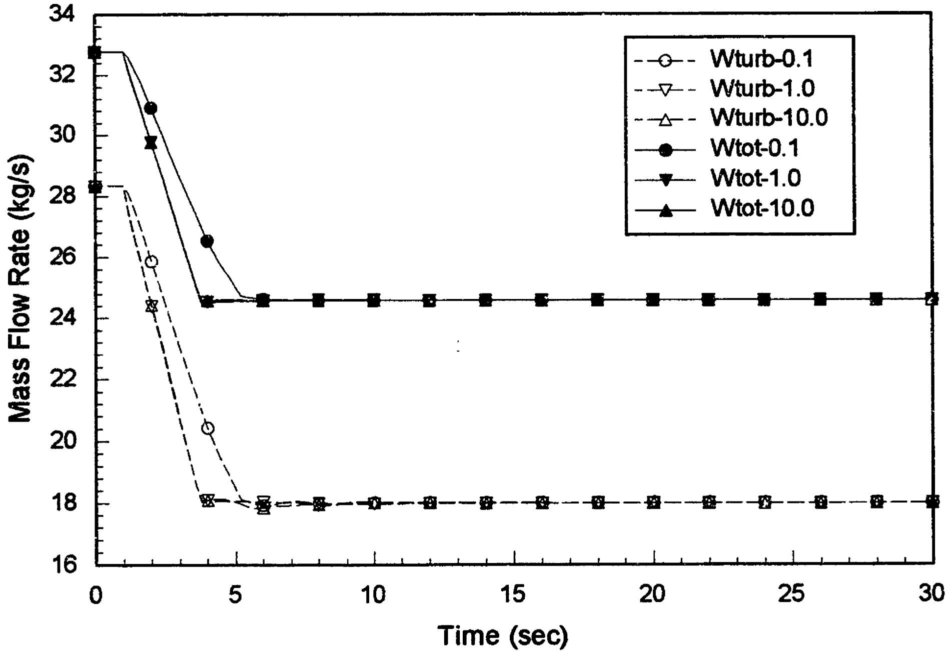

Figure 4.28 Mass Flow Rate Response During Throttle to 75% with Different VLVLAM's

4.3.3 NERVA Engine

4.3.3.1 Introduction and Benchmark Strategy

As was performed for the steady state cases, it is desirable to compare the transient model to available data from the NERVA program. Reference [W-6] provides several graphs of reactor parameters for startup and shutdown scenarios. Data points from these curves are plotted against the ENGTRANS results for similar transients. The Reference [W-6] profiles were used as the temperature and pressure traces for the ENGTRANS simulations of an engine with a similarly sized reactor. While the reactor flow paths and engine cycle are different, a comparison of the parameter trends can show that the ENGTRANS code is capable of providing results consistent with other more detailed models. A shutdown case from a power level of 50% was also run using the engine size of Reference [C-3] to show the versatility of the code. Throttle transients to different power levels for this lower power engine are also presented to show the ability of the code to follow rapid and large demanded transients.

4.3.3.2 NERVA Startup Transient Evaluation

The Reference [W-6] startup ramps were used as the basis for the ENGTRANS inputs. The reference startup consists of a 7 second bootstrap phase in which the control drums are rapidly rotated outward to raise the power. The rise in power increases the system temperatures and enhances the capability of the turbo-pump to drive the flow. At the end of the first ramp, the temperature and pressure have reached the point that they can be controlled in closed loop mode. The second trajectory is an 18 second ramp of the chamber temperature from 600 K to the rated 2360 K and a chamber pressure ramp from 400 kPa to the throttle point of 2015 kPa. The final trajectory is a 3 second ramp of the pressure from 2015 kPa to the rated 3100 kPa while holding the temperature constant. For the ENGTRANS case, some modifications had to made to these trajectories. This was partly due to the mode of control of the system and partly due to the engine design configuration. In the design modeled in this report, the only place heat is added to the system before the turbine is through the inefficiency of the pump and the cooling of the nozzle and reflector. For startups, this causes the hydrogen to be in a low temperature regime. Besides the problem of the hydrogen switching from liquid to a gas phase, the properties also undergo rapid changes. As was shown in Figure 2.18, the heat capacity of hydrogen changes dramatically at low temperatures. As the temperature reaches the saturation temperature for a given pressure, the heat input changes the gas from liquid the gas while holding the temperature constant. Once the hydrogen is in the gas form, the temperature will rapidly increase for the same amount of heat input, due to the rapid decrease in the heat capacity. This causes problems during the startup because the turbine power increases with increases in the inlet temperature. The TBCV ramps open quickly to limit the turbine flow, but the increase in temperature increases the system flow. This perturbation permeates though the system, as then the reactor temperature control must react to the flow changes. If some other heat source existed in the piping (e.g. latent heat) or the flow was split before the nozzle cooling, the temperature at the turbine inlet would be greater and control would be more stable. The Reference [W-6] curves indicate that there was some preheat, because the reflector and core inlet temperatures start the transient at 300 K and decrease over the course of the startup to 150 K. These temperatures are well above the temperatures determined by ENGTRANS. To avoid some of these problems and to have a higher temperature entering the reflector, the startup ramp was commenced at a higher pressure and temperature level.

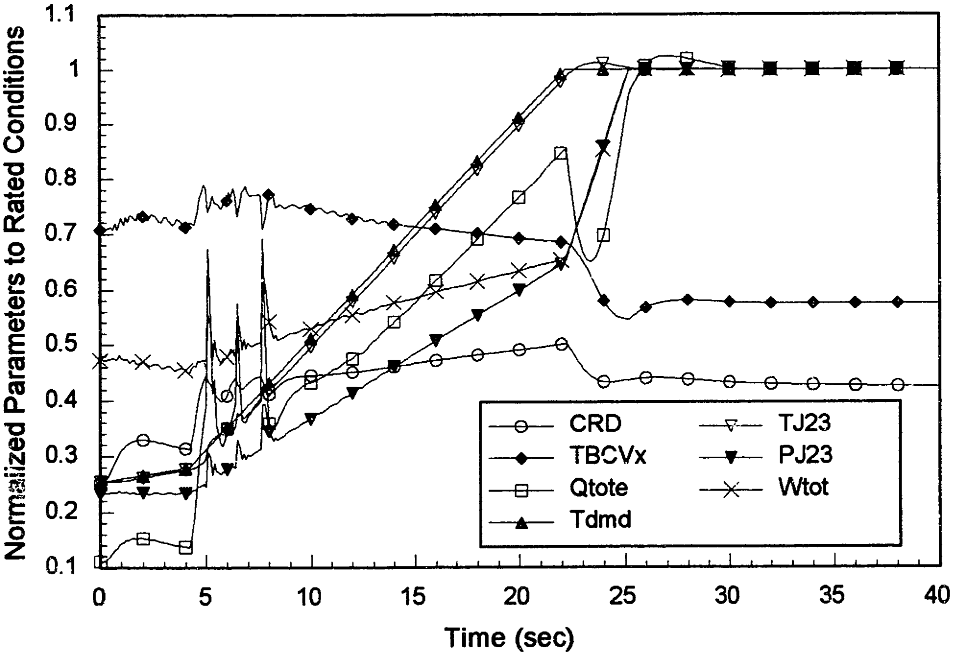

Figure 4.29 Reference [W-6] NERVA Engine Response to Startup Transient

The startup studied for the Reference [W-6] based NERVA reactor, consists of a slow 4 second ramp in temperature from 700 K to 750K while holding the pressure constant at 750 kPa. The second ramp is a 18 second ramp of the temperature to its rated 2360 K level while the pressure is ramped to the 65% throttle point of 2015 kPa. The final ramp is the same as the Reference [W-6] ramp that brings the pressure to its rated level of 3100 kPa in 3 seconds. The startup transient response is shown in Figure 4.29. A full listing of the input file used for this run is given in Appendix A. The parameters show good behavior, except for a 3 second period at the beginning for the second ramp. The spikes during this time frame are in part numerical due to the rapid power change demanded and in part physical due to the hydrogen properties at these temperature and pressure conditions. The controllers are able to bring the system back to a stable startup trajectory once the hydrogen temperatures have passed through the saturation point. This number of spikes was not noticed in the transients run in Section 4.3.2.2, but the changes in engine rating and control make the effect more pronounced. Figure 4.29 also shows that the trajectories are able to be stopped at their respective demanded hold points with little overshoot.

During the first ramp the flow rate decreases as the chamber temperature increases. The control drums rotate quickly outward to start the power ascension and as the temperature begins to increase, the power rise can be slowed. The drums must be slowly rotated inward to keep the temperature on the proper ramp rate. The second ramp also includes an initial outward rotation of the control drums to bring the power and chamber temperature on the desired trajectory. As the power rises, the heat load on the reflector is increased, so the hydrogen changes phase in the reflector and causes a rapid rise in the turbine inlet temperature. This increases the turbine power and therefore the system flow. The increase in flow reduces the chamber temperature, so the flow increases and the demanded power rises. The TBCV cycles open rapidly to counter the turbine inlet temperature rise and the drums also rotate out quickly to raise the chamber temperature. This continues until the reflector temperatures are above the saturation point. Because the hydrogen properties routine are a set of overlapping tabular regions, some discontinuities may exist between the saturation curves and the gas curves, which can then cause some of the perturbations as well. At the 8 second point in the transient, the system has stabilized and the parameters behave more as expected. The TBCV cycles shut to increase the pressure while the drums continue to rotate outward to bring the power and temperature along the demanded trajectory while the flow is increasing. Once the temperature hold point is reached, the rods are rotated rapidly inward. This cuts the power so that the temperature will hold at 2360 K with little overshoot. The pressure now must rise to its rated level in 3 seconds so the TBCV rapidly cycles closed. The increase in flow requires that the power increase to hold the chamber temperature constant. The drums must rotate out a few degrees, but the positive hydrogen mass reactivity coefficient adds reactivity as the pressure increases. When the pressure hold point is reached, the drums and TBCV adjust to the system temperatures and the delayed neutrons reaching their rated steady state conditions. While the transient is not exactly the same as the Reference [W-6] startup, the ENGTRANS code does yield similar trends. A detailed presentation of the startup is shown in Figures 4.30 through 4.35. The Reference [W-6] values for the temperature, pressure, power and mass flow rate are plotted on these as a means for comparison.

The chamber, turbine inlet, and Junction 4 and 7 temperatures are shown in Figure 4.30. The Junction 4 temperature holds nearly constant during the first ramp, because the chamber pressure is being held constant. The pump inefficiency and work done on the fluid causes the temperature to rise, but it is only 2 K above the tank temperature. The Junction 7 temperature increases only slightly and remains near the saturation critical point as the nozzle temperatures and power increase. The turbine inlet temperature is affected by the power in the reflector. As the reactor power increases and decreases to bring the chamber temperature along the desired path, the turbine inlet temperature also rises and falls. The chamber temperature is able to reach the desired ramp about 2 seconds into the transient, but at the beginning of the second ramp, the chamber temperature lags behind the demanded trace due to the increase in flow from the now increasing chamber pressure. The power period shortens as the temperature falls further behind and this causes a sharp rise in the reflector temperature rise, due to the hydrogen properties behavior. The Junction 7 temperature also increases due to the increase in nozzle temperature and power loading on the nozzle. The Junction 4 temperature increases later when the pressure rapidly increases from the increase in turbine power. The controller acts to limit the chamber temperature rise once it reaches the desired trajectory and this causes a cut back in the drum rotation. This continues through the next 3 seconds as the chamber temperature cycles between being on track and falling below the desired trace. The turbine inlet temperature reacts to the power changes occurring to hold the chamber temperature. The Junction 7 temperature proceeds to increase through the region close to the critical temperature. The critical temperature is reached somewhere in the reflector at this point of the transient. The hydrogen temperatures have stabilized, the transient proceed along a smoother path. The Junction 4 temperature increases as the pressure increases. When the final pressure ramp is commenced, this temperature increases more rapidly, but not proportional to the pressure increase due to the changing pump efficiency from the homologous pump curves. The Junction 7 temperature increases at slightly higher rate because the flow stream picks up additional heat from the nozzle cooling. The turbine inlet temperature continues to increase as the power to the reflector increases. At the end of the temperature ramp, the inlet temperature decreases rapidly while the pressure and system flow are increased. The junction regains some of its value once the pressure ramp is over and the reflector material move towards its final steady state temperatures. The chamber temperature has a slight overshoot of approximately 60 K due to the thermal lag of the reactor fuel. The system reaches steady state within 5 seconds of completing the pressure ramp. The curve shows that the Reference [W-6] temperature ramp is slightly faster due to its lower starting point. The reference temperature also does not meet its desired temperature until after the pressure ramp is over. This shows that there may be some advantage to the proposed method of control, since that the demanded temperature can be met at the required time. However, issues on the initial cold start must be resolved.

The chamber pressure and TBCV position responses are given in Figure 4.31. The pressure follows the demanded curve except for the 3 second period just after the second ramp begins. During the first temperature ramp, the TBCV must cycle about 1% of travel in order to compensate for the fluctuations in the chamber pressure. The fluctuations are small, but at these values of pressure, the small changes are on a relative scale, large. This causes the flow rate to fluctuate by the same proportion. The TBCV must compensate for the changing turbine inlet temperature and the changing relation of turbine flow to bypass flow needed to drive the system flow. The turbine inlet effect can be seen by the trend average rise and fall and the mass flow compensation is seen as the oscillation about the mean. When the turbine inlet temperature increases rapidly at the 5 second point, the TBCV cycles open rapidly. Then as the system recovers from this large perturbation, the TBCV acts to regain control of the pressure. Because the system also has power and temperature perturbations and the controller is acting independently to bring the pressure along the demanded track, the TBCV overcompensates. The large spikes downward, coincide with when the chamber temperature crosses the demanded line. This is required because the flow rate is demanded to be large to bring the pressure up to its demanded level and the cut the temperature rise. After the major perturbation period is over, the TBCV continues to react to small flow oscillations due to the low pressure flow effects. The general trend is to close the bypass valve because the required turbine flow increases. During the pressure ramp, the TBCV must cycle shut rapidly to put the required amount of drive flow to the turbine. At the end of the pressure ramp, as the turbine inlet temperature recovers from the reflector overcooling, the TBCV cycles open because the amount of turbine flow now required is less due to the increased inlet temperature. The system response stabilizes within 5 seconds of the end of the pressure ramp. The Reference [W-6] pressure is shown for comparison. The first and second ramps do not match, due to the different start points, but the final ramp and hold level do match.

Figure 4.32 presents the engine powers and control drum position response during the transient. Initially the drums rotate out quickly to bring the chamber temperature up to its desired trajectory. The demanded reactor power is determined to overcome the thermal capacitance of the fuel and raise the chamber temperature. The ENGTRANS reactor core model is comprised entirely of the fuel element geometry while the Reference [W-6] includes structural components in addition to the fuel elements. This changes the response of the power and temperature. Also because the reference pressure is lower, the required power in Reference [W-6] is also lower during the first transient ramps. The control drums rotate inward slightly as the power required to maintain the temperature ramp is reduced. At the beginning of the second ramp, the drums rotate out quickly to put the reactor on the require period, but as the turbine inlet temperature responds, the rods must move further. The increase in flow from the turbine power increase lowers the chamber temperature, so the demanded power also increases. This continues until the power is rising fast enough to raise the temperature. Once the temperature is at the desired level, the drums rotate inward to cut the power, but then the temperature falls behind again and the power must be increased. As the perturbations are occurring, the control drums cycle to adjust to the flow variation impact on the chamber temperature and the resultant demands for the reactor period. After the perturbations, the drums continue to rotate outward to keep the power and temperature on the desired track. Once the temperature hold point is reached, the drums rotate in to halt the temperature rise and to balance the positive reactivity addition from the pressure increase. The thermal inertia of the system maintains the temperature near the hold level as the flow rate is increased with the pressure. Eventually the power must be increased to keep the temperature from undershooting the demanded level. The drums do not need to rotate very much in this case, because the reactivity added by the pressure increase is able to add most of the reactivity required for the demanded reactor period. Once the pressure ramp is over, the drums continue to rotate in slowly, because the demanded total reactivity continues to decrease as the delayed neutron precursors build in to their rated levels. The Reference [W-6] power profile shows the same trend of sharp distinctions during the transition from one ramp to the next. The differences in the first ramp are due to the different start transients, as the reference case needed to bring the temperature up over a larger distance. Both of the powers ramp back at the same time for the second ramp and the depth of the drop is the same. However, the reference case power must increase sooner because it has less inertial heat in the system, due to continually operating about 200 MW below the ENGTRANS simulation. By the end of the transient the effective total power and the Reference [W-6] power have reached the same value.

The reactivities are shown in Figure 4.33. The control reactivity reflects the rod motion explained in the last paragraph. The sharp increase at the 5 second point is due to the chamber temperature lagging the demanded curve and the turbine inlet temperature affecting the hydrogen mass in the core. The increase in turbine inlet temperature and decrease in density is reflected in the drop in the feedback reactivity. The control reactivity must compensate for this drop, in addition to increasing the total reactivity to raise the chamber temperature. Once the temperature requirement has been met, the feedback and total reactivity fluctuate as the system flow and the chamber temperature undergo their perturbations. The spikes in the total reactivity are those required to raise the temperature back up to the desired level at the time that the pressure is above the desired level. After the perturbations are over, the total reactivity is nearly constant as the required period is nearly constant during the second ramp of the transient. The feedback reactivity continues to decrease as the hydrogen and fuel temperatures increase, but the pressure increase helps to slow the rate of this change. Once the temperature is at the hold point, the feedback reactivity increases proportional to the pressure increase. The control reactivity must compensate for this increase in reactivity, while also adjusting the total reactivity required to maintain the temperature at the hold point. Within 5 seconds of the end of the pressure ramp, the feedback reactivity has reached its steady state value and thereafter the control reactivity must only compensate for the required reactivity changes to hold the operating conditions during the build in of the delayed neutron precursors.

The curves in Figure 4.34 depict the mass flow rate during the NERVA startup. The demanded flow rate decreases during the first ramp because of the increase in the chamber temperature. The actual flow remains somewhat above this level because the temperature is not at the demanded level and it fluctuates in response to the TBCV variations. Over the same time period, the Reference [W-6] flow is increasing rapidly due to different starting point and power ramp conditions. The second ramp is marked by the flow perturbations induced by the turbine inlet temperature and power fluctuations. The turbine flow shows large spikes due to the TBCV closure in response to the demand to increase the flow to lower the chamber temperature. If one looks closely, the total of the bypass flow and the turbine flow do not add up to the displayed total flow. This is explained by the sequence that the flows are calculated and output to file. The turbine and bypass flows are the flows from the current time step, while the total flow is the new flow to be used in the next time step's calculations, because it is determined at the end of the loop from the current time step chamber temperature and pressure conditions. After the perturbations, the actual flow parallels the desired trajectory on the high side because the chamber temperature lags the demanded trace by a small amount. The turbine flow increases during this ramp in order to provide the required turbine power. During the pressure ramp, the total flow increases along the demanded path. At this point the Reference [W-6] flow matches the ENGTRANS flow because the transient maps are the same. The turbine flow must rapidly increase to provide the turbine with enough energy to drive the system mass flow. The bypass flow decreases during this ramp in response to the required turbine flow and the TBCV closure. After the pressure hold point is reached, the turbine and bypass flows adjust to the changes in the turbine inlet temperature while holding the total flow constant. This adjustment is completed within 5 seconds of the end of the pressure ramp. The thrust and specific impulse are shown in Figure 4.35. The thrust is nearly proportional to the chamber pressure, therefore, its trace is nearly identical in shape to the pressure curve presented in Figure 4.31. The slight reduction in thrust during the first ramp is due to the decrease in hydrogen mass flow rate while holding the pressure constant. The specific impulse follows the trend of the chamber temperature during the course of the startup. The sharp increase in the Isp at the 5 second point of the transient follows the rapid increase in the chamber temperature as the turbine inlet and the core power both rapidly increase their levels. The thrust response indicates that the controller is able to bring the rocket thrust along very specific trajectories with little problem. The Isp also follows a specific path. Both these qualities would be of interest to the mission planner when developing rocket burns for s specific mission.

This concludes the NERVA startup transient simulation analysis. While the ENGTRANS simulation displayed some limitations for startups from low power, it was able to model the rapid temperature ascension and thrust build up. The next sections will show the capabilities of the computer model under several simulated throttle transients.

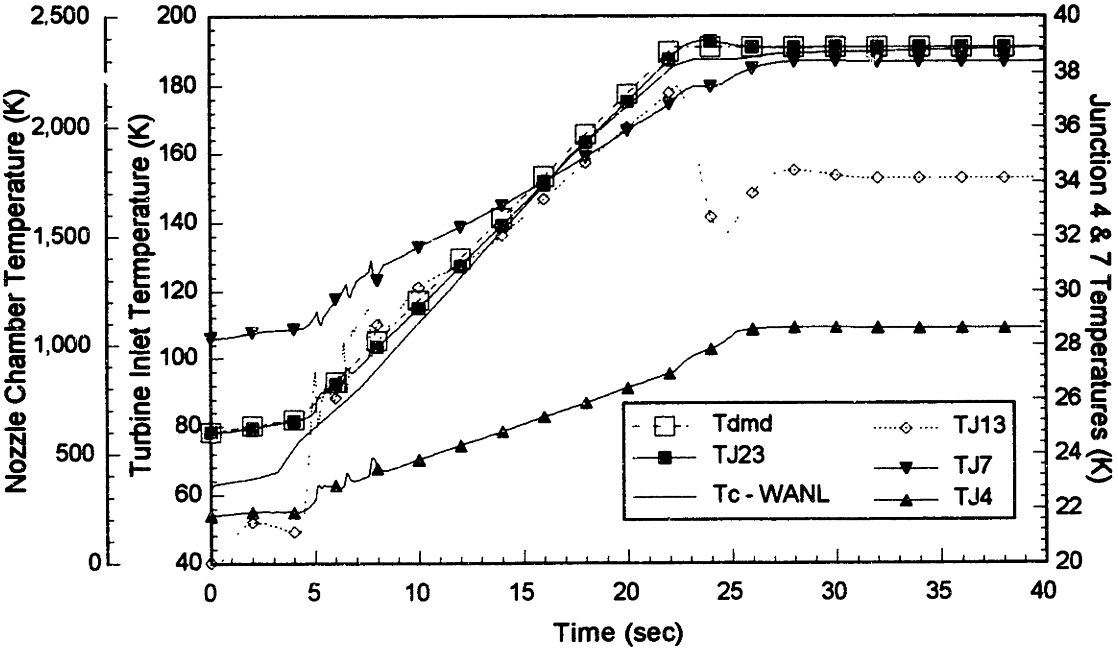

Figure 4.30 Temperature Response During NERVA Startup Transient

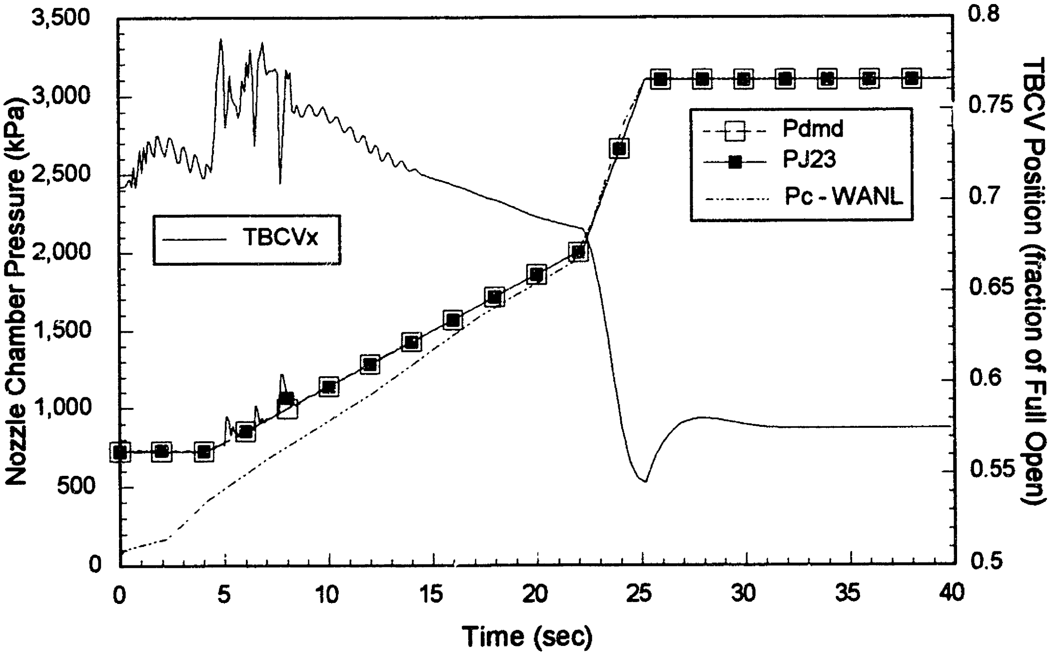

Figure 4.31 Pressure and TBCV Position Response During NERVA Startup Transient

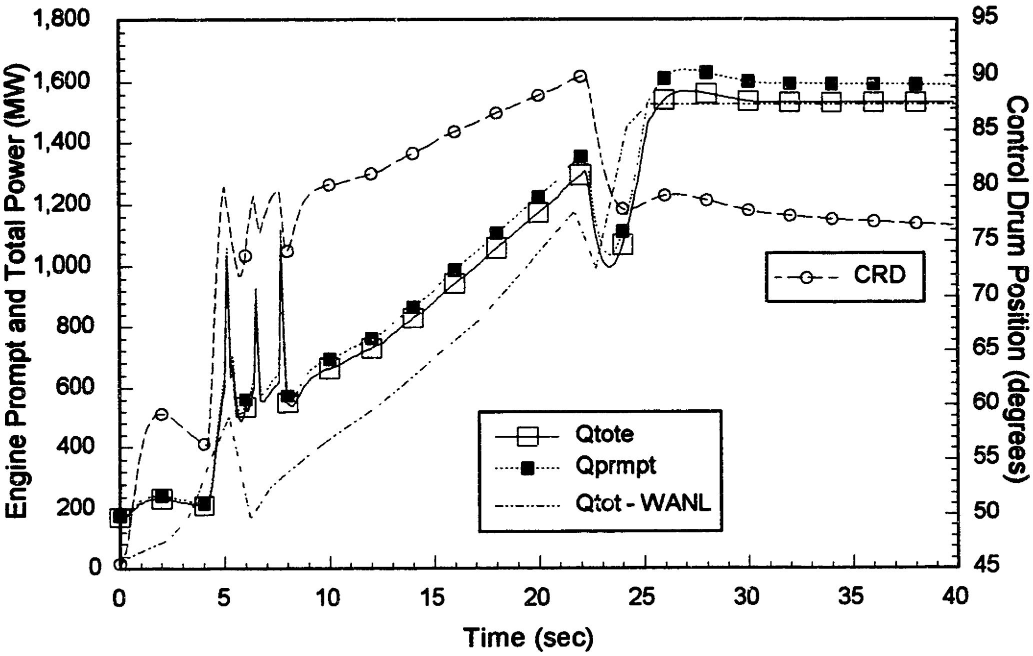

Figure 4.32 Power and Control Drum Response During NERVA Startup Transient

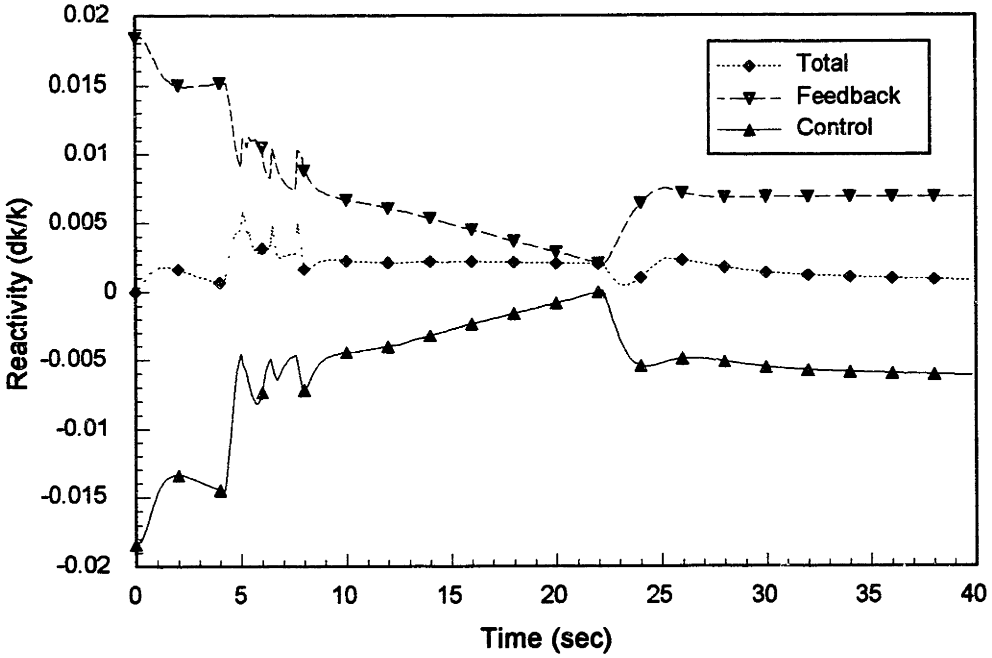

Figure 4.33 Reactivities Response During NERVA Startup Transient

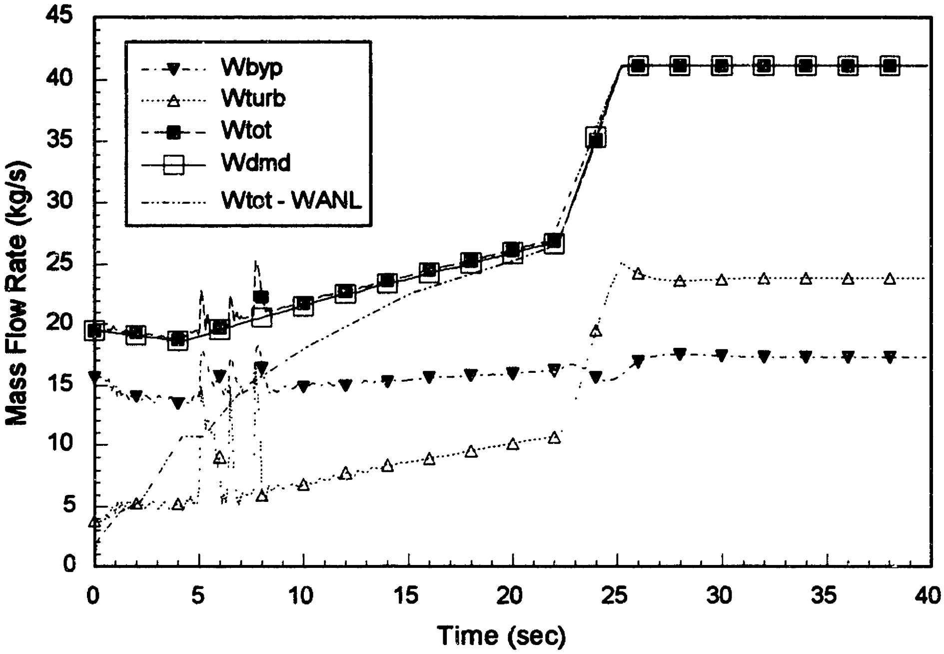

Figure 4.34 Mass Flow Rates Response During NERVA Startup Transient

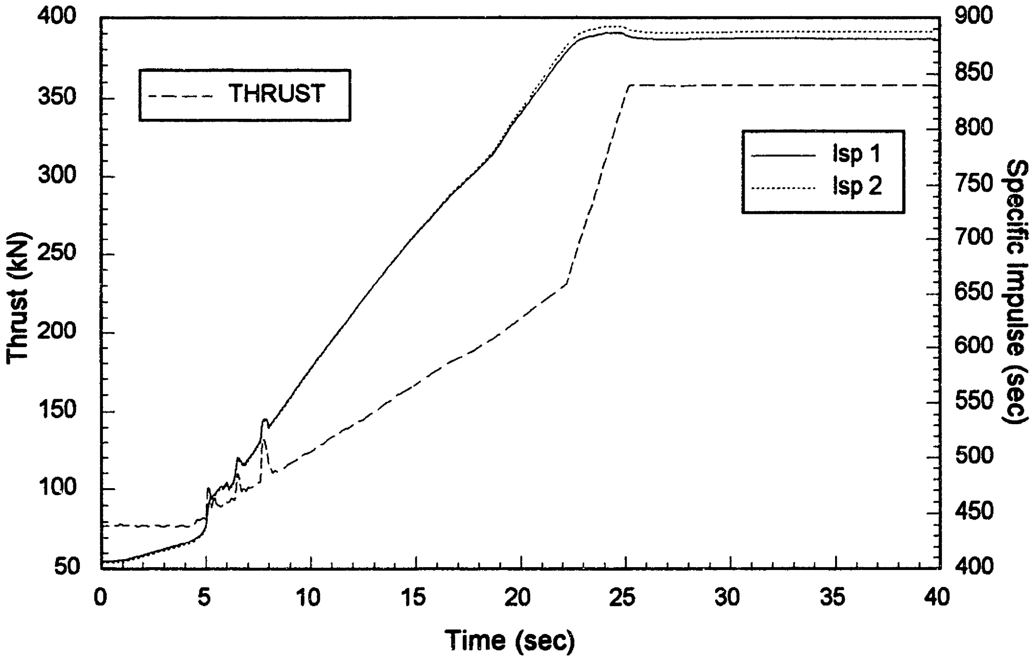

Figure 4.35 Thrust and Specific Impulse Response During NERVA Startup Transient

4.3.3.3 NERVA Throttle Transient Evaluation

The ENGTRANS computer code was used to evaluate the throttling capability of the NERVA engine sized from the Reference [C-3] reactor performance. The throttling consists of ramping the nozzle chamber pressure from 100% rated conditions to 75%, 50%, and 25% of rated conditions followed by a hold period. The rate of pressure reduction was keep constant for each case and was keep less than the NERVA program maximum of 345 kPa/sec. The cases were run with the turbine control valve parameter VLVLAM equal to 10.0 and the control drum specifications for maximum speed of 10 degrees/second and CRDLAM equal to 20.0. The response to this demanded transient is good despite the low rod speed. In all cases, the response eventually stabilizes to the desired steady state value. Curves for the parameter response are shown in Figures 4.36 through 4.40.

The nozzle chamber and turbine inlet temperatures are shown in Figure 4.36. Each of the transients follow the same trend until the throttle point is reached. As was explained for the throttle transients in section 4.2.3.2, the chamber temperature initially increases due to the power to flow mismatch. Once the throttle point is met, the temperature then decreases to some point below the setpoint value. For the lowest throttle point, the overshoots are the largest. This is due to the drum speed being limited to 10 degrees/second. During the downpower, the drum can not move fast enough to bring the temperature down and once the pressure setpoint has been met, the drums can not move quickly enough to keep the temperature from undershooting by approximately 20 K. Figure 4.37 shows that the pressure response follows the desired trajectory, despite the temperature swings. The TBCV position, however, must compensate for the changing turbine inlet temperature. For the lowest throttle power, the valve must vary its position by 5% of travel during the large temperature swing and there after, decreasingly less motion is required as the new steady state level is held. The power and control drum positions are shown in Figure 4.38. The drums are initially positioned at near their maximum differential worth. As the throttle proceeds to lower the power level, the drums must accelerate their rotation to maintain the same rate of change of control reactivity. drum rotation required for the throttle to 75% is less than 5 degrees. This is partly due to the pressure reduction reducing the hydrogen mass in the core region, thus adding negative reactivity. The deeper throttles must counter act the delayed neutrons so the drums must rotate further. Once the throttle point is reached, the drums must rotate to a position greater than where they started due to the reduced pressure. The 25% throttle case has not reached the point where it is able to rotate to its new steady state position by the end of the calculation run. The powers in each case undershoot the final value in order to reduce the chamber temperature back to its setpoint value. The 25% throttle shows the worst response, due to the limits on the drum rotation speed. The system flow rates are shown in Figure 4.39. Because the chamber temperature and pressure are able to be maintained close to their setpoints, the flow rate also responds accordingly. Once the throttle point is met, the total flow is maintained nearly constant. The turbine flow and bypass flow oscillate in accordance with the TBCV motion required to compensate for the turbine inlet temperature perturbations. The thrust profile shown in Figure 4.40 also matches the pressure response. This sort of control on the thrust transient could be useful for mission planners, because the response is nearly linear between the two hold points. The specific impulse, however does oscillate nearly proportionally to the chamber temperature. The maximum Isp swings occur during the 25% throttle case and are less than 6 seconds out of an initial 860 seconds. The Isp increases for each decrease in throttle point, due to the change in the hydrogen properties and their impact on the nozzle flow calculations. The maximum change is approximately 10 seconds which represents only a 1.2% change from the initial value.

This section has shown the throttling capability of the selected NERVA core rocket engine and the ability for the ENGTRANS code to model the transients. The system behavior is as expected. Parameters that could affect the system response are the hydrogen mass reactivity coefficient and the controller response times. The next section will present results from the shutdown transients as specified in Reference [W-6].

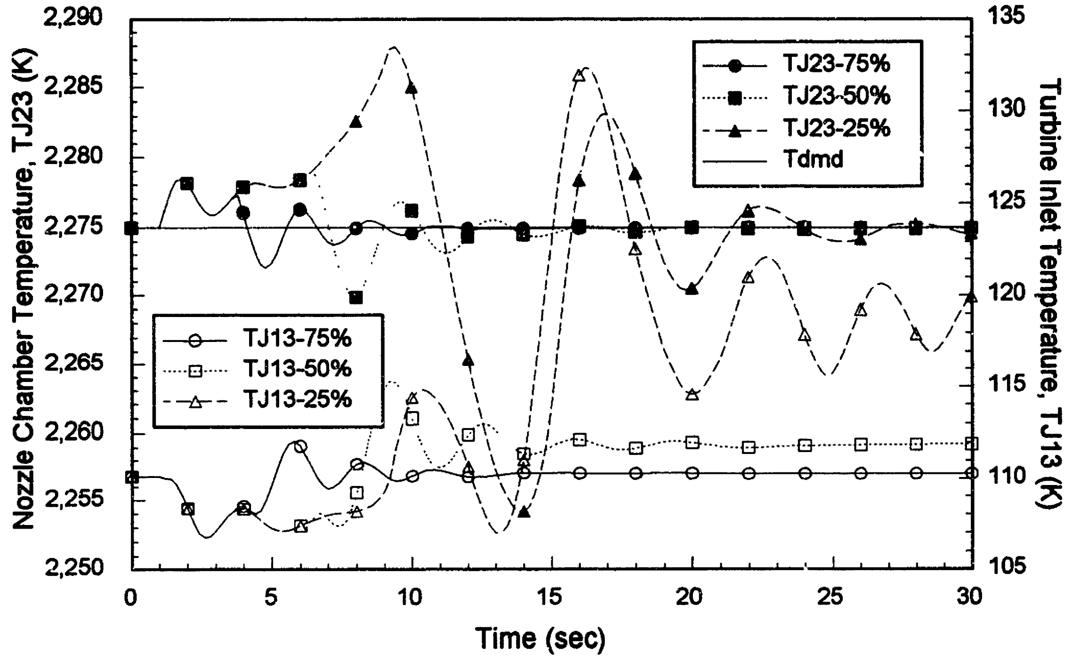

Figure 4.36 Temperature Response During NERVA Throttle Transients

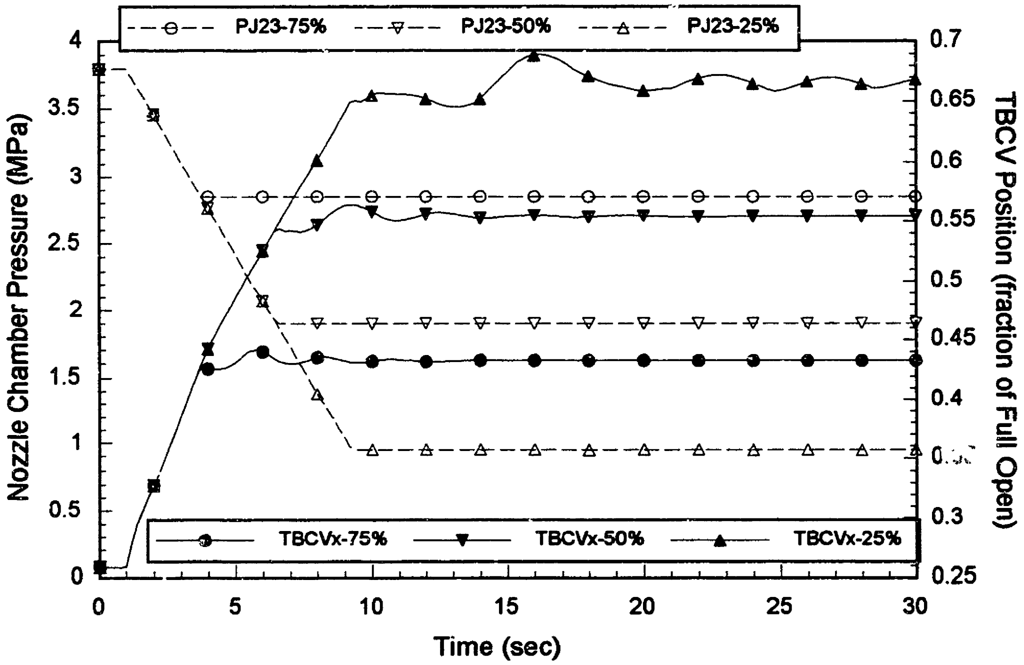

Figure 4.37 Pressure and TBCV Response During NERVA Throttle Transients

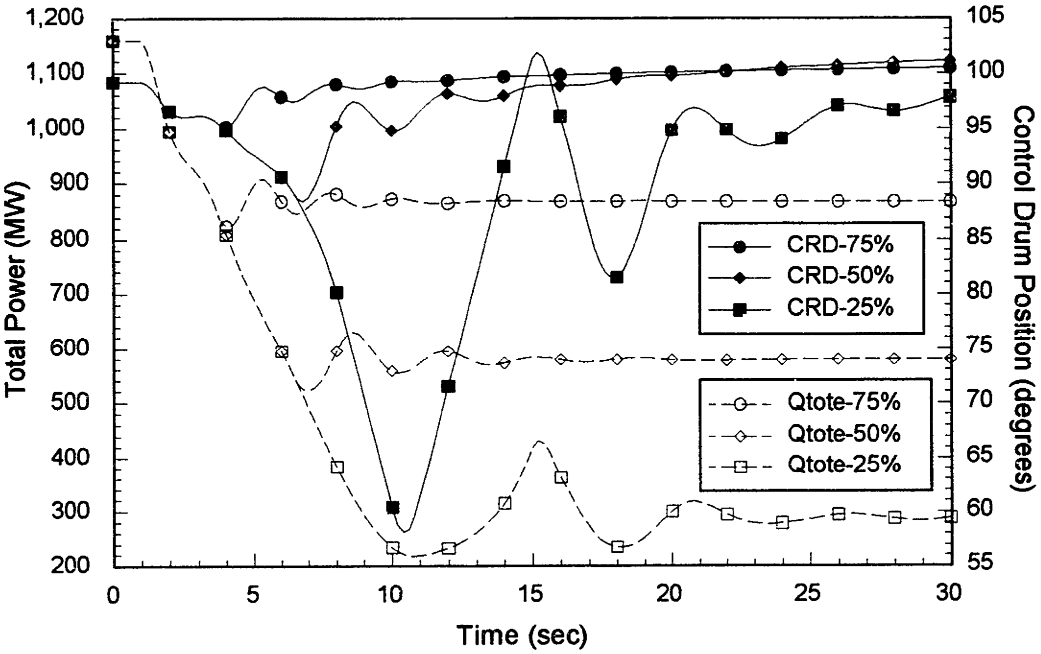

Figure 4.38 Power and CRD Response During NERVA Throttle Transients

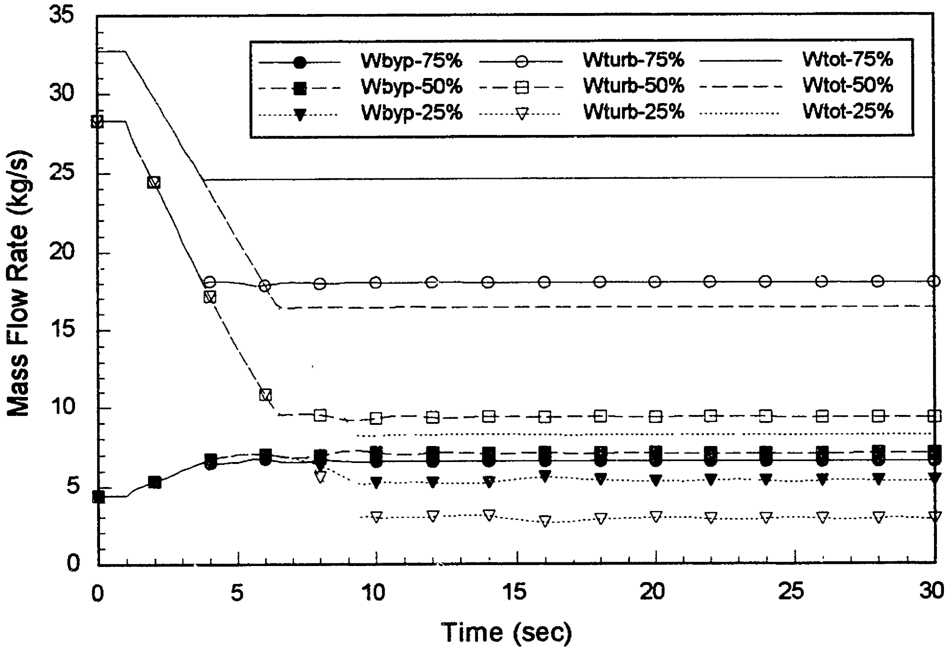

Figure 4.39 Mass Flow Rates Response During NERVA Throttle Transients

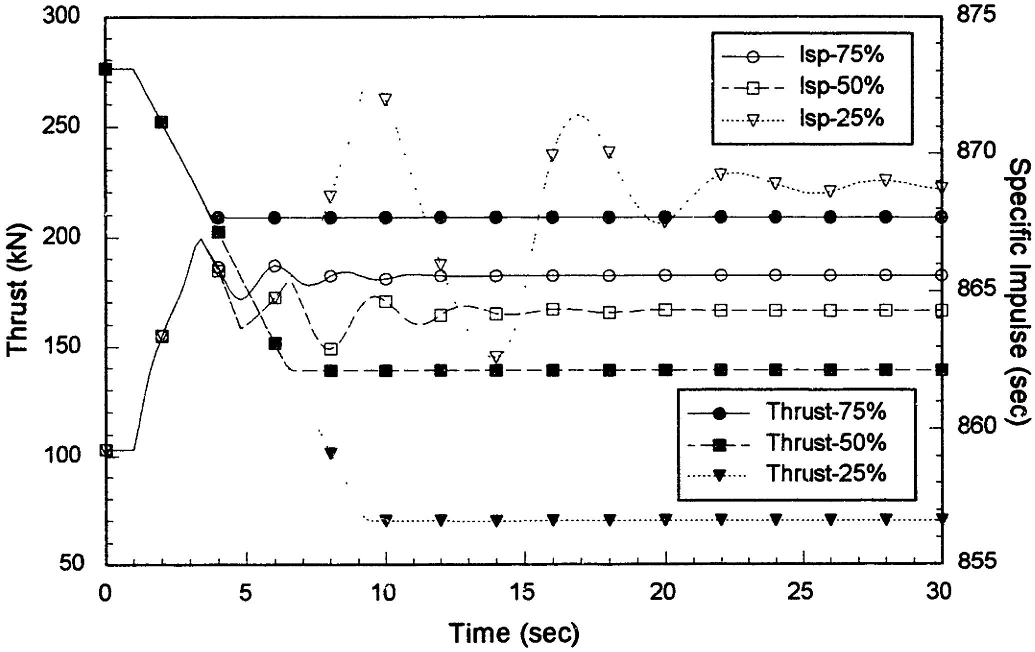

Figure 4.40 Thrust and Isp Response During NERVA Throttle Transients

4.3.3.4 NERVA Shutdown Transient Evaluation

The shutdown profile transient in Reference [W-6] was run for both NERVA engines considered in this report. The shutdown consists of an initial pressure ramp back to the throttle hold point. The system is held at this point for a certain amount of time, to allow some of the decay heat to be reduced and to allow the temperature ramp to begin at a lower pressure. The temperature retreat is commenced at the same time the reactor receives a scram signal. The drums are rotated in at their maximum speed at this point. Because the power is not a controllable variable at this time, the temperature control is now based off the flow rate and pressure. The chamber pressure is adjusted by varying the TBCV position, so as to cause the temperature to be placed on the desired trajectory. The reference simply ramped the valve to its 90% open position, while in the ENGTRANS model, the valve remains under active control. The demanded pressure is not allowed to exceed the throttle hold value, in order to minimize positive reactivity addition during the scram and to ensure the pump is operated within its capacities. As will be shown there are some important reactivity feedback effects that must be considered during the shutdown phase of operation. The final temperature hold point is at a value that can be maintained with minimal pressure. The shutdown phase of operation is governed by the decay heat loading due to the operational history of the reactor. The reference profile assumes a one hour maximum burntime, so the initialization time used for the decay heat and delayed neutron precursors was 3600 seconds. The minimal pressure is chosen for the economy of hydrogen propellant and the temperature is chosen for material and engine restart considerations. For these shutdowns, VLVLAM was equal to 10.0, CRDLAM was equal to 20.0, and the maximum drum rotation was 10 degrees/second. The temperature control used 5% of neutron power ratio and 95% temperature ratio for the determination of the desired reactor period, and 100% neutron power for the calculation of the inverse reactor period.

The key parameters for each engine shutdown case are shown in Figures 4.41 and 4.42 normalized to the 100% rated conditions. These figures allow the reader to see the complicated interrelations of the various system parameters and controllers. The throttle transient is the same as described in Section 4.2.3.3. After holding for 20 seconds, the reactor scram is commenced. Some differences between these shutdowns and the one presented in Reference [W-6] are related to the different engine cycle, core fuel geometry, TBCV control strategy, and hydrogen mass reactivity coefficient. For the smaller NERVA engine shutdown presented in Figure 4.42, the hydrogen reactivity coefficient used was 0.001 dk/k/kg. This reduces the positive reactivity addition as the hydrogen temperature is reduced. Starting the shutdown at the 50% throttle point also helps to limit the amount of positive feedback reactivity added to the reactor during the shutdown. The control drum worth is sufficiently strong so as to be able to keep the power trend on a negative period. By the time the drums are rotated fully in, the temperature has reached its desired trajectory, so the pressure ramps back to maintain the constant rate of change. This acts to add more negative reactivity, thereby ensuring reactor shutdown. The system mass flow rate increases while holding the pressure constant due to the temperature reduction at the nozzle chamber. The TBCV cycles open in order to maintain the pressure. Once the final temperature hold point is reached, the TBCV opens rapidly to reduce the pressure and, therefore, the flow. This acts to keep the temperature constant. A minimum pressure of 225 kPa was chosen for the shutdown phase of control, due to the hydrogen property code limitations, the nozzle flow calculations, and the flow requirements to drive the turbine. This causes a slight undershoot in the chamber temperature, but after the 52 second point of the transient, the temperature is slowly returning to the desired hold point. This is due to the decay heat power and the slight under flow conditions while at the minimum pressure.

The shutdown transient for the NERVA engine based on Rererence [W-6] is shown in Figure 4.42. This transient proceeds similarly to the one presented in Figure 4.41, except that it starts at the 75% throttle pressure point. Because the core is slightly larger, the thermal inertia tends to keep the temperature higher. This forces the controller to demand a higher pressure to assure the flow rate is sufficient to drop the temperature to the desired level. A hydrogen reactivity coefficient of 0.01 dk/k/kg was used for this case. This higher positive reactivity coefficient actually causes the power to rise near the end of the temperature ramp. The strong positive reactivity feedback of the hydrogen is one reason the Reference [W-6] shutdown scenario reduces the pressure by opening the TBCV when the reactor is scrammed. The NERVA program had experienced a situation that the reactor went critical after the plant had been scrammed due to over chilling of the system[W-5]. For this transient the total reactivity remains negative, but the pressure acts to slow the initial scram and increases the total reactivity once the drums are fully rotated. In this case, the temperature never reaches the demanded temperature trace, but once the final hold point is reached, the temperature levels off with minimal undershoot. Once the point is reached, the pressure ramps back quickly, which in turn rapidly reduces the power. Had the pressure been forced to ramp earlier, the power would have dropped off sooner, and allowed the temperature to drop off more rapidly. As was done with the startup transient, a comparison the ENGTRANS results to the Reference [W-6] key engine parameters will allow one to determine the computer model capabilities. A detailed presentation of ENGTRANS individual parameters for the Reference [W-6] NERVA engine shutdown is given in Figures 4.43 through 4.48.

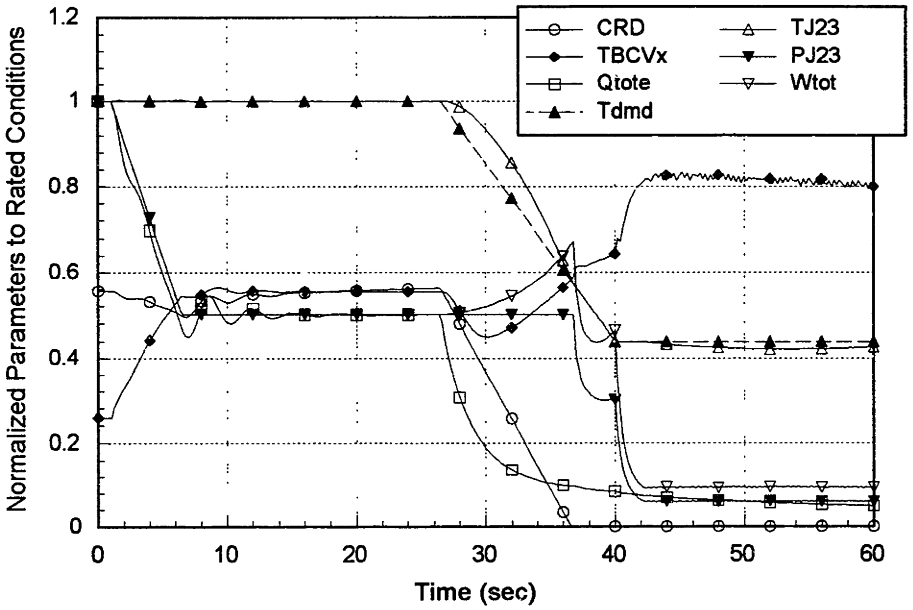

Figure 4.41 Reference [C- 2] NERVA Engine Response to Shutdown Transient

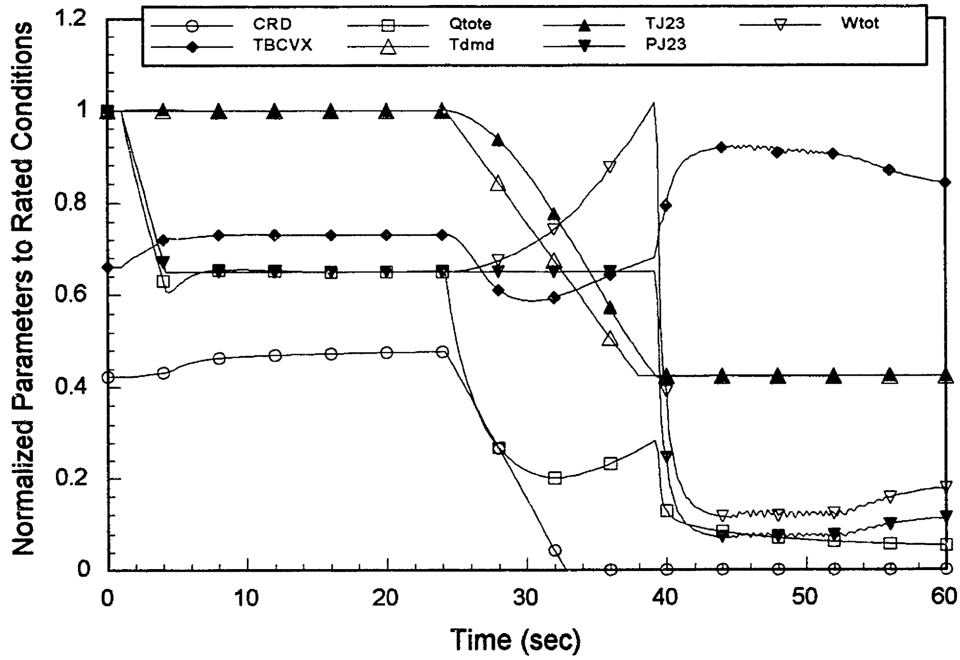

Figure 4.42 Reference [W-6] NERVA Engine Response to Shutdown Transient

Three sets of temperatures are plotted in Figure 4.43. The Junction 4 & 7 temperatures show the trends for the pump heat input and the nozzle heat transfer. The linear reduction in the Junction 7 temperature during the temperature ramp is due mainly to the nozzle hot side gas temperature. The Junction 4 temperature is related to the nozzle pressure and the efficiency of the pump. The turbine inlet temperature is affected by the power reduction and the increase in system flow. This temperature does not increase when the power does between 35 and 40 seconds, because the flow rate through the system has also increased, so the reflector receives enough cooling flow to hold the temperature lower. Once the pressure and power are rapidly reduced, the turbine inlet temperature increases because of the thermal inertia of the reflector and the reduced flow rate. It has not reached its new steady state value by the end of the 60 second transient calculation. The nozzle chamber temperature lags behind the demand temperature ramp due to the thermal inertia of the core and the hydrogen reactivity of the core slowing the power reduction. Data points from Reference [W-6] plots are also shown in this figure. The reference temperature trace starts at a lower temperature, but then follows the demanded trajectory more closely. At the end of the ramp, however, the temperature undershoots the desired value by 400 K before returning to the desired value.

The pressure and TBCV trends are shown in Figure 4.44. The pressure follows the demanded path with little error. The scram that commences at 24 seconds and the simultaneous opening of the TBCV in the Reference [W-6] calculations causes the reference pressure to drop of rapidly. This was the control strategy used at that point of the NERVA program. The ENGTRANS pressure is required to remain at the throttle level until the temperature is reduced to its final hold point. In order to keep the pressure up with a turbine inlet temperature that is decreasing, the TBCV must be closed down to reduce the bypass flow. As the flow rate increases, the pressure drop relations across the turbine and the TBCV change so that the valve then begins to slowly open. Once the final hold point is reached, the valve rapidly opens to reduce the turbine drive flow and thus the pressure.

The power and control drum position as depicted in Figure 4.45. The throttle ramp behaves similar to those described in Section 4.2.3.3, but because of the larger hydrogen reactivity coefficient, the drums start off with less rotation. Later in the throttle, the drums must slowly rotate outward a few degrees to prevent an overly fast power reduction. Once the scram point is reached, the drums are rotated inward at the maximum speed of 10 degrees/second. The drums in Reference [W-6] started at approximately 60 degrees due to a negative bias offset in the drum worth curve, so the drums in that case are able to reach full in 3 seconds earlier. The power response for the two cases is similar for the throttle ramp. For the scram ramp, the Reference [W-6] power drops off more quickly, due to the extra negative reactivity added by the rapid pressure reduction. The ENGTRANS case power is held up because the rods must rotate over a longer period of time and because the negative control reactivity is competing against the positive feedback reactivity. While the magnitude is not as large, the reference power does exhibit the upward trend near the end of the temperature ramp. This occurs after the reference case drums are at zero degrees and the temperature is continuing to drop. Once the temperature hold point is met, the powers rapidly reduce to the decay heat level.

The reactivities for the transient are shown in Figure 4.46. The control reactivity follows the drum position trend that was shown in Figure 4.45. The trace during the scram rotation is not linear due to the sinusoidal nature of the drum worth. The feedback reactivity is dominated by the hydrogen mass component. The throttle ramp lowers the pressure while maintaining the temperature, so the average gas density is reduced. During the temperature retreat, the pressure is being held constant by the temperature controller, so the density in this case is increasing. This adds a large amount of reactivity to the system. The total reactivity reflects the combination of these two reactivities. Initially the drum worth is sufficient to drive the total reactivity negative. Once the rate of change of the control reactivity becomes less than the feedback reactivity, the total begins to head in the positive direction. The total reactivity remains less than zero, but the rate of change causes the power to rise. Had the temperature ramp proceeded to a lower temperature, the reactor would have gone critical again and reached some steady state level. Because the controller is attempting to drive the temperature to its final point, the pressure would be maintained at the maximum throttle hold point and the temperature would increase until the feedback reactivity was equal in magnitude to the control reactivity. When the reactivity excursion was encountered in the NERVA program, the system hydrogen flow rate, and thus the pressure, were reduced to shut the reactor back down[W-5]. For this reason the control strategy in Reference [W-6] was such that the

TBCV was opened to 90% of its travel. The shutdown control strategy implemented in ENGTRANS is adequate, but its limitations are that the drum worth must be sufficient to override the hydrogen worth and that an evaluation of the hydrogen worth is necessary to ensure operation in regions of high feedback reactivities is avoided.

The hydrogen mass flow rates are shown in Figure 4.47. The throttle ramp flows follow the demanded trajectory, as expected because the flow is approximately proportional to the chamber pressure during this ramp. During the temperature retreat, the demanded flow rate is that which would exist if the chamber temperature where at its demanded level. The actual total flow rate lags this desired value because the pressure is constrained to its throttle point as a maximum. The flow rate is able to increase because the temperature is decreasing and now the flow is approximately proportional to the inverse of the square root of the chamber temperature. Once the final hold point temperature is reached, the demanded and actual flows follow the same trajectory. As the bypass valve ramps open the bypass flow becomes the majority flow. As the turbine inlet temperature decreases, the turbine flow must increase to drive the same amount of flow. Also, the total flow rate must increase to maintain the chamber temperature constant as the rest of the system reaches their new "steady state" conditions. The system flow from Reference [W-6] is similar to the ENGTRANS results up to the scram point. At this time, the mass flow rate ramps back as the pressure is quickly reduced. Then, as the chamber temperature is decreasing, the reference flow rate then increases and follows the ENGTRANS bypass flow. This suggests that if the TBCV had been ramped outward earlier, the total flow rate would have followed this same trend. Once the final hold point is reached, the flow rates differ first due to the times that this temperature is met, and then due to the reference system having to reduce the flow further in order to bring the temperature back up to the hold level.

Finally, the thrust and specific impulse are depicted in Figure 4.48. The thrust follows the pressure profile fairly closely. There is a slight drop off in the thrust performance during the temperature retreat due to the changing nozzle performance and heat transfer. The increase in system flow increases the nozzle cooling so that the nozzle exit pressure and velocity conditions are affected. The calculated impulses follow the chamber temperature trends. The small temperature oscillations during the throttle ramp appear more readily in the impulse curve because the scale is shorter. The control strategy implemented for the ENGTRANS shutdown allows the impulse as a function of time to be well defined. The thrust is also well defined over much of the transient. These results indicate that, if mission planners require a certain thrust and Isp trajectory for a mission, the control method implemented in ENGTRANS may be able to provide the desired performance.

This concludes the analysis for the NERVA engine cores. The ENGTRANS computer code was shown to yield comparable results to reference profiles and to be robust enough to handle different core configurations and transient requirements. In the next section, startup, throttle, and shutdown transients run for the PBR engine will be discussed.

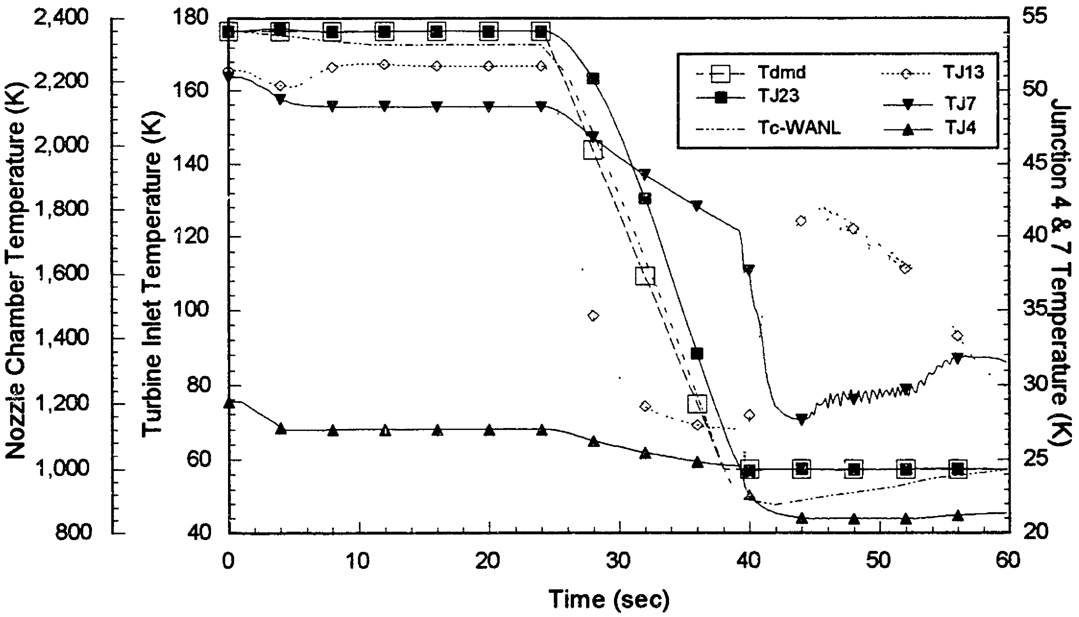

Figure 4.43 Temperature Response During NERVA Shutdown Transient

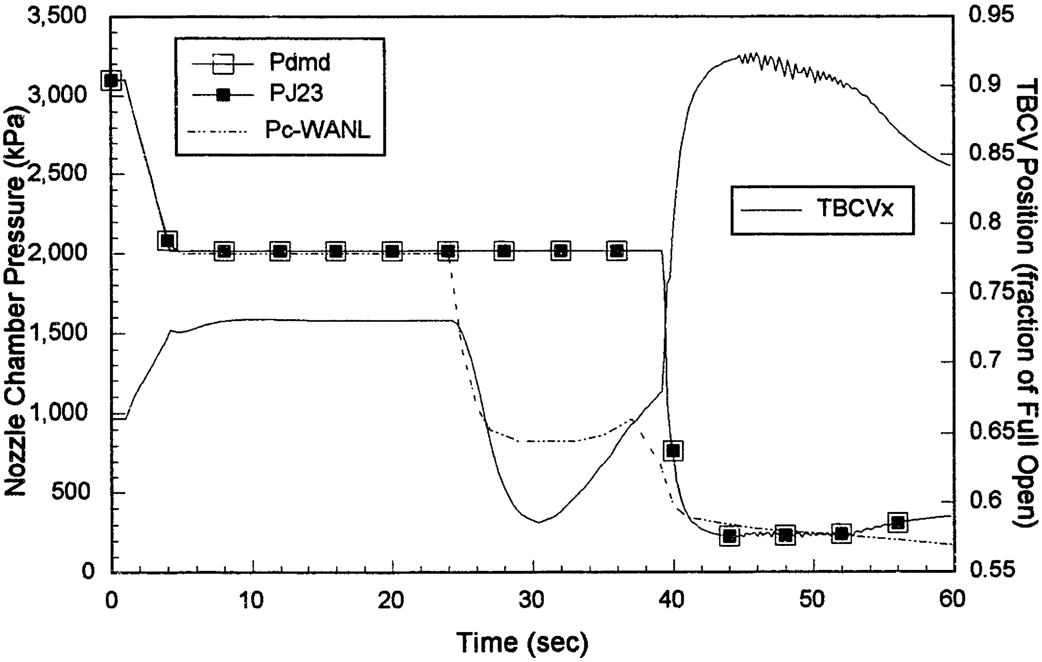

Figure 4.44 Pressure and TBCV Position Response During NERVA Shutdown Transient

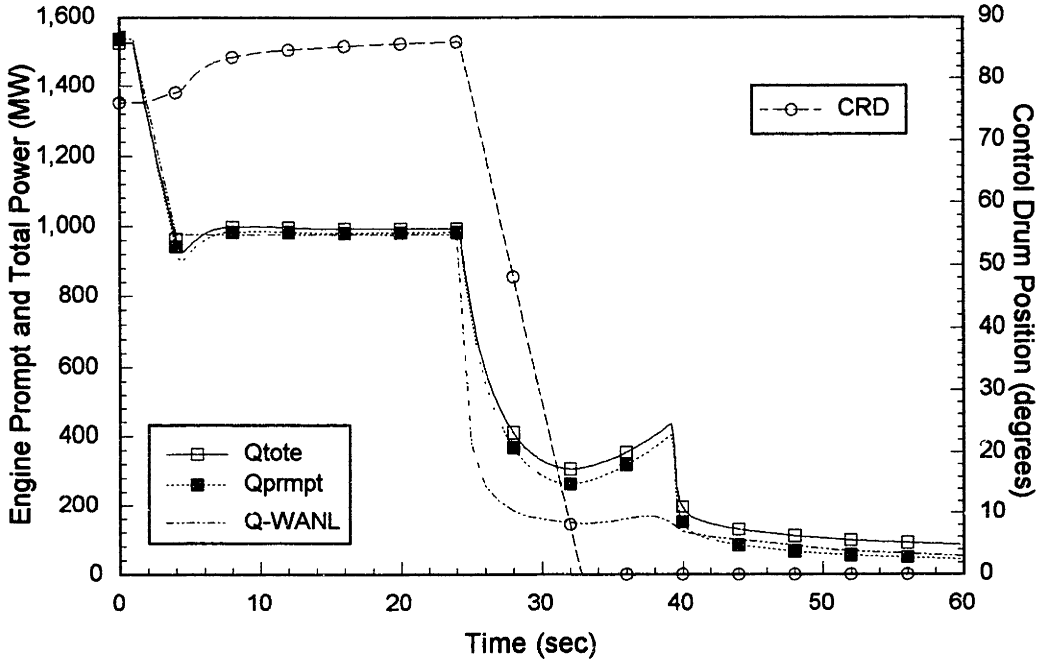

Figure 4.45 Power and Control Drum Response During NERVA Shutdown Transient

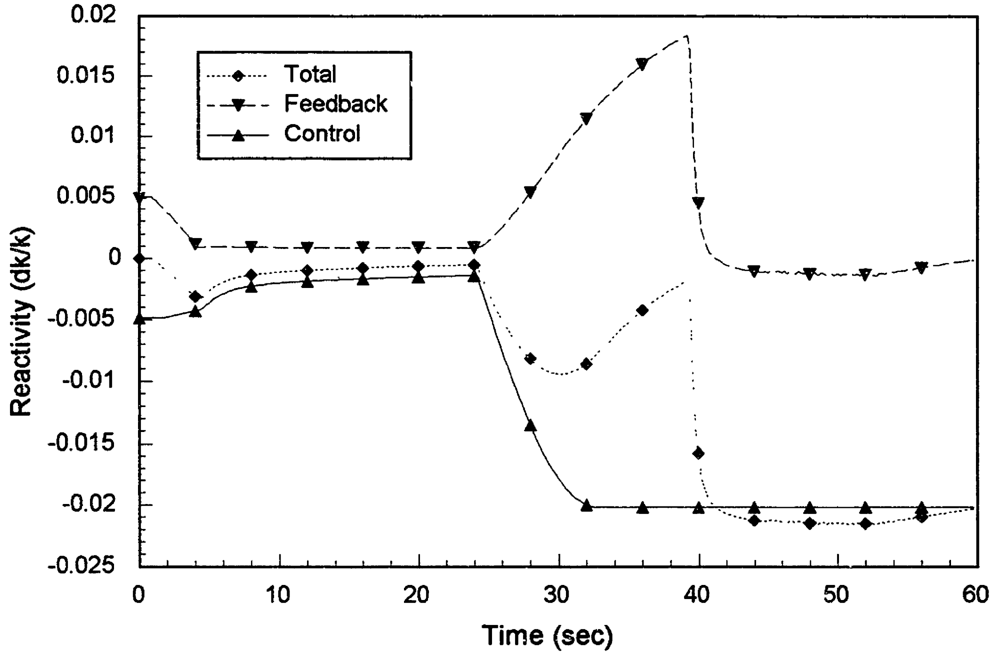

Figure 4.46 Reactivities Response During NERVA Shutdown Transient

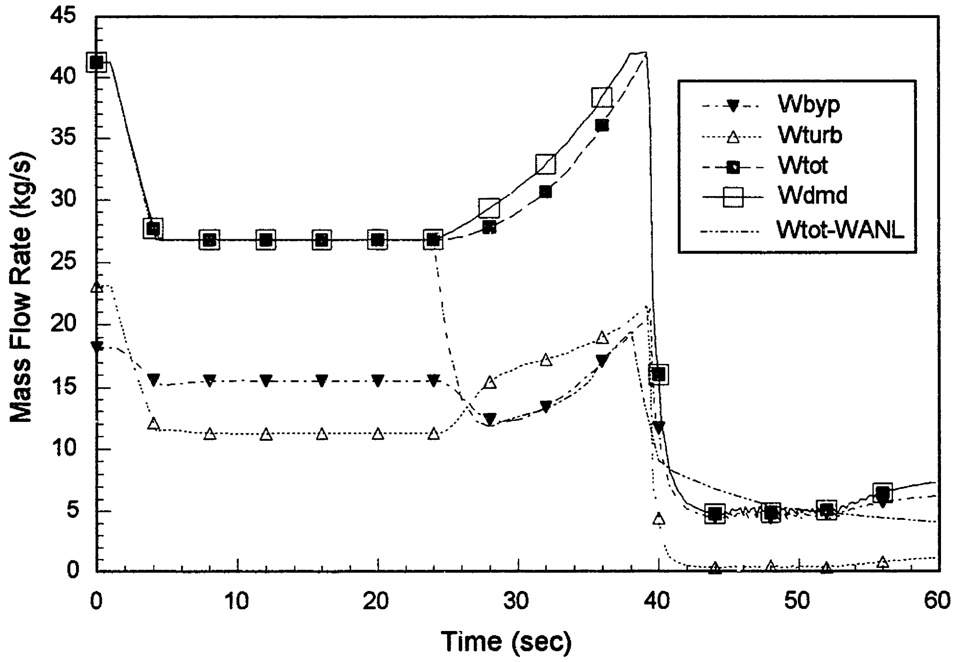

Figure 4.47 Mass Flow Rates Response During NERVA Shutdown Transient

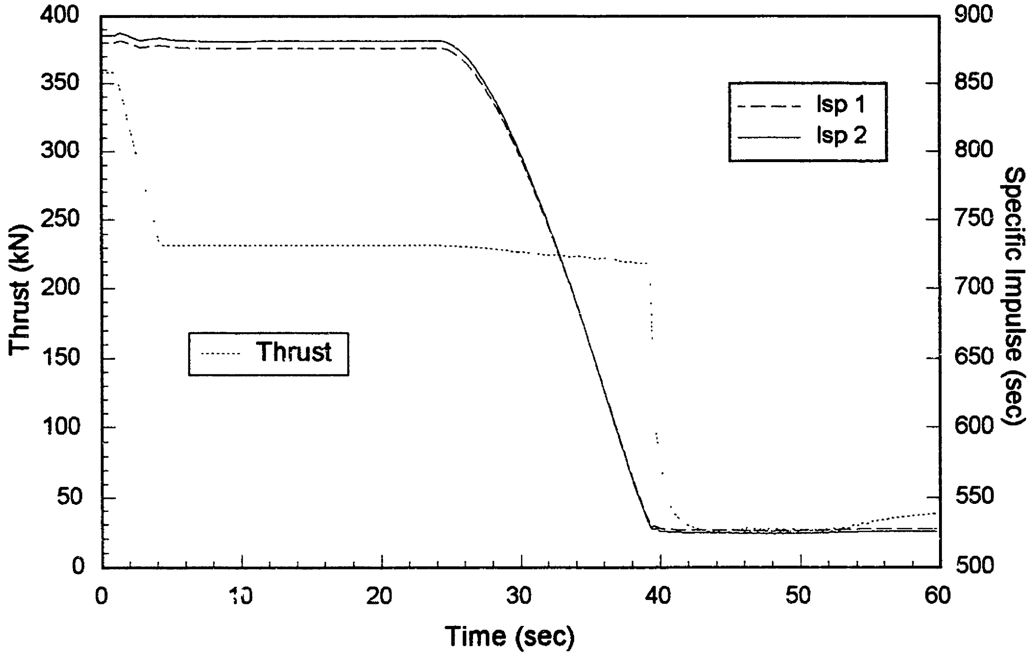

Figure 4.48 Thrust and Specific Impulse Response During NERVA Shutdown Transient

4.3.4 PBR Engine

4.3.4.1 Introduction

A set of startup, throttle, and shutdown transients similar to the NERVA engine transients were run on the Particle Bed Reactor engine. The transients ramp rates were selected to take advantage of the PBR performance parameters. These include faster rates of change in chamber temperature and chamber pressure. During the course of the transients studies it was necessary to change the element size to ensure the flow stability requirements are met. In addition to the parameter traces presented for the NERVA transients, the stability criterion map is plotted to show the area of operation during the transient. The cases run for the PBR show that the ENGTRANS code is able to handle the faster transients and bring up some new considerations for the operation of the PBR. These will be discussed in the next sections.

4.3.4.2 PBR Startup Transient Evaluation

The startup transient run on the PBR consists of a 5 second build up in pressure and temperature to 10% power and then a 7 second ramp of the chamber temperature to its rated condition coupled with a fast ramp in pressure to its 75% throttle value. The final 3 seconds of the startup consists of a fast ramp of the chamber pressure to its rated condition. The full listing for the input file for this run is given in Appendix A. The key parameter values during the transient are shown in Figure 4.49. This plot is a little busy, because the parameters are all ramping quickly to their rated conditions. The control drums rotate out to bring the power up to raise the temperature. Once the temperature is on the desired trajectory, the drums must rotate inward to prevent a temperature overshoot. Despite the demanded increase in pressure, the TBCV cycles open to bring the pressure up, because the turbine inlet temperature is increasing. During the second phase of the uppower, the drum rotate outward to bring the power up on a shorter period. The TBCV now must cycle closed, due to the faster pressure ramp demanded. The chamber temperature is below the desired trajectory for only 3 seconds before the power has increased enough to maintain the proper ramp rate. Once the final temperature is met the temperature is held at the demanded level, while the pressure is increased. This final pressure ramp requires the TBCV to cycle close more rapidly and the control drums to rotate inward to compensate for the increase in feedback reactivity and the build in of the delayed neutron precursors. The individual responses are shown more clearly in Figures 4.50 through 4.56.

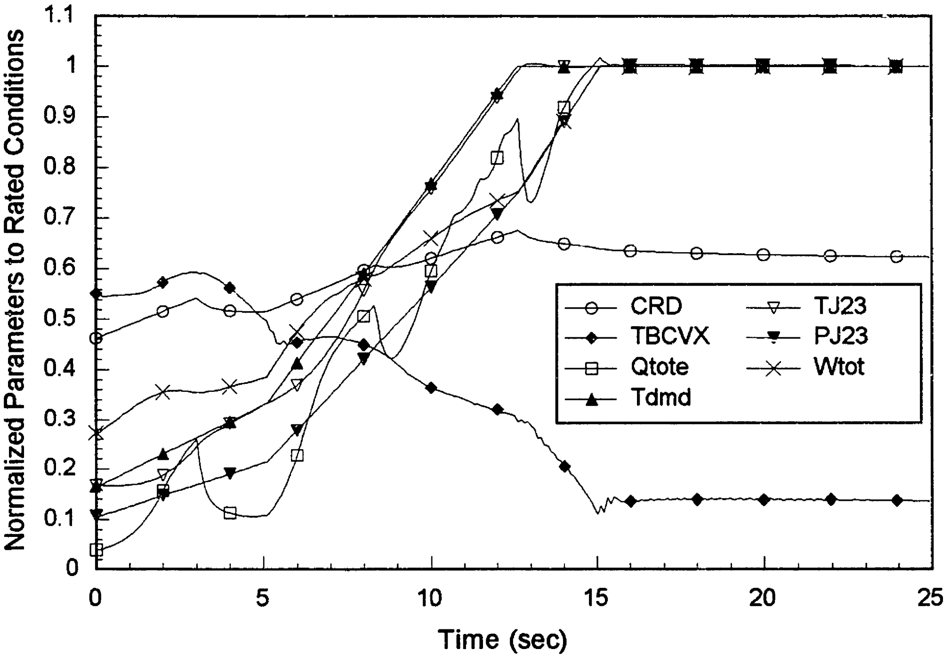

Figure 4.49 Normalized Parameter Response to Prototypic PBR Startup Ramp

The chamber, turbine inlet and the Junction 4 and 7 temperatures are shown in Figure 4.50. The Junction 4 temperature follows the pressure rise trace due to the relation of the pump power and inefficiency to the heat input to the hydrogen fluid. The Junction 7 temperature begins at a temperature above the critical temperature for hydrogen, so this transient does not suffer from the same problem that was encountered with the modeling of the NERVA engine startup. This is due to the higher system pressure and the higher heat addition from the pump and nozzle. The temperature increases along the same trend as the chamber temperature due to the heat transfer across the nozzle wall. The turbine inlet temperature undergoes swings due to the swings in the heat input from the reactor power as it adjusts to the chamber temperature demands. The chamber temperature initially lags the demanded curve because the power is not rising fast enough to increase the temperature and compete with the increase in flow. Within four seconds of the start of the transient, the chamber temperature has reached the desired trajectory. Then as the rate of change is increased, there is another period of mismatch. In both cases the error is less than 200 K. Once the final temperature hold point is reached, the overshoot is less than 20 K and the temperature is held constant. The overshoot is kept low due to the pressure ramp that continues for three seconds longer.

The pressure and TBCV position response are shown in Figure 4.51. The chamber pressure follows the demanded trajectory with negligible error. The TBCV initially must cycle open to account for the rise in the turbine inlet temperature that reduces the required turbine flow to drive the turbopump. As the turbine temperature decreases and the pressure demand continues to increase the TBCV must cycle shut. The bulge during the second ramp is again due to the turbine inlet temperature changes. The final ramp requires the TBCV to ramp shut more quickly. Once the final pressure hold point is reached, the valve responds quickly and is able to hold the pressure constant with motion of less than 5% travel.

Figure 4.52 shows the response of the engine powers and the control drum position during the startup transient. The drums initially ramp out at 5 degrees/second to raise the reactor power to bring the chamber temperature up to the desired trajectory. Once the temperature meets the trajectory curve, the power must be ramped back to keep the temperature from over shooting the trace. At the start of the large temperature ramp, the rods must again rapidly rotate out to bring the temperature to the desired trajectory. The power quickly increases and then cuts back once the temperature reaches the demanded condition. Because the pressure is also increasing quickly during this ramp, the power must continue to increase in order to maintain the proper rate of change of chamber temperature. Once the temperature hold point is reached, the rods must rotate inward to stop the temperature ramp and then to compensate for the positive reactivity addition from the pressure rise. Once the pressure is at its hold point, the rods continue to rotate inward in order to compensate for the build in of the delayed neutron precursors and the decay heat component of the total engine power. The prompt engine power is greater than the total effective power during the transient, but at the hold point, the prompt power slowly reduces as the decay power builds in. As will be shown in the shutdown transients, given enough time the prompt power will drop to be nearly equal to the total effective power, consistent with the power equations presented in Section 2.8.

The various system reactivities are plotted in Figure 4.53. The control reactivity follows the drum rotation trends and adds approximately 0.7 dollars during the first ramp. The feedback reactivity used in the PBR engine is a combination of a temperature coefficients for the fuel and hydrogen temperatures and a pressure coefficient for the hydrogen pressure. The reflector was assigned the same reactivity coefficients as were used in the NERVA engine analyses. The temperature effects dominate the feedback reactivity during the ramps until the temperature hold point is reached. During the final thrust ramp, the feedback reactivity moves slightly positive as the pressure increases. The total reactivity transient is fairly smooth compared to the large changes in the control and feedback reactivities. These curves point out the need for good evaluations of the reactivity coefficients and control drum worths, to assure the reactor can be operated safely under the rapid power transients.

The mass flow rates are presented in Figure 4.54. Initially the turbine flow is less than the bypass flow, but when the second pressure ramp begins, the turbine flow increases along with the total system flow. The total flow exceeds the demanded flow during the initial portions of the first two ramps. Because the chamber temperature is less than its demanded temperature and the pressure is on the correct trajectory, the actual flow is high. Once the temperature is on track with the desired trace, the system flow matches the demanded flow. The thrust and specific impulse are shown in Figure 4.55. The nozzle pressure follows its demanded curve thus, the thrust also follows a well defined path. The specific impulse is also well behaved, due to the chamber temperature response. The ability for the controller to maintain such performance traces could be useful for the implementation for very specific thrust and impulse requirements.

Finally, Figure 4.56 presents the flow stability operating conditions. The curve labeled "Phi B&D/M" is the curve derived using the methods of Bussard & DeLauer/Maise, that were presented in Section 3.5.2.1. The curve labeled "Phi JKW" is the stability criteria line determined using the numerical simulation model of the element, as was presented in 3.5.2.2. The curve labeled "Phi Startup" is the trace of the fuel region temperature rise factor versus the fuel inlet Reynolds number. The values remain in a relatively small band due to the changes in the inlet temperature. Even though the flow rate is increasing, the viscosity is also increasing, so that the Reynolds number cycles between 130 and 230. The temperature ratio actual ends up lower at the higher power level, again due to the fuel inlet temperature being sufficiently high. If the element design is changed to allow a lower power density, the Reynolds number will also lower. Changing the core to a 37 element core also reduces the Reynolds number. For these reasons a high power density, 19 element core was selected for the transient studies.

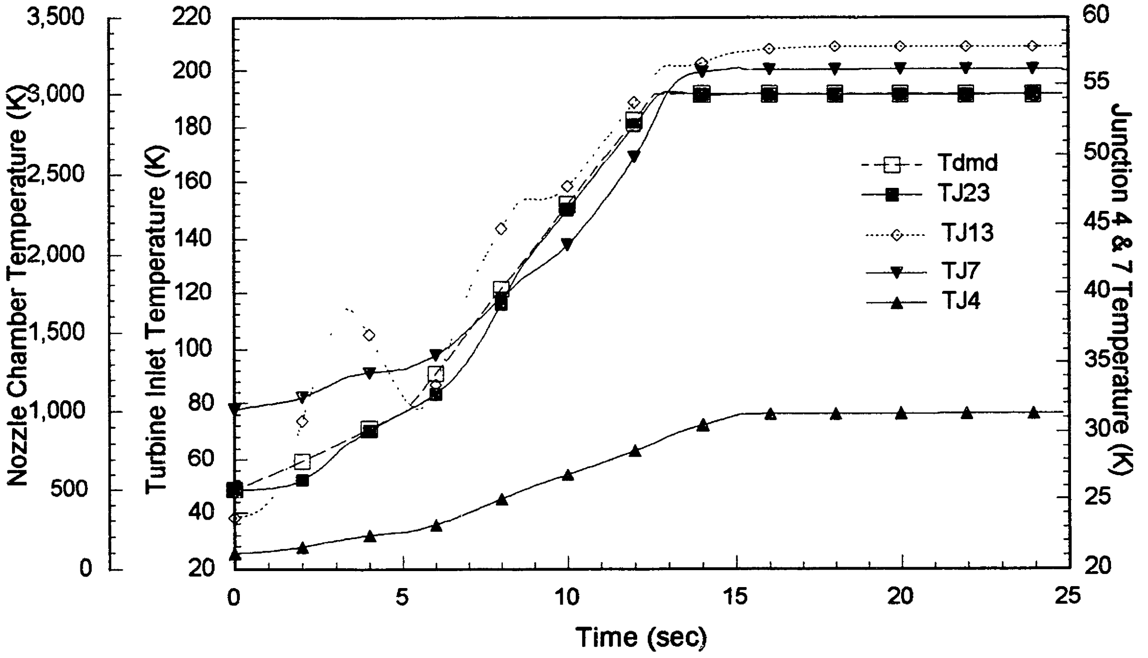

Figure 4.50 Temperature Response During Prototypic PBR Startup Ramp

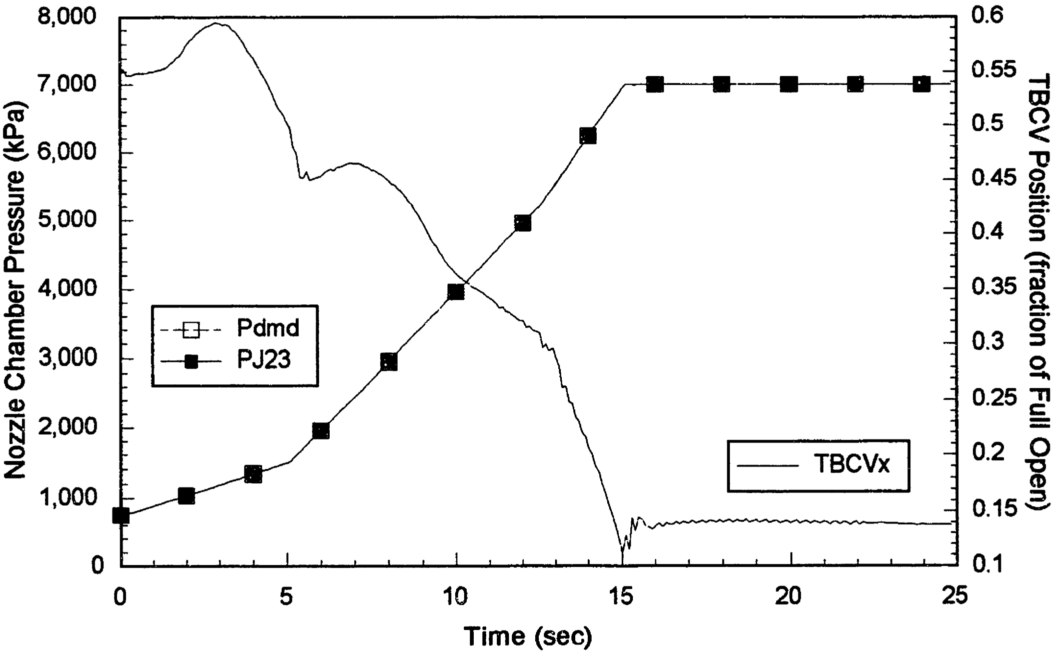

Figure 4.51 Pressure and TBCV Position Response During Prototypic PBR Startup Ramp

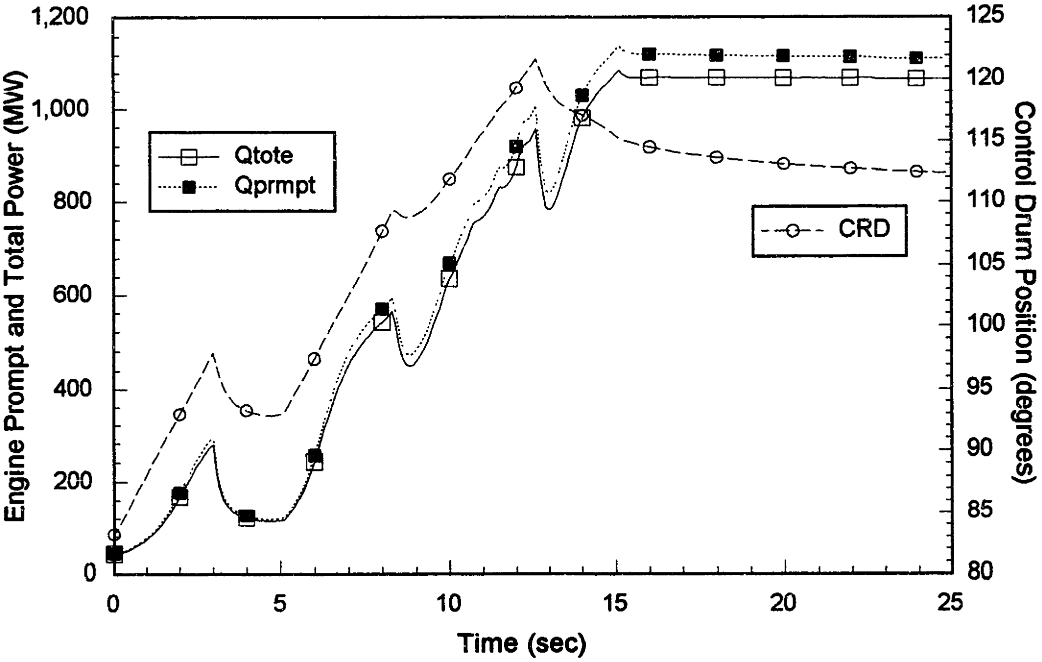

Figure 4.52 Power and CRD Position Response During Prototypic PBR Startup Ramp

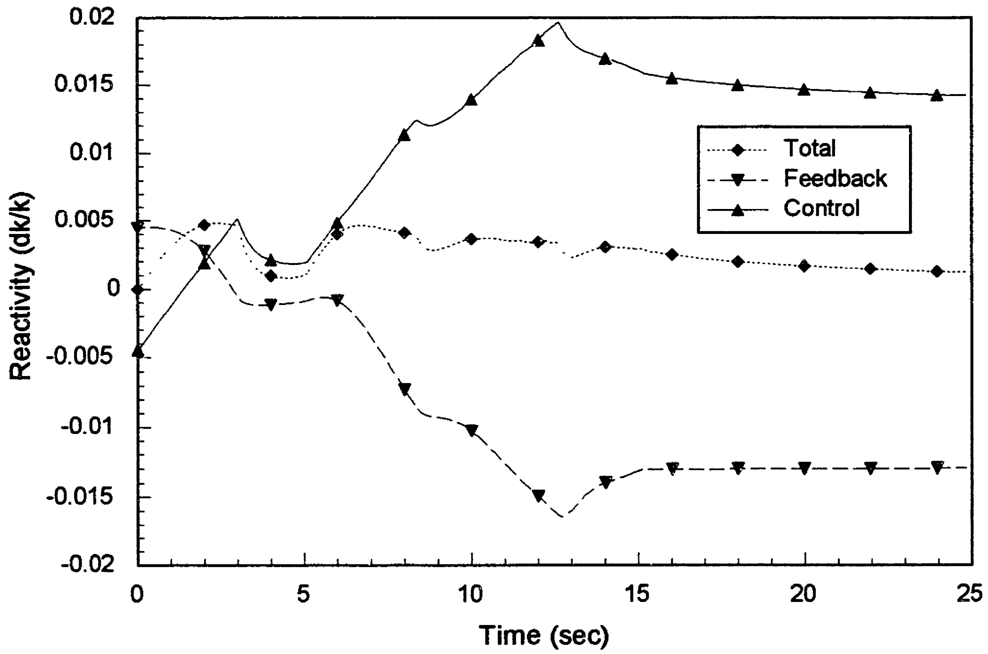

Figure 4.53 Reactivity Response During Prototypic PBR Startup Ramp

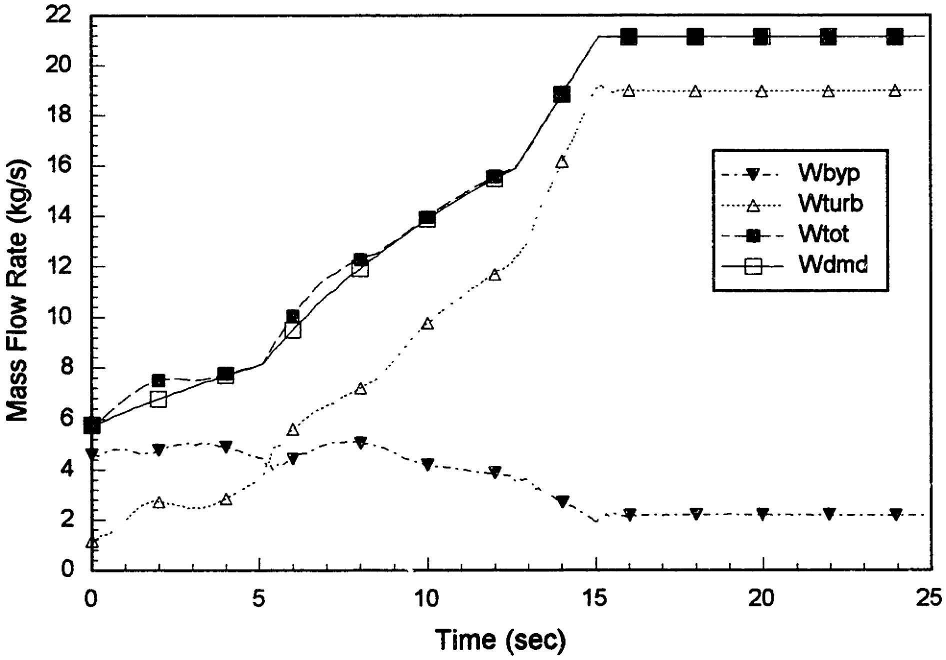

Figure 4.54 Mass Flow Rate Response During Prototypic PBR Startup Ramp

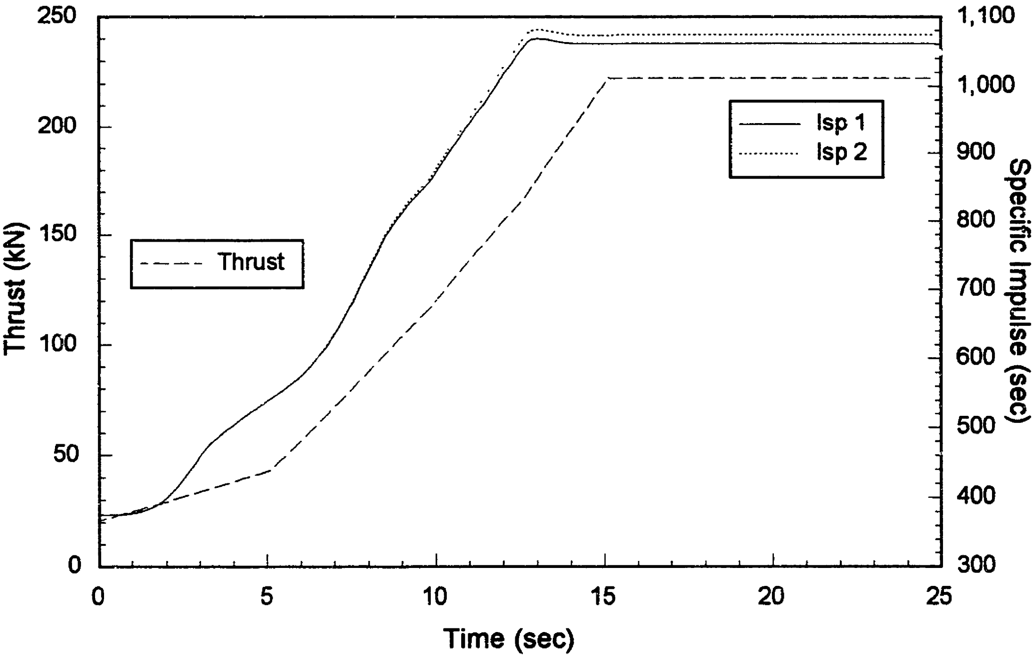

Figure 4.55 Thrust and Specific Impulse Response During Prototypic PBR Startup Ramp

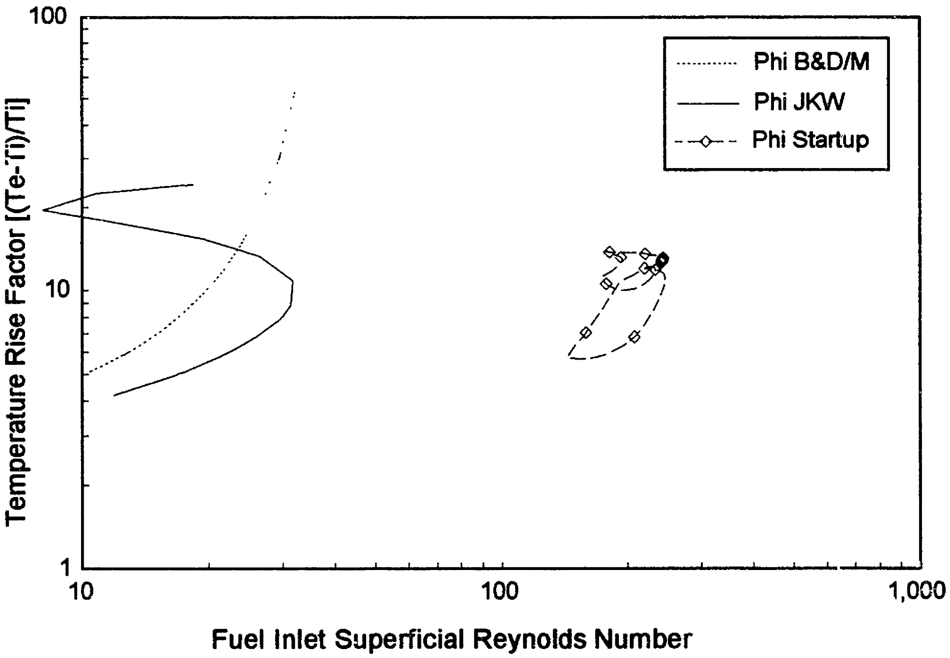

Figure 4.56 Stability Criterion Response During Prototypic PBR Startup Ramp

4.3.4.3 PBR Throttle Transient Evaluation

The throttle transient to 75% thrust was run for two pressure ramp rates. One case ramps the pressure back at the same 345 kPa/second rate as the NERVA engine transients. The second case ramps the pressure back at twice that rate. This was done to show the ability of the ENGTRANS code to be able to handle rapid transients and to see the effects of such rapid transients on the system parameters. The parameter responses are shown in Figures 4.57 through 4.62.

The nozzle chamber and turbine inlet temperatures are shown in Figure 4.57. The turbine inlet temperature increases over the course of the throttle maneuver due to the reduced flow though the reflector. The increase is less than 10 K and the new steady state value is reached within 4 seconds after the throttle point has been reached. The delay is due to the thermal capacitance of the reflector region. The chamber temperature is maintained at the desired 3000 K within error bands of -3 K to +9 K. The spike nature of the temperature curve is due to the accuracy of the hydrogen properties routine when it finds the temperature from the enthalpy and pressure. Because the gas is partially dissociated at this point, as the pressure decreases, the routines must determine the new amount of dissociation. Also the nozzle flow calculations will have slight variations that will also add to the shape of the temperature curve. The chamber temperature does return to within 1 K of the demanded temperature within 1 second of reaching the throttle hold point.

The chamber pressure and TBCV position response is shown in Figure 4.58. In both cases the pressure ramps back along the demanded trajectory and hold with little oscillation. The TBCV cycles open until the hold point is reached. At this point, the valve moves to account for the change in turbine inlet temperature and the small perturbations in the chamber pressure.

Figure 4.59 presents the engine total effective power and the control drum motion during the transient. The positive pressure reactivity coefficient causes the temperature controller to ramp the control drums outward, despite the transient being a downpower maneuver. The shapes of the curves are not as smooth as for the startup case because the calculated pressure fluctuates slightly from a linear downward ramp. The controller responds to the measured increase in chamber temperature by quickly ramping the control drums inward for a short period of time. Once the throttle point is met, the drum continue to rotate slowly outward to compensate for the decaying of the delayed neutron precursors.

The mass flows rate shown in Figure 4.60 also show good behavior during the transient. Because the chamber temperature is nearly constant, the flow falls off proportional to the chamber pressure. Because the turbine inlet temperature increases over the course of the transient, the bypass flow must increase. The thrust and specific impulse are shown in Figure 4.61. The thrust follows a path proportional to the pressure response. It reaches the demanded throttle point when required and holds steady for the remainder of the transient. The Isp experiences the same spikes as the chamber temperature due to its relation to that parameter. The Isp also increases by 3 seconds at the throttle hold point. This is due to the change in the gas nozzle exit velocity conditions from the lower pressure and the nozzle heat transfer.

The flow stability conditions for the transient are shown in Figure 4.62. In this case the Reynolds number drops off with the flow. The slight increase in the turbine inlet temperature also causes the core inlet temperature to be slightly higher. The reduced flow causes a larger temperature rise input from the core moderator heat node and increases the fuel region inlet temperature. This acts to reduce the Reynolds number. It also acts to reduce the temperature rise factor, because the chamber conditions are fixed at 3000K. The fuel element is shown to be operated well away from any possible flow instability situation.

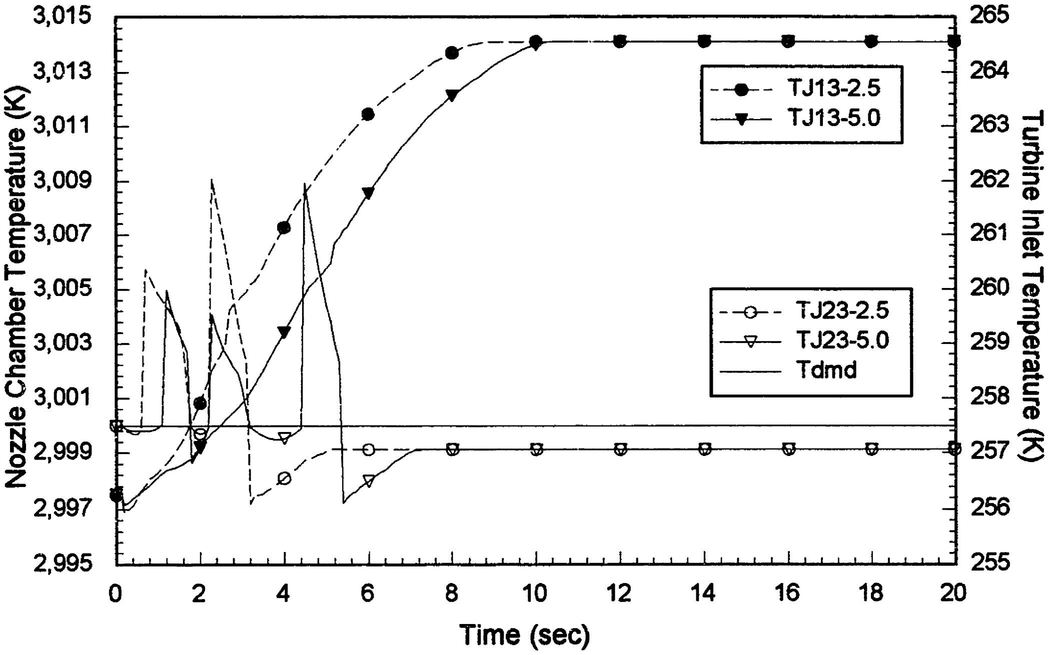

Figure 4.57 Temperature Response During PBR Throttle to 75%

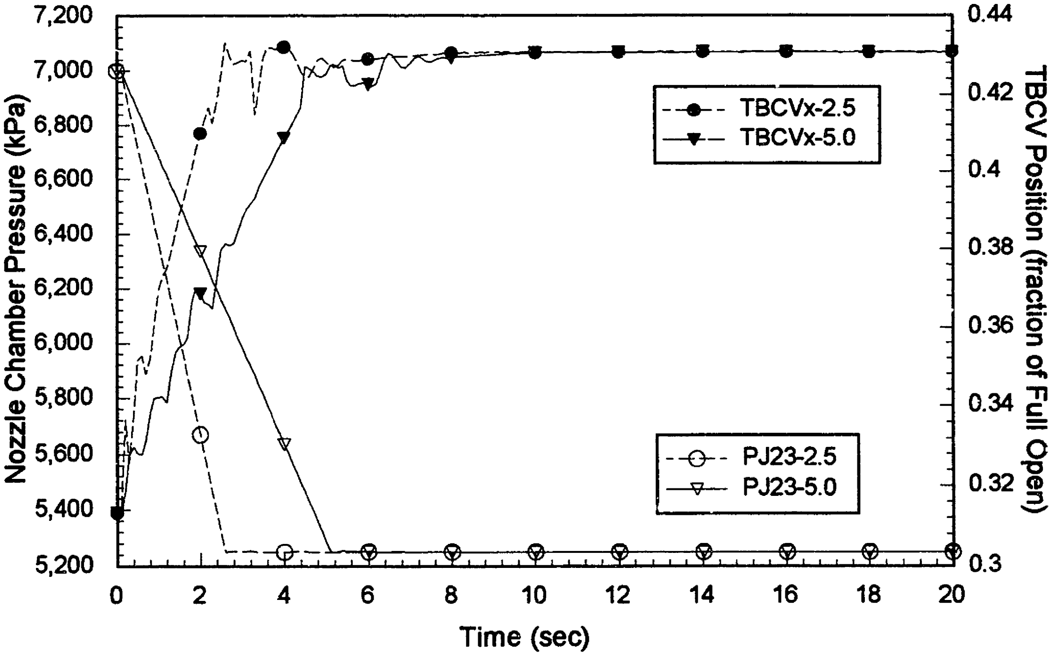

Figure 4.58 Pressure and TBCV Position Response During PBR Throttle to 75%

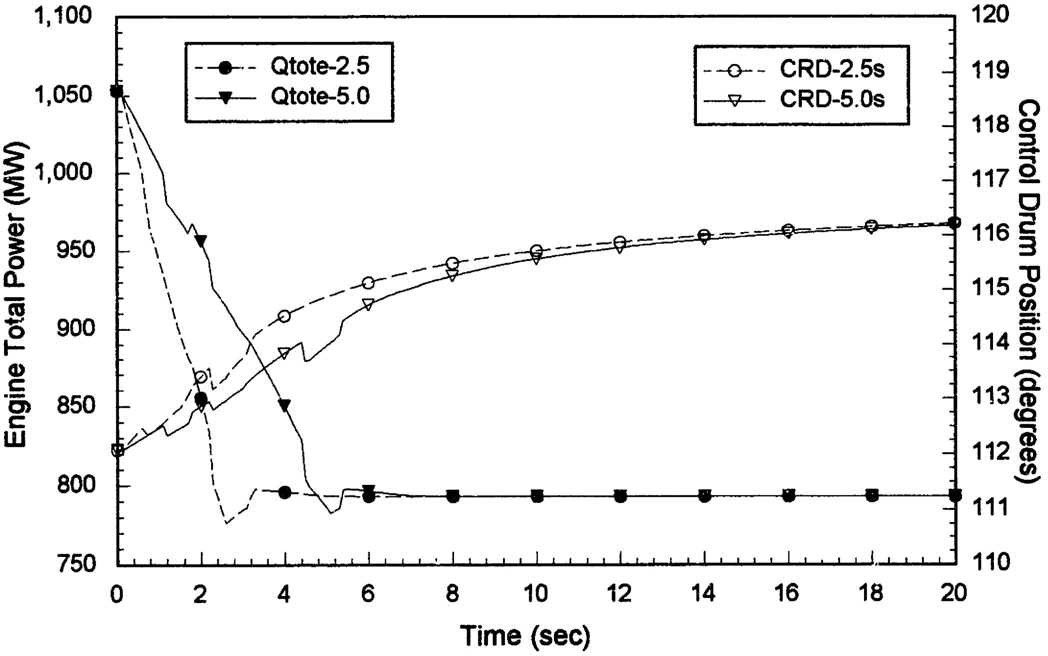

Figure 4.59 Power and CRD Position Response During PBR Throttle to 75%

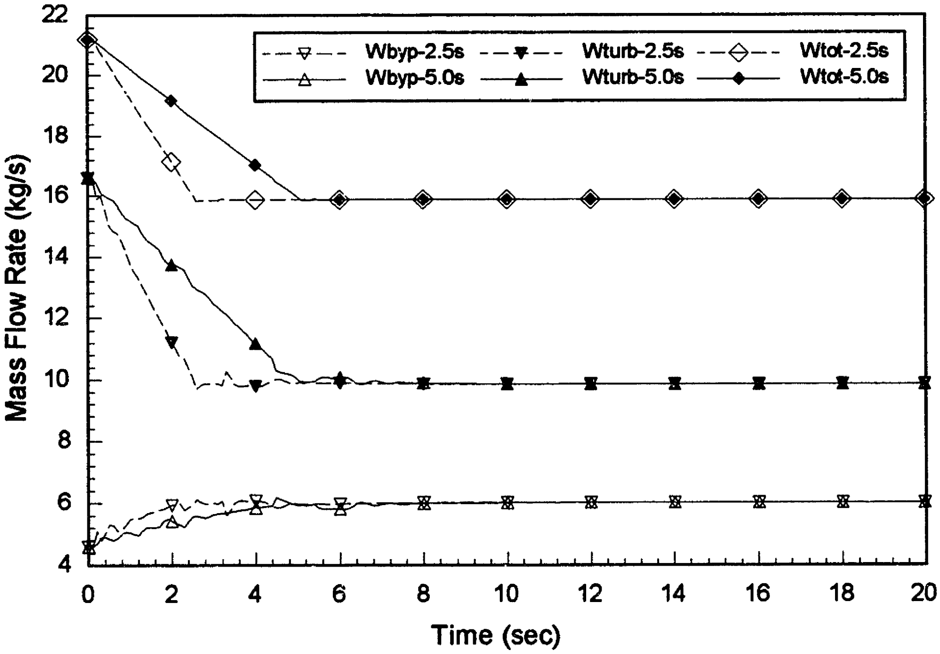

Figure 4.60 Mass Flow Rate Response During PBR Throttle to 75%

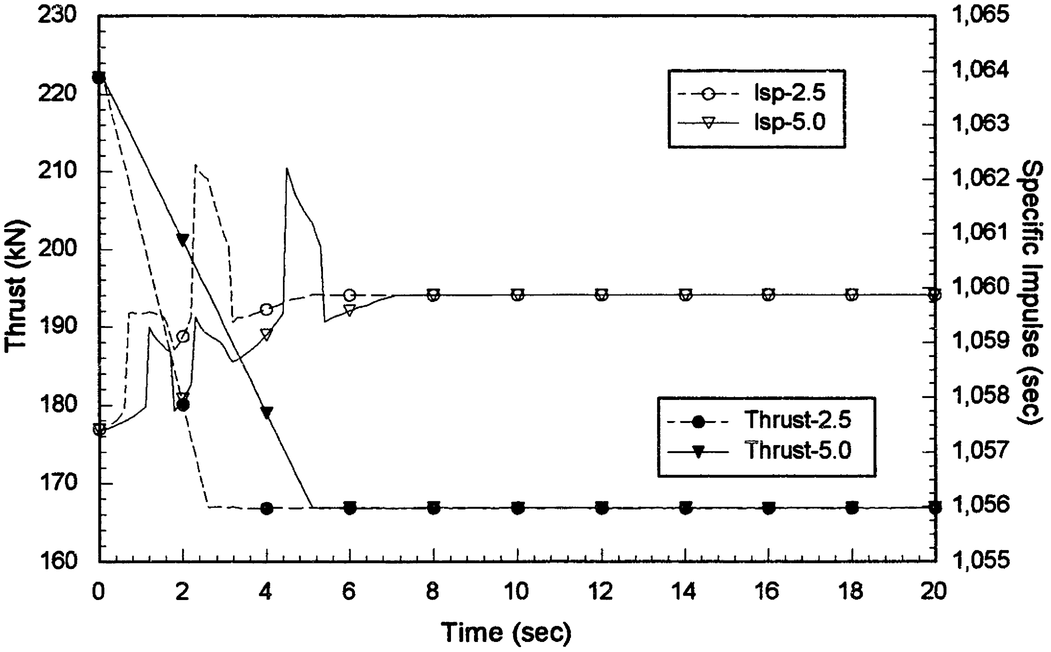

Figure 4.61 Thrust and Specific Impulse Response During PBR Throttle to 75%

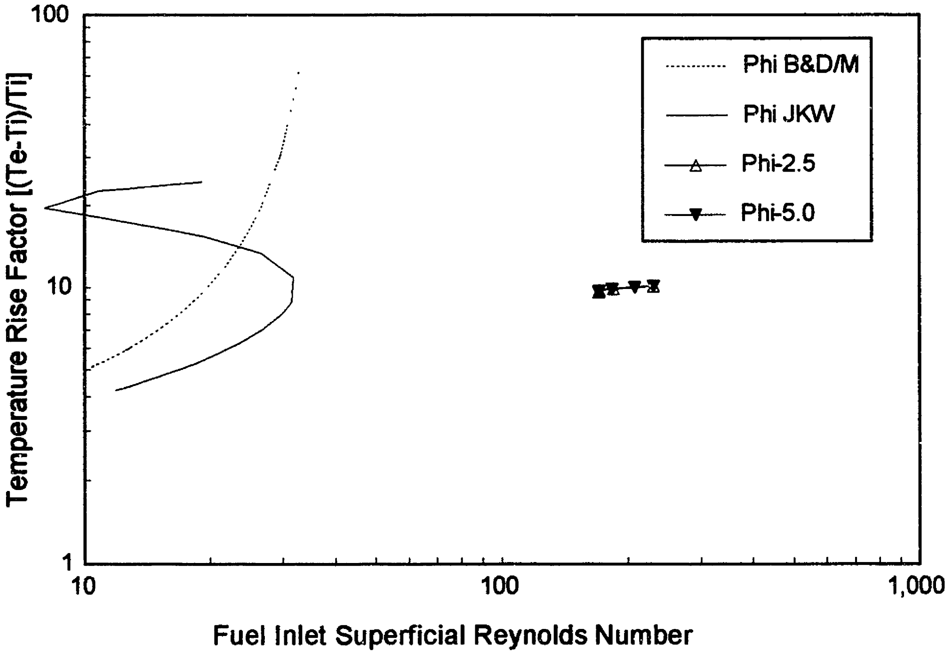

Figure 4.62 Stability Criterion Response During PBR Throttle to 75%

4.3.4.4 PBR Shutdown Transient Evaluation

The final transient to be evaluated is a PBR rocket engine shutdown. For the PBR, it was found necessary to shut the reactor down in a slightly different mode of control. This was due to the faster response time of the cooling of the fuel. When the transient was modeled as a throttle to 65% and then a reactor scram, the fuel cooled off too quickly for the pressure controller to be able to handle. The result was that the flow rate increased beyond the capacity of the turbo-pump. The rapid temperature response lead to a different shutdown strategy and also some concerns for the scram capability for the PBR concept. The shutdown scenario studied in this section consists of a 5 second throttle to 50% followed immediately by a 10 second controlled pressure and temperature reduction. During the course of the shutdown, the control drums end up shutting the reactor down. Once end of the demanded temperature retreat is reached, the control switches to the same as the post scram control used in the NERVA engine cases. The response of the key parameters is shown in Figure 4.63. The transient is well behaved up until the point that the final temperature hold point is reached. Then, the pressure control reacts dramatically to the temperature exceeding the desired hold point. This will be discussed in more detail in the following paragraphs. A detailed presentation of the engine parameters appears in Figures 4.64 through 4.70.

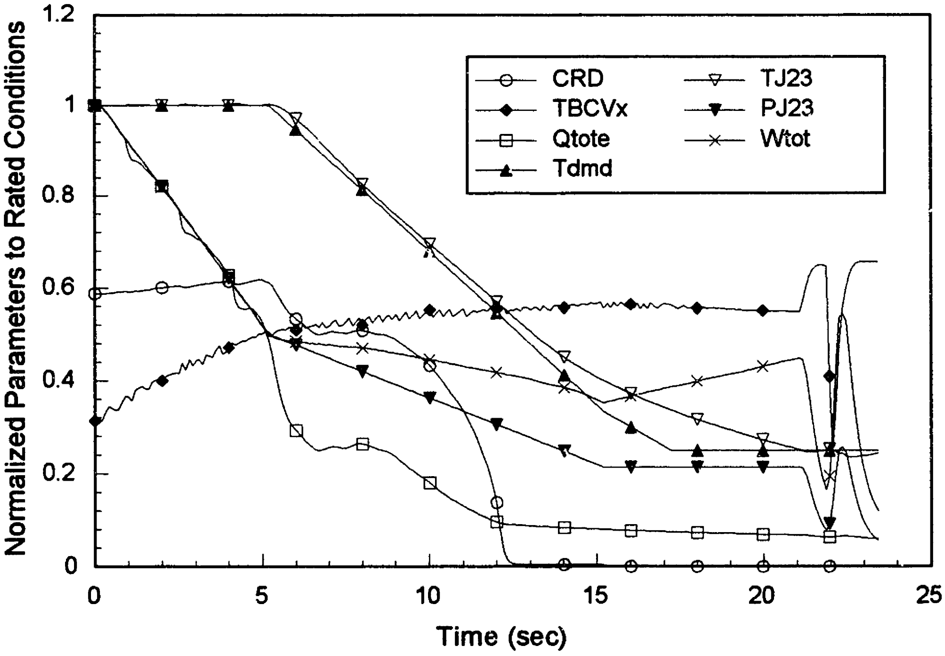

Figure 4.63 Prototypic PBR Engine Response to Shutdown Transient

The chamber, turbine inlet, and Junctions 4 and 7 temperatures are shown in Figure 4.64. The Junction 4 temperature decreases due to the reduction in the pumping power requirements for lower mass flow rates. The Junction 7 temperature increases during the throttle ramp due to the nozzle temperatures remaining high and the flow decreasing. Then as the nozzle temperatures are ramped down, the Junction 7 temperature also decreases, but at a slower rate. The turbine inlet temperature increases by approximately 10 K over the course of the throttle transient. This is due to the combination of the increase in Junction 7 temperature and the decrease in flow and power in the reflector region. During the temperature retreat, the turbine inlet temperature also follows the retreat, but has a slight reduction in its ramp rate when the power is held up at the 7 second point of the transient. The power is held up in order to prevent the chamber temperature from undershooting the desired trajectory. The chamber temperature hold constant during the throttle transient and then lags only by 100 K during the temperature retreat. Once the control drums are fully in, the temperature ramp diverges from the desired rate, because at this point the power can not be driven down any faster and the pressure is still under active control. At the 15 second point, the pressure shifts to the post scram mode of control, however, it is not until the 21 second point that the temperature reaches the hold point and the pressure can be ramped back. The small undershoot in temperature is tolerated by the controller, but once the temperature exceeds the desired value, the TBCV control acts too quickly and causes a large puff of flow to cool the system. At this point it would probably suite the system to switch to a preset TBCV position open loop control scheme. The final temperature demanded was 750 K instead of the 1000 K value used in the NERVA analysis in an attempt to lower the temperature rise factor across the fuel and thus increase the margin to possible flow instability.

Figure 4.65 depicts the response of the pressure and the TBCV position. The chamber pressure follows the demanded trajectory throughout the transient. This is even the case at the end of the transient when the controller cycles the flow to maintain the temperature. The control valve cycles open rapidly during the throttle transient and then more slowly during the temperature retreat. The rate is slowed during the later phase because the turbine inlet temperature is decreasing and flow path resistances are changing. The final stages of the shutdown are marked by rapid pressure puffs to keep the chamber temperature close to its demanded level. Because the nozzle flow rate is sensitive to the pressure at low pressures, the flow rate will respond as dramatically. The temperature response is fast for the PBR thus, the duration of the puffs can be short. If the transient were to be run for a longer period, the pressure spikes should appear less frequently and have a lower magnitude because the rate of change of the chamber temperature is lower than the original reduction rate at the 21 second point.

The power and control drum response is given in Figure 4.66. As was seen during the throttle discussions in the last section, the control drums rotate outward during the this phase of the shutdown. The power is reduced to the 50% level due to the negative reactivity added by the pressure reduction at rated chamber temperature conditions. The temperature retreat is commenced with a rapid inward rotation of the drums. This is done to drop the power rapidly so that the temperature will decrease as demanded. Once the temperature is on the desired ramp rate, the rate of power change is reduced to keep the temperature from undershooting the trajectory line. Because the pressure and flow rate are decreasing, the power must also be reduced to continue the temperature retreat. The drums must then be rotated inward in an increasingly fast rate as the differential drum worth becomes lower. The drums reach the full in position at 12.5 seconds into the transient. At this point the temperature reduction begins to diverge because the power is no longer able to be reduced beyond the rate that the delayed fissions and the decay heat die out.

Figure 4.67 shows the reactivity transient for this case. The positive reactivity addition due to the temperature reduction can be adequately handled because the drums have a full span worth of 10 dollars. During the throttle transient, the feedback reactivity becomes more negative due to the pressure reduction. Once the pressure and temperature begin their retreat, the negative feedback from the hydrogen reactivity is reduced. further positive reactivity is added by the fuel temperature reduction. At the end of the transient, the pressure coefficient can be seen in the oscillation of the reactivity. Because the temperature change is small during this time, this effect is primarily due to the pressure change. The total reactivity is that required to maintain the temperature at the demanded level up until the point that the drums are full in. During the throttle transient, this is inserted by the pressure reduction and the drums must add positive reactivity to maintain the proper reactor period. During the parameter retreat, the drums add the required negative reactivity against the now increasing feedback reactivity. Once the drums are full in, the total reactivity increases parallel to the feedback reactivity, but remains well below the critical point. Because a different shutdown strategy and different reactivity coefficients were used for this PBR study, the power and reactivity effects are less pronounced than in the NERVA engine shutdown.

The mass flow rates are shown in Figure 4.68. The system flow is ramped back to the 50% level during the throttle transient. The bypass flow remains nearly constant as the bypass valve opens to reduce the turbine drive flow and power. During the second phase of the shutdown, the flow is maintained nearly constant as the pressure and temperature are reduced. This reduction path was selected by studying the operating map shown in Figure 4.14 and bringing the power down along a path that is close to the 10kg/sec flow line. This assured that the turbopump would be capable of the flow conditions and the fuel element avoided possible flow instability conditions. The flow perturbations at the end of the transient are large due to the flow being proportional to the chamber pressure. The thrust and specific impulse are plotted in Figure 4.69. As explained in previous sections, these parameters follow the chamber pressure and temperature responses closely.

Finally, Figure 4.70 presents the response of the flow stability conditions during the shutdown. During the throttle transient, the Reynolds number is reduced by the flow reduction and the rise in gas viscosity, while the temperature rise factor is held fairly constant around 10. On this curve, the transient begins at the upper right portion of the "Phi Shutdown" curve. As the temperature and pressure are reduced, the Reynolds number increases. This occurs because the flow rate is being held nearly constant while the inlet temperature reduces the gas viscosity. The temperature rise factor decreases because the chamber temperature is being lowered. Once the final temperature hold point is reached, the Reynolds number undergoes some oscillations. These coincide with the pressure oscillations required to hold the temperature constant. As a point of time reference and a means to compare this curve to the other curves, the triangle markers coincide with the markers on the previous curves.

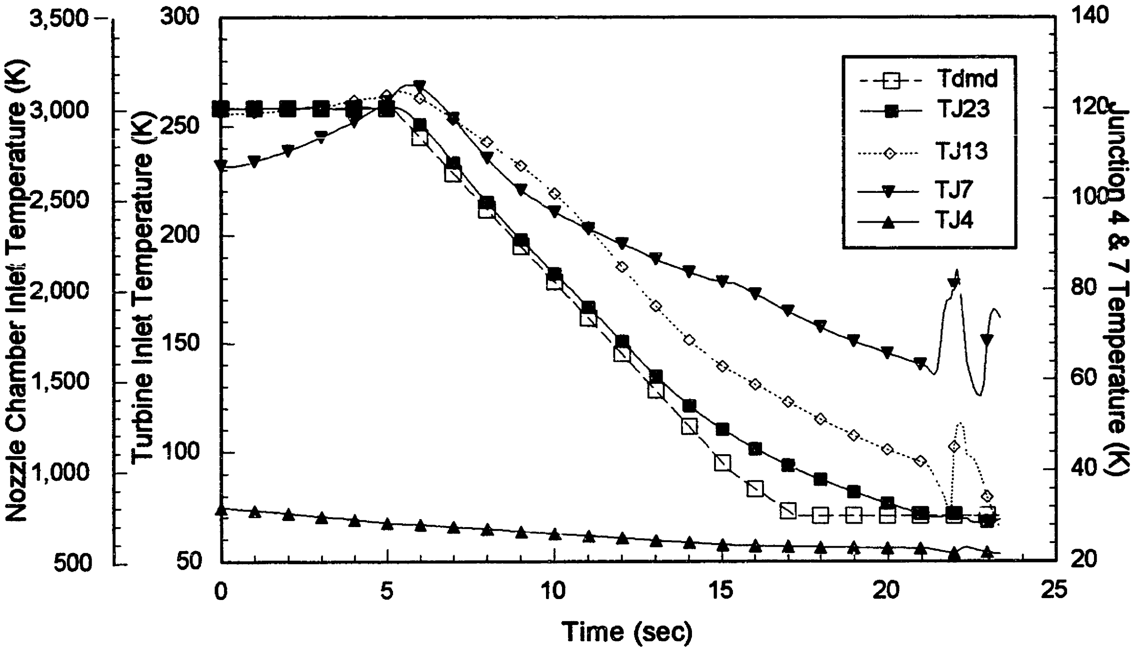

Figure 4.64 Temperature Response During Prototypic PBR Shutdown Transient

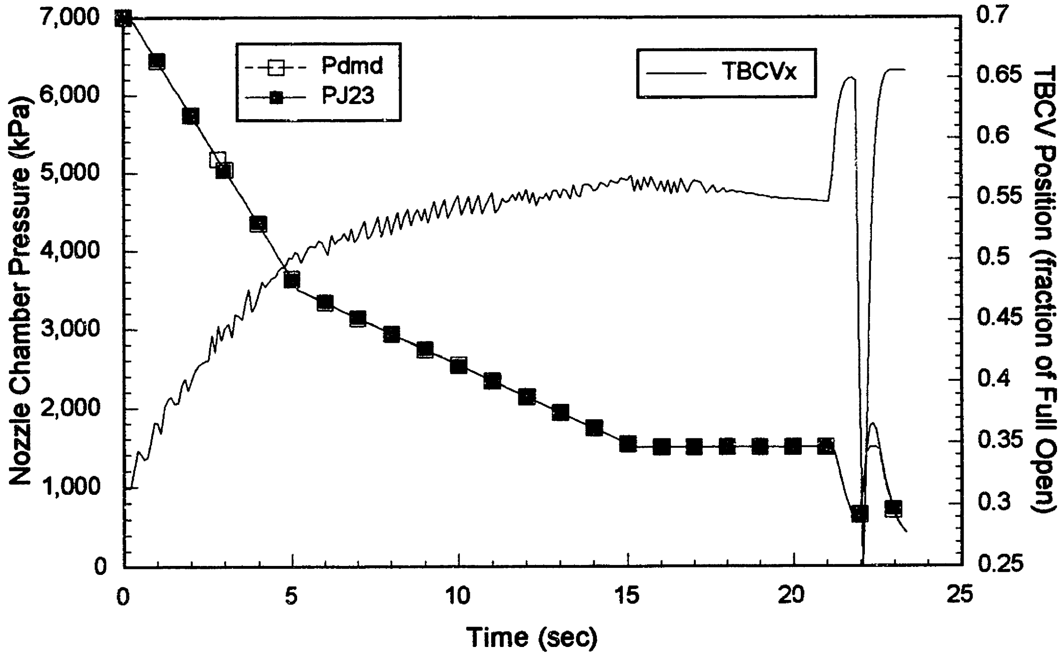

Figure 4.65 Pressure and TBCV Position Response During Prototypic PBR Shutdown Transient

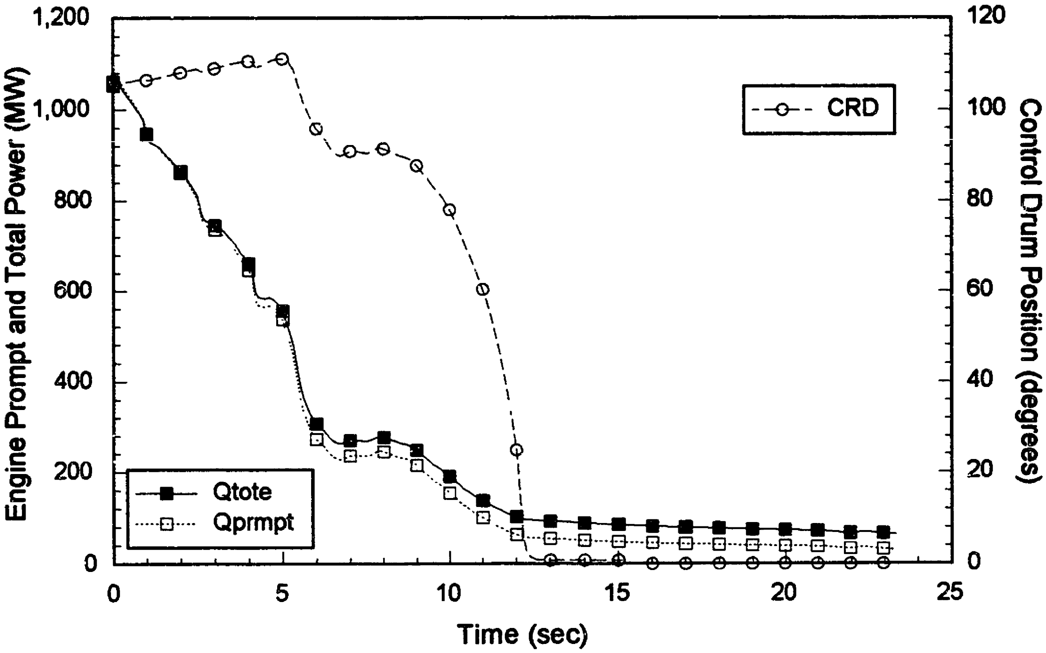

Figure 4.66 Power and CRD Position Response During Prototypic PBR Shutdown Transient

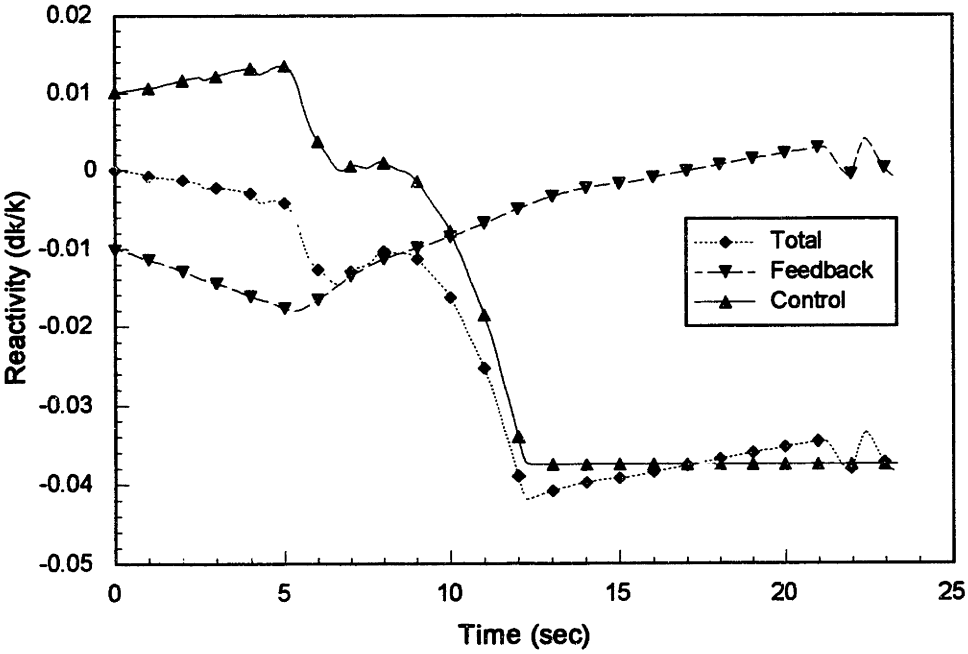

Figure 4.67 Reactivity Response During Prototypic PBR Shutdown Transient

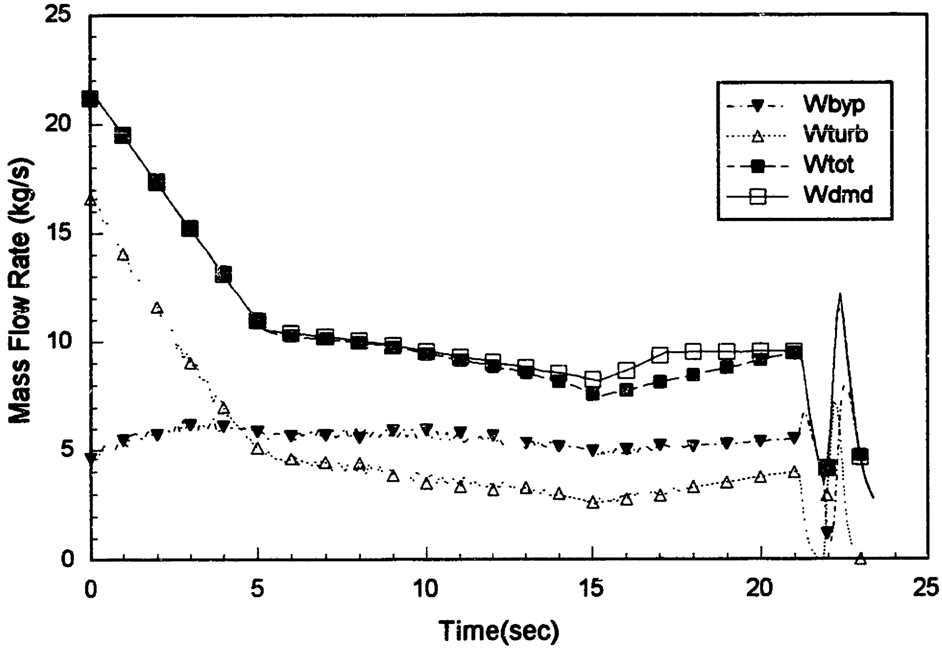

Figure 4.68 Mass Flow Rate Response During Prototypic PBR Shutdown Transient

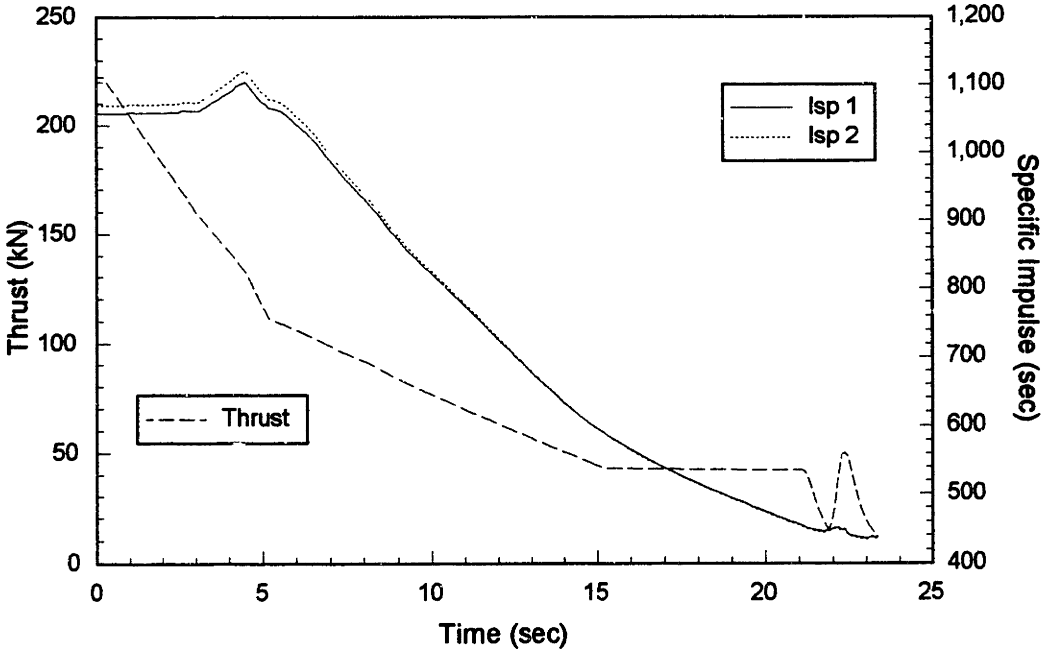

Figure 4.69 Thrust and Specific Impulse Response During Prototypic PBR Shutdown Transient

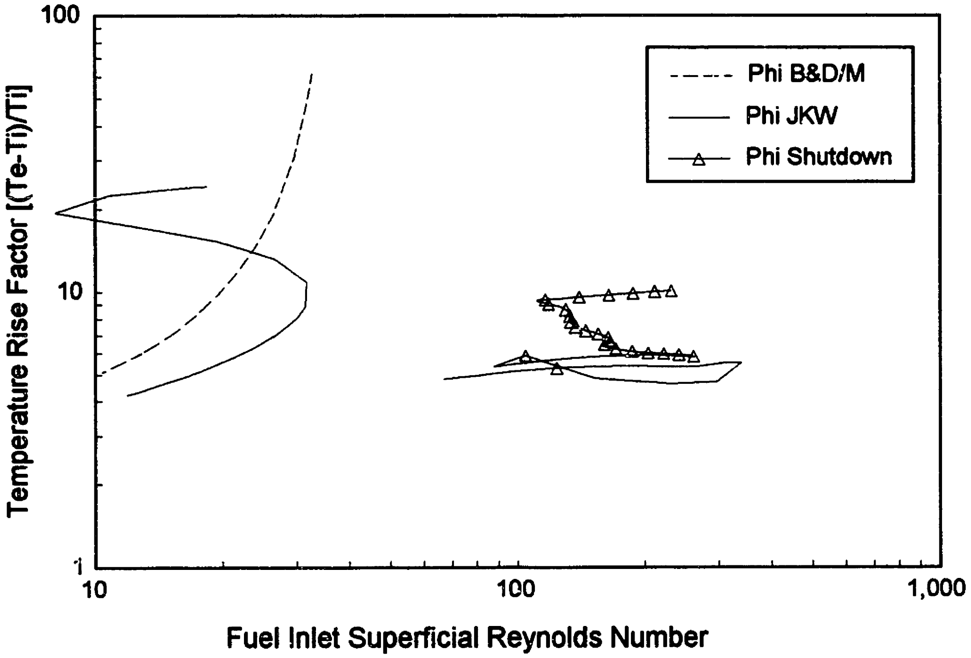

Figure 4.70 Stability Criterion Response During Prototypic PBR Shutdown Transient

This concludes the transient analysis for the PBR engine concept. The studies show that ENGTRANS can model the PBR engine and that some changes to the power maneuver trajectories may be needed. The scram shutdown scenario used by the NERVA program could not be used for the PBR with the current control strategy implemented in ENGTRANS. Because the temperature response is faster, the cooldown occurs more quickly for a given chamber pressure. This in turn can cause a large reactivity addition if the system pressure is not reduced quickly enough and can also act to increase the mass flow rate. The ENGTRANS simulations run on the PBR indicate a possible method for shutting the reactor down in a controlled manner, but scram situations may required a different means of reducing the pressure while maintaining the fuel operating outside the possible flow stability region.

4.4 Chapter Summary

This chapter presented the results from studies on the NERVA and PBR engines using the full engine computer models developed as part of this research effort. The steady state analysis was used to show the operational state points during bleed flow and power operation. The power operation NERVA cases were benchmarked to the existing CAC code results. The PBR cases were presented as an extension of the element models in Chapter 3 and the NERVA engine cases. The methodology for generating operating maps from the steady state point was discussed and then applied for the prototypic NERVA and PBR rocket engines. The maps were used to determine chamber temperature and pressure trajectories for transient evaluations. Transient studies were undertaken to show the behavior of the control systems and the engine components. The controls were shown to be affected by the control drum rotation speed and the response rate of the drums and the turbine bypass control valve. The ENGTRANS code was shown to model the NERVA engine transients presented in Reference [W-6]. The ability for the computer code to model deep throttle transients was also shown. The same series of transient were run on the PBR engine to show some of the different operational considerations and possibilities for this concept. The core design used was shown to avoid possible flow instability regions throughout each of the transients. The code was shown to be able to handle rapid transients that may be utilized to take advantage of the PBR heat transfer characteristics. Numerical and physical problems were shown to exist during startups from low power when there is little heat addition to the hydrogen flow stream before the turbine. These problems occur when the hydrogen is in a state near the saturation and/or critical temperature and pressure when entering the reflector region. Special design considerations may be necessary to maintain sufficient reactivity margins during off normal operating conditions.

Chapter Five - Summary, Conclusions, and Recommendations

5.1 Summary

5.1.1 Summary of Existing Thermal Hydraulic Models

A review of the computer codes that were found to be applicable to the modeling of nuclear rocket systems was presented in Chapter 1. The programs each had some limitations when it came down to modeling the entire engine system. The CAC computer program, obtained from NASA Lewis, is a useful tool for the analysis of the NERVA reactor thermal hydraulic behavior. The Sandia SAFSIM code, selected as the baseline code for the NASA-DOE-DOD Phase I modeling effort, was also obtained from NASA for use by the MIT Nuclear Engineering Department. This code continues to be developed as part of the NASA-DOE-DOD effort. These codes are limited for simulation of the entire rocket engine because some components are not modeled. The ROCETS code has been used by Pratt & Whitney to simulate chemical rockets, but is currently only in the early stages of being able to model nuclear reactors. For these reasons, new programs were developed to be able to model both the NERVA and PBR fuel geometries.

5.1.2 Summary of One Dimensional PBR Element Modeling

The one dimensional PBR fuel element models were presented in Chapter 3. The steady state code, PBRFMP, and transient code, TRITRAN, are an extension of the STEADY and UPPOWER computer codes written by William Casey in Reference [C-5]. Enhancements to the steady state model included adding more control volumes, allowing different boundary conditions to be specified, and changing the heat transfer calculation to the Achenbach correlation. In addition to the changes made for the steady state code, the transient code added the capability to model three ramps of the boundary conditions and modeled the power and reactivity with the MIT/SNL control law methods. A correction to the hydrogen mass calculation for the fuel region node was made that removed the time lag noticed by Casey in Reference [C-5]. Results from cases run using the data from Reference [C-5] validated the new computer code. The cases run showed the ability of the transient code to handle a wide variety of operational transients and provided the basis for the methodology adopted for the full engine model.

5.1.3 Summary of Two Dimensional PBR Element Modeling

The two dimensional modeling focused on the use of the SIMBED code that was acquired from the Brookhaven National Laboratory. The code proved to be a useful tool for studying the thermal hydraulic conditions in the PBR fuel element. Enhancements to the program included added the capability to model cold frit flow resistance distributions, non-uniform power shapes, and single node porosity variations. Examples of the impact of these parameters on the flow pattern and gas temperature were given in graphical form to show the capability of SIMBED and to help understand the flow behavior through visualization. The power shape was shown to have an impact on the temperature and flow distributions, with the higher power regions having a hotter temperature and lower flow. Running cases with a linear or parabolic distribution for the cold frit flow resistance terms showed that this can be an effective method for flattening the flow maldistribution effects from non-uniform power shapes. Cases run with a single node porosity change showed that the effects are highly localized to the perturbed radial flow stream.

5.1.4 Summary of Flow Instability Analysis

Flow instability in the PBR fuel element is a concern due to the limited design safety margin while operating at high power densities and temperatures. If the flow were to be unstable in the bed, the damage could be catastrophic. One dimensional flow instability analysis was presented as an extension of a qualitative method developed at Brookhaven National Laboratory by George Maise, which itself was adapted from early work by Bussard and DeLauer. The approach taken in this research was to use the one dimensional PBR fuel element computer model and modify it to find the locus of the critical flow rates and temperature rise factors for a given power level. The critical points are determined at the minimis of the pressure drop versus flow rate curve. Plotting the results of this quantitative method for an actual element geometry against the simple qualitative stability criterion showed curves with similar shapes. The stability criterion line is affected by element geometry factors and inlet hydrogen conditions. The two dimensional SIMBED model was used to determine flow stability critical points from the average pressure drops in the radial direction. These points were shown to yield consistent results with the one dimensional model. The SIMBED code was also used to evaluate the flow behavior in the fuel region when there is a power shape and the element is operating near the one dimensional flow instability line. The shift in temperature and mass flow rate distribution over the course of iterations was shown to be consistent with flow behavior predicted in Reference [V-1].

5.1.5 Summary of Full Engine Modeling

The full engine modeling effort was presented in Chapter 4. The computer code ENGBLEED was developed to study steady state conditions for engine operation with only the tank head as the propellant driver. The code was used to show the decay heat removal capability and the pre-bootstrap phase of operation. Another steady state code ENGSS was written to determine operating points for an engine with pump flow. The ENGSS NERVA reactor model was validated by comparing results from the NASA CAC program. The PBR reactor model is essentially an extension of the single element model that was validated as part of the work performed in Chapter 3. The ENGSS program was then used to define the operating maps for the engines used in the transient analysis of this report. The final computer program developed was the ENGTRANS code for studying the transient response of a user defined rocket engine. The code was benchmarked by comparing results from NERVA engine startup and shutdown simulations to data taken from graphs in Reference [W-6]. While the engine cycles were not the same, portions of the transients behaved similar to those given in Reference [W-6]. Results from startup, throttling, and shutdown transient cases were presented for both the NERVA and PBR engines to show the versatility of the computer code.

5.2 Conclusions

Several conclusions can be drawn from the computer code development and the studies completed with the programs. These will be presented in the next sections.

5.2.1 Conclusions on One Dimensional PBR Element Modeling

1. The PBR element can be adequately modeled in a one dimensional geometry in order to gain an understanding of the broad thermal hydraulic behavior of the element. This includes the radial temperature distributions of the effective fuel temperature and the hydrogen gas and the radial pressure distributions. Quick element geometry studies can be performed to ensure the element exit Mach number is less than 0.2, while still maintaining values of flow rate and temperature rise so that the flow remains in the stable region. The validity of the one dimensional code was confirmed by comparing results to the two dimensional code results.
2. The extension of the UPPOWER code to have a point kinetics with feedback model for the reactor power, to implement the MIT/SNL control method, and to allow multiple boundary condition ramps was successfully implemented. The TRITRAN code showed that the PBR element has a fast thermal response. It also set the methodology framework for the full engine computer models.

5.2.2 Conclusions on Two Dimensional PBR Element Modeling

1. The SIMBED code modifications allow evaluations to be performed for more realistic heat deposition shapes and cold frit flow resistance distributions. The power distribution will cause a temperature profile to be set up with the same general shape and a radial flow distribution to be set up with an inverse shape. Varying the cold frit flow resistance was shown to be an effective means of modifying the fuel region temperature distribution for a particular operating condition.
2. Off normal perturbations in single nodes show that the disturbances in the flow stream parameters are highly localized. The SIMBED code can adequately model such perturbations.

5.2.3 Conclusions on Flow Instability Analysis

1. The one dimensional, steady state, PBR fuel element model was successfully modified to generate flow stability maps for a user defined geometry and inlet boundary condition. The numerical maps show that the geometry and "real" gas

properties expands the region of instability to higher Reynolds numbers and lower temperature rise factors. The dissociation of hydrogen at the higher gas temperatures and lower pressures can help the element flow stability for the radial flow pressure drop considerations. Designs for operations and fuel must consider methods to avoid the possible flow instability regions.

2. The two dimensional flow instability analysis yielded similar results to the one dimensional case when consideration was given to the average radial pressure drop. This indicates that the one dimensional analysis is adequate for defining the region of interest for stability concerns.
3. When used to analyze the impact of non-uniform heat deposition distributions, the SIMBED code indicates that these shapes can have a negative impact on stability. The growing divergence of the flow maldistribution as the program iterations proceed is consistent with theoretical predictions; however, no definitive conclusion can be drawn from this two dimensional steady state analysis.

5.2.4 Conclusions on Full Engine Modeling

1. The effort to model a nuclear thermal propulsion engine was successfully completed. The model can handle both the NERVA and PBR fuel geometries. The user is able to define the system piping dimensions and performance parameters for a preset expander/topping cycle configuration. The thermal conductivity and heat capacity values for the reflector, nozzle, fuel, and moderator materials are also able to be defined by the user as a function of temperature. Because much of the model is able to be user defined, the tool can be as detailed as desired.
2. Flow stability concerns can be alleviated through the proper selection of a fuel element geometry and core design. The engine model for the PBR fuel shows that the temperature rise factor stays within a narrow band due to the changing inlet conditions from the heating of the fluid before it reaches the fuel. The Reynolds number is also affected by these changing conditions so that, even at lower flows, the element continues to operate outside the regions of instability.
3. The properties of hydrogen at low temperatures can impact the design, simulation, and control of the rocket engines. The spikes observed during the startup transients

described in Chapter 4 indicate that the flow is more sensitive to pressure and temperature changes at these lower values than when closer to rated conditions. Because the properties have large gradients and are also changing quickly with time, numerical evaluations may have a difficult time in handling perturbations. The design of the rocket must ensure that sufficient heat is added to the flow stream in order to drive the turbine and to ensure that the reactivity worth is not to large in the reflector and at the reactor entrance. The control of the reactor during initial startup and final shutdown phases may require open loop scheduling of the control drums and the turbine bypass control valve.

4. The Particle Bed Reactor appears to require a different strategy for shutdown than was used for the NERVA program, due to the faster thermal response of the fuel form. The pressure and temperature should be reduced together in order to possible avoid flow instability regions and to allow the final temperature decrease rate to be controllable. Once the final temperature hold point is reached, the turbine bypass valve should be set to a position that will allow the temperature to be maintained close to the final temperature, but allowed to drift as the power level decays with time.
5. The impact of excess positive feedback reactivity was noticed for the NERVA shutdown case. Maintaining the chamber pressure relatively high while trying to reduce the temperature along a trajectory path contributed to the hold up of the temperature drop due to a small power increase as the hydrogen mass content increased in the core and reflector regions. For the PBR, the shutdown strategy had to be altered to accomodate the more rapid cooldown upon the loss of power. If the PBR reactor were to scram, the rapid cooldown indicates that one would want to ensure that the pressure is also reduced quickly to avoid the reactivity and power excursions noticed in early NERVA tests.

5.3 Recommendations

5.3.1 Further Two Dimensional PBR Element Studies

1. One study that should be considered is a case with a variable fuel region porosity. The case run in this report used a constant value for regions away from the wall, except for the single node perturbation studies. The variable porosity study could be implemented with the use of a random number generator to calculate a value of porosity for a particular node from a statistical distribution of the fuel bed porosity. This study could provide insights into the effects that "real" bed packings have on the thermal hydraulic conditions of the element.
2. Obtain the two dimensional transient version of SIMBED and run a null transient at the element conditions used in section 3.5.3 in order to determine if the divergence noted is real and to determine the time constant of the flow maldistribution. Cases could also be run from an initial operating condition outside the stability line and back the operating point towards the line in order to see if flow instabilities can be found.

5.3.2 Enhancements to Robustness of Engine Simulation

1. The engine simulation code ENGTRANS was shown to be capable of modeling a wide variety of transients and engine sizes. It is, however, limited to the geometry defined by Figure 4.1. Since bleed flow engines have been proposed and may be easier to develop the turbine drive flow, an option for this engine type should be developed. To address the issues of the low temperature hydrogen with respect to the turbine and reactor control, different flow paths could be added to flow bypass the nozzle and the reflector and then rejoin after the turbine. The would force a higher temperature at the turbine inlet, but should have a negligible effect at the core inlet due to the total energy balance before the core remaining the same. When this model is completed, comparisons of the engine types could be performed to show the tradeoffs between the concept operational behavior and requirements.
2. To date, the transient code has not been optimized for speed. Due to the short transients involved with rocket operations and the variation in the hydrogen

properties, short time steps are required. Adding variable time stepping routines and optimizing the program logic could improve the speed of the simulations.

3. Additional modes of control and operation should be added to study the impact of an unanticipated scram. This would allow one to evaluate the importance that the cooldown and depressurization rate play in the shutdown transient. The high reactivity worth of the hydrogen makes it necessary to minimize the hydrogen mass or pressure in the reflector and the core in order to keep the reactor on a negative period. As was used in the NERVA experiments, the rapid opening of the turbine control valve helps to reduce the pressure quickly and helps to maintain the overall reactivity within the bounds of the control drum safe shutdown reactivity worth.

5.3.3 Coupling Neutronics to Thermal Hydraulics

1. The ENGTRANS code was written with the consideration for allowing power inputs from a reactor physics code. The peaking factors for the radial and axial positions provide the mechanism for this interface. The thermal hydraulic parameters can be readily obtained from the ENGTRANS code and can be used as input to the neutronic models. The ring geometry of the ENGTRANS core makes the use of an R-Z code such as ZAQ [B-13] a viable candidate for such an undertaking.

5.3.4 Three Dimensional and Transient Analysis of Flow Stability in PBR Element

1. The two dimensional analysis presented in Chapter 3 gave understanding of some of the flow phenomena in the PBR fuel element. The flow in a packed particle bed is really a three dimensional phenomena, therefore it would be desirable to repeat the cases run in two dimensions with a full three dimensional model. The SAFSIM code does have a three dimensional steady state and transient version, but this was not available for distribution at the time of this writing. Another code that has been used to model the PBR fuel element is the TEMPEST thermal hydraulic code from Oak Ridge National Laboratory and could be obtained from the DOE Energy Software Center.
2. When the computer codes become available, three dimensional transient cases should be run to gain a better understanding of the flow behavior in the packed bed. These

runs should also be able to determine more definitively the possibility and mechanisms involved with the flow maldistribution or instability under various operating conditions. Clarification of the element temperature and mass flux behavior described in section 3.5.3 could provide insight to whether this phenomenon occurs only when close to the stability line or this can occur over a larger range of Reynolds numbers and temperature ratios.

References

A-1 S. Anghaie, et al, "A Numercial Simulation Package for Analysis of Neutronics and Thermal Fluids of Space Nuclear Power and Propulsion Systems," in Proceedings of Tenth Symposium on Space Nuclear Power and Propulsion, CONF-930103, M. S. El-Genk and M. D. Hoover, eds., American Institute of Physics, New York, 1993 1697.

A-2 E. Achenbach, "Heat Transfer and Pressure Drop of Pebble Beds up to High Reynolds Number," in Proceedings of the Seventh International Heat Transfer Conference, Munchen, FRG, Volume 6, Hemisphere Publiching Corp., 1982 3.

B-1 D. L. Black and S. V. Gunn, "A Techinical Summary of Engine and Reactor Subsystem Design Performance During the NERVA Program," AIAA 91-3450, 1991.

B-2 R. M. Ball, et al, "Operational Performance of the Three Bean Salad Control Algorithm on the ACRR," in Proceedings of Eigth Symposium on Space Nuclear Power Systems, CONF-910116, M. S. El-Genk and M. D. Hoover, eds., American Institute of Physics, New York, 1991 687.

B-3 J. A. Bernard, "A Comparison of Proportional and Model-Based Control Techniques for Nuclear Reactors," in Proceedings of Eigth Symposium on Space Nuclear Power Systems, CONF-910116, M. S. El-Genk and M. D. Hoover, eds., American Institute of Physics, New York, 1991 693.

B-4 R. W. Bussard and R. D. DeLauer, Nuclear Rocket Propulsion, McGraw-Hill, New York, 1958.

B-5 R. W. Bussard and R. D. DeLauer, Fundamentals of Nuclear Flight, McGraw-Hill, New York, 1965.

B-6 D. L. Black, G. E. Klinzig, and J. W. Tierney, "Temperature Induced Laminar Instabilities in a Gaseous Heated Channel," Nuclear Engineering and Design, Volume 40, 1977 225.

B-7 M. Barrere, et al, Rocket Propulsion, Elsevier Publishing Company, New York, 1960.

B-8 J. A Bernard, Formulation and Experimental Evaluation of Closed-Form Control Laws for the Rapid Maneuvering of Reactor Neutronic Power, MITNRL-030, Massachusetts Institute of Technology Nuclear Reaactor Laboratory, Cambridge, MA, September 1989.

B-9 J. A Bernard, D. D. Lanning, "Quarterly Progress Report on Grant #DE-F607-90ER12930 Closed Loop digital Control of Multi-Modular Reactors," Massachusetts Institute of Technololgy Nuclear Reactor Laboratory, Cambridge, MA, Septermber 1991.

B-10 R. F. Benenati, C. B Brosilow, "Void Fraction Distribution in Beds of Spheres," Amercan Institute of Chemical Engineering Journal, Volume 8, Number 3, July 1962 359.

B-11 J. J. Barker, "Heat Transfer in Packed Beds," Industrial and Engineering Chemisty, Volume 57, Number 4, April 1965 45.

B-12 D. L. Black, G. E. Klingzing, J. W. Tierney, "Laminar Flow Instability in Multiple Channels," Nuclear Engineering and Design, Volume 53, 1979 355.

B-13 M. E. Byers, "A Transient Nodal Method for Reactor Models in R-Z Geometry," Ph. D. Thesis, Department of Nuclear Engineering, Massachusetts Institute of Technology, September 1992.

C-1 J. S. Clark (Editor), Nuclear Thermal Propulsion, A Joint NASA/DOE/DOE Workshop, NASA CP-10079, Cleveland, OH, July 10-12, 1990, 1990.

C-2 J. S. Clark, "Analytic and Experimental Study of Startup Characteristics of a Full-Scale Unfueled Nuclear Rocket-Core Assembly," NASA TM X-1231, 1966.

C-3 J. S. Clark, "Comparison of Predicted and Experimental Operating Characteristics of a Nuclear-Rocket-Core Assembly," NASA TM X-1232, 1966.

C-4 M. Charmchi, et al, "Thermo-Hydraulic Characteristics of Gas-Cooled Particle Bed Reactor," in Proceedings of 4th International Topical Meeting of Nuclear Reactor Thermal Hydraulics (NURETH-IV), Karlsruhe, FRG, Volume 1, 1989 139.

C-5 W. E. Casey, "Thermal-Hydraulic Transient Analysis of a Packed Particle Bed Reactor Fuel Element," SM and Naval Engineer Thesis, Department of Nuclear Engineering, Massachusetts Institute of Technology, May 1990.

D-1 D. Dobranich, "SAFSIM Input Manual, A Computer Program for the Engineering Simulation of Flow Systems," SAND92-0694, Sandia National Laboratories, September, 1992.

D-2 D. Dobranich, "Parametric Calculations: Effect of Reduced Thrust Levels on the Performance of a Particle bed Reactor Propulsion System," internal memo to Dave Beck, Sandia National Laboratory, August 14, 1992.

E-1 S. Ergun, "Fluid Flow Through Packed Columns," Chemical Engineering Progress, Volume 48, February 1952 89.

H-1 R. R. Holman and B. L. Pierce, "Development of NERVA Reactor for Space Nuclear Propulsion," AIAA 86-1582, 1986.

H-2 D. P. Harry, "Formulation and Digital Coding of Approximate Hydrogen Properties for Application to Heat-Transfer and Fluid Flow Computations," NASA TND-1664, May 1963.

H-3 A. F. Henry, Nuclear Ractor Analysis, The MIT Press, Cambridge, MA 1975.

H-4 J. C. Hedstrom, W. L. Kirk, L. J. Sapir, "Phoebus Reactivity Analysis (U)," LA-4180-MS, Los Alamos Scientific Laboratory, June 1969.

I-1 INEL, "ATHENA Computer Code," Description sheet BL422DD-R0289-1M-T, Idaho National Engineering Laboratory, 1990.

K-1 D. R. Koenig, "Experienced Gained from the Space Nuclear Rocket Program (Rover)," LA-10062-H, Los Alamos National Laboratory, May 1986.

L-1 S. K. Lee, "Application of a General Fluid Mechancis Program to NTP System Modeling," in Proceedings of Tenth Symposium on Space Nuclear Power and Propulsion, CONF-930103, M. S. El-Genk and M. D. Hoover, eds., American Institute of Physics, New York, 1993 1505.

L-2 Lockheed, "RIFT System Analysis, Volume 5: Propulsion," NASA-CR-63492, Lockheed Missiles & Space Company, April 1964.

M-1 R. R. Mohler and J. E. Perry, "Nuclear Rocket Engine Control," Nucleonics, Volume 19, Number 4, April 1961.

M-2 W. W. Madsen, et al, "Nuclear Propulsion Systems Engineering," AIAA 91-3447, 1991.

M-3 G. Maise, "Flow Stability in the Particle Bed Reactor," Informal Report BNL/RSD-91-002, Brookhaven National Laboratory, January 1991.

M-4 R. D. McCarty, J. Hard, H. M. Roder, National Bureau of Standards Nomograph 168, United States Department of Commerce, February, 1981.

N-1 NASA, "Nuclear Thermal Rocket Engine Requirements," NPO-2, Revision 3, National Aeronautics and Space Administration, Lewis Research Center, Cleveland, OH, February 1992.

N-2 H. H. Norman, et al, "NERVA Flight Engine Control System Design," Nuclear Technology, Volume 15, September 1972.

P-1 J. R. Powell, T. E. Botts, "Particle Bed Reactors and Related Concepts," in Proceeding of a Symposium on Advanced Compact Reactor Systems, National Academy of Sciences, Washington D. C., November 15-17, 1982, 1983 95.

P-2 D. G. Pelaccio, et al, "Nuclear Thermal Propulsion Engine System Design Analysis Code Development," in Proceedings Ninth Symposium on Space Nuclear Power Systems, CONF-920104, M. S. El-Genk and M. D. Hoover, eds., American Institute of Physics, New York, 1992 937.

P-3 J. R. Powell, et al, "Particle Bed Reactor Multimegawatt Concepts," BNL-39495, Brookhaven National Laboratory, March 1987.

R-1 W. H. Robbins, H. B. Finger, "An Historical Perspective of the NERVA Nuclear Rocket Engine Technology Program," AIAA 91-3451, 1991.

R-2 L. H. S. Roblee, R. M. Baird, J. W. Tierney, "Radial Porosity Variations in Packed Beds," American Institute of Chemical Engineering Journal, Volume 4, Number 4, December 1958 460.

S-1 Stafford (Chairman), "America's Space Exploration Initiative: America at the Threshold," The Report of the Stafford Committee to the President of the United States, May 1991.

S-2 E. A. Sheridan and H. S. Kirschbaum, "Nuclear Rocket Engine Controls," AIAA Paper No. 66-1005, 1966.

S-3 C. M. Scheil, D. G. Pelaccio, and L. J. Petrosky, "Nuclear Engine System Simulation (NESS) Program Update," in Proceedings of Tenth Symposium on Space Nuclear Power and Propulsion, CONF-930103, M. S. El-Genk and M. D. Hoover, eds., American Institute of Physics, New York, 1993 1523.

S-4 D. E. Suzuki, "Development and Analysis of Startup Strategies for a Particle Bed Nuclear Rocket Engine," SM Thesis, Departments of Aeronautics and Astronautics and Nuclear Engineering, Massachusetts Institute of Technology, May 1993.

S-5 A. H. Shapiro, The Dynamics and Thermodynamics of Compressible Fluid Flow, Volume I, The Ronald Press Company, New York, 1953.

S-6 E. M. Sparrow, "Temperature Distribution and Heat Transfer Results for an Internally Cooled, Heat Generating Solid," Journal of Heat Transfer, November 1960 389.

S-7 R. M. Stubbs, et al, "Analysis of Nuclear Thermal Propulsion Systems using Computational Fluid Dynamics", in Proceedings of Tenth Symposium on Space Nuclear Power and Propulsion, CONF-930103, M. S. El-Genk and M. D. Hoover, eds., American Institute of Physics, New York, 1993 1569.

S-8 D. E. Suzuki, personal communication, Massachusetts Institute of Technology, turbopump homologous curves obtained while on internship at Grumman Electronic Systems Division, September 1992.

S-9 A. H. Stenning, "Rapid Approximate Method for Analyizing Nuclear Rocket Performance," American Rocket Society Journal, February 1960 169.

S-10 H. P. Smith, "Dynamics and Control of Nuclear Rocket Engines," PhD Thesis, Nuclear Engineering Deparment, Massachusetts Institute of Technology, September 1960.

S-11 V. Stanek, J. Szekely, "The effects of Non-Uniform Porosity in Causing Flow Maldistributions in Isothermal Packed Beds," The Canadian Journal of Chemical Engineering, Vol 50, February 1972 9.

T-1 R. S. Tuddenham, "Thermal Hydraulic Analysis of a Packed Bed Reactor Fuel Element," SM and Nuclear Engineer Thesis, Department of Nuclear Engineering, May 1989.

T-2 G. E. Turney, J. M. Smith, A. J. Juhasz, "Steady-State Investigation of Laminar-Flow Instability Problem Resulting from Large Increases in Temperature of Normal Hydrogen Gas Flowing in Small Diameter Heated Tubes," NASA TND-3347, NTIS, Springfield, VA, 1966.

T-3 T. B. Tippets, P. S. Evans, G. K. Riffle, "A High Resolution Pneumatic Stepping Actuator for Harsh Reactor Environments," in Proceedings of Tenth Symposium on Space Nuclear Power and Propulsion, CONF-930103, M. S. El-Genk and M. D. Hoover, eds., American Institute of Physics, New York, 1993 1297.

V-1 R. Viskanti, "Some Heat Transfer and Fluid Flow Considerations for a Packed-Bed Fuel Element," Report ANL-6366, Argonne National Laboratory, May 1961.

V-2 K. Vafai, "Convective Flow and Heat Transfer in Variable-Porosity Media," Journal of Fluid Mechanics, Volume 147, 1984 233.

V-3 D. Vortmeyer, "Packed Bed Models and Convective Flow," in Proceedings of the 1988 National Heat Transfer Conference, held in Houston July 1988, H. R. Jacobs Ed., ASME-HTD-96, Volume 1, 1988 755.

V-4 P. Vingerhold, E.R. Kolbe, E. Reshotko, "Observations of Flow Excursions in a Simulated Gas-Cooled Reactor Passage," NASA CR-1538, NTIS, Springfield VA, 1970.

W-1 J. T. Walton, et al, "Program CAC, Nuclear Thermal Rocket Core Analysis Code, Version 1.00," LEW-15400, NASA Lewis Research Center, Cleveland, OH,1991.

W-2 J. T. Walton, "NBS Parahydrogen Properties Data Base Program (NBS-pH2)", LEW-15505, NASA Lewis Resaerch Center, Cleveland, OH, 1992.

W-3 J. T. Walton, et al, "System Model Development for Nuclear Thermal Propulsion," NASA TM-105761, August 1992.

W-4 J. T. Walton, "Development of NASA/DOE NTP Sytem Performance Models," in Proceedings of Tenth Symposium on Space Nuclear Power and Propulsion, CONF-930103, M. S. El-Genk and M. D. Hoover, eds., American Institute of Physics, New York, 1993 1499.

W-5 Westinghouse, "Technical Summary Report of NERVA Program, Phase I NRX & XE, Volume I, Engineering Design & Analysis Techniques and Development" WANL TNR-230, Westinghouse Astronuclear Laboratory, July, 1972.

W-6 Westinghouse, "Thermal and Fluid Flow Analysis Report," WANL-TME-2753, Westinghouse Astronuclear Laboratory, February 1971.

W-7 J. T. Walton, "Program ELM: A Tool for Rapid Thermal -Hydraulic Analysis of Solid Core Nuclear Rockt Fuel Elements," NASA TM-105867, November 1992.

W-8 Westinghouse, "TAP-A A Program for Computing Transient or Steady State Temperature Distributions," WANL-TME-1872, Westinghouse Astronuclear Laboratory, December 1969.

W-9 J. K. Witter, D. D. Lanning, J. E. Meyer, "Flow Stability Analysis of a Particle Bed Reactor Fuel Element," in Proceedings of Tenth Symposium on Space Nuclear Power and Propulsion, CONF-930103, M. S. El-Genk and M. D. Hoover, eds., American Institute of Physics, New York, 1993 1541.

Appendix A - Problem Specifications

A.1 One Dimensional Codes

A.1.1 Description

The one dimensional codes use an routine to interact with the user after the initial default values are read in from the program input file. The input files contain the element geometry and solid material property data to be used in the calculations. Sample input and output files from the PBRFMP computer codes are given in the next section. The TRITRAN input is the same, except for additional default values for the transient ramps.

A.1.2 Sample PBRFMP Input File

```
0.05          |RORF
0.05          |ORFLEN
0.0387        |RIP
0.0357        |RCF
0.0327        |RPB
0.0227        |RHF
0.0202        |ROP
0.6           |PBRLEN
0.05          |EXTLEN
0.63          |ECF
0.37          |EPB
0.5           |EHF  .23
1.3067e13     |ACF
4.25197e7     |BCF
0.0005        |DPB
6.8820e9      |AHF
2.02756e4     |BHF
0.95          |MANIN
1.1           |MANOUT
0.000117      |RF
0.00015       |R1
0.0002        |R2
0.00025       |R3
10500.        |RHOF
1000.         |RHO1
1900.         |RHO2
6300.         |RHO3
200.          |CPF
3000.         |CP1
3000.         |CP2
200.          |CP3
30.           |KF
```

```
1.5             |K1
3.              |K2
40.             |K3
200.            |TINO
3000.           |TCHMB
7000.           |POUTO
24.75           |POWDENO
```

A.1.3 Sample PBRFMPD Output File

```
 OUTPUT INFORMATION FROM PBRFMPD.EXE
 MDOT FOR FLOW PATH =       1.021802
 AVERAGE BED POWER DENSITY =      38.500000
 TOTAL FUEL ELEMENT POWER =      47.679010
 OUTLET CHANNEL SONIC VELOCITY =    3938.000000
 OUTLET CHANNEL VELOCITY =     648.114300
 OUTLET CHANNEL MACH NUMBER =   1.645796E-01
 SUPERFICIAL BED INLET REYNOLDS # =     392.586900
 TEMPERATURE RISE FACTOR, PHI =      10.111110


VOL   INLET     DELTA     INLET     AVERAGE    AVERAGE    REYNOLDS
#     PRESS     PRESS    H2 TEMP    H2 TEMP    F TEMP      NUMBER

 1  8478.8200     .3387   270.0000   270.0000   270.0000  3.211744E+06
 2  8478.4810     .2473   270.0000   270.0000   270.0000  1.058162E+05
 3  8478.2340     .0000   270.0000   270.0000   270.0000  6.023881E+04
 4  8478.2340     .0003   270.0000   270.0000   270.0000  8.470543E+05
 5  8478.2340  1019.0950   270.0000   270.0000   270.0000  2.723813E+00
 6  7459.1390     .5966   270.0000   446.5300   902.9457  1.217598E+03
 7  7458.5420    1.1140   623.0600   795.1559  1200.0920  8.436027E+02
 8  7457.4290    1.6841   967.2518  1129.4720  1500.5370  6.804290E+02
 9  7455.7450    2.3269  1291.6920  1444.1720  1789.7490  5.884941E+02
10  7453.4170    3.0037  1596.6520  1739.0930  2063.5050  5.305876E+02
11  7450.4140    3.7360  1881.5340  2015.5180  2325.5730  4.918119E+02
12  7446.6780    4.4868  2149.5010  2274.2630  2567.1590  4.687694E+02
13  7442.1910    5.2871  2399.0250  2511.6410  2786.3340  4.490604E+02
14  7436.9040    6.1189  2624.2560  2724.6130  2980.6030  4.355562E+02
15  7430.7850    6.9768  2824.9690  2912.4840  3151.2810  4.267572E+02
16  7423.8080     .4417  3000.0000  3000.0000  3151.2810  4.076505E+01
17  7423.3670   421.4492  3000.0000  3000.0000  3151.2810  2.465643E+04
18  7001.9170    1.9176  3000.0000  3000.0000  3151.2810  5.054269E+05
    7000.0000
```

A.2 Two Dimensional SIMBED Code Input Deck

A.2.1 Description

The SIMBED computer code input file is fairly simple. The element geometry is defined and then the heat transfer information is supplied. The modifications by the author added four variables to the end of the numerical input. These variables are COSCHOP, TAUFAC, EPSFAC, and CFDIST. A sample input deck from the cases run in Section 3.4 is provided in the next section with definitions of the variables.

A.2.2 Sample SIMBED Input File

Input File Value	*Variable Description*
500	LAST = Total number of iterations to be performed in each run.
0	NSTART = Flag: 0 = Use initial guess; 1 = Read data from disk.
0	NPRINT = Flag: 0 = No printing; 1 = Print data field at end of run.
25	MSAVE = Number of iterations at which the intermediate data is saved; recommended value = 50.
1	NSAVE = Flag: 0 = Do not save the data at end of run; 1 = Save the data.
20	KIP = I index of the grid point at which the values of the variables are printed at selected iterations.
18	KJP = J index of the grid point at which the values of the variables are printed at selected iterations.
40	L1 = Number of grid points in the Z-direction.
30	M1 = Number of grid points in the R-direction.
14	JR1 = J index for the last point in the inner tube.
16	JR2 = J index for the last point in the hot frit.
22	JR3 = J index for the last point in the bed.
24	JR4 = J index for the last point in the cold frit.
20.2	R1 = Inner radius of the Hot frit, @ X=0 [mm].
22.7	R2 = Outer radius of the Hot frit, @ X=0 [mm].
32.7	R3 = Inner radius of the Cold frit, @ X=0 [mm].
35.7	R4 = Outer radius of the Cold frit, @ X=0 [mm].
38.7	R5 = Outer radius of the inlet channel, @ X=0 [mm]. (If the inlet channel does not exist, CASE 2, R5 = R4).

Input File Value	*Variable Description*
20.2	RR1 = Inner radius of the Hot frit, @ X=H [mm].
22.7	RR2 = Outer radius of the Hot frit, @ X=H [mm].
32.7	RR3 = Inner radius of the Cold frit, @ X=H [mm].
35.7	RR4 = Outer radius of the Cold frit, @ X=H [mm].
38.7	RR5 = Outer radius of the inlet channel, @ X=H [mm]. (If the inlet channel does not exist, CASE 2, RR5 = RR4).
0.5	DP = Diameter of the fuel particle [mm].
0.0025	DCF = Diameter of the Cold frit particle [mm].
0.1	DHF = Diameter of the Hot frit particle [mm].
600.0	H = Length of the system [mm].
0.37	EPSO = Porosity of the porous layer far from the walls.
0.5	RELXV = Relaxation factor for velocity components; 0.5 is recommended.
1.0	RELXT = Relaxation factor for the temperatures; 1. is recommended.
1.0	RLXRHO = Relaxation factor for the fluid density (= 1. for most cases).
0.541	FLMASS = Total mass flow rate entering the system [Kg/sec].
200.0	TIN = Temperature of the fluid entering the system [K].
7.983d+6	PIN = Pressure of the fluid entering the system [Pa].
5662.0	RHOS = Density of the solid phase in the porous layer [Kg/m3].
1300.0	CPS = Specific Heat of the solid phase in the porous layer [J/Kg-K].
25.0	CONDS = Thermal conductivity of the solid phase in the porous layer [W/m-K].
1.3067D+13	ALPHCF = Viscous Resistance Coefficient of the cold frit [1/m2].
4.25197D+7	BETACF = Inertial Resistance Coefficient of the cold frit [1/m].
2700.0	RHOCF = Density of the solid phase in the cold frit [kg/m3].
0.78	EMSCF = Emissivity of the solid phase in the cold frit.
800.0	CPCF = Specific Heat of the solid phase in the cold frit [J/Kg-K].
237.0	CONDCF = Thermal Conductivity of the solid phase in the cold frit [W/m-K].
6.8820D+9	ALPHHF = Viscous Resistance Coefficient of the hot frit [1/m2].
2.02756D+4	BETAHF = Interial Resistance Coefficent of the hot frit [1/m].
1900.0	RHOHF = Density of the solid phase in the hot frit [Kg/m3].
1.0	EMSHF = Emissivity of the solid phase in the hot frit.
1884.06	CPHF = Specific Heat of the solid phase in the hot frit [J/Kg-K].

Input File Value	*Variable Description*
41.868	CONDHF = Thermal Conductivity of the solid phase in the hot frit [W/m-K].
24.75d+9	UHEAT = Power Density of the fuel bed [W/m3].
0.01	GAMA = Residual reduction factor used in SOLVE (use 0.01 to 0.2).
0.5	DELTA = Relaxation parameter used in SOLVE (use 0.0 to 0.5).
-75008.0	CFDIST = Cold Frit Resistance Distribution Code (ss0cc.cc)
15001.5	COSCHOP = Skewed Cosine Axial Power Shape Code (ss0cc.cc)
2.5	TAUFAC = Exponential Radial Power Shape Factor (R)
0.33	EPSFAC = Porosity Value for Single Node KIP,KJP
'epbref.out'	DATAFILE = Name of file from which to read and write data for the run.

A.3 NTP Engine Codes

A.3.1 Description

The input files for the steady state and transient versions of the engine codes are the same format. The baseline input files for the NERVA CAC benchmark, NERVA WANL transient benchmark, and PBR transient studies are provided in the next section. The detailed output files are included as examples of the information that is presented for the NERVA and PBR engines. The detail output file is updated after a certain number of iterations defined by the user with the variable ISAVE2.

A.3.2 Sample Engine Input Files

A.3.2.1 NERVA CAC Input File for Steady State Benchmark

```
## NEXT CARD IS TITLE
 CAC REACTOR; DATA FROM WANL-TME-2753, TABLE 2-1 NERVA ROCKET DIMENSIONS
## NEXT IS FOR THE REACTOR TYPE (1 - NERVA, 2 - PBR)
 1
## NEXT IS THE CONTROL VOLUME INFO FORMAT (I6,2X,I4,6(2X,E10.5))
##NC  DHV(K)-- -FLOWL(K)- -FLOWA(K)-  -PVOL(K)---TVOL(K)--
 1  0.12065   1.00      0.0        240000.0  20.0
 2  0.12065   0.0503    0.0        3500000.0  20.0
 3  0.12065   7.56285   0.0        7000000.0  20.0
 4  0.014148  0.68      0.041252  7000000.0  50.0
 5  0.014148  0.68      0.041252  6800000.0  70.0
 6  0.100     0.12369   0.0       6700000.0  75.0
 7  0.003175  1.32      0.0       6600000.0  200.0
```

```
 8  0.182575  0.378    0.0     6500000.0 320.0
 9  0.182575  0.183    0.0     6480000.0 320.0
 10 0.182575  0.378    0.0     6460000.0 320.0
 11 0.182575  0.183    0.0     6450000.0 320.0
 12 0.182575  0.93853  0.0     6440000.0 320.0
 13 0.182575  0.98270  0.0     5450000.0 310.0
 14 0.182575  0.88265  0.0     5150000.0 300.0
 15 0.182575  0.183    0.0     5100000.0 320.0
 16 0.182575  0.49135  0.0     6440000.0 320.0
 17 0.182575  0.49135  0.0     5150000.0 310.0
 18 0.182575  0.88265  0.0     5000000.0 310.0
 19 0.01      0.5      0.06    5000000.0 310.0
 20 0.0024155 1.32     0.0     4250000.0 1250.0
 21 .86       0.12369  0.0     3500000.0 2900.0
 22 0.54      0.68     0.0     3000000.0 2900.0
 23 0.54      0.68     0.0     2000000.0 2000.0
 24 1.1985    2.0      0.0     1000000.0 500.0
 25 5.0    1000.0      0.0     200001.0  20.0
 26 10.0    20.0       0.0     240000.0  20.0
 27 0.0508   12.0      0.0     300000.0  320.0
 28 0.0508   12.0      0.0     6480000.0 320.0
## NEXT IS THE JUNCTION INFORMATION
## NC, DHJ, AJUN, FJUNF,PJUN,TJUN j23 .2785
 1  0.12065   0.0      0.05  240000.0  20.0
 2  0.12065   0.0      0.0   240000.0  20.0
 3  0.12065   0.0      0.25  7000000.0 20.0
 4  0.014148  0.041252 20.   7000000.0 20.0
 5  0.014148  0.041252 0.0   6900000.0 60.0
 6  0.014148  0.041252 0.0   6750000.0 75.0
 7  0.003175  0.0      0.0   6700000.0 75.0
 8  0.003175  0.0      0.0   6550000.0 150.0
 9  0.182575  0.0      0.0   6500000.0 150.0
 10 0.182575  0.0      0.0   6480000.0 150.0
 11 0.182575  0.0      0.0   6460000.0 150.0
 12 0.182575  0.0      0.0   6450000.0 150.0
 13 0.182575  0.0      0.0   6440000.0 150.0
 14 0.182575  0.0      0.0   5150000.0 150.0
 15 0.182575  0.0      0.25  5100000.0 150.0
 16 0.182575  0.0      0.5   6460000.0 150.0
 17 0.182575  0.0      0.5   5750000.0 150.0
 18 0.182575  0.0      0.0   5100000.0 150.0
 19 0.182575  0.0      0.0   5100000.0 150.0
 20 0.182575  0.0      0.0   5000000.0 150.0
 21 0.0024155 0.0      0.0   5000000.0 150.0
 22 0.002415  0.0      0.0   4000000.0 2275.0
 23 0.86         0.0      0.0   3800000.0 2275.0
 24 0.222        0.0      0.0   3000000.0 2200.0
 25 0.86      0.0      0.0   1500000.0 800.0
 26 3.1113    0.0      0.0   800000.0  300.0
 27 0.0508    0.0      0.0   240000.0  320.0
 28 0.0508    0.0      0.0   3400000.0 320.0
 29 0.0508    0.0      0.0   6480000.0 320.0
## NEXT IS FOR THE NOZZLE THICKNESS AND MATERIAL THERMAL DATA
## THCKNZL, PFNZL1, PFNZL2, FLOWBLK
```

```
 0.005  0.0005  0.0005  0.5
## DENSITY OF THE NOZZLE MATERIAL
 1700.00
## TKNT   TKN  CPNT  CPN   (PYROGRAPHITE)
 1   0.0  15.0    0.0     0.0
 2  55.56 59.81  55.56  156.7
 3 111.1 101.4  111.1   522.2
 4 166.7 123.8  166.7   731.1
 5 222.2 140.4  222.2   814.7
 6 333.3 157.8  333.3   908.7
 7 444.4 167.8  555.6   997.4
 8 555.6 186.1  666.7  1044.0
 9 666.7 179.4  777.8  1097.0
 10 888.9 167.8  888.9  1149.0
## NEXT IS THE REFLECTOR GEOMETRY, MATERIALS DATA & AXIAL SHAPE
## ROREFL,RIREFL,EPSREFL,PFREFL,NAXIAL,COSCHOP
## 0.685 0.565 0.4 0.025 10 15001.5
 0.58 0.43 0.4 0.025 10 15001.5
## DENSITY OF THE REFLECTOR MATERIAL
 2803.0
## TKRT  TKR   CPRT  CPR  (BERYLLIUM)
 1    0.0    0.0    0.0    0.0
 2   69.4  190.19  69.44  34.68
 3   104.2  240.43 104.2  174.2
 4   138.9  230.92 138.9  556.9
 5   208.3  200.69 208.9  1079.0
 6   277.8  170.94 277.8  1671.0
 7   416.7  140.45 416.7  2211.0
 8   555.6  120.34 555.6  2489.0
 9   555.7  120.34 555.7  2489.0
 10  555.8  120.34 555.8  2489.0
## NEXT IS THE CORE DATA
## ROCORE,DFLATC,NRING,NHOLES,PFCOR,PFMOD
 0.42672 0.01905 6       19  0.974 0.0
## RING POWER FRACTION -  PKR
 1.1031 1.077 1.0429 0.99474 0.9326 1.0429
##  1.0 1.0 1.0 1.0 1.0 1.0
## (ORIFICE SIZE DIAMETER ratio)^2 used by nerva-  ORF
## 0.12782 0.12782 0.12782 0.12782 0.12782
 0.2339742 0.1769202  0.1432946 0.120415 0.099506 0.1278186
## AREA PRESSURE LOSS TERM  - CAYL
 1.44    1.520 1.575 1.610 1.645 1.600
##  1.6 1.6 1.6 1.6 1.6
## FUEL ELEMENT DIMENSIONS FOR NERVA
## RING RADIA  RR(IR)
##   0.42672
 0.06858 0.14097 0.206502 0.255524 0.365252 0.42672
## RHO OF FUEL
  3500.0
## TKFT TKF CPFT CPF ** from NASA tm-x-1232
 1   0.0    0.0      0.0  0.0
 2  277.8  103.2    277.8  0.6684e+3
 3  555.5   77.01   555.5  1.337e+3
 4  833.3   60.56   833.3  1.671e+3
```

```
 5 1111.0   38.88  1111.0  1.858e+3
 6 1389.0   31.40  1389.0  1.964e+3
 7 1667.0   24.67  1667.0  2.047e+3
 8 1994.0   20.93  1994.0  2.089e+3
 9 2778.0   19.44  2778.0  2.131e+3
 10 3333.0   19.44  3333.0  2.298e+3
## rho of carbon
 1700.0
## TKCT TKC  CPCT  CPC (PYRO GRAPHITE)
 1    0.0  0.0       0.0     0.0
 2   139.0  0.5981   140.0  330.9
 3   278.0  2.093    278.0  661.3
 4   417.0  1.965    417.0  1149.0
 5   555.6  1.709    555.6  1323.0
 6   833.3  1.367    833.3  1633.0
 7  1111.0  1.175    1111.0  1883.0
 8  1667.0  0.880    1389.0  1984.0
 9  2778.0  0.4272   2778.0  2124.0
 10 3333.0  0.3055   3333.0  2177.0
## THIS IS THE PUMP INFORMATION
## ERSHPMP, PND,PQD,PRD,PHD,PED,PHPD,NPDAT
  .05 420.  0.8  72.0  9000.0  0.8  3.8e+6  19
## THE HOMOLOGOUS INFO
## NC,PQRAT,PERAT,PHRAT,PHPRAT
 1  0.0001   0.0001   1.174   0.586
 2  0.1   0.195   1.213   0.622
 3  0.2   0.365   1.230   0.673
 4  0.3   0.513   1.246   0.728
 5  0.4   0.644   1.252   0.777
 6  0.5   0.758   1.241   0.818
 7  0.6   0.848   1.213   0.858
 8  0.7   0.914   1.176   0.900
 9  0.8   0.962   1.122   0.933
 10  0.9   0.993   1.070   0.968
 11  1.0   1.0    1.0     1.0
 12  1.1   0.994   0.939   1.039
 13  1.2   0.974   0.861   1.061
 14  1.3   0.950   0.776   1.062
 15  1.4   0.897   0.678   1.058
 16  1.5   0.828   0.565   1.023
 17  1.6   0.675   0.409   0.970
 18  1.7   0.449   0.239   0.905
 19  1.76  0.0001    0.0001    0.860
## THIS IS THE TURBINE INFORMATION
## EFFT,PRTRB, ERSHTRB, TBTMIN
  0.8   1.425   0.045   40.
## TURBINE CONTROL VALVE INFORMATION
## TBCVA,TBCVB : VLVKL=EXP(A-Bx), VLVLAM
 16.19625  7.7626  10.00
## POINT KINETICS INFORMATION
## --BETA1--- --BETA2--- --BETA3--- --BETA4--- --BETA5--- --BETA6---
 0.00028    0.00159   0.00141    0.00305    0.00096   0.00020
## -LAMBDA1-- -LAMBDA2-- -LAMBDA3-- -LAMBDA4-- -LAMBDA5-- -LAMBDA6--
  0.01323      0.039      0.139        0.359       1.41       4.03
```

```
## THE REACTIVITY COEFFICIENTS, FOR NOW CONSTANT
## --PRMPT--|-ALPHAP-|--ALPHAT-|--ALPHAD-|--ALPHAM-|
   24.9E-6  0.0      0.0   -5.0e-6    0.001
## --CRWRTH-|--CDDPS-|-CRDLAM-|
    5.4     10.0    20.0
## THE TRANSIENT INFORMATION
## ISS  FLAG FOR TRANSIENTS
   1
## DURTC1,DURTC2,DURTC3,TC1,TC2,TC3,TC4
## DURPC1,DURPC2,DURPC3,PC1,PC2,PC3,PC4
## DELAYT,AFTERT,DT,ISAVE1,ISAVE2
  7.0   18.  5.  2275.0  2275.0  2275.0 2275.0
  7.0   18.  5.  3800000.0 3800000.0  3800000. 3800000.
  0.2   20.  0.0005  200  10000
##  THE DECAY HEAT CONCENTRATION INFORMATION
##  DHGAM(I)
  0.00299  0.00825  0.0155  0.01935  0.01165  0.00645
## DHLAMB(I)
  1.772  0.5724  0.06743  0.006214  4.739E-4  4.81E-5
##  TDHINIT (SEC), QDHFAC , QMAX
  3600.0  1.0  1.5e+9
```

A.3.2.2 NERVA WANL Input File for Transient Benchmark

```
## NEXT COARD IS THE TITLE CARD
   WANL  NERVA  CORE,  DATA  FROM  WANL-TME-2753,  TABLE  2-1  NERVA  ROCKET
DIMENSIONS
##  NEXT IS FOR THE REACTOR TYPE (1 - NERVA, 2 - PBR)
 1
##  NEXT IS THE CONTROL VOLUME INFO FORMAT
##NC  DHV(K)--  -FLOWL(K)- -FLOWA(K)-  -PVOL(K)--      -TVOL(K)--
 1  0.12065    1.00       0.0        240000.0   20.0
 2  0.12065    0.0503     0.0        3500000.0  20.0
 3  0.12065    7.56285    0.0        7000000.0  20.0
 4  0.014148   0.68       0.041252  7000000.0  50.0
 5  0.014148   0.68       0.041252  6800000.0  70.0
 6  0.100      0.12369    0.0        6700000.0  75.0
 7  0.003175   1.32       0.0        6600000.0  150.0
 8  0.182575   0.378      0.0        6500000.0  150.0
 9  0.182575   0.183      0.0        6480000.0  150.0
 10  0.182575   0.378      0.0        6460000.0  150.0
 11  0.182575   0.183      0.0        6450000.0  150.0
 12  0.182575   0.93853    0.0        6440000.0  150.0
 13  0.182575   0.98270    0.0        5450000.0  150.0
 14  0.182575   0.88265    0.0        5150000.0  150.0
 15  0.182575   0.183      0.0        5100000.0  150.0
 16  0.182575   0.49135    0.0        6440000.0  150.0
 17  0.182575   0.49135    0.0        5150000.0  150.0
 18  0.182575   0.88265    0.0        5000000.0  150.0
 19  0.01       0.5        0.06       5000000.0  150.0
 20  0.0024155  1.32       0.0        4250000.0  1250.0
```

```
 21 1.11      0.12369   0.0      3500000.0 2900.0
 22 0.64      0.68      0.0      3000000.0 2900.0
 23 0.54      0.68      0.0      2000000.0 2000.0
 24 1.1985    2.0       0.0      1000000.0  500.0
 25 5.0    1000.0       0.0       200001.0   20.0
 26 10.0     20.0       0.0       240000.0   20.0
 27 0.0508   12.0       0.0       300000.0  320.0
 28 0.0508   12.0       0.0      6480000.0  320.0
## NEXT IS THE JUNCTION INFORMATION
## NC, DHJ, AJUN, FJUNF,PJUN,TJUN
 1  0.12065   0.0       0.05  240000.0   20.0
 2  0.12065   0.0       0.0   240000.0   20.0
 3  0.12065   0.0       0.25 7000000.0   20.0
 4  0.014148  0.041252 20.0  7000000.0   20.0
 5  0.014148  0.041252  0.0  6900000.0   60.0
 6  0.014148  0.041252  0.0  6750000.0   75.0
 7  0.003175  0.0       0.0  6700000.0   75.0
 8  0.003175  0.0       0.0  6550000.0  150.0
 9  0.182575  0.0       0.0  6500000.0  150.0
 10 0.182575  0.0       0.0  6480000.0  150.0
 11 0.182575  0.0       0.0  6460000.0  150.0
 12 0.182575  0.0       0.0  6450000.0  150.0
 13 0.182575  0.0       0.0  6440000.0  150.0
 14 0.182575  0.0       0.0  5150000.0  150.0
 15 0.182575  0.0       0.25  5100000.0  150.0
 16 0.182575  0.0       0.5  6460000.0  150.0
 17 0.182575  0.0       0.5  5750000.0  150.0
 18 0.182575  0.0       0.0  5100000.0  150.0
 19 0.182575  0.0       0.0  5100000.0  150.0
 20 0.182575  0.0       0.0  5000000.0  150.0
 21 0.0024155 0.0       0.0  5000000.0  150.0
 22 0.0024155 0.0       0.0  4000000.0 2275.0
 23 1.11          0.0     0.0  3100000.0 2360.0
 24 0.2785        0.0     0.0  3000000.0 2200.0
 25 0.86     0.0      0.0   1500000.0  800.0
 26 3.1113    0.0      0.0    800000.0  300.0
 27 0.0508    0.0      0.0    240000.0  320.0
 28 0.0508    0.0      0.0   3400000.0  320.0
 29 0.0508    0.0      0.0   6480000.0  320.0
## NEXT IS FOR THE NOZZLE THICKNESS AND MATERIAL THERMAL DATA
## THCKNZL, PFNZL1, PFNZL2, FLOWBLK
 0.005  0.0005  0.0005  0.5
## DENSITY OF THE NOZZLE MATERIAL
 1700.00
## TKNT   TKN  CPNT  CPN   (PYROGRAPHITE)
 1   0.0  15.0    0.0     0.0
 2  55.56 59.81   55.56  156.7
 3 111.1  101.4  111.1   522.2
 4 166.7  123.8  166.7   731.1
 5 222.2  140.4  222.2   814.7
 6 333.3  157.8  333.3   908.7
 7 444.4  167.8  555.6   997.4
 8 555.6  186.1  666.7  1044.
 9 666.7  179.4  777.8  1097.
```

```
 10 888.9  167.8   888.9   1149.
## NEXT IS THE REFLECTOR GEOMETRY, MATERIALS DATA & AXIAL SHAPE
## ROREFL,RIREFL,EPSREFL,PFREFL,NAXIAL,COSCHOP
 0.685  0.565  0.4  0.05  10  15001.5
## DENSITY OF THE REFLECTOR MATERIAL
 2803.0
## TKRT  TKR    CPRT   CPR   (BERYLLIUM)
 1    0.0     0.0     0.0     0.0
 2    69.4   190.19  69.44   34.68
 3   104.2   240.43  104.2   174.2
 4   138.9   230.92  138.9   556.9
 5   208.3   200.69  208.9  1079.0
 6   277.8   170.94  277.8  1671.0
 7   416.7   140.45  416.7  2211.0
 8   555.6   120.34  555.6  2489.0
 9   555.7   120.34  555.7  2489.0
 10  555.8   120.34  555.8  2489.0
## NEXT IS THE CORE DATA
## ROCORE,DFLATC,NRING,NHOLES,PFCOR,PFMOD
 0.555  0.01905  1          19  0.949 0.0
## RING POWER FRACTION -  PKR
##  1.1031 1.077 1.0429  0.99474  0.9326 1.0429
  1.0  1.0  1.0  1.0  1.0 1.0
## (ORIFICE SIZE DIAMETER ratio)^2 used by nerva-  ORF
 0.12782  0.12782  0.12782  0.12782  0.12782
##  0.2339742  0.17692020.1432946  0.120415  0.099506  0.1278186
## AREA PRESSURE LOSS TERM  - CAYL
##  1.44 1.520  1.575  1.610  1.645  1.600
  1.6  1.6  1.6  1.6  1.6
## FUEL ELEMENT DIMENSIONS FOR NERVA
## RING RADIA  RR(IR)
##  0.15  0.25  0.40  0.555
   0.555
##  RHO OF FUEL
  3500.0
##  TKFT TKF CPFT CPF ** from NASA tm-x-1232
 1    0.0     0.0      0.0   0.0
 2  277.8   103.2    277.8   0.6684e+3
 3  555.5    77.01   555.5   1.337e+3
 4  833.3    60.56   833.3   1.671e+3
 5  1111.0   38.88   1111.0   1.858e+3
 6  1389.0   31.40   1389.0   1.964e+3
 7  1667.0   24.67   1667.0   2.047e+3
 8  1994.0   20.93   1994.0   2.089e+3
 9  2778.0   19.44   2778.0   2.131e+3
 10 3333.0   19.44   3333.0   2.298e+3
##  rho of carbon
 1700.0
## TKCT TKC  CPCT  CPC (PYRO GRAPHITE)
 1    0.0  0.0       0.0    0.0
 2   139.0  0.5981   140.0  330.9
 3   278.0  2.093    278.0  661.3
 4   417.0  1.965    417.0 1149.0
 5   555.6  1.709    555.6 1323.0
```

```
 6  833.3  1.367    833.3  1633.0
 7  1111.0  1.175   1111.0  1883.0
 8  1667.0  0.880   1389.0  1984.0
 9  2778.0  0.4272  2778.0  2124.0
 10 3333.0  0.3055  3333.0  2177.0
## THIS IS THE PUMP INFORMATION
##  ERSHPMP, PND,PQD,PRD,PHD,PED,PHPD,NPDAT
  .045  500.  1.20  72.0  9000.0  0.8  3.8e+6  19
## THE HOMOLOGOUS INFO
## NC,PQRAT,PERAT,PHRAT,PHPRAT
 1  0.0001   0.0001   1.174   0.586
 2  0.1    0.195   1.213   0.622
 3  0.2    0.365   1.230   0.673
 4  0.3    0.513   1.246   0.728
 5  0.4    0.644   1.252   0.777
 6  0.5    0.758   1.241   0.818
 7  0.6    0.848   1.213   0.858
 8  0.7    0.914   1.176   0.900
 9  0.8    0.962   1.122   0.933
 10  0.9   0.993   1.070   0.968
 11  1.0   1.0     1.0     1.0
 12  1.1   0.994   0.939   1.039
 13  1.2   0.974   0.861   1.061
 14  1.3   0.950   0.776   1.062
 15  1.4   0.897   0.678   1.058
 16  1.5   0.828   0.565   1.023
 17  1.6   0.675   0.409   0.970
 18  1.7   0.449   0.239   0.905
 19  1.76  0.0001    0.0001    0.860
## THIS IS THE TURBINE INFORMATION
## EFFT,PRTRB, ERSHTRB, TBTMIN
  0.8   1.6   2.00   40.
##  TURBINE CONTROL VALVE INFORMATION
##  TBCVA,TBCVB : VLVKL=EXP(A-Bx), VLVLAM
 16.19625  7.7626  10.00
## POINT KINETICS INFORMATION
## --BETA1--- --BETA2--- --BETA3--- --BETA4--- --BETA5--- --BETA6---
 0.00028   0.00159   0.00141   0.00305   0.00096   0.00020
## -LAMBDA1-- -LAMBDA2-- -LAMBDA3-- -LAMBDA4-- -LAMBDA5-- -LAMBDA6--
  0.01323      0.039      0.139      0.359      1.41      4.03
## THE REACTIVITY COEFFICIENTS, FOR NOW CONSTANT
## --PRMPT--|-ALPHAP-|--ALPHAT-|--ALPHAD-|--ALPHAM-|
   24.9E-6  0.0      0.0    -5.0e-6    0.002
## --CRWRTH-|--CDDPS-|-CRDLAM-|
    6.0      10.0     20.0
## THE TRANSIENT INFORMATION
## ISS  FLAG FOR TRANSIENT
   1
## DURTC1,DURTC2,DURTC3,TC1,TC2,TC3,TC4
## DURPC1,DURPC2,DURPC2,PC1,PC2,PC3,PC4
## DELAYT,AFTERT,DT,ISAVE1,ISAVE2
  3.0   10. -14.  2360.0   2360.0  2360.0 1000.0
  3.0   5.    5.  3100000.0 2015000.0  2015000. 2015000.
  10.2   20.  0.0005  400  10000
```

```
## THE DECAY HEAT CONCENTRATION INFORMATION
## DHGAM(I)
 0.00299  0.00825  0.0155  0.01935  0.01165  0.00645
## DHLAMB(I)
 1.772  0.5724  0.06743  0.006214  4.739E-4  4.81E-5
## TDHINIT (SEC), QDHFAC , QMAX
       3600.0  1.0  1.75e+9
```

A.3.2.3 37 Element PBR Input File for Orificing Study

```
## NEXT CARD IS THE TITLE CARD
 37 ELEMENT PBR, PIPING DATA FROM WANL-TME-2753, TABLE 2-1 NERVA ROCKET
## NEXT IS FOR THE REACTOR TYPE (1 - NERVA, 2 - PBR)
 2
## NEXT IS THE CONTROL VOLUME INFO
##NC  DHV(K)---FLOWL(K)- -FLOWA(K)- -PVOL(K)-- --TVOL(K)--
 1  0.12065   1.00      0.0       240000.0  20.0
 2  0.12065   0.0503    0.0       3500000.0  20.0
 3  0.12065   7.56285   0.0       7000000.0  30.0
 4  0.014148  1.00      0.041252  7000000.0  50.0
 5  0.014148  1.00      0.041252  6800000.0  70.0
 6  0.100     0.12369   0.0       6700000.0  75.0
 7  0.003175  0.800     0.0       6600000.0  200.0
 8  0.182575  0.378     0.0       6500000.0  320.0
 9  0.182575  0.183     0.0       6480000.0  320.0
 10  0.182575  0.378     0.0       6460000.0  320.0
 11  0.182575  0.183     0.0       6450000.0  320.0
 12  0.182575  0.93853   0.0       6440000.0  320.0
 13  0.182575  0.98270   0.0       5450000.0  310.0
 14  0.182575  0.88265   0.0       5150000.0  300.0
 15  0.182575  0.183     0.0       5100000.0  320.0
 16  0.182575  0.49135   0.0       6440000.0  320.0
 17  0.182575  0.49135   0.0       5150000.0  310.0
 18  0.182575  0.88265   0.0       5000000.0  310.0
 19  0.01      0.5       0.06      5000000.0  310.0
 20  0.038     0.800     0.0       4250000.0  1250.0
 21  0.80      0.12369   0.0       3500000.0  2900.0
 22  0.6       0.866     0.0       3000000.0  2900.0
 23  0.6       0.866     0.0       2000000.0  2000.0
 24  1.91      2.0       0.0       1000000.0  500.0
 25  5.0       1000.0    0.0       200001.0  20.0
 26  10.0      20.0      0.0       240000.0  20.0
 27  0.0508    12.0      0.0       300000.0  320.0
 28  0.0508    12.0      0.0       6480000.0  320.0
## NEXT IS THE JUNCTION INFORMATION
## NC, DHJ, AJUN, FJUNF,PJUN,TJUN
 1  0.12065   0.0       0.25  240000.0   20.0
 2  0.12065   0.0       0.0   240000.0   20.0
 3  0.12065   0.0       0.25  7000000.0   30.0
 4  0.014148  0.041252  20.0  7000000.0   30.0
 5  0.014148  0.041252  0.0   6900000.0   60.0
```

```
 6  0.014148  0.041252 0.0   6750000.0   75.0
 7  0.003175  0.0      0.0   6700000.0   75.0
 8  0.003175  0.0      0.0   6550000.0  150.0
 9  0.182575  0.0      0.0   6500000.0  150.0
 10 0.182575  0.0      0.0   6480000.0  150.0
 11 0.182575  0.0      0.0   6460000.0  150.0
 12 0.182575  0.0      0.0   6450000.0  150.0
 13 0.182575  0.0      0.0   6440000.0  150.0
 14 0.182575  0.0      0.0   5150000.0  150.0
 15 0.182575  0.0      0.0   5100000.0  150.0
 16 0.182575  0.0      0.0   6460000.0  150.0
 17 0.182575  0.0      0.0   5750000.0  150.0
 18 0.182575  0.0      0.0   5100000.0  150.0
 19 0.182575  0.0      0.0   5100000.0  150.0
 20 0.182575  0.0      0.0   5000000.0  150.0
 21 0.038     0.0     0.0   5000000.0  150.0
 22 0.80      0.0     0.0   3500000.0 2250.0
 23 0.800     0.0     0.0   7000000.0 3000.0
 24 0.1425    0.0     0.0   3000000.0 2200.0
 25 0.800     0.0     0.0   1500000.0  800.0
 26 2.82      0.0     0.0    800000.0  300.0
 27 0.0508    0.0     0.0    240000.0  320.0
 28 0.0508    0.0     0.0   3400000.0  320.0
 29 0.0508    0.0     0.0   6480000.0  320.0
## NEXT IS FOR THE NOZZLE THICKNESS AND MATERIAL THERMAL DATA
## THCKNZL, PFNZL1, PFNZL2, FLOWBLK
 0.003  0.0005  0.0005  0.5
## DENSITY OF THE NOZZLE MATERIAL
 1700.00
## TKNT   TKN   CPNT  CPN   (PYROGRAPHITE)
 1   0.0  15.0    0.0     0.0
 2  55.56 59.81  55.56  156.7
 3  111.1 101.4  111.1   522.2
 4  166.7 123.8  166.7   731.1
 5  222.2 140.4  222.2   814.7
 6  333.3 157.8  333.3   908.7
 7  444.4 167.8  555.6   997.4
 8  555.6 186.1  666.7  1044.0
 9  666.7 179.4  777.8  1097.0
 10 888.9 167.8  888.9  1149.0
## NEXT IS THE REFLECTOR GEOMETRY, MATERIALS DATA & AXIAL SHAPE
## ROREFL,RIREFL,EPSREFL,PFREFL,NAXIAL,COSCHOP
 0.56 0.41 0.3 0.05 10 15001.5
## DENSITY OF THE REFLECTOR MATERIAL
 2803.0
## TKRT  TKR   CPRT  CPR  (BERYLLIUM)
 1    0.0    0.0    0.0    0.0
 2   69.44 190.19  69.44  34.68
 3   104.2 240.43 104.2  174.2
 4   138.9 230.92 138.9  556.9
 5   208.3 200.69 208.9 1079.0
 6   277.8 170.94 277.8 1671.0
 7   416.7 140.45 416.7 2211.0
 8   555.6 120.34 555.6 2489.0
```

```
 9  555.7  120.34 555.7 2489.0
 10 555.8  120.34 555.8 2489.0
## NEXT IS THE CORE DATA
## ROCORE,DFLATC,NRING,NHOLES,PFCOR,PFMOD
 0.5 .1 4 1 0.939 0.01
## RING POWER FRACTION -  PKR
 1.15 1.075 1.025 0.95
##  1.0 1.0 1.0 1.0
## ORIFICE SIZE DIAMETER ratio -  ORF
  1.0 1.0 1.0 1.0
## AREA PRESSURE LOSS TERM - CAYL
##   1.0 1.0 1.0 1.0
 .65 1.0 1.075 1.4
## FUEL ELEMENT DIMENSIONS FOR PBR
##  RIP,RCF,RPB,RHF,ROP, ORFLEN,EXTLEN - ELEMENT RADIA
   0.0387 0.0357 0.0327 0.0227 0.0202 0.1 0.1
##  ECF,ACF,BCF,EHF,AHF,BHF     - FRIT ETA & RESISTANCE TERMS
  0.5 1.3067e+13  4.252e+7  0.5  6.882e+9  2.0275e+4
## RFK,RF1,RF2,RF3      - PARTICLE FUEL LAYER RADIA
  0.000117 0.00015 0.00020 0.00025
## RHO OF FUEL LAYERS - RHOF,RHO1,RHO2,RHO3
 10500.  1000.  1900.  6300.
##  VARIOUS ELEMENT PARAMETERS - DPB,EPB,NFR,TAUFAC
 0.0005 0.37  10   2.5
## NUMBER OF ELEMENTS PER RING
  1  6  12  18  24
## 37
##  RHO OF FUEL
  13500.0
##  TKFT TKF CPFT CPF ** TEMPORARY UNTIL GET THE UC DATA
 1     0.0    0.0       0.0      0.0
 2   100.0   24.50    140.0    330.9
 3   400.0   24.50    278.0    661.3
 4   500.0   23.13    417.0   1149.0
 5   600.0   22.28    555.6   1323.0
 6   800.0   21.20    833.3   1633.0
 7  1100.0   20.20   1111.0   1883.0
 8  1700.0   19.05   1389.0   1984.0
 9  2800.0   17.91   2778.0   2124.0
 10 3900.0   17.22   3333.0   2177.0
## rho of carbon
 1700.0
## TKCT TKC  CPCT  CPC (PYRO GRAPHITE)
 1     0.0  0.0        0.0      0.0
 2   139.0  0.5981   140.0    330.9
 3   278.0  2.093    278.0    661.3
 4   417.0  1.965    417.0   1149.0
 5   555.6  1.709    555.6   1323.0
 6   833.3  1.367    833.3   1633.0
 7  1111.0  1.175   1111.0   1883.0
 8  1667.0  0.880   1389.0   1984.0
 9  2778.0  0.4272  2778.0   2124.0
 10 3333.0  0.3055  3333.0   2177.0
## THIS IS PBR MODERATOR INFO - ZRH2
```

```
## RHOMOD
## 7000.
## NC, TKMT,TKM,CPMT,CPM
## 1 0.0    0.0 0.0  0.0
## 2 100.0
## 3
## 4
## 5
## 6
## 7
## 8
## 9
## 10
## THIS IS THE PUMP INFORMATION
## ERSHPMP, PND,PQD,PRD,PHD,PED,PHPD,NPDAT
 0.045 900. 0.4 73.00 20000.0 0.8 3.8e+6 19
## THE HOMOLOGOUS INFO
## NC,PQRAT,PERAT,PHRAT,PHPRAT
 1 0.0   0.0   1.174  0.586
 2 0.1   0.195  1.213  0.622
 3 0.2   0.365  1.230  0.673
 4 0.3   0.513  1.246  0.728
 5 0.4   0.644  1.252  0.777
 6 0.5   0.758  1.241  0.818
 7 0.6   0.848  1.213  0.858
 8 0.7   0.914  1.176  0.900
 9 0.8   0.962  1.122  0.933
 10 0.9  0.993  1.070  0.968
 11 1.0  1.0   1.0   1.0
 12 1.1  0.994  0.939  1.039
 13 1.2  0.974  0.861  1.061
 14 1.3  0.950  0.776  1.062
 15 1.4  0.897  0.678  1.058
 16 1.5  0.828  0.565  1.023
 17 1.6  0.675  0.409  0.970
 18 1.7  0.449  0.239  0.905
 19 1.76 0.0   0.0   0.860
## THIS IS THE TURBINE INFORMATION
## EFFT,PRTRB, ERSHTRB, TBTMIN
 0.8  1.3  2.0  40.
## TURBINE CONTROL VALVE INFORMATION
## TBCVA,TBCVB : VLVKL=EXP(A-Bx), VLVLAM
 17.3 9.5 10.0
## POINT KINETICS INFORMATION
## --BETA1--- --BETA2--- --BETA3--- --BETA4--- --BETA5--- --BETA6---
 0.00028  0.00159  0.00141  0.00305  0.00096  0.00020
## -LAMBDA1-- -LAMBDA2-- -LAMBDA3-- -LAMBDA4-- -LAMBDA5-- -LAMBDA6--
 0.01323    0.039    0.139     0.359    1.41    4.03
## THE REACTIVITY COEFFICIENTS, FOR NOW CONSTANT
## --PRMPT--|--ALPHAP--|--ALPHAT--|--ALPHAD-|-ALPHAM-|
  33.4E-6  9.8E-10  -1.6E-5  -4.5E-6  1.0E-6
## --CRWRTH--|--CDDPS-|-CRDLAM-|
   8.0     180.0  20.0
## THE TRANSIENT INFORMATION
```

```
## ISS  FLAG FOR TRANSIENT
  1
## DURTC1,DURTC2,DURTC2,TC1,TC2,TC3,TC4
## DURPC1,DURPC2,DURPC3,PC1,PC2,PC3,PC4
## DELAYT,AFTERT,DT,ISAVE1,ISAVE2
  10.0  10.0  5.0  1000.0  3000.  3000.  3000.
  10.0  10. 5.0  1000000.0  2000000.  7000000. 7000000.
  0.2  14.8  0.0001  2000  100000
##  THE DECAY HEAT CONCENTRATION INFORMATION
##  DHGAM(I)
  0.00299  0.00825  0.0155  0.01935  0.01165  0.00645
## DHLAMB(I)
  1.772  0.5724  0.06743  0.006214  4.739E-4  4.81E-5
##  TDHINIT (SEC)  QDHFAC,  QMAX
        3600.0    1.0   1.25e+9
```

A.3.3 Sample Engine Output Files

A.3.3.1 NERVA CAC Output File for Steady State Benchmark

```
TIME:  0.
TURBOPUMP INFORMATION
PUMP SPEED : 395.292 RPS  TURBINE POWER:  5.664 MW   PUMP POWER:  3.095 MW
TBCV TRAVEL:   0.240     TURBINE EFFIC:  0.800     PUMP EFFIC:  0.683
BYPASS FLOW:   4.192 Kg/s TURBINE FLOW : 28.566 Kg/s PUMP FLOW : 32.759 Kg/s

NOZZLE INFORMATION
CHAMBER PRESS: 3800.124 kPa  DEMANDED Pc: 3800.000 kPa   Isp1:  859.529 sec
CHAMBER TEMP : 2275.055 K    DEMANDED Tc: 2275.000 K     Isp2:  860.160 sec
THRUST:          276.142 kN

VOLC TC (K)    QV (W)    TN (K)    QV (W)   Taw (K)  TStg (K)  TH (K)  VOLH
 5   47.30   0.546e+07   558.05  -0.489e+07  2255.42  2271.46  2139.53   22
 4   35.93   0.666e+07   741.64  -0.607e+07  2088.57  2262.32   831.98   23

VOLUME AND JUNCTION INFORMATION
Vol PVOL(kPa) TVOL(K) RHOV(Kg/m3)  QVOL (W)  PJUN(kPa) TJUN(K) RHOJ(Kg/m3) Jun
  1   236.03    20.00  71.281   0.0000e+00   240.00    20.00    71.292     1
  2  3607.27    23.83  71.428   0.4531e+07   232.07    20.01    71.271     2
  3  6982.46    27.56  71.571   0.0000e+00  6982.46    27.54    71.621     3
  4  6930.68    35.93  62.478   0.6661e+07  6930.67    27.58    71.521     4
  5  6823.01    47.30  46.721   0.5465e+07  6823.00    42.53    53.556     5
  6  6814.25    51.77  40.493   0.0000e+00  6814.24    51.81    40.618     6
  7  6739.07    78.70  21.431   0.2897e+08  6739.06    51.74    40.367     7
  8  6712.14   107.98  14.665   0.0000e+00  6712.13   107.99    14.686     8
  9  6690.95   107.98  14.643   0.0000e+00  6690.94   107.98    14.644     9
 10  6690.42   107.98  14.641   0.0000e+00  6690.42   107.98    14.643    10
 11  6689.09   107.98  14.640   0.0000e+00  6689.34   107.98    14.640    11
 12  6687.79   107.98  14.637   0.0000e+00  6688.82   107.98    14.639    12
 13  5689.61   101.00  13.498  -0.5664e+07  6686.75   107.98    14.635    13
 14  4691.31    93.50  12.251   0.0000e+00  4692.46    93.50    12.254    14
 15  4680.04    95.24  11.969   0.0000e+00  4690.15    93.50    12.248    15
```

```
16 6688.85   107.98 14.639  0.0000e+00  6689.08  107.98   14.640    16
17 5684.33   107.47 12.603  0.0000e+00  6688.61  107.98   14.639    17
18 4668.40    95.23 11.941  0.0000e+00  4680.04  106.89   10.507    18
19 4651.13    95.21 11.900  0.0000e+00  4669.93   95.23   11.945    19
20 4231.66  1242.37  0.823  0.1129e+10  4666.85   95.23   11.938    20
21 3813.97  2275.01  0.405  0.0000e+00  4635.39   95.20   11.862    21
22 3629.95  2139.53  0.410 -0.4885e+07  3828.05 2275.02    0.407    22
23  436.02   831.98  0.127 -0.6075e+07  3800.12 2275.05    0.404    23
24   10.53   571.23  0.004  0.0000e+00  2098.37 1970.11    0.258    24
                              20.44   666.14    0.007    25
                               0.63   297.01    0.001    26

REFLECTOR INFORMATION
NODE  PRESS      H2     REFL
IZ  (kPa)   TH2(K)  TWALL(K)  TREFL(K)  TMAX(K)  PKZ
0   6739.06   51.74   0.       0.       0.       0.
1   6738.86   52.81   59.02    59.09    59.12    0.44781
2   6738.40   55.52   65.20    65.30    65.34    0.68056
3   6737.88   59.43   72.40    72.53    72.58    0.88358
4   6737.27   64.54   80.36    80.50    80.55    1.04798
5   6736.58   70.76   88.65    88.80    88.86    1.16657
6   6735.79   77.78   96.79    96.94    97.00    1.23418
7   6734.92   85.18   103.83   103.97   104.03   1.24786
8   6733.98   92.47   109.83   109.97   110.02   1.20699
9   6732.97   99.30   114.70   114.83   114.88   1.11337
10  6722.29   105.24  118.16   118.27   118.32   0.97110
11  6712.13   107.99  0.       0.       0.       0.

REACTOR INFORMATION

RING:  1
RING FLOW :    0.972 Kg/s
CHANNEL EXIT MACH NUMBER:  0.15931
NUMBER OF FLOW PASSAGES:      893.26
FLOW PER PASSAGE: 0.00108798
RING POWER:  0.3216e+08 W
RING POWER DENSITY:   2.281 GW/m^3

  Z(m)      PRESS    TH2 (K)  TWALL(K)  TFUEL(K)  TFMAX(K)
 0.         4635.39  95.201   0.        0.        0.
 0.06600    4595.43  194.299  628.609   645.438   651.399
 0.19800    4540.70  422.280  854.400   878.666   887.262
 0.33000    4505.09  685.727  1092.633  1131.778  1145.643
 0.46200    4456.60  961.116  1338.715  1388.066  1405.547
 0.59400    4394.65  1231.506 1573.904  1634.137  1655.473
 0.72600    4319.37  1483.977 1783.151  1847.281  1869.997
 0.85800    4231.84  1709.689 1962.525  2024.929  2047.034
 0.99000    4132.98  1900.882 2102.985  2156.237  2175.100
 1.12200    4024.16  2051.859 2199.889  2241.229  2255.872
 1.25400    3897.71  2158.393 2251.549  2278.845  2288.514
 1.32000    3828.05  2200.611 0.        0.        0.

RING:  2
RING FLOW :    2.999 Kg/s
```

```
CHANNEL EXIT MACH NUMBER:  0.15486
NUMBER OF FLOW PASSAGES:     2881.04
FLOW PER PASSAGE: 0.00104109
RING POWER:  0.1013e+09 W
RING POWER DENSITY:    2.227 GW/m^3

   Z(m)     PRESS    TH2 (K)  TWALL(K)  TFUEL(K)  TFMAX(K)
  0.       4635.39   95.201    0.        0.        0.
  0.06600   4573.89   196.321   636.063   652.591   658.446
  0.19800   4498.90   429.502   865.336   889.380   897.898
  0.33000   4465.21   698.407  1108.437  1147.070  1160.754
  0.46200   4419.28   979.183  1359.267  1408.214  1425.552
  0.59400   4360.65  1254.237  1598.451  1658.663  1679.992
  0.72600   4289.69  1511.241  1812.124  1875.648  1898.149
  0.85800   4207.26  1740.844  1995.057  2056.158  2077.802
  0.99000   4114.05  1935.064  2138.023  2190.178  2208.652
  1.12200   4011.64  2088.001  2236.015  2276.510  2290.854
  1.25400   3893.16  2196.752  2289.968  2316.713  2326.187
  1.32000   3828.05  2237.940    0.        0.        0.

RING:  3
RING FLOW :     4.303 Kg/s
CHANNEL EXIT MACH NUMBER:  0.14950
NUMBER OF FLOW PASSAGES:     4324.70
FLOW PER PASSAGE: 0.00099503
RING POWER:  0.1472e+09 W
RING POWER DENSITY:    2.156 GW/m^3

   Z(m)     PRESS    TH2 (K)  TWALL(K)  TFUEL(K)  TFMAX(K)
  0.       4635.39   95.201    0.        0.        0.
  0.06600   4551.54   197.587   638.713   654.746   660.426
  0.19800   4454.51   434.037   870.280   893.705   902.002
  0.33000   4422.92   706.342  1116.501  1154.098  1167.416
  0.46200   4379.83   990.538  1370.524  1418.298  1435.220
  0.59400   4324.83  1268.526  1612.341  1671.239  1692.102
  0.72600   4258.42  1528.377  1828.944  1890.943  1912.905
  0.85800   4181.33  1760.416  2014.265  2073.526  2094.518
  0.99000   4094.19  1956.517  2158.981  2209.575  2227.497
  1.12200   3998.58  2110.657  2257.859  2297.147  2311.064
  1.25400   3888.40  2219.754  2312.184  2338.135  2347.327
  1.32000   3828.05  2261.286    0.        0.        0.

RING:  4
RING FLOW :     4.101 Kg/s
CHANNEL EXIT MACH NUMBER:  0.14275
NUMBER OF FLOW PASSAGES:     4301.70
FLOW PER PASSAGE: 0.00095337
RING POWER:  0.1397e+09 W
RING POWER DENSITY:    2.057 GW/m^3

   Z(m)     PRESS    TH2 (K)  TWALL(K)  TFUEL(K)  TFMAX(K)
  0.       4635.39   95.201    0.        0.        0.
  0.06600   4526.67   197.162   631.483   646.674   652.055
  0.19800   4406.13   432.535   862.746   884.815   892.632
```

```
 0.33000   4376.84  703.696 1108.524 1144.132 1156.745
 0.46200   4336.91  986.731 1362.001 1407.173 1423.173
 0.59400   4285.97 1263.722 1603.463 1659.100 1678.807
 0.72600   4224.50 1522.605 1819.672 1878.428 1899.241
 0.85800   4153.24 1753.817 2004.801 2061.262 2081.261
 0.99000   4072.83 1949.278 2149.559 2197.764 2214.839
 1.12200   3984.74 2103.007 2248.800 2286.236 2299.496
 1.25400   3883.47 2212.047 2303.720 2328.449 2337.209
 1.32000   3828.05 2253.417    0.       0.       0.

RING: 5
 RING FLOW :   11.584 Kg/s
 CHANNEL EXIT MACH NUMBER:  0.13389
 NUMBER OF FLOW PASSAGES:     12937.05
 FLOW PER PASSAGE: 0.00089543
 RING POWER:  0.3938e+09 W
 RING POWER DENSITY:    1.928 GW/m^3

   Z(m)     PRESS    TH2 (K)  TWALL(K)  TFUEL(K)  TFMAX(K)
 0.        4635.39    95.201    0.       0.       0.
 0.06600   4494.95  196.986  623.692  637.831  642.840
 0.19800   4343.99  431.933  855.170  875.600  882.836
 0.33000   4317.71  702.624 1101.203 1134.358 1146.102
 0.46200   4281.88  985.179 1354.847 1396.858 1411.739
 0.59400   4236.20 1261.757 1596.558 1648.170 1666.452
 0.72600   4181.12 1520.238 1813.043 1867.830 1887.237
 0.85800   4117.37 1751.103 1998.548 2051.434 2070.167
 0.99000   4045.56 1946.292 2143.798 2188.955 2204.950
 1.12200   3967.09 2099.842 2243.691 2278.763 2291.187
 1.25400   3877.16 2208.851 2299.354 2322.526 2330.734
 1.32000   3828.05 2250.153    0.       0.       0.

RING: 6
 RING FLOW :    8.798 Kg/s
 CHANNEL EXIT MACH NUMBER:  0.14837
 NUMBER OF FLOW PASSAGES:      9245.75
 FLOW PER PASSAGE: 0.00095161
 RING POWER:  0.3147e+09 W
 RING POWER DENSITY:    2.156 GW/m^3

   Z(m)     PRESS    TH2 (K)  TWALL(K)  TFUEL(K)  TFMAX(K)
 0.        4635.39    95.201    0.       0.       0.
 0.06600   4539.01  202.223  661.459  677.806  683.597
 0.19800   4430.00  450.404  900.104  924.585  933.257
 0.33000   4399.54  734.967 1156.448 1195.181 1208.901
 0.46200   4357.99 1030.973 1420.649 1470.474 1488.123
 0.59400   4305.22 1320.147 1671.494 1732.106 1753.576
 0.72600   4241.33 1590.302 1897.642 1962.008 1984.807
 0.85800   4166.90 1830.289 2089.240 2148.912 2170.049
 0.99000   4083.11 2033.036 2238.317 2289.287 2307.342
 1.12200   3991.30 2192.713 2341.155 2380.752 2394.778
 1.25400   3885.74 2302.584 2394.871 2421.025 2430.289
 1.32000   3828.05 2345.982    0.       0.       0.
```

```
REACTIVITY INFORMATION
OMEGAD:  0.   /s THETA   : 99.542  DEMANDED POWER: 0.1129e+10 W
TAUINV:  0.   /s THETADOT:  0.     ACTUAL POWER  : 0.1129e+10 W

REACT : 0.      REACC : 0.003353  REACF :-0.003353
REACTT: 0.       REACTD:-0.006827  REACTM: 0.000287  REACTP: 0.
```

A.3.3.2 NERVA WANL Output File for Transient Benchmark

```
TIME:  0.
TURBOPUMP INFORMATION
PUMP SPEED : 464.820 RPS  TURBINE POWER:  7.787 MW   PUMP POWER:  3.882 MW
TBCV TRAVEL:  0.661      TURBINE EFFIC:  0.800      PUMP EFFIC:  0.623
BYPASS FLOW:  18.142 Kg/s TURBINE FLOW : 23.115 Kg/s PUMP FLOW : 41.257 Kg/s

NOZZLE INFORMATION
CHAMBER PRESS: 3099.991 kPa  DEMANDED Pc: 3100.000 kPa   Isp1:  879.902 sec
CHAMBER TEMP : 2360.001 K    DEMANDED Tc: 2360.000 K     Isp2:  885.479 sec
THRUST:       358.017 kN

VOLC TC (K)     QV (W)    TN (K)     QV (W)    Taw (K)  TStg (K)  TH (K)  VOLH
 5   46.87   0.645e+07   497.61  -0.569e+07  2338.06  2356.82  2206.44   22
 4   36.41   0.785e+07   754.68  -0.710e+07  2185.24  2348.63  1039.24   23

VOLUME AND JUNCTION INFORMATION
Vol PVOL(kPa) TVOL(K) RHOV(Kg/m3)  QVOL (W)  PJUN(kPa) TJUN(K) RHOJ(Kg/m3) Jun
  1   233.83    20.00  71.276   0.0000e+00   240.00    20.00    71.292     1
  2  3552.52    24.49  70.668   0.6229e+07   227.66    20.01    71.260     2
  3  6877.38    28.82  70.219   0.0000e+00  6877.37    28.80    70.299     3
  4  6796.17    36.41  61.542   0.7852e+07  6796.16    28.85    70.139     4
  5  6623.40    46.87  46.520   0.6451e+07  6623.40    42.47    53.020     5
  6  6609.98    50.99  40.487   0.0000e+00  6609.98    51.05    40.690     6
  7  6488.45   109.77  13.873   0.7631e+08  6488.45    50.94    40.284     7
  8  6419.85   165.63   8.973   0.0000e+00  6419.85   165.63     9.010     8
  9  6363.72   165.63   8.935   0.0000e+00  6363.72   165.63     8.936     9
 10  6362.33   165.63   8.932   0.0000e+00  6362.32   165.63     8.934    10
 11  6358.75   165.63   8.929   0.0000e+00  6359.45   165.63     8.930    11
 12  6356.87   165.63   8.927   0.0000e+00  6358.06   165.63     8.928    12
 13  5163.99   155.52   7.804  -0.7787e+07  6355.68   165.63     8.925    13
 14  3970.76   145.23   6.495   0.0000e+00  3972.30   145.23     6.498    14
 15  3926.32   154.12   6.048   0.0000e+00  3969.22   145.23     6.493    15
 16  6351.57   165.63   8.920   0.0000e+00  6358.75   165.63     8.929    16
 17  5135.35   165.55   7.283   0.0000e+00  6344.39   165.63     8.910    17
 18  3878.09   154.11   5.976   0.0000e+00  3926.31   165.44     5.622    18
 19  3821.51   154.10   5.891   0.0000e+00  3883.41   154.11     5.984    19
 20  3444.86  1323.82   0.631   0.1448e+10  3872.77   154.11     5.968    20
 21  3109.74  2360.02   0.319   0.0000e+00  3770.25   154.09     5.815    21
 22  2962.11  2206.44   0.324  -0.5688e+07  3119.46  2360.04     0.320    22
 23   370.69  1039.24   0.086  -0.7097e+07  3099.99  2360.00     0.318    23
 24    17.04   735.08   0.006   0.0000e+00  1721.18  2059.96     0.203    24
                                              33.06   851.35     0.009    25
```

```
                    1.02  394.13   0.001   26

REFLECTOR INFORMATION
NODE  PRESS     H2     REFL
 IZ  (kPa)   TH2(K)  TWALL(K)  TREFL(K)  TMAX(K)  PKZ
 0  6488.45   50.94   0.      0.      0.      0.
 1  6488.06   53.15   67.29   67.47   67.54   0.44781
 2  6487.15   58.92   81.73   81.97   82.07   0.68056
 3  6485.99   67.74   98.83   99.10   99.21   0.88358
 4  6484.54   79.54  116.87  117.19  117.32   1.04798
 5  6482.80   93.38  132.16  132.53  132.67   1.16657
 6  6480.80  107.92  145.59  145.99  146.14   1.23418
 7  6478.57  122.35  157.53  157.94  158.10   1.24786
 8  6476.13  136.15  168.33  168.74  168.90   1.20699
 9  6473.51  148.91  177.58  177.96  178.11   1.11337
10   6446.00  160.32  184.67  185.01  185.14   0.97110
11   6419.85  165.63   0.      0.      0.      0.

REACTOR INFORMATION

RING: 1
 RING FLOW :   41.257 Kg/s
 CHANNEL EXIT MACH NUMBER:  0.13555
 NUMBER OF FLOW PASSAGES:    58501.75
 FLOW PER PASSAGE: 0.00070523
 RING POWER:  0.1448e+10 W
 RING POWER DENSITY:   1.568 GW/m^3

   Z(m)     PRESS    TH2 (K)  TWALL(K)  TFUEL(K)  TFMAX(K)
  0.        3770.25  154.088   0.        0.        0.
  0.06600   3664.72  259.738   660.881   672.723   676.917
  0.19800   3549.82  508.382   903.421   921.139   927.415
  0.33000   3527.18  787.402  1165.257  1193.392  1203.358
  0.46200   3496.76 1076.292  1428.965  1465.044  1477.824
  0.59400   3458.56 1359.032  1678.906  1722.797  1738.344
  0.72600   3412.56 1622.575  1903.314  1949.826  1966.301
  0.85800   3359.26 1857.001  2093.819  2137.175  2152.533
  0.99000   3299.59 2055.009  2242.463  2279.503  2292.623
  1.12200   3234.47 2210.781  2346.370  2375.156  2385.352
  1.25400   3160.07 2317.674  2401.710  2420.732  2427.470
  1.32000   3119.46 2360.037   0.        0.        0.

REACTIVITY INFORMATION
OMEGAD:  0.    /s THETA   : 100.310  DEMANDED POWER: 0.1448e+10 W
TAUINV:  0.    /s THETADOT:  0.     ACTUAL POWER  : 0.1448e+10 W

REACT : 0.       REACC : 0.004022  REACF :-0.004022
REACTT: 0.       REACTD:-0.007069  REACTM: 0.000674  REACTP: 0.
```

A.3.3.3 37 Element PBR Output File for Orificing Study

```
TIME:  0.
TURBOPUMP INFORMATION
PUMP SPEED : 752.329 RPS  TURBINE POWER:  5.016 MW   PUMP POWER:  3.155 MW
TBCV TRAVEL:  0.274     TURBINE EFFIC:  0.800     PUMP EFFIC:  0.786
BYPASS FLOW:   3.224 Kg/s TURBINE FLOW : 17.972 Kg/s PUMP FLOW : 21.196 Kg/s

NOZZLE INFORMATION
CHAMBER PRESS: 7000.187 kPa  DEMANDED Pc: 7000.000 kPa  Isp1: 1057.703 sec
CHAMBER TEMP : 3000.000 K   DEMANDED Tc: 3000.000 K    Isp2: 1069.624 sec
THRUST:       222.188 kN

VOLC TC (K)    QV (W)    TN (K)    QV (W)   Taw (K)  TStg (K)  TH (K)  VOLH
 5   86.02  0.993e+07  535.45  -0.940e+07  2961.96  2991.26  2799.03   22
 4   51.91  0.127e+08  657.22  -0.122e+08  2692.60  2970.95  1145.49   23

VOLUME AND JUNCTION INFORMATION
Vol PVOL(kPa) TVOL(K) RHOV(Kg/m3)  QVOL (W)  PJUN(kPa) TJUN(K) RHOJ(Kg/m3) Jun
 1  235.86    20.00  71.281   0.0000e+00   240.00    20.00    71.292     1
 2 5672.17    24.43  73.089   0.4013e+07   231.71    20.01    71.270     2
 3 11112.63   28.78  74.400   0.0000e+00  11112.62   28.77    74.418     3
 4 11090.49   51.91  52.907   0.1270e+08  11090.48   28.79    74.383     4
 5 11034.14   86.02  29.809   0.9927e+07  11034.12   70.88    37.318     5
 6 11025.46  101.02  24.725   0.0000e+00  11025.44  101.02    24.772     6
 7 10974.42  174.55  14.070   0.5270e+08  10974.41  101.01    24.677     7
 8 10957.25  250.42   9.893   0.0000e+00  10957.24  250.42     9.898     8
 9 10945.59  250.43   9.888   0.0000e+00  10945.58  250.43     9.888     9
10 10945.22  250.43   9.887   0.0000e+00  10945.21  250.43     9.888    10
11 10944.27  250.43   9.887   0.0000e+00  10944.45  250.43     9.887    11
12 10943.39  250.43   9.886   0.0000e+00  10944.08  250.43     9.887    12
13  9680.07  241.82   9.115  -0.5016e+07  10942.68  250.43     9.886    13
14  8416.68  233.30   8.285   0.0000e+00   8417.45  233.30     8.286    14
15  8415.22  235.96   8.189   0.0000e+00   8415.89  233.30     8.284    15
16 10944.26  250.43   9.887   0.0000e+00  10944.26  250.43     9.887    16
17  9679.73  250.73   8.809   0.0000e+00  10944.23  250.43     9.887    17
18  8413.46  235.96   8.187   0.0000e+00   8415.21  251.03     7.713    18
19  8402.33  235.96   8.177   0.0000e+00   8414.53  235.96     8.188    19
20  7696.39 1780.17   1.040   0.1000e+10   8412.38  235.96     8.186    20
21  7000.26 3000.00   0.558   0.0000e+00   8392.25  235.97     8.168    21
22  6693.04 2799.03   0.574  -0.9400e+07   7000.71 3000.00     0.558    22
23   799.12 1145.49   0.169  -0.1221e+08   7000.19 3000.00     0.558    23
24     8.68  793.82   0.003   0.0000e+00   3928.75 2660.51     0.356    24
                                             16.71  901.87     0.004    25
                                              0.65  479.18     0.000    26

REFLECTOR INFORMATION
NODE  PRESS     H2     REFL
IZ  (kPa)   TH2(K)  TWALL(K)  TREFL(K)  TMAX(K)  PKZ
0  10974.41  101.01    0.       0.       0.      0.
1  10974.23  104.45  131.54   131.85   131.96   0.44781
2  10973.82  113.07  153.64   154.13   154.31   0.68056
```

```
 3  10973.34   124.77   175.83   176.49   176.73    0.88358
 4  10972.79   138.89   197.38   198.20   198.50    1.04798
 5  10972.19   154.87   218.57   219.52   219.87    1.16657
 6  10971.51   172.28   238.75   239.80   240.18    1.23418
 7  10970.77   190.47   257.27   258.38   258.79    1.24786
 8  10969.97   208.80   273.24   274.36   274.77    1.20699
 9  10969.12   226.50   285.76   286.81   287.20    1.11337
 10  10962.97   242.72   294.12   295.05   295.39    0.97110
 11  10957.24   250.42    0.       0.       0.       0.

 REACTOR INFORMATION

RING:  1        NUMBER ELEMENTS IN RING:  1
 ELEMENT FLOW : 0.662 Kg/s        MODERATOR POWER:    0.3276e+06 Wt
 ELEMENT POWER: 0.3076e+08 Wt     MODERATOR TEMP:           678.99 K
 POWER DENSITY:  29.4582 GW/m3    INLET PLENUM H2 TEMP:   251.74 K
 ELEMENT EXIT MACH NUMBER:  0.23675
 INLET REYN # :  203.76           TEMP RISE FACTOR:         10.18

   R(cm)      PRESS     TH2 (K)  TWALL(K)  TFUEL(K)   PKFRB
  3.27000    8016.92   267.806    0.        0.        0.
  3.22000    7779.69   528.134   887.067  1015.177    1.421
  3.12000    7778.87  1019.089  1278.344  1395.238    1.297
  3.02000    7777.44  1432.799  1633.880  1740.539    1.183
  2.92000    7775.40  1780.052  1941.201  2038.521    1.079
  2.82000    7772.71  2072.507  2204.833  2293.633    0.985
  2.72000    7769.39  2319.061  2426.445  2507.469    0.899
  2.62000    7765.42  2523.981  2610.137  2684.067    0.820
  2.52000    7760.77  2692.074  2760.694  2828.151    0.748
  2.42000    7755.44  2830.716  2885.677  2947.228    0.683
  2.32000    7749.39  2942.371  2986.609  3042.771    0.623
  2.27000    7738.17  2990.579    0.        0.        0.

RING:  2        NUMBER ELEMENTS IN RING:  6
 ELEMENT FLOW : 0.599 Kg/s        MODERATOR POWER:    0.3062e+06 Wt
 ELEMENT POWER: 0.2876e+08 Wt     MODERATOR TEMP:           679.72 K
 POWER DENSITY:  27.5370 GW/m3    INLET PLENUM H2 TEMP:   252.23 K
 ELEMENT EXIT MACH NUMBER:  0.21768
 INLET REYN # :  181.79           TEMP RISE FACTOR:         10.34

   R(cm)      PRESS     TH2 (K)  TWALL(K)  TFUEL(K)   PKFRB
  3.27000    7972.19   268.826    0.        0.        0.
  3.22000    7656.56   537.766   891.197  1010.953    1.421
  3.12000    7655.84  1043.704  1297.429  1406.699    1.297
  3.02000    7654.59  1468.950  1664.670  1764.372    1.183
  2.92000    7652.78  1825.503  1981.252  2072.226    1.079
  2.82000    7650.40  2125.197  2252.368  2335.375    0.985
  2.72000    7647.45  2377.237  2479.489  2555.229    0.899
  2.62000    7643.92  2585.066  2665.991  2735.099    0.820
  2.52000    7639.79  2753.272  2816.785  2879.843    0.748
  2.42000    7635.07  2889.414  2939.579  2997.115    0.683
  2.32000    7629.71  3003.755  3044.184  3096.683    0.623
  2.27000    7621.70  3045.356    0.        0.        0.
```

```
RING:  3        NUMBER ELEMENTS IN RING: 12
 ELEMENT FLOW : 0.591 Kg/s         MODERATOR POWER:    0.2920e+06 Wt
 ELEMENT POWER: 0.2742e+08 Wt     MODERATOR TEMP:          659.90 K
 POWER DENSITY:  26.2562 GW/m3    INLET PLENUM H2 TEMP:   251.72 K
 ELEMENT EXIT MACH NUMBER:  0.21073
 INLET REYN # :  181.94           TEMP RISE FACTOR:       10.17

  R(cm)     PRESS    TH2 (K)  TWALL(K)  TFUEL(K)   PKFRB
 3.27000   7954.55   267.786     0.        0.        0.
 3.22000   7627.11   527.859   870.033   984.219   1.421
 3.12000   7626.43  1018.270  1265.427  1369.614   1.297
 3.02000   7625.23  1431.556  1623.283  1718.348   1.183
 2.92000   7623.50  1778.439  1931.545  2018.287   1.079
 2.82000   7621.23  2070.631  2196.839  2275.986   0.985
 2.72000   7618.42  2316.918  2419.354  2491.571   0.899
 2.62000   7615.05  2521.607  2603.787  2669.681   0.820
 2.52000   7611.11  2689.524  2754.974  2815.099   0.748
 2.42000   7606.60  2828.090  2880.521  2935.382   0.683
 2.32000   7601.47  2939.386  2981.577  3031.634   0.623
 2.27000   7591.78  2988.317     0.        0.        0.

RING:  4        NUMBER ELEMENTS IN RING: 18
 ELEMENT FLOW : 0.547 Kg/s         MODERATOR POWER:    0.2706e+06 Wt
 ELEMENT POWER: 0.2541e+08 Wt     MODERATOR TEMP:          648.59 K
 POWER DENSITY:  24.3350 GW/m3    INLET PLENUM H2 TEMP:   251.73 K
 ELEMENT EXIT MACH NUMBER:  0.19507
 INLET REYN # :  168.44           TEMP RISE FACTOR:       10.17

  R(cm)     PRESS    TH2 (K)  TWALL(K)  TFUEL(K)   PKFRB
 3.27000   7919.87   267.817     0.        0.        0.
 3.22000   7541.87   528.123   859.833   965.663   1.421
 3.12000   7541.26  1018.884  1258.404  1354.969   1.297
 3.02000   7540.20  1432.434  1618.196  1706.306   1.183
 2.92000   7538.66  1779.545  1927.544  2007.938   1.079
 2.82000   7536.63  2071.872  2194.088  2267.444   0.985
 2.72000   7534.11  2318.249  2417.405  2484.338   0.899
 2.62000   7531.09  2522.936  2602.430  2663.503   0.820
 2.52000   7527.57  2690.763  2754.028  2809.753   0.748
 2.42000   7523.52  2829.182  2879.833  2930.680   0.683
 2.32000   7518.93  2940.425  2981.168  3027.563   0.623
 2.27000   7510.23  2989.713     0.        0.        0.

 REACTIVITY INFORMATION
 OMEGAD:   0.0000 /s  THETA   : 119.573  DEMANDED POWER: 0.9897e+09 W
 TAUINV:   0.    /s  THETADOT:   0.137  ACTUAL POWER  : 0.9897e+09 W

 REACT : 0.000000  REACC : 0.014786  REACF :-0.014786
 REACTT:-0.021185  REACTD:-0.002261  REACTM: 0.000358  REACTP: 0.007431
```

A.3.3.4 Summary of Comma Separated Value Plot Files

Several output files are generated with data that can be easily imported into spreadsheets for plotting. The data is in comma separated value format with the time as the first variable. The data is saved after a certain number of iterations, that is defined by the user with the variable ISAVE1. The various files and variables that they contain are given in Table A.1

Table A.1 Transient Engine Simulation Code Output Data Plot File Descriptions

Filename	*Content*
FLOWS.CSV	System flow rates
PERIOD.CSV	Reactor period information from controller calculations
POWERS.CSV	System powers
PRESS.CSV	Various junction pressures
REACC.CSV	Control Drum reactivity and position information
REACF.CSV	Individual feedback reacitivity values
REACT.CSV	Total system and feedback reactivity information
STABLE.CSV	Flow stability information for the PBR fuel element
TEMPS.CSV	Various junction temperatures
THRUST.CSV	Nozzle thrust and specific impulse values
TPA.CSV	Turbo-pump control and performance values